



**HAL**  
open science

# Adsorption of chiral molecules in oxide-supported heterogeneous catalysts : a model approach

Elisa Meriggio

► **To cite this version:**

Elisa Meriggio. Adsorption of chiral molecules in oxide-supported heterogeneous catalysts : a model approach. Materials Science [cond-mat.mtrl-sci]. Sorbonne Université, 2019. English. NNT : 2019SORUS550 . tel-03128912

**HAL Id: tel-03128912**

**<https://theses.hal.science/tel-03128912>**

Submitted on 2 Feb 2021

**HAL** is a multi-disciplinary open access archive for the deposit and dissemination of scientific research documents, whether they are published or not. The documents may come from teaching and research institutions in France or abroad, or from public or private research centers.

L'archive ouverte pluridisciplinaire **HAL**, est destinée au dépôt et à la diffusion de documents scientifiques de niveau recherche, publiés ou non, émanant des établissements d'enseignement et de recherche français ou étrangers, des laboratoires publics ou privés.



## SORBONNE UNIVERSITÉ

École Doctorale 397 Physique et Chimie des Matériaux

Laboratoire de Réactivité de Surface  
Institut des NanoSciences de Paris

# Adsorption of chiral molecules in oxide-supported heterogeneous catalysts: a model approach

Par Elisa MERIGGIO

Soutenue le 24/09/2019 devant le jury composé de :

M. <sup>me</sup>	ROBERT-GOUMET Christine	Rapporteur
M. <sup>me</sup>	SAVIO Letizia	Rapporteur
M. <sup>me</sup>	CABARET Delphine	Examineur
M. <sup>me</sup>	D'ANGELO Marie	Examineur
M.	MERCIER Dimitri	Examineur
M.	CARRIER Xavier	Directeur de thèse
M.	HUMBLLOT Vincent	Co-encadrant - Invité
M.	CABAILH Gregory	Co-encadrant - Invité







## Remerciements

À l'issue de ces trois années de thèse, je tiens à remercier tous ceux qui, de près ou de loin, ont contribué à la réalisation de ce travail.

Je souhaite exprimer tout d'abord ma profonde gratitude envers mes directeurs et encadrants de thèse, pour la confiance qu'ils m'ont accordée, leur encadrement et conseils tout au long de ce travail doctoral. Un grand merci à Xavier Carrier pour sa rigueur, sa constante disponibilité et ses qualités pédagogiques que j'ai énormément apprécié et qui m'ont permis de beaucoup m'améliorer. Merci également pour tous les 'bravo' lors de nos réunions, qui m'ont encouragée à faire toujours mieux. Merci à Vincent Humblot, pour son optimisme, son aide et son support toutes les fois où j'ai eu à le solliciter. Je garderai toujours un bon souvenir de la conférence ECOSS, à laquelle on a participé ensemble et pour laquelle ta présence a été d'une grande importance pour moi. Un grand merci à Greg Cabailh, pour avoir toujours été disponible tant sur un plan scientifique que humain malgré ses nombreuses contraintes, pour sa capacité d'écoute et de compréhension tout au long de ces trois années. J'ai beaucoup appris en travaillant avec vous comme encadrants et cela toujours dans une ambiance de confiance et de bonne humeur : je n'aurais pas pu souhaiter mieux. Ces trois années avec vous ont passé si vite et c'est avec un brin de nostalgie que je termine ce parcours.

Un énorme merci va également à Christophe Méthivier, pour sa disponibilité constante, son investissement dans ce projet et tout son aide, qui va bien au-delà du simple encadrement pour l'utilisation du bâti ultravide au LRS. Ses conseils techniques et scientifiques, sa gentillesse et son soutien sont autant de choses qui m'ont permis d'aboutir à cette thèse. Encore merci pour tout cela.

Je désire grandement remercier Rémi Lazzari pour sa patience, tous ses conseils avisés et le temps qu'il a toujours su me dédier. J'ai beaucoup appris en travaillant à vos côtés depuis maintenant le stage de M2 et pour cela je vous en suis très reconnaissante.

Un grand merci à Stéphane Chenot pour son aide, sa gentillesse et sa disponibilité permanente à m'aider lors des manips. Merci également à Pascal David pour l'aide technique, pour sa bonne humeur et son enthousiasme. J'ai beaucoup appris en travaillant avec vous deux et je garderai toujours un bon souvenir de nos nombreuses et agréables discussions.

Je tiens à remercier l'ensemble des membres de mon jury de thèse pour avoir accepté de juger ce travail et pour l'intérêt qu'il lui ont porté. J'adresse également tous mes remerciements à l'école doctorale 397, Physique et Chimie des Matériaux, ainsi qu'au Labex MATISSE pour avoir financé ce travail. Je suis également reconnaissante aux membres de mon Comité de Suivi de Thèse à l'ED397, Dimitri Mercier et Patrick Perrin, pour avoir suivi l'évolution de ce travail au cours de ces trois années.

Je tiens à remercier l'ensemble des membres des deux laboratoires qui m'ont accueillie, le LRS et l'INSP. Si j'ai atteint cet objectif c'est aussi grâce à une ambiance de travail saine et sympathique. Un grand remerciement à tous les membres de l'équipe Oxydes en

basses dimensions de l'INSP, avec qui j'ai passé d'agréables moments. Merci à Slavica Stankic pour sa gentillesse et Jacques Jupille pour ses conseils depuis mon arrivé en stage de M2. Merci également à Hervé Cruguel pour son support pendant mes manipulations au STM environnementale et à Yunlin Zheng pour ces conseils tout au long de ces trois années de thèse. Merci également à Franck Launay pour la discussion initiale sur le sujet de thèse. Sur un plan administratif, merci aux équipes des gestionnaires du LRS et de l'INSP pour leur efficacité et leur aide lors de mes soucis informatiques et administratifs.

Merci à tous les stagiaires, doctorants et post-docs que j'ai pu connaître tout au long de mon parcours à l'INSP et au LRS. Une pensée spéciale va à Nadia, Estelle, Achraf, Roberta, Lionel, Louay, David, Yacine, Ricardo, Bertille, Camille, Zongbei, Miao (et à tous ceux que j'aurai sans doute oubliés). Mille merci également à Maya et Sofiane, qui sont devenus bien plus que des collègues, mais aussi des amis précieux. Un grand merci par ailleurs à Patrizia, qui m'a suivie et conseillé depuis le début et qui a contribué à développer mon gout pour la science des surfaces. Je garderai un heureux souvenir de nos moments passés dans la salle des manip.

S'il y a quelqu'un avec qui j'ai partagé ce long chemin depuis le début c'est mon amie Silvia. L'arrivée sur Paris a été beaucoup plus douce avec toi à mes côtés et tu es toujours là maintenant, dans ce moment important de ma vie. Peu importe ce que l'avenir nous réserve, tu occuperas toujours une place spéciale dans mon cœur. Je remercie également mes chères amies Niki et Fede pour avoir partagé avec moi les joies et les peines d'une thèse. Malgré les kilomètres qui me séparent du Portugal et de l'Italie, votre présence a toujours été d'une aide précieuse pour moi. Un énorme merci va à Danilo e Diletta, pour toute leur aide, leur bonne humeur, le soutien réciproque et les agréables soirées insouciantes passées ensemble. J'ai rencontré à Gênes deux chers et fidèles amis et mon arrivé sur Paris n'a fait que le confirmer.

Maintenant des remerciements plus personnels, à commencer naturellement par mes parents et ma sœur Chiara, pour m'avoir toujours encouragée dans mes choix et avoir su apaiser mes préoccupations. Votre présence sans faille a été essentielle dans ce parcours. Merci de m'avoir toujours soutenue et fait réaliser que tous les problèmes qui paraissent insurmontables ont finalement une solution. Je remercie également mon Ber, de m'avoir supportée et soutenue tout au long de ces trois années. Merci, d'avoir toujours cru en moi, peut-être parfois plus que moi-même, de ton soutien moral continu et pour tout le temps que tu as passé à écouter mes présentations.

C'est à vous tous que je dédie cette thèse.

## Résumé

La catalyse asymétrique hétérogène est une méthode de choix pour la synthèse de composés chiraux énantio-purs. Une approche courante implique la modification d'une surface métallique par un inducteur chiral. Malgré son potentiel, seul un petit nombre de systèmes ont été mis au point jusqu'à présent avec succès. De plus, si l'interaction de cette molécule asymétrique avec des surfaces métalliques monocristallines est maintenant bien comprise, le rôle du support oxyde dans des catalyseurs à base de nanoparticules métalliques supportées demeure encore peu étudié. La conception raisonnée du catalyseur repose sur la maîtrise des interactions à l'échelle moléculaire entre l'oxyde, les nanoparticules métalliques et l'inducteur chiral.

Dans ce contexte, cette étude vise à comprendre les interactions entre ces trois partenaires grâce à une approche de type science des surfaces. Pour représenter le système catalytique, des monocristaux de rutile  $\text{TiO}_2(110)$ , l'acide tartrique (AT) et des nanoparticules de nickel ont été sélectionnés. La nature chimique de l'AT sur  $\text{TiO}_2(110)$  est étudiée par Photoémission X (XPS) et UV et Spectroscopie de Perte d'Énergie d'Électrons Lents à Haute Résolution. La structure de la couche moléculaire et ses points d'ancrage sont étudiés par Microscopie à Effet Tunnel (STM) et Diffraction d'Électrons Lents. Le comportement de décomposition de l'AT est obtenu par désorption thermique (TPD). Les techniques XPS, STM et la Réflectivité Différentielle de Surface sont utilisées pour sonder la croissance du Ni sur le  $\text{TiO}_2$  lorsque la couverture en Ni augmente. Enfin, des perspectives sur le système AT / Ni /  $\text{TiO}_2$  sont proposées principalement par XPS et TPD.





**Contents**

<b>Introduction</b>	<b>1</b>
Aim of the thesis . . . . .	2
Thesis outline . . . . .	3
<b>1 Experimental methods</b>	<b>5</b>
1.1 The Ultra-High Vacuum (UHV) apparatus . . . . .	5
1.1.1 The UHV chamber . . . . .	5
1.1.2 Pumping systems and pressure detection . . . . .	6
1.2 Sample preparation . . . . .	7
1.3 X-Ray Photoemission Spectroscopy . . . . .	8
1.3.1 Basic principles of photoemission . . . . .	8
1.3.2 XPS: a surface sensitive technique . . . . .	9
1.3.3 Spectrum characterisation . . . . .	9
1.3.3.1 XPS background . . . . .	9
1.3.3.2 Core level peaks . . . . .	10
1.3.3.3 Auger peaks . . . . .	11
1.3.3.4 Plasmon losses . . . . .	12
1.3.3.5 Shake-up and shake-off peaks . . . . .	12
1.3.3.6 Sample charging effects . . . . .	12
1.3.4 XPS analysis . . . . .	13
1.3.4.1 Background removal and peak fitting . . . . .	13
1.3.4.2 Thickness estimation . . . . .	14
1.3.5 Instrumentation . . . . .	15
1.4 Ultraviolet Photoemission Spectroscopy . . . . .	16
1.4.1 UPS for the valence band analysis . . . . .	16
1.4.2 UPS for work function measurements . . . . .	17
1.4.3 Instrumentation . . . . .	17
1.5 Scanning Tunnelling Microscopy . . . . .	18
1.5.1 Basic principles . . . . .	19
1.5.2 Tunnelling theory . . . . .	21
1.5.3 Experimental details . . . . .	22
1.6 Low Energy Electron Diffraction . . . . .	23
1.6.1 Basic principles . . . . .	23
1.6.2 Adsorbate superstructures . . . . .	24
1.6.3 Experimental set-up . . . . .	25
1.7 Temperature Programmed Desorption . . . . .	26
1.7.1 TPD theory . . . . .	26

1.7.2	Experimental apparatus . . . . .	27
1.8	Polarisation Modulation-Reflection Absorption InfraRed Spectroscopy . . .	27
1.8.1	Basic principles of RAIRS . . . . .	28
1.8.2	PM-RAIRS . . . . .	29
1.8.3	Experimental setup . . . . .	29
1.9	High Resolution Electron Energy Loss Spectroscopy . . . . .	31
1.9.1	Theoretical details . . . . .	31
1.9.2	Dipole scattering . . . . .	31
1.9.3	Experimental apparatus . . . . .	33
1.10	Surface Differential Reflectivity Spectroscopy . . . . .	34
1.10.1	Experimental apparatus . . . . .	35
<b>2</b>	<b>State of the art</b>	<b>37</b>
2.1	Chirality . . . . .	37
2.2	Heterogeneous asymmetric catalysis . . . . .	38
2.3	Supported enantioselective catalysts . . . . .	40
2.4	Chirality at surfaces . . . . .	41
2.5	Tartaric acid adsorption on metal surfaces . . . . .	43
2.6	The rutile TiO <sub>2</sub> structure . . . . .	46
2.6.1	Bulk structure . . . . .	46
2.6.2	The rutile TiO <sub>2</sub> (110) surface . . . . .	47
2.7	Carboxylic acid adsorption on TiO <sub>2</sub> (110) . . . . .	49
2.7.1	Formic acid adsorption on rutile TiO <sub>2</sub> (110) . . . . .	49
2.7.2	Other carboxyl-containing molecules on TiO <sub>2</sub> (110) . . . . .	52
2.8	Chiral molecule adsorption on rutile TiO <sub>2</sub> (110) . . . . .	55
2.9	Nickel growth on rutile TiO <sub>2</sub> (110) . . . . .	55
2.9.1	Growth modes . . . . .	56
2.9.2	Previous studies on Ni nucleation and growth . . . . .	57
2.10	Conclusion . . . . .	62
<b>3</b>	<b>Tartaric acid adsorption on TiO<sub>2</sub>(110)</b>	<b>65</b>
3.1	Infrared spectroscopy on oxide surfaces . . . . .	66
3.2	RR-TA adsorption on Au(111) and Cu(110): PM-RAIRS and XPS results .	68
3.2.1	RR-TA adsorption on Au(111) . . . . .	68
3.2.2	RR-TA adsorption on Cu(110) . . . . .	70
3.3	RR-TA adsorption on rutile TiO <sub>2</sub> (110) . . . . .	71
3.3.1	Chemical analysis . . . . .	71
3.3.2	Vibrational measurements . . . . .	74
3.3.2.1	General considerations: HR spectra of oxide surfaces, de-convolution method . . . . .	74
3.3.2.2	Results . . . . .	76
3.3.3	Structural results . . . . .	78
3.3.4	Proposed adsorption model . . . . .	79
3.4	UPS measurements . . . . .	80
3.4.1	Adsorbate-induced work function variations . . . . .	80
3.4.2	Results . . . . .	81
3.5	Conclusion . . . . .	84

<b>4</b>	<b>Chemical nature and thermal decomposition behaviour of RR-TA multilayers on rutile TiO<sub>2</sub>(110)</b>	<b>85</b>
4.1	Experimental aspects . . . . .	85
4.2	Thermal stability of RR-TA on rutile TiO <sub>2</sub> (110) . . . . .	87
4.2.1	Introduction . . . . .	87
4.2.2	Temperature programmed desorption results . . . . .	87
4.2.3	Activation energy for RR-TA desorption in the multilayer regime . . . . .	90
4.3	Chemical nature of RR-TA multilayers on rutile TiO <sub>2</sub> (110) . . . . .	91
4.4	Conclusion . . . . .	94
<b>5</b>	<b>Ni adsorption on TiO<sub>2</sub>(110)</b>	<b>95</b>
5.1	Morphologic study of Ni clusters . . . . .	96
5.1.1	Technical aspects of Ni cluster size measurement . . . . .	96
5.1.2	Ni cluster growth . . . . .	96
5.2	XPS analysis of Ni cluster growth . . . . .	97
5.2.1	Chemical analysis . . . . .	97
5.2.2	XPS modelling of Ni clusters . . . . .	101
5.3	Morphology of Ni clusters as seen by differential reflectivity . . . . .	103
5.3.1	Theory behind SDRS . . . . .	103
5.3.2	Optical dielectric functions of Ni and TiO <sub>2</sub> . . . . .	105
5.3.3	Dielectric simulations . . . . .	107
5.3.4	SDRS experimental spectra . . . . .	109
5.3.5	Film growth stages: the evolution of SDRS integrated intensity . . . . .	111
5.4	Conclusion . . . . .	112
<b>6</b>	<b>Modelling the complete catalytic system: perspectives on TA adsorption on Ni-covered TiO<sub>2</sub>(110)</b>	<b>113</b>
6.1	Chemical analysis . . . . .	113
6.2	Thermal stability of RR-TA . . . . .	116
6.2.1	Thermal stability of RR-TA on Ni(111) . . . . .	116
6.2.2	Thermal stability of RR-TA on Ni/TiO <sub>2</sub> (110) . . . . .	118
6.3	Conclusion . . . . .	122
	<b>Conclusion</b>	<b>125</b>
	<b>Bibliography</b>	<b>129</b>



---

## Introduction

---

The production of enantioenriched to enantiopure compounds has gathered an increasing scientific interest both in the academic and industrial context. Their importance stems from the chiral character of many biological building blocks, which exist in only one enantiomeric form [1]. For example, sugars are exclusively right-handed while amino acids appear only in the left-handed form. Biological homochirality leads to different interaction with opposite enantiomers, in such a way that if an enantiomer of a drug has beneficial effects, the opposite one may be toxic, thus leading to potential drastic consequences. To avoid this, the enantiomeric purity required for pharmaceuticals is higher than 99%, while slightly less for agrochemicals, around 80% [2].

Several strategies have been developed in response to the increasing demand for non-racemic chiral compounds, among which one of the most promising is asymmetric catalysis. In asymmetric catalysis the synthesis of a chiral compound is induced by the presence of a chiral catalyst. Both homogeneous and heterogeneous asymmetric catalysis have been developed, depending on whether or not the catalyst is in the same phase as the reactants and products. With homogeneous asymmetric reactions high activities and selectivities have been obtained over a wide range of reactions. However, major drawbacks are related to the difficulty of separation, recovery and reuse of the expensive chiral catalysts, which is nowadays an important requirement for the development at the industrial scale. Among the major advantages offered by heterogeneous catalysis over the homogeneous counterpart, there is the easier separation of reactants, catalysts and reaction products. Different routes have been explored for the design of heterogeneous asymmetric catalysis and one of the most promising method is the modification of a catalytic metal surface by an appropriate organic chiral modifier. The simple but effective concept behind this approach is to merge the catalytic activity provided by the metal surface with the asymmetric induction assured by the chiral modifier. Nevertheless, despite its great potential and economic advantages, a limited number of successful systems have been developed so far, namely the enantioselective hydrogenation of  $\alpha$ -keto esters over modified Pt catalysts and the asymmetric hydrogenation of  $\beta$ -keto esters over modified Ni catalysts. Both  $\alpha$ -amino acids (such as alanine) and  $\alpha$ -hydroxy acids (such as tartaric acid) have shown to be successful chiral modifiers in Ni-based catalysts [3].

Real catalytic systems are complex, so that unravelling the fundamental mechanisms behind, which is an essential requirement for the development of new efficient systems, is complicated. Many studies have thus focused on a surface science approach, which consists in modelling the catalytic system with single crystal metal surfaces, on which chiral modifiers are adsorbed in the controlled conditions of ultra high vacuum (UHV) [4,5]. Over the past decades, most of fundamental works have been devoted to such model systems based on single crystal metal surfaces, while the role of the oxide support in

supported metal catalysts has usually been overlooked. Nevertheless, supported metal catalysts present several advantages with respect to bulk systems. First of all, the metal catalyst is deposited in the form of particles dispersed on a support, which reduces the metal quantity needed and consequently the total cost. Second, but not less important, the presence of metal particles increases the surface area where catalytic reactions take place. Moreover, the metal particle reactivity can be very different from that of bulk metallic systems and can be tuned by changing their size and electronic properties. A classical example is provided by gold, which despite being chemically inert in its bulk form, it is instead chemically active as supported nanoparticles and is able to catalyse several reactions, such as carbon monoxide oxidation [6–8]. Moreover, the catalytic activity may strongly depend on the nanoparticle size, as shown in the case of gold, where active particles are smaller than  $\sim 5$  nm [6]. It must also be added that sometimes the support, besides stabilising nanoparticles and ensuring mechanical strength, is not inert and may provide additional active sites for the reaction. Interactions between the support and the metal catalysts may also occur and change the catalytic activity, selectivity and stability, as in the case of reducible metal oxides (such as  $\text{TiO}_2$ ) where strong metal-support interactions are known to exist [9, 10].

Fundamental questions remain on the role of the oxide support on the chiral induction during the reaction. A detailed understanding of the reaction mechanism and the mode of action of the oxide support and chiral modifier requires therefore knowledge of the interactions at a molecular level between the three fundamental partners of the catalytic system: oxide support, metal nanoparticles and chiral modifier.

## Aim of the thesis

In this context, the present thesis seeks to explore some aspects of these complex heterogeneous enantioselective catalytic systems, focussing on the interactions between the three fundamental components. For this purpose, we have modelled a catalytic system with (R,R)-Tartaric acid (RR-TA) molecules, nickel nanoparticles and rutile  $\text{TiO}_2(110)$  single crystals, selected as the prototypical chiral modifier, metal catalyst and the oxide support, respectively. Rutile  $\text{TiO}_2(110)$  single crystals are used as test-bed oxide supports due to their great availability and versatility for their characterisation through surface science techniques. Indeed, while being a wide band gap semiconductor (band gap  $\sim 3$  eV),  $\text{TiO}_2$  single crystals can be made sufficiently conductive by reducing the samples under UHV conditions. Being an efficient enantioselective hydrogenation catalyst, nickel has been chosen as prototypical metal catalyst, while RR-TA molecules have been selected as model chiral modifier being one of the most successful one. Moreover, the adsorption of RR-TA has been extensively addressed in previous studies on Ni(111) and (110) surfaces, which are also the main facets found in Ni nanoparticles.

Each step of the catalyst preparation is characterised by a fundamental surface science approach, where nickel and RR-TA molecules are deposited by evaporation on the well-defined rutile single crystal surfaces in the clean and controlled conditions of UHV. A variety of surface science techniques is then used to gain insight into the physics and chemistry behind the system. While being a model approach, this method allows indeed the investigation and comprehension of this complex system at the nanoscale.

Due to the complexity of the catalytic system, the investigation of the interactions between chiral modifier, metal catalyst and oxide support is addressed step by step. With

this aim, the first part of the work has been devoted to RR-TA deposition on a clean rutile  $\text{TiO}_2(110)$  surface. The evaporation of Ni on  $\text{TiO}_2(110)$  has been subsequently addressed, at first without the presence of the chiral modifier. Finally, the three fundamental partners of the catalytic system are considered together.

## Thesis outline

The present thesis is organised as follows. Besides this general introduction, six chapters composes this work, followed by the conclusion and prospects on future research directions.

The first chapter describes the experimental set-up and techniques used all along this work. The different UHV chambers at the Laboratoire de Réactivité de Surface (LRS) and the Institut de Nanoscience de Paris (INSP) are presented together with the details on the sample preparation, a fundamental step in surface science studies. A general overview is then proposed about the basic principles of the main experimental techniques used to decipher the fundamental interactions between RR-TA molecules and Ni with  $\text{TiO}_2(110)$  single crystals.

The second chapter is a bibliographic study, in which the attention is first addressed to some fundamental aspects of the concepts of chirality and heterogeneous asymmetric catalysis useful in the following chapters. The emphasis is then put on RR-TA molecules and more precisely on their adsorption on metal surfaces, such as  $\text{Cu}(110)$ ,  $\text{Ni}(110)$  and  $\text{Ni}(111)$ , which are exemplary cases of how chirality may be imparted to a metallic surface at different levels. The rutile  $\text{TiO}_2$  structure is then described, with a particular attention to the  $(110)$  surface, chosen as model metal oxide substrate for this study. A state of the art of the reactivity of the rutile  $\text{TiO}_2(110)$  surface with other carboxyl-containing but non chiral molecules is presented. These are important starting points to understand the adsorption of RR-TA on the same surface. The few studies of chiral molecules on  $\text{TiO}_2(110)$  are also discussed. Finally, in the last section of the chapter, previous results of Ni adsorption on  $\text{TiO}_2(110)$  are reviewed.

In chapters 3, 4 and 5 the main results obtained are presented. More precisely, chapter 3 describes RR-TA adsorption on the rutile  $\text{TiO}_2(110)$  surface in the monolayer regime. Several surface science techniques have been employed to adress different aspects of the molecular adsorption. Information on RR-TA chemical nature are gained by X-Ray Photoemission Spectroscopy (XPS) and by depositing RR-TA in parallel on model metal surfaces, namely  $\text{Au}(111)$  and  $\text{Cu}(110)$  on which the TA molecular form is well known. The results obtained are supported by High Resolution Electron Energy Loss Spectroscopy data, which provides information on the molecular vibrational modes and thus on the TA chemical state. The 2D molecular layer ordering and anchoring sites on the  $\text{TiO}_2(110)$  surface are deciphered by means of Scanning Tunnelling Microscopy (STM) and Low Energy Electron Diffraction.

The study of RR-TA adsorption is then extended from the monolayer to the multi-layer regime in chapter 4. Moreover the question of the molecular thermal stability and decomposition on  $\text{TiO}_2(110)$  is addressed by Temperature Programmed Desorption (TPD).

Chapter 5 presents the main results on Ni adsorption on rutile  $\text{TiO}_2(110)$ . STM and XPS are combined to study the structure, growth mode and chemical state of Ni. It fol-



lows a detailed introduction of the fundamental theory behind the technique of Surface Differential Reflectivity Spectroscopy (SDRS), a less popular but well suited technique for the real-time and *in-situ* characterisation of metal growth on oxide substrates. Dielectric simulations are performed in parallel to see the influence of the metal particle aspect ratio on the optical response. A comparison with the recorded differential reflectivity spectra enables to gain information on the particle shape over a wide range of Ni coverages. Moreover, different stages of film growth can be monitored by SDRS as well as by looking at the integrated signal.

Chapter 6 is devoted to some perspective studies on the complete catalytic system, TA/Ni/ TiO<sub>2</sub>(110). In particular, XPS is used for the chemical analysis, while TPD probes the decomposition of RR-TA molecules for different Ni coverages deposited on TiO<sub>2</sub>(110). RR-TA decomposition is studied in parallel on Ni(111) and compared to the reactivity of Ni nanoparticles.

The thesis ends with a summary of the main findings of the previous chapters and an outlook to future research directions.

# CHAPTER 1

---

## Experimental methods

---

### 1.1 The Ultra-High Vacuum (UHV) apparatus

#### 1.1.1 The UHV chamber

Since we are interested in studying physical and chemical processes taking place at surfaces and interfaces, the controlled conditions of Ultra-High Vacuum (UHV) are of paramount importance to keep samples clean throughout the time scale of experiments. All manipulations have thus been carried out with base pressures of  $10^{-10}$  mbar or better. The rapidity in covering the surface depends on the sticking coefficient  $S$ , defined as the ratio of particles sticking to a surface over the total amount colliding with it. Generally speaking, if a monoatomic gas with  $S=1$  is considered, it will take approximately 1 s for contaminants to completely coat the surface at a pressure of  $10^{-6}$  mbar. For pressures of the order of  $10^{-10}$  mbar the time necessary to form one monolayer accordingly increases to  $10^4$  s (just under 3 hours), thus allowing to perform the desired analysis with negligible amount of surface contamination. Moreover, when techniques employing particle beams as probe are used, UHV is necessary to increase the particle inelastic mean free path (IMFP) and let them reach the sample or detector without being scattered by gas molecules. Last but not least, many facilities such as X-ray sources, electron sources and detectors necessitate UHV pressures to operate.

Four different UHV systems were used in this work (figure 1.1). Beside a loadlock which allows a quick sample introduction without breaking the vacuum, these UHV vessels generally present two independent parts: a preparation chamber which provides facilities for sample preparation (detailed in section 1.2) and an analysis chamber, containing characterisation techniques specific to each chamber. To go into more details, the first chamber at INSP (figure 1.1a) is equipped with an X-Ray Photoemission Spectroscopy (XPS) Omicron EA 125 (5 channeltrons) hemispherical analyser with non-monochromatic dual anode Al- $K\alpha$  (1486.6 eV) and Mg- $K\alpha$  (1253.6 eV) sources, a Low Energy Electron Diffractometer (ErLEED from SPECS) and a Scanning Tunnelling Microscope (STM) with an Omicron Variable Temperature (VT)-AFM head controlled by Matrix electronics. STM imaging is also performed in an Omicron Vakuumphysik XA VT-STM chamber called 'STM-environmental' at the INSP (shared between the INSP/LRS/LCPMR laboratories, figure 1.1b), which is combined with a LEED-AES (Low Energy Electron Diffraction-Auger Electron Spectroscopy). The UHV chamber in figure 1.1c (INSP) houses a High Resolution

Electron Energy Loss spectrometer LK2000 from LK-Tech, which is described in section 1.9. Lastly, the UHV vessel at the LRS (figure 1.1d) is equipped with a monochromatised Al  $K\alpha$  X-ray source together with hemispherical analyser from SPECS (Phoibos 100 1D Delay Line Detector) for XPS analysis, a Low Energy Electron Diffractometer and a Polarisation Modulation-Reflection Absorption InfraRed Spectroscopy (PM-RAIRS) setup, thoroughly described in 1.8.

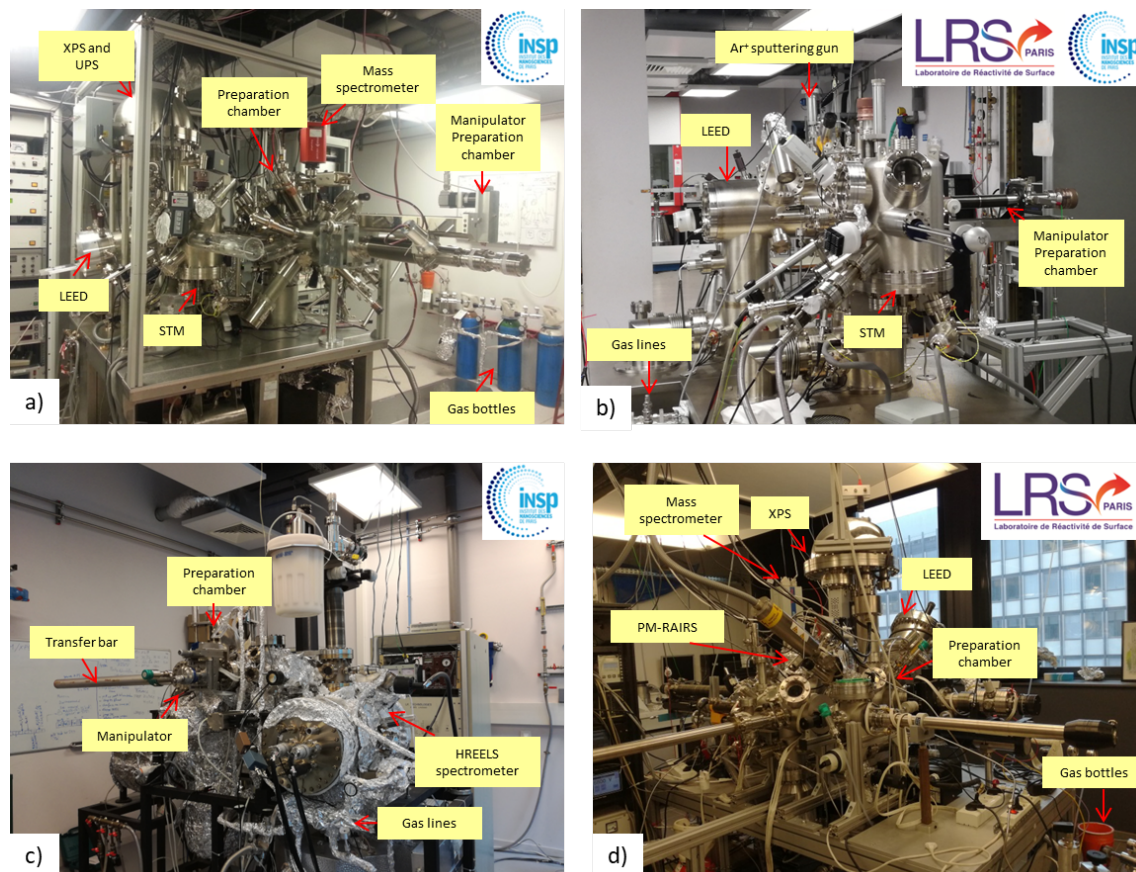


Figure 1.1: The UHV chambers used in this work.

Generally speaking, for the UHV chamber conception, suitable materials with a low vapour pressure and endurance to the high bake-out temperatures are used: ceramics for electrical isolation, glass, metals as copper, aluminium, tantalum, tungsten and molybdenum are just a few examples. Moreover, the vacuum vessels are made of stainless steel or of  $\mu$ -metal, a nickel-iron alloy, when shielding from stray magnetic fields is required. Samples are transferred between the different parts with magnetic transfer arms and wobble-sticks. Sometimes sample preparation requires the use of specific gases, such as Ar and O<sub>2</sub>, which are introduced inside the chamber by means of leak valves. The relative gas lines are baked-out and flushed before being used to ensure the gas purity.

### 1.1.2 Pumping systems and pressure detection

To maintain the UHV chambers at such low pressures, a combination of several pumps is necessary. For a rough vacuum ( $10^{-3}$  mbar), rotary/scroll pumps are employed, while to reach the UHV conditions ( $10^{-10}$  mbar), turbomolecular pumps and ion pumps in conjunction with titanium sublimation pumps are used. A suitable pumping system is not

the only requirement to be able to reach such low pressures. In fact, UHV chambers are periodically baked out, *i.e.* heated at high temperature for several hours (130°C for 2 – 3 days in our case) to degas atoms and molecules adsorbed on the walls, mainly water, when the chamber is occasionally opened for maintenance and thus exposed to air.

In parallel to the pumping system, different types of gauges are used to monitor the pressure over the whole range. Pirani gauges are employed down to  $10^{-4}$  mbar, while Bayard-Alpert ones are used for lower pressure measurements.

## 1.2 Sample preparation

Throughout this work, rutile  $\text{TiO}_2(110)$  single crystals and occasionally  $\text{Au}(111)$ ,  $\text{Cu}(110)$  and  $\text{Ni}(111)$  have been studied. Rutile  $\text{TiO}_2(110)$  single crystals were provided by Mateck GmbH, while  $\text{Cu}(110)$  and  $\text{Au}(111)$  were supplied by Surface Preparation Laboratory, The Netherlands. Samples were mounted on Mo or Ta supports by means of Ta clips or wire. Since we are interested in studying phenomena occurring at the very surface, samples need to be atomically clean. A typical UHV sample preparation consists in several cycles of  $\text{Ar}^+$  ion sputtering to remove the first surface layers followed by annealing at different temperatures depending on the sample to restore the surface crystallinity. For  $\text{TiO}_2(110)$  single crystals the annealing temperature is around 1000 K, while 900 K is suitable for Ni and 750 K for Au and Cu. In chambers of figure 1.1a and c, sample heating is performed using a home-made electron beam furnace. The sample is resistively heated up to 800 K, by flowing current into a spiral metallic filament placed behind the sample holder, and then a high voltage of 1 kV is applied between the sample and the filament to reach higher temperatures by electron bombardment. In chambers 1.1b and d annealing is instead provided by a PBN (Pyrolytic Boron Nitride)-coated graphite heating element. Depending on the chamber, sample temperatures are measured either by means of optical pyrometers (Impac IGA 140) or by thermocouples spot-welded on the manipulators. The absence of contamination on the surface is then checked by X-Ray Photoemission Spectroscopy (XPS) (see section 1.3), while a good surface reconstruction is confirmed by LEED (see section 1.6) and by STM in the dedicated chambers (see section 1.5).

(R,R)-Tartaric acid (TA) powder is provided by Acros Organics (Fisher Scientific SAS - Illkirch - France). It is deposited on the single crystal surfaces by thermal evaporation using a Knudsen cell. More precisely, the evaporant is placed in a glass tube and resistively heated by a tantalum wire spirally wound around it. The evaporator is initially isolated from the main UHV chamber using a gate valve and pumped by a turbomolecular pump. Before being used, TA powder is carefully degassed for several hours, even between different depositions. During dosing, the gate valve is opened to introduce the evaporator inside the main chamber, in front of the crystal surfaces. During dosing the base pressure never exceeds  $10^{-9}$  mbar.

Ni is deposited by evaporation, using an EFM3 evaporator. The evaporation cell is placed in a water cooled Cu tube and Ni is evaporated from a crucible by electron bombardment heating with a base pressure of  $10^{-10}$  mbar during dosing. Electrons are emitted by flowing current in a thoriated-tungsten filament and a high voltage is applied between the filament and the crucible. A flux monitor allows to control the evaporation rate and a shutter is also integrated to expose the sample only when the desired evaporation conditions are attained. Ni thickness on the rutile  $\text{TiO}_2$  surface is estimated both by STM images and XPS from the attenuation of the Ti 2p peak intensity.

### 1.3 X-Ray Photoemission Spectroscopy

X-Ray Photoemission Spectroscopy (XPS) also known as ESCA (Electron Spectroscopy for Chemical Analysis) is a surface science technique widely employed for chemical characterisation. Both qualitative and quantitative information on the sample chemical composition and on the chemical (oxidation) state can be obtained.

#### 1.3.1 Basic principles of photoemission

Photoemission spectroscopy is based on the photoelectric effect, first revealed by H. Hertz in 1887 and subsequently conceptualized by A. Einstein in 1905 [11]. The actual XPS technology was mainly developed by the Swedish Siegbahn in the 1960s, who was awarded with the Nobel Price in 1981 [12].

When a sample surface is irradiated with photons of energy  $h\nu$ , electrons are excited to higher energy levels or, if the photon energy is larger than their binding energies  $E_b$ , ejected from the sample with kinetic energies  $E_k$  given by Koopman's equation in the one particle approximation:

$$E_k = h\nu - E_b - \phi_s \quad (1.1)$$

where  $\phi_s$  is the sample work function, *i.e.* the minimum energy required to remove an electron to infinity from the sample surface. The photoemitted electrons are analysed in energy by an electrostatic analyser, to give the typical XPS spectrum showing the intensity versus electron energy. Since atomic orbital binding energies are specific to each element, it is thus possible to identify the elements and gain information on the sample chemical composition from its spectrum.

While performing an experiment, analyser and sample are put in electrical contact and their Fermi levels are aligned (figure 1.2). Since the analyser is characterised by its own work function  $\phi_a$ , a contact potential ( $\phi_s - \phi_a$ ) is established, which shifts the measured  $E_k$  to:

$$E_k = h\nu - E_b - \phi_s + (\phi_s - \phi_a) = h\nu - E_b - \phi_a \quad (1.2)$$

Equation (1.2) indicates that the electron energy depends only on  $\phi_a$ , which is determined by calibrating the analyser kinetic energy scale with standards, usually with conducting substrates. In our case calibration was checked with a Ag single crystal sample, by setting the Ag 3d core level peak at 368.2 eV in  $E_b$ .

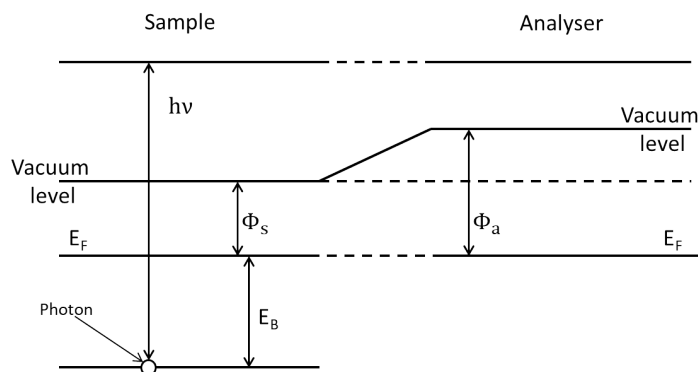


Figure 1.2: Energy level alignment when sample and spectrometer are put in electrical contact.

Depending on the incident photon energy used, two different techniques are distinguished: X-Ray Photoemission Spectroscopy (XPS), used to probe the deep core levels with photon energies usually in the range of 100 eV - 10 KeV and Ultraviolet Photoemission Spectroscopy (UPS), which employs low energy photons between 10 and 50 eV to excite valence electrons.

### 1.3.2 XPS: a surface sensitive technique

While incident photons have long penetration depths and the ionisation process thus occurs over several micrometers from the sample surface, only those electrons coming from the topmost layers, within tens of angstroms, will reach the detector without suffering energy losses [13, 14]. The probability for an electron to interact with matter is indeed significantly higher than for a photon and leads to plasmon losses, core level ionisations and valence band electronic excitations. Because of such attenuation and inelastic effects, the photoelectron escape probability is well described by an exponential law. The signal intensity originating from a thin layer  $dx$  at a distance  $x$  from the sample surface is indeed proportional to:

$$dI \propto e^{-x/\lambda(E) \cdot \cos \theta} \cdot dx \quad (1.3)$$

where  $\theta$  is the take-off angle of the emitted photoelectrons with respect to the surface normal and  $\lambda$  is the inelastic mean free path (IMFP) defined as the mean distance travelled by an electron between two subsequent inelastic scattering collisions with atoms.

By integrating equation (1.3) from 0, the sample surface, to  $t$ , the layer thickness, the total intensity is expressed as:

$$I = I_0[1 - e^{-t/\lambda(E) \cdot \cos \theta}] \quad (1.4)$$

From equation (1.4), 95% of the photoemitted intensity comes from a depth  $< 3\lambda \cos(\theta)$ , thus commonly defined as the probed depth. The maximum sampling depth is obtained when photoelectrons are collected at normal emission ( $\theta = 0^\circ$ ), while grazing emission measurements ensure the highest surface sensitivity. The IMFP is described by a universal curve common to a broad variety of materials [15]. For electron kinetic energies between 10 and 2000 eV,  $\lambda$  is comprised between 5 and 20 Å [16], hence the XPS surface sensitivity.

### 1.3.3 Spectrum characterisation

A typical XPS survey spectrum for the rutile  $\text{TiO}_2(110)$  surface is shown in figure 1.3. The photoelectron intensity is plotted as a function of the binding energy, increasing from right to left. The intense and sharp lines observed for binding energies higher than 20 eV are attributed to core levels. Further information is often obtained from the valence band region located at lower binding energies (usually between 0 and 15 eV). To a first approximation, the XPS spectrum reflects the density of the occupied states of the probed materials [17]. In reality spectra are more complicated due to the presence of Auger peaks, most often the KLL and the LMM transitions, plasmon losses and satellite peaks, superimposed to a continuous step-like background arising from electrons that have suffered energy losses.

#### 1.3.3.1 XPS background

In figure 1.3, peaks overlap a continuous background, with a step-like structure, whose origin involves several different contributions. On the low binding energy side, the background is mainly due to Bremsstrahlung processes and secondary electrons, while on the

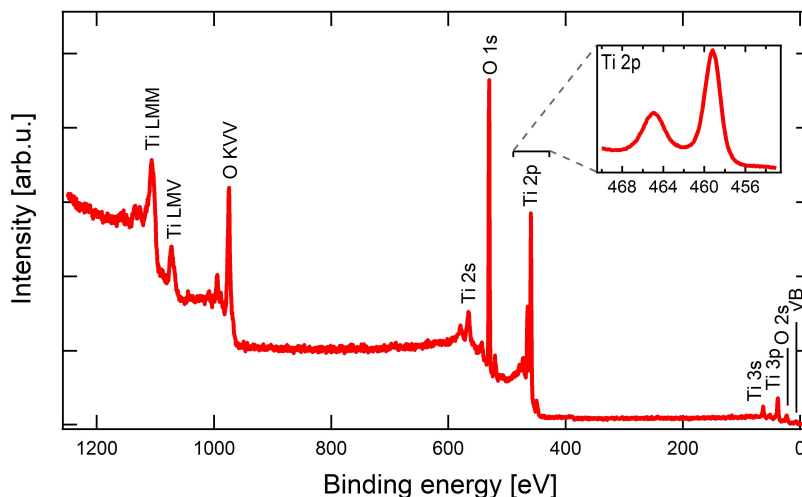


Figure 1.3: XPS survey spectrum of rutile TiO<sub>2</sub>(110) recorded with an unmonochromatised Al K $\alpha$  source at 1486.7 eV. A zoom on the Ti 2p region is shown in the inset.

high binding energy side, the main contributions arise from photoelectrons which have undergone inelastic processes [18, 19]. Moreover, the background is continuous since inelastic events are multiple and random [13]. When monochromatic sources are employed, the background level may be significantly reduced.

### 1.3.3.2 Core level peaks

The sharpest and most prominent peaks observed in a XPS spectrum arise from photoelectrons emitted from core levels which do not have suffered inelastic scattering processes. Besides elucidating the sample composition, core level peaks provide additional information on chemical (oxidation) states. Indeed, different chemical states of the same element give rise to the so-called chemical shifts. With the term chemical shifts we refer to small changes in the electron  $E_b$ , ranging from fractions of eV up to several eV, for example in the case of transition metal oxides when passing from a metal to its oxide. The origin of the chemical shifts must be sought not only in the electron  $E_b$  dependence on the initial energy level from which the photoelectron is ejected, but also in its sensitivity to the atomic chemical environment and oxidation state. When chemical bonds are formed, valence electron charge transfers occur between the atoms involved, thus affecting the charge density and the screening of the nucleus Coulomb attraction. That changes the electron binding energy in orbitals and results in a shift of the XPS peaks. Generally speaking, the greater the electronegativity, the higher the shift to lower binding energies. When chemical shifts are comparable with the peak linewidth and when elements are found in many different oxidation states, a peak fitting procedure is often required for an accurate analysis. Moreover the use of monochromators may facilitate the spectrum interpretation since a better resolution is achieved [15, 18].

For organic molecules containing significant quantities of carbon and oxygen, chemical shifts of the C 1s and O 1s core levels may be considered to decipher the molecular chemical state [15]. They were indeed used in this work to provide useful information on the tartaric acid form.

Another important feature observed in core level peaks is the core level splitting, which occurs when photoelectrons are ejected from energy levels with an orbital angular momen-

tum  $l$  greater than zero. A splitting of the corresponding XPS peak is then observed, as it can be seen for example for the Ti 2p peak in the inset of figure 1.3. The physical reason behind the doublet formation is the spin-orbit coupling, *i.e.* the coupling between the electron spin momentum and its orbital angular momentum. This gives rise to two possible states with different values of the total angular momentum  $j$ , namely  $j_1 = |l - 1/2|$ , which correspond to the high binding energy doublet peak and  $j_2 = |l + 1/2|$ , assigned to the low binding energy peak. The area ratio of the two components is given by the ratio of their respective degeneracies:  $(2j_1 + 1)/(2j_2 + 1)$ , thus assuming the values of 1/2, 2/3 and 3/4 for  $p$ ,  $d$  and  $f$  doublets, respectively.

When non-monochromatic sources are employed, additional emission lines appear, which are due to a family of less probable and thus less intense transitions with respect to the main  $K\alpha_{1,2}$  line. In the emission spectrum they give rise to the so-called satellite peaks whose energy displacement and relative intensities are summarised in Table 1.1 [18,20–22].

Table 1.1: X-ray satellite energy displacements and their relative intensities with respect to the main  $K\alpha_{1,2}$  line [14].

	$\alpha_{1,2}$	$\alpha_3$	$\alpha_4$	$\alpha_5$	$\alpha_6$	$\beta$
Al displacement [eV]	0	9.8	11.8	20.1	23.4	69.7
Relative intensity	100	6.4	3.2	0.4	0.3	0.6
Mg displacement [eV]	0	8.4	10.2	17.5	20.6	48.7
Relative intensity	100	8.0	4.1	0.55	0.5	0.5

Moreover, ghost peaks may occasionally appear. They may arise from impurities on the anode surface, for instance when it is partially oxidised, from the anode base structure made of Cu, from the Al window in the source used to protect the sample from electron bombardment or even from the unused anode in twin anode sources [13,23]. For example, if the lamp is set on the Al anode, ghost peaks from the Mg  $K\alpha$  radiation will be shifted by 233 eV to lower kinetic energy with respect to those generated by Al  $K\alpha$  radiation.

### 1.3.3.3 Auger peaks

After the photoemission process, the atom is left in a highly unstable excited state. To release the excess energy, two competitive relaxation mechanisms may take place: as shown schematically in figure 1.4, the core hole is filled by an electron from a higher orbital, causing the emission of either an X-ray photon or of another electron, called Auger electron [18].

Auger transitions are named after the three energy levels involved in the process, in the order of intervention. Let us consider for example a generic  $XYZ$  Auger transition: the photoemitted electron is ejected from level  $X$ , the core hole created is filled by a second electron from level  $Y$  and the excess energy is released by the ejection of an Auger electron from the level  $Z$  with kinetic energy:

$$E_{k,Auger} = E_{b,X} - E_{b,Y} - E_{b,Z} - \phi_s \quad (1.5)$$

where  $E_{b,X}$ ,  $E_{b,Y}$  and  $E_{b,Z}$  are the binding energies of the electrons in levels  $X$ ,  $Y$  and  $Z$ , respectively. Both X-ray and Auger mechanisms are characteristic of the probed atoms, since the Auger and the photoemitted electron energies depend on the binding energies of the levels involved in the transitions, which themselves vary from one element to another. That is the reason why XPS is used to study the chemical composition, hence the name



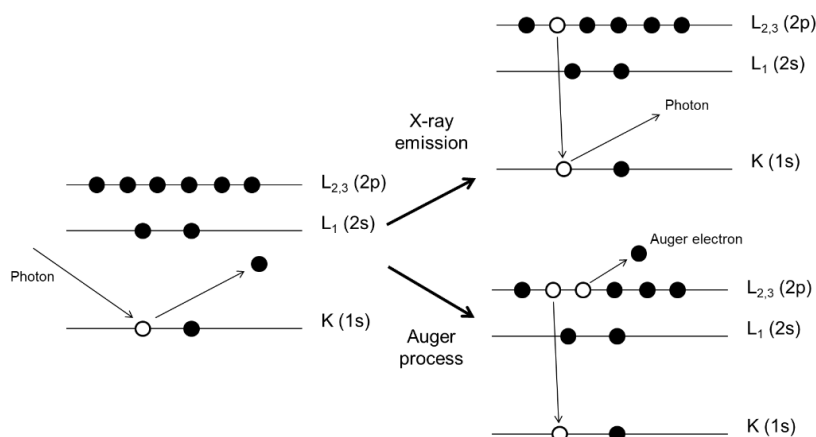


Figure 1.4: Schematic representation of the two competitive relaxation mechanisms after the core-hole creation: X-ray emission and Auger process.

### ESCA.

In a typical XPS spectrum, Auger peaks are distinguished from the sharp core level peaks, because they usually appear broader and with a more complex structure. Moreover, compared to photoemitted electrons, the kinetic energy of Auger electrons does not depend on the photon energy (see Equation 1.5), thus allowing to distinguish between the two contributions by simply changing the photon energy for example by switching the anode in a dual anode source.

#### 1.3.3.4 Plasmon losses

Another process taking place during the electron escape toward the sample surface, giving rise to additional peaks in the XPS spectrum, is the electron-plasmon interaction: part of the kinetic energy of the ejected electron may be given to the electronic collective excitations in the bulk. The energy loss is  $\hbar\omega_b$ , with  $\omega_b$  the bulk plasmon frequency. In the emission spectrum near a given main line at  $E_b$ , these losses appear as a series of discrete peaks of decreasing intensity at binding energies  $E_b + n\hbar\omega_b$ , where  $n$  is the harmonic order. Surface plasmons at  $\hbar\omega_b/\sqrt{2}$  may also be excited but their observation is more difficult.

#### 1.3.3.5 Shake-up and shake-off peaks

Koopman's equation (1.1) describes the photoemission process in the so-called sudden approximation, where the photoemitted electrons do not interact with the system thus experiencing the same binding energy before and after the photoemission process. In reality after the photoelectron ejection, valence electrons are less efficiently screened and feel a greater nuclear charge. The subsequent rearrangement of the valence band may cause the excitation of one valence electron to a higher energy state (figure 1.5). If it is a bound state, the process is called shake-up, otherwise if the valence electron is excited to the continuum above the vacuum state, a shake-off peak appears [18].

#### 1.3.3.6 Sample charging effects

Since the XPS process involves the emission of charged particles, a positive charge will build up on the sample if photoemitted electrons are not compensated by other electrons

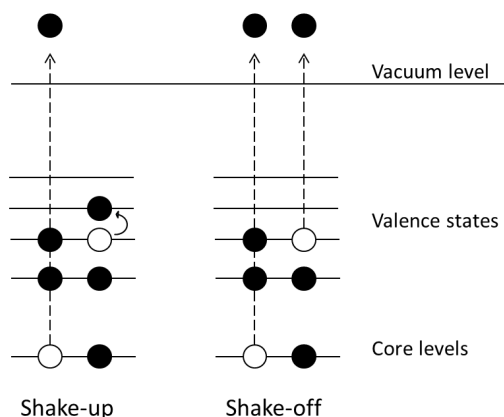


Figure 1.5: Schematic representation of shake-up and shake-off processes.

from the ground. This positive charge generates an electric field which decreases the photoemitted electron kinetic energy, thus resulting in a high  $E_b$  energy shift and eventually in a distortion of the XPS spectrum peaks. With conductive materials, the problem is simply overcome when the sample is grounded. However, different precautions must be taken when dealing with insulating materials. To overcompensate for the sample positive charge, possible solutions involve a thin layer deposition of the insulating material on a conductive support, when possible, or the use of low energy electron flood guns, also referred to as charge compensators, which replace the XPS emitted photoelectrons [18]. In our case, despite the stoichiometric  $\text{TiO}_2$  single crystals being insulators, the bulk reduction process occurring during the sample preparation increases its conductivity, thus making the XPS analysis possible without charge compensation.

### 1.3.4 XPS analysis

Because of the several features detailed so far, like inelastic background, plasmon losses, shake-up and shake-off peaks, XPS spectra might become quite complex and care should be taken when performing the analysis. A detailed XPS spectrum interpretation often requires a fitting procedure to resolve overlapping different chemical states of a given peak. Moreover, prior to any fit, a background subtraction is essential to eliminate the inelastic scattering component.

#### 1.3.4.1 Background removal and peak fitting

The choice of an appropriate background is essential especially when a quantitative analysis is requested. A range of background lineshapes have been proposed: linear, the simplest method; Shirley and Tougaard backgrounds. The Shirley background consists in an iterative method in which the background intensity at a given binding energy is proportional to the elastic peak area at lower binding energies [24]. Tougaard background assumes the existence of an inelastic scattering cross section which describes the probability for an electron to suffer inelastic scattering during its travel through the solid as a function of its kinetic energy [25,26]. In this work the background has been subtracted according to the Shirley method.

As mentioned, XPS data interpretation often requires curve fitting. Different factors affect peak lineshapes and broadening: the excitation source lineshape, the finite lifetime

of the core-hole, thermal broadening, surface potential inhomogeneities, surface charging and the analyser resolution. To model peak lineshapes, Voigt functions are often used. A Voigt function  $V(E)$  is mathematically described as the convolution of a Lorentzian  $L(E)$  function, arising from the finite core-hole lifetime and energy width of the photon source, and a Gaussian  $G(E)$  function, accounting for the instrumental response and the other broadening sources:

$$V(E) = A \int_{-\infty}^{+\infty} L(E')G(E - E')dE' \quad (1.6)$$

where

$$L(E) = \frac{1}{\pi\omega_L} \frac{\gamma_L}{(E - E_0)^2 + \gamma_L} \quad (1.7)$$

$$G(E) = \sqrt{\frac{\ln 2}{\pi}} \frac{1}{\gamma_G} \exp\left[-\frac{E^2 \ln 2}{\gamma_G^2}\right] \quad (1.8)$$

$\gamma_L$  and  $\gamma_G$  are the Full Width at Half Maximum (FWHM) of the Lorentian and Gaussian functions, respectively,  $E_0$  is the peak position and  $A$  the peak area. However in practice an analytical form for the convolution of Gaussian and Lorentzian functions is long [24,27] and a linear combination of the two curves was thus used. In addition to plasmon losses, electron-hole pair creations have to be accounted for when a metal sample is considered. In particular, the latter introduce a high  $E_b$  asymmetry to the peak. To take these contributions into account and model the asymmetric peak lineshape, a Doniach-Sunjc function is used:

$$DS(E, \alpha) = A \frac{\cos\left[\pi \frac{\alpha}{2} (1 - \alpha) \arctan\left(\frac{E - E_0}{\gamma_{DS}}\right)\right]}{[(E - E_0)^2 + \gamma_{DS}^2]^{\frac{1-\alpha}{2}}} \quad (1.9)$$

where  $\alpha$  is an asymmetry parameter and  $\gamma_{DS}$  is related to the FWHM. When  $\alpha = 0$  a Lorentzian function is obtained. To take into account the instrumental broadening,  $DS(E)$  must be convoluted with a Gaussian function. In this work, spectra were fitted using the Casa XPS Software.

### 1.3.4.2 Thickness estimation

As previously mentioned, quantitative information on adsorbate surface coverage, overlayer thickness and atomic density may be gathered from XPS analysis [13,28,29]. When a semi-infinite substrate is considered, the photoelectron intensity  $I$  at kinetic energy  $E_k$  for a thin layer of thickness  $dz$  at a depth  $z$  from the surface can be written as:

$$I \propto \Phi AD\Omega T(E_k)\sigma(E_k) \exp\left[\frac{-z}{\lambda(E_k)\cos\theta}\right]n(z)dz \quad (1.10)$$

where  $\Phi$  is the average X-ray flux impinging on the sample,  $A$  is the sample area irradiated by the X-ray radiation and detected by the analyser,  $D$  is the detector efficiency,  $\Omega$  is the solid angle which defines the angular acceptance of the analyser,  $T(E_k)$  is the analyser transmission function which may be considered proportional to  $1/E_k$  for a perfect hemispherical analyser [30],  $\sigma(E_k)$  is the photo-ionisation cross-section of the probed core-level [31],  $\lambda(E_k)\cos(\theta)$  is the probed depth as previously defined,  $n(z)$  is the atomic concentration for the considered element. The IMFP were estimated using the program QUASES-IMFP-TPP2M [32] from the predictive formula of Tanuma, Powell and Penn [16,33–39]. To obtain quantitative information, the easiest way is to look at the peak ratios and establish a model reflecting the growth geometry. Calculations are simplified

by the fact that in equation (1.10)  $\Phi$ ,  $A$ ,  $D$  and  $\Omega$  are considered as constants due to their weak dependence on the kinetic energy, while  $\sigma(E_k)$ ,  $\lambda(E_k)$  and  $T(E_k)$  are obtained from tabulated data or estimated. In the simplest case of growth of a uniform thin film  $B$  of thickness  $t$  on a semi-infinite substrate  $A$ , the bulk and overlayer intensities are obtained by properly integrating equation (1.10) from  $-\infty$  to 0 and from 0 to  $t$ , respectively:

$$I_A \propto T_A \sigma_A n_A \int_{-\infty}^0 \exp[-t/\lambda_{B,A} \cos(\theta)] \exp[z/\lambda_{A,A} \cos(\theta)] dz = \quad (1.11)$$

$$T_A \sigma_A n_A \lambda_{A,A} \cos(\theta) \exp[-t/\lambda_{B,A}]$$

$$I_B \propto T_B \sigma_B n_B \int_{-t}^0 \exp[z/\lambda_{B,B} \cos(\theta)] dz = T_B \sigma_B n_B \lambda_{B,B} \cos(\theta) [1 - \exp[-t/\lambda_{B,B}]] \quad (1.12)$$

$\lambda_{A,A}$ ,  $\lambda_{B,B}$  and  $\lambda_{B,A}$  are the IMFP of a substrate photoelectron in the substrate, of an adsorbate photoelectron in the overlayer and of a substrate photoelectron in the overlayer, respectively. The additional damping factor  $\exp[-t/\lambda_{B,A} \cos(\theta)]$  introduced in equation (1.11) thus corresponds to the attenuation of the substrate signal by the overlayer. The thickness  $t$  is obtained by considering the intensity ratio  $I_A/I_B$  and by solving it by dichotomy. More complex models accounting for nanoparticle growth can be simulated as well by properly integrating equation (1.10) and will be detailed in chapter 5.

### 1.3.5 Instrumentation

In a typical XPS setup, X-rays emitted by the source impinge on the sample, where the photoemission process takes place. The ejected electrons are then collected by a lens system and focused at the entrance of the hemispherical analyser, where they are dispersed according to their kinetic energy. At the analyser exit slit, the detector converts the signal into a current, which is then processed and displayed as a typical XPS spectrum by means of the electronics and software system.

Typical laboratory XPS sources consist of X-ray tubes, where the radiation is produced by high-energy electron bombardment of a water-cooled metallic anode. A heated filament, the cathode, emits the electrons which are accelerated by a large electric potential (usually 5-20 KV) onto the anode. The radiative de-excitation of the anode core holes thus produces the X-ray emission. The source emission lines depend on the anode composition: the most widely employed are Mg and Al, with characteristic emissions at 1253.6 eV for Mg and 1486.7 eV for Al which correspond to  $K\alpha_{1,2}$  unresolved doublet ( $2p_{3/2,1/2} \rightarrow 1s$  transitions). Their respective linewidths are 0.7 eV for the Mg  $K\alpha$  and 0.85 eV for the Al  $K\alpha$ .

Another source of radiation in the XPS tube is called Bremsstrahlung radiation which is produced by the inelastic interaction between electrons and anode nuclei. It contributes to the continuous background which superimposes to the photoemission peaks in a typical XPS spectrum.

To avoid the presence of satellite features which may further complicate the spectrum interpretation, to increase the resolution while reducing the Bremsstrahlung inelastic background, monochromated sources are successfully employed. The monochromator consists of a crystal used to sort X-rays depending on their energy, according to the Bragg equation  $p\lambda = 2d\sin(\theta)$ , where  $p$  is the diffraction order,  $\lambda$  the diffracted wavelength,  $d$  the crystal lattice spacing and  $\theta$  the diffraction angle with respect to the crystal plane. Commercial monochromators employ bent quartz crystals combined with Al anodes. As a consequence, the Al  $K\alpha$  linewidth is reduced from 0.85 eV to about 0.25 eV. [22].

In the present work XPS spectra were recorded at the INSP laboratory using an unmonochromatised twin anode Al/Mg source which allows to select as desired either the Mg or Al anodes. At the LRS laboratory XPS analysis was instead carried out by means of a monochromatised aluminium  $K\alpha$  X-ray source.

Following the photoemission process, an electrostatic lens system focuses the ejected electrons at the entrance slit of the analyser, while accelerating/decelerating them so that only those electrons having the right energy, the so-called pass energy  $E_p$ , will be transmitted and will arrive to the detector at the analyser exit slit. On the other hand, the photoemitted electrons travelling too slow or too fast will hit the internal walls of the analyser, which thus works as a band pass filter. In this work hemispherical analysers were used. The centrifugal force of the electrons travelling through it is balanced by the electric field between its inner and outer hemispherical walls, set at two different potentials. If  $R_0$  is the mean radius of the hemispheres, the energy resolution is given by:

$$\Delta E = E_p \cdot \left( \frac{W}{2R_0} + \alpha^2 \right) \quad (1.13)$$

thus depending on the pass energy, the lens system acceptance angle  $\alpha$  and the slit width  $W$ . The smaller  $E_p$ , the better the resolution but to the detriment of the number of counts. There are two analyser working modes:

- Constant Retard Ratio (CRR) when  $E_p$  is continuously varied to hold at a fixed value the ratio of kinetic energy and pass energy and thus the analyser transmission;
- Constant Analyser Energy (CAE), used in this work, when  $E_p$  is kept constant, thus insuring a constant resolution throughout the analysis for all binding energies.

Finally, at the analyser exit plane, the electron detection is provided by multiple-channel detectors (5 at the INSP), where the signal is amplified by a factor of  $10^8$ . The signal current passes then through a preamplifier and it is finally processed by the software system to produce the energy spectrum.

## 1.4 Ultraviolet Photoemission Spectroscopy

A technique closely associated to XPS which provides complementary information is Ultraviolet Photoemission Spectroscopy (UPS). UPS works indeed on the same principle as XPS, *i.e.* the photoelectric effect, but employing a much lower photon energy, in the range of 10 - 50 eV. At such low energies most core level peaks are not accessible, therefore limiting the analysis to the shallow weakly bound valence states. Since the outermost, less localised VB states are involved in chemical bonds, information on adsorbate filled bonding orbitals is gained as well. Beyond valence band (VB) analysis, UPS is also used for measurements of the work function, which is extremely sensitive to surface changes and thus useful as a complementary technique to track elementary surface reaction steps.

### 1.4.1 UPS for the valence band analysis

Valence electrons which occupy the outermost orbitals are responsible for the formation of chemical bonds and give rise to peaks very close in energy, which make UPS spectra difficult to interpret. The exaltation of the photoionization cross section of valence electrons for low photon energies warrants the use of UV sources to obtain high resolved valence band structures.

In numerous studies UPS has been employed to study the adsorption, decomposition and reactions of molecules on solid surfaces, but support from theoretical calculation is often needed for an unambiguous peak assignment [40–42]. One of the potential drawbacks common to XPS and UPS is the occurrence of photon stimulated adsorbate desorption or beam damage, for which an accurate check is always recommended [42].

### 1.4.2 UPS for work function measurements

As previously reminded, the work function  $\phi_s$  corresponds to the minimum energy required to extract an electron from the sample or, in other words, to the energy barrier required to an electron to escape from the material into the vacuum. For a given electron to exit the sample with kinetic energy  $E_k$  and be collected by the detector, the excitation energy must therefore exceed the sum of its binding energy (BE) and  $\phi_s$ .

Figure 1.6 shows an UPS spectrum recorded on the clean  $\text{TiO}_2$  (110) rutile surface. The Fermi level  $E_F$  represents the zero of the binding energy scale. At about 0.9 eV below  $E_F$  the band gap state appears, followed by the valence band. On the left side of the spectrum a sudden drop is observed. Its origin is ascribed to secondary electrons coming from deeper layers in the sample and having lost most or all of their energy in scattering events. This high BE edge called secondary cut-off (SCO) does not represent a true BE value, but those photoelectrons having left the sample with zero kinetic energy. To be able to record this minimal kinetic electron energy level and thus allow these electrons to reach the detector, a negative voltage has to be applied to the sample. Knowing that at the SCO  $E_{kin}(\text{SCO})=0$  while at  $E_F$  electrons possess a kinetic energy equal to

$$E_{kin}(E_F) = h\nu - \Phi_s \quad (1.14)$$

we obtain:

$$E_{kin}(E_F) - E_{kin}(E_{SCO}) = h\nu - \Phi_s \quad (1.15)$$

The sample work function is thus directly estimated by the energy difference between the photon source and the total width of the UPS spectrum after the correction of the applied voltage [43]. Since the  $E_F$  is not visible in a semiconductor spectrum,  $\Phi_s$  cannot be directly determined from its spectrum. The only readily identifiable points are the SCO at zero kinetic energy and the Valence Band Maximum (VBM). From these two values, only the ionization energy can be estimated. To be able to accurately calculate  $\Phi_s$ , the analyser is first calibrated using a conducting substrate: this allows to check the precision of the binding energy scale and locate the  $E_F$  at 0 eV. When the semiconducting sample is subsequently connected to the analyser, their Fermi levels align, thus equilibrating the semiconductor internal energy scale and allowing  $\Phi_s$  estimation. In practice, the SCO position is determined from an UPS spectrum by fitting a straight line into the high BE edge. Since the  $E_F$  is not visible on  $\text{TiO}_2$ , this procedure has been applied to calibrate figure 1.6 vs the Fermi edge of a FeAl sample. With respect to other techniques such as Kelvin probe which provides relative measurements, a considerable advantage of UPS is that absolute work function values are obtained.

### 1.4.3 Instrumentation

In laboratory facilities, the ultraviolet radiation source consists in a gas discharge lamp, in which the gas discharge is confined in a capillary tube. A differential pumping system is required to allow the lamp to operate at a pressure of several mbar while maintaining the analyser in good vacuum conditions (about  $10^{-8}$  mbar in our case). Being inert, noble

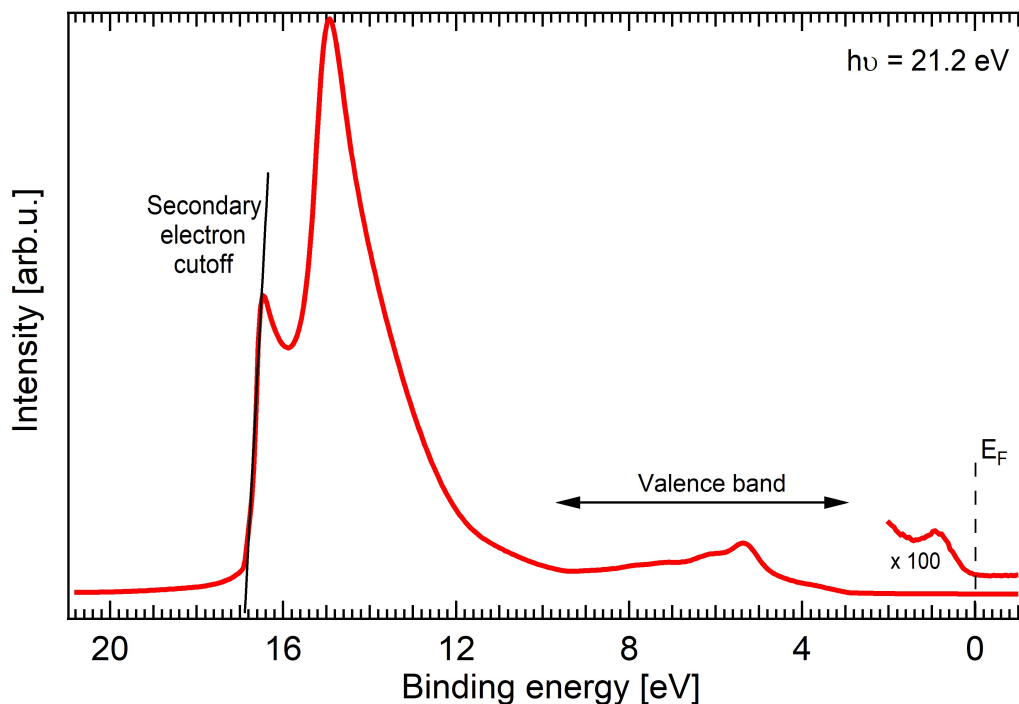


Figure 1.6: UPS spectrum recorded on the clean  $\text{TiO}_2$  (110) rutile surface.

gases are often employed, such as neon, argon, krypton, xenon or helium. To ensure the easy start and smooth functioning of the lamp a high gas purity is an essential requirement. In this work, the main discharge line used is the He I at 21.2 eV, which originates from excitations of the neutral He atoms. However, additional spectral lines of lower intensity are always present. For example, by decreasing the gas pressure and attaining values not far from the lamp extinguishing, the He II emission at 40.8 eV is maximised, this line originating from excited  $\text{He}^+$  ions. Consistently, being characteristic of the emitted radiation, the color of the lamp will pass from a yellowish violet to a greenish blue, typical of the He I and II radiations, respectively. To obtain a good compromise between an optimal resolution and a sufficient signal intensity, the pass energy was set to 5 eV in our measurements.

## 1.5 Scanning Tunnelling Microscopy

Scanning Probe Microscopies (SPM) include a family of techniques for the microscopic surface analysis. They all have in common the use of probe tips placed at atomic distances from the sample surface by means of piezoelectric elements and the presence of a feedback system, to keep the tip-sample interaction constant. What differentiates and defines them is the type of tip-sample interaction and the physical quantity sensed: just to name a few, Scanning Tunnelling Microscopy (STM), used in this work, is based on the tunnelling current, Atomic Force Microscopy (AFM) on the interatomic forces, while Kelvin Probe Force Microscopy (KPFM) on the local work function.

### 1.5.1 Basic principles

Scanning Tunnelling Microscopy (STM) was first developed by Binnig and Rohrer in 1982, honoured with the Nobel Prize in 1986. As previously mentioned, the basic principle is the quantum mechanical tunnelling effect established between a sharp metallic tip (ideally ending with one single atom) and a conducting sample, when they are placed at atomic distances and a bias voltage is applied between them. In fact, at a distance of a few Å, the sample and tip wavefunctions overlap and electrons tunnel from one to the other. When the sample is positively biased with respect to the tip, electrons flow from the occupied states of the tip into the empty states of the sample, otherwise electrons tunnel from the sample filled states into the tip empty states (figure 1.7). In our system the sample is grounded while a potential is applied to the tip.

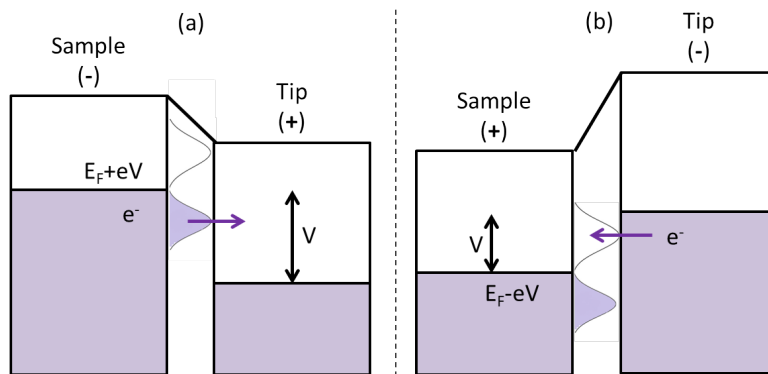


Figure 1.7: Schematic representation of the tip-sample tunnelling junction: (a) when the tip is positively biased with respect to the sample and (b) when the tip is negatively biased with respect to the sample. The violet area represents the electron occupied states. The violet arrows indicate the electron flowing direction.

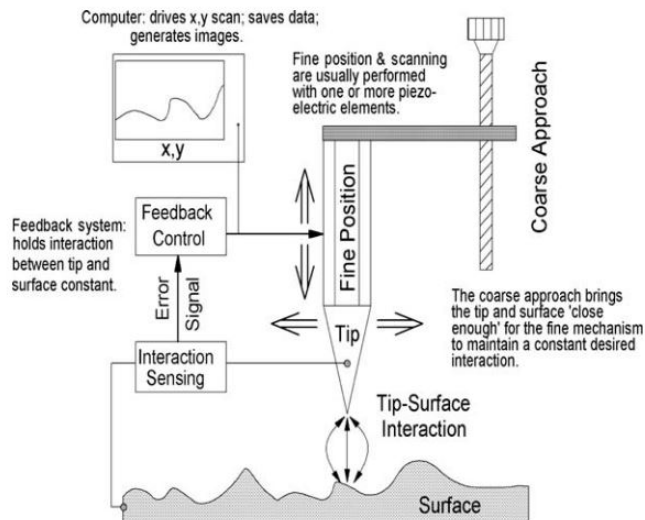


Figure 1.8: Schematic of the main STM components [18].

Figure 1.8 displays the essential STM components. A metallic tip is rastered over the sample surface by means of a piezoelectrically controlled scanner, while the tunnelling current is measured. The tip to sample approach involves two steps: a coarse approach



and a fine positioning. The feedback system, an essential component of the STM set-up, holds the tip/sample interaction constant. One of the first developed system consists of a piezoelectric tripod holding the tip and a piezoelectric support where the sample is situated (figure 1.9). The coarse approach is achieved by applying appropriate voltage to the electrostatic legs, while the fine positioning is provided by the tripod. The application of a voltage to the three orthogonal piezoelectric legs causes their expansion or contraction thus controlling the tip displacement along the three space directions  $x$ ,  $y$  and  $z$ . However, because of the manufacture complexity and structure asymmetry of this set-up, the more compact design of Besocke is nowadays preferred [44]. Three external piezoelectric tubes are used for the rough control of tip-sample distance by applying appropriate voltages while the central rod holding the tip acts as scanner in the  $x$  and  $y$  directions with asymmetric voltages applied between the inner and outer electrodes.

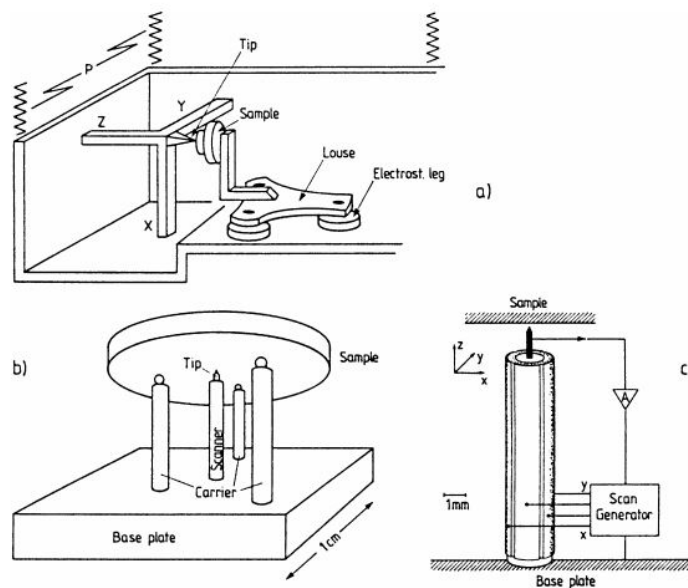


Figure 1.9: (a) Schematic representation of the classic STM designs. (b) Schematic representation of the more recent and compact Besocke STM. (c) Enlarged view of the scanner in figure (b) holding the tip [21].

Two different working modes are used in STM. The constant current mode, used in this work, consists in adjusting the tip height as the tip scans the sample surface, so that the current and voltage are kept constant. The current control and tip vertical position adjustment is provided by the feedback electronics. More precisely, the feedback loop is negative, so that if the tunnelling current increases/decreases, the tip is retracted/approached with respect to the sample. The second working mode is the constant height mode, when the feedback is usually switched off and tip vertical position is kept constant while the current is measured.

To start a measurement, the tip must be approached to the sample surface, at a distance of about  $1 \text{ \AA}$ . The approach consists in two phases: firstly the user approaches the tip ideally with the help of a camera, while the fine positioning is realised automatically by means of the feedback system and the tip is brought increasingly closer to the surface until the tunnel current and voltage values set by the user are attained.

An essential requirement to reach atomic resolution is the vibration isolation from natural external noise which is always present and may interfere with data acquisition: the

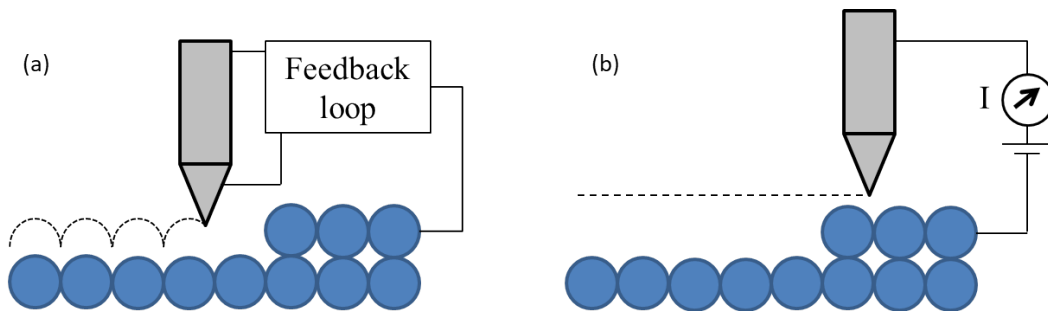


Figure 1.10: Different STM working modes: (a) constant current mode and (b) constant height mode.

vacuum pumping systems, building vibrations (generally between 5 and 100 Hz), people walking and other occasional events. To this purpose, a rigid bench allows the suppression of high-frequency noise. Moreover, to keep the noise below  $0.01 \text{ \AA}$  in the  $z$  direction, the tip/sample stage is suspended by means of springs and additional eddy current dampers are used for low-frequency vibrations. In detail, the STM is mounted on a copper ring with evenly spaced palettes and magnets in between. A vibration in the horizontal plane will vary the relative distance between palettes and magnets, inducing eddy currents in the first. A magnetic field opposite to the one creating the eddy currents is generated, thus damping the vibration amplitude.

### 1.5.2 Tunnelling theory

In a one-dimensional approximation, at a given position  $z$  the Schrödinger equation reads:

$$-\frac{\hbar^2}{2m} \frac{d^2}{dz^2} \psi(z) + U(z) \psi(z) = E \psi(z) \quad (1.16)$$

where  $U(z)$  is the potential barrier felt by the electron ( $U(z) = 0$  if  $z < 0$  and  $U(z) = U$  if  $z > 0$ ), which is described by the wavefunction  $\psi(z)$ . When  $E > U$ , the solutions are:

$$\psi(z) = \psi(0) e^{\pm ikz} \quad (1.17)$$

where  $k = \sqrt{\frac{2m(E-U)}{\hbar^2}}$  is the wave vector. Within the classically forbidden barrier where  $E < U$ ,  $k$  becomes imaginary and the solution reads:

$$\psi(z) = \psi(0) e^{-kz} \quad (1.18)$$

The probability to observe an electron at a position  $z > 0$  is non zero and proportional to  $|\psi(z)|^2 = |\psi(0)|^2 e^{-2kz}$ . The tunnelling current is thus proportional to the number of sample states  $\psi_n$  in the energy interval  $eV$ :

$$I \propto \sum_{E_n=E_F-eV}^{E_F} |\psi_n(0)|^2 e^{-2kz} \quad (1.19)$$

If the applied voltage is much smaller than the sample and tip work functions,  $eV < \Phi$ , the density of states does not change significantly in the energy interval  $eV$  and equation 1.19 is rewritten in terms of the local density of states (LDOS) at the Fermi level. The local

density of states is defined as the number of electrons per unit volume per unit energy, at a given energy and position:

$$\rho_S(z, E) \equiv \frac{1}{\epsilon} \sum_{E_n=E-\epsilon}^E |\psi_n(z)|^2 \quad (1.20)$$

Equation 1.19 is thus rewritten as:

$$I \propto eV \rho_S(0, E_F) e^{-2kz} \quad (1.21)$$

which implies that in a constant current mode, STM maps the constant LDOS of the sample surface.

This simple model is nevertheless effective to explain some important features of the sample-vacuum-tip junction, where the potential barrier is represented by the sample and tip work function  $\Phi$  (assumed equal). For a metal,  $\Phi$  varies between 4 and 5.5 eV [45] and  $k$  is of the order of  $1 \text{ \AA}^{-1}$ . This implies that a variation of the tip/sample of  $1 \text{ \AA}$  will increase or decrease the tunnelling current of one order of magnitude. The exponential dependence of the current on the tunnelling distance justifies the extremely high sensitivity of STM on the sample corrugation (in the  $z$  direction).

A more complete formalism, accounting for the whole system, was developed in 1961 by Bardeen and applied to STM by Tersoff and Hamann in 1983 [46–48]. By considering separately each side of the barrier (tip/vacuum and vacuum/sample), the tunnelling current is not a constant LDOS of the sample surface at the Fermi level, but the convolution of the density of states of the sample  $\rho_S$  and tip  $\rho_T$ :

$$I \propto \int_0^{eV} \rho_S(E_F - eV + \epsilon) \rho_T(E_F + \epsilon) d\epsilon \quad (1.22)$$

### 1.5.3 Experimental details

Of course tips are only ideally terminated by one single atom and STM images are thus a convolution between tip and sample shapes. When the tip curvature radius is larger than the size of probed features, artifacts appear in the STM images. Protrusions such as nanoparticles will thus appear larger, while holes narrower and shallower (figure 1.11).

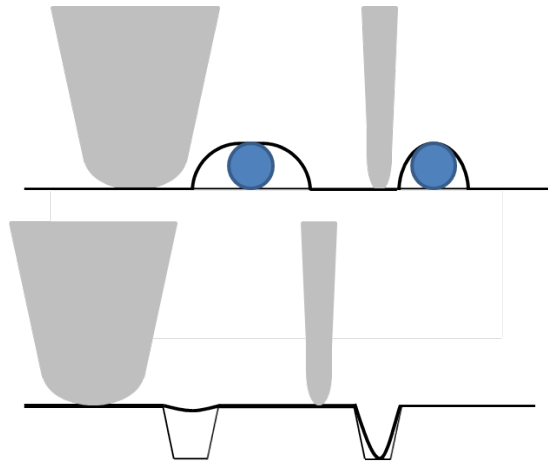
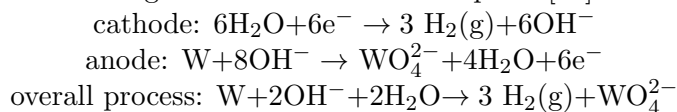


Figure 1.11: Examples of tip effects.

Tips are usually made of PtIr alloy or W. In this work, W tips obtained by electrochemical

etching in a basic solution are used. The tip is partially immersed in a KOH solution ( $\sim 4$  M) and placed in the center of a stainless steel ring, the cathode, also in contact with the basic solution. When a potential difference is applied ( $\sim 7$  V in this work) between the ring and the tip, the following chemical reactions take place [49]:



The tip thus starts to etch at the meniscus and the process will continue until the immersed fragment becomes too heavy and drops off. Once the wire breaks at the meniscus, the electrochemical reaction is automatically stopped. The freshly prepared tip is rinsed with ultrapure water and alcohol and its morphology checked with an optical microscope. After mounting on gold coated holders, tips are introduced in the UHV chamber and thoroughly degassed for several hours.

All STM images are analysed using the Gwyddion 2.51 software. Drift correction is either applied during scan or, when not possible, in the subsequent analysis. A further typical image analysis involved plane fit correction and three point levelling, sometimes image cropping when contrast optimisation between different terraces is requested and line profile extraction to estimate distances.

## 1.6 Low Energy Electron Diffraction

Low Energy Electron Diffraction (LEED) is a surface science technique employed for structural investigations, which provides information on surface crystallinity, periodicity and reconstruction. In the case of adsorbate deposition on a substrate, like in this work, LEED is used to determine the possible presence of organised superstructures. Moreover, when a deeper quantitative analysis of the atomic positions within the unit cell is needed, the intensities of the diffraction spots are recorded as a function of the incident electron energy, in the so-called I-V curves [20].

### 1.6.1 Basic principles

As the name suggests, LEED experiments employ electrons of low energy, in the range of 20-300 eV. At such low energies the probed depth is limited to the first atomic layers, hence the surface sensitivity, and the electron wavelength (1-2 Å) is of the same order as the interatomic distances, an essential requirement for atomic diffraction. The diffraction pattern produced is linked to the sample reciprocal lattice through a mathematical equation known as the Laue condition [20], which represents the momentum conservation during the scattering process:

$$\mathbf{k} - \mathbf{k}_0 = \Delta\mathbf{k} = \mathbf{G} \quad (1.23)$$

where  $\mathbf{k}_0$  and  $\mathbf{k}$  are the wave vectors of the incident and the outgoing waves, respectively,  $\Delta\mathbf{k}$  is the diffracted wave vector and  $\mathbf{G}$  is the reciprocal lattice vector. Moreover, since elastic scattering is considered, the norms of the vectors are equal,  $k = k_0$ . In other words, a given wave will be diffracted by a crystal, thus contributing to the diffraction pattern, only if its scattering wavevector corresponds to a reciprocal lattice vector.

The fulfilment of the diffraction condition is graphically displayed by a geometrical construction known as the *Ewald sphere* (figure 1.12). To build it, the reciprocal lattice is first represented. The incident wave vector  $\mathbf{k}_0$  is then drawn starting from an origin  $O$  chosen in such a way that  $\mathbf{k}_0$  points to a reciprocal lattice point. The Ewald sphere with radius  $k = k_0$  (since elastic scattering is considered) thus takes shape. The directions in

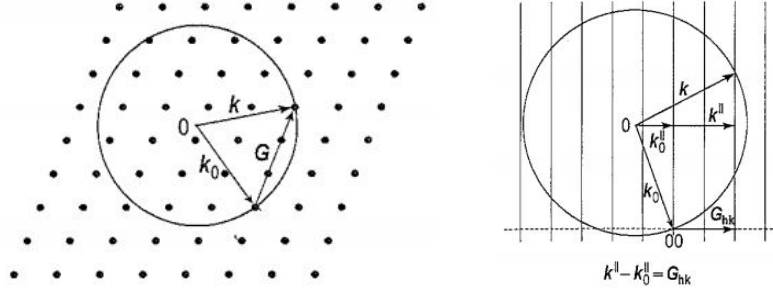


Figure 1.12: Left: Ewald construction for diffraction from a 3D lattice. Right: Ewald construction for diffraction on a 2D surface lattice [20].

which the Ewald sphere intersects the reciprocal lattice points correspond to the diffracted beams  $\mathbf{k}$ , in which the diffraction condition  $\mathbf{k} - \mathbf{k}_0 = \Delta\mathbf{k} = \mathbf{G}$  is satisfied [14, 20].

However, due to the limited probed depth of low energy electrons, diffraction occurs from the 2D surface lattice and periodicity is broken in the direction perpendicular to the surface. The momentum conservation thus applies only to the wave vector components parallel to the surface and the Laue conditions now reads:

$$\mathbf{k}_{\parallel} - \mathbf{k}_{0\parallel} = \Delta\mathbf{k}_{\parallel} = \mathbf{G}_{2D} \quad (1.24)$$

where  $\mathbf{G}_{2D}$  is a vector of the surface reciprocal lattice. When moving from 3D to 2D, the reciprocal lattice points in the Ewald construction are replaced by infinite rods perpendicular to the crystal surface (figure 1.12). In analogy to the 3D case, the diffraction condition is verified whenever the Ewald construction intersects a reciprocal lattice rod [20].

### 1.6.2 Adsorbate superstructures

When adsorbates form long-range ordered structures on a substrate with a different periodicity with respect to the bulk, extra spots appear in the corresponding LEED pattern. Several notations are possible, one of which proposed by Park and Madden is based on a simple vectorial representation [14]. In this case, a 2x2 matrix  $\mathbf{M}$  is used which relates the substrate vectors  $\mathbf{a}_i$  to the ones of the overlayer  $\mathbf{b}_i$  [21]:

$$\begin{pmatrix} \mathbf{b}_1 \\ \mathbf{b}_2 \end{pmatrix} = \mathbf{M} \begin{pmatrix} \mathbf{a}_1 \\ \mathbf{a}_2 \end{pmatrix} \quad (1.25)$$

A similar matrix relationship applies in the reciprocal space:

$$\begin{pmatrix} \mathbf{b}_1^* \\ \mathbf{b}_2^* \end{pmatrix} = \mathbf{M}^* \begin{pmatrix} \mathbf{a}_1^* \\ \mathbf{a}_2^* \end{pmatrix} \quad (1.26)$$

where  $\mathbf{a}_i^*$  and  $\mathbf{b}_i^*$  are the vectors describing the substrate and the adsorbate reciprocal lattice, respectively, while  $\mathbf{M}^*$  is the transpose inverse matrix of  $\mathbf{M}$ :

$$\mathbf{M}^* = (\mathbf{M}^{-1})^T \quad (1.27)$$

Another notation often used in crystallography is the one proposed by Wood, which gives the ratio between the substrate and adsorbate lengths together with the angle of rotation  $\Phi$  of the surface unit vectors with respect to the adlayer ones. For the adsorbate

reconstruction on the  $(hkl)$  crystalline plane of substrate X described by

$$\begin{aligned}\mathbf{b}_1 &= p\mathbf{a}_1 \\ \mathbf{b}_2 &= q\mathbf{a}_2\end{aligned}$$

the following notation is used [14, 20, 21]:

$$X\{hkl\}(p \times q) - \Phi \quad (1.28)$$

When  $\Phi = 0$  equation (1.28) simplifies to  $p \times q$ . However, the Wood notation is applied only if the angle between  $\mathbf{a}_1$  and  $\mathbf{a}_2$  is the same as the one between  $\mathbf{b}_1$  and  $\mathbf{b}_2$ .

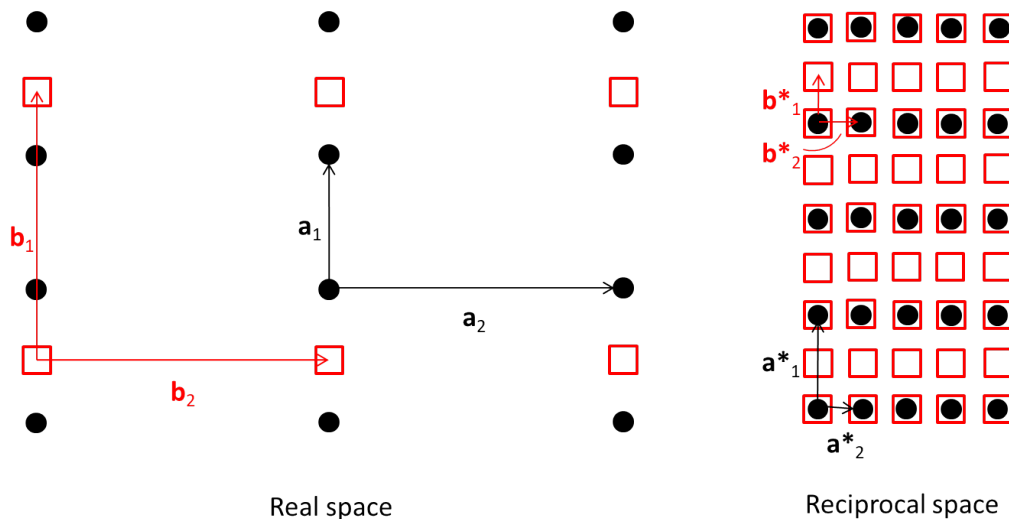


Figure 1.13: Example of adsorbate overlayer in real space and reciprocal space. The substrate and adsorbate 2D lattices are indicated by black dots and red squares, respectively.

Figure 1.13 shows an example of superstructure formation on rutile  $\text{TiO}_2(110)$  in real space and the corresponding one in reciprocal space. The substrate 2D surface lattice is indicated by black dots, while the adsorbate one by red squares. In this specific case the adsorbate overlayer possesses a unit cell which has the double and the same length in the  $\mathbf{a}_1$  and  $\mathbf{a}_2$  crystallographic directions, respectively, compared to the substrate unit cell. A  $2 \times 1$  or  $\begin{pmatrix} 2 & 0 \\ 0 & 1 \end{pmatrix}$  superlattice is thus formed on the surface upon adsorbate deposition.

### 1.6.3 Experimental set-up

Figure 1.14 shows a typical rear-view LEED experimental set-up, consisting of an electron gun, a series of retarding grids held at different potentials and a fluorescent screen. The electron gun produces low energy electrons which are accelerated and collide with the sample at normal incidence. The backscattered electrons emitted by the sample travel back to the screen, passing through the grids. While the first and the last grids are grounded, to produce a field-free region between the analysed sample and the screen, the two in the middle are held at a negative voltage and work as an energy filter to prevent inelastically backscattered electrons to reach the screen [21]. A potential between 2 and 5 kV is applied to the latter to finally accelerate the elastically backscattered electrons, thus producing the diffraction pattern.

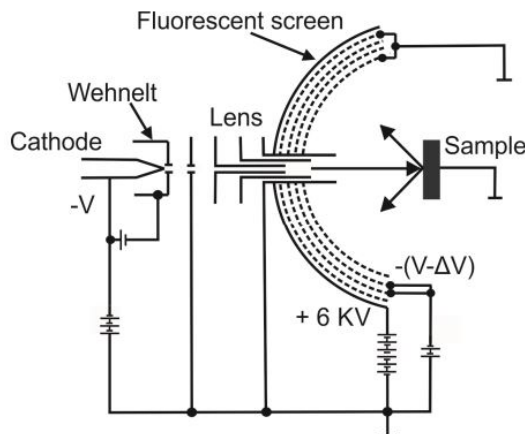


Figure 1.14: Schematic representation of a conventional rear-view LEED setup [20]. The viewer is considered to be on the left side of the image.

## 1.7 Temperature Programmed Desorption

Temperature Programmed Desorption (TPD) is a technique commonly used in the field of catalysis. It consists of first exposing the sample to some given atoms or molecules, then gradually increasing its temperature at a constant rate to desorb the adsorbates while recording the pressure. The so-obtained desorption spectra are used to gain information on the activation energies and desorption kinetics. The activation energy of adsorption being often negligible, desorption activation energies are equivalent to the adsorption heats [50].

### 1.7.1 TPD theory

The desorption process is estimated by the desorption rate, defined as the number of particles which desorb from the surface per surface unit and time. Assuming particle conservation between those desorbed from the sample and those being pumped, the desorption rate is generally written as [20, 21, 51, 52]:

$$r_d = -\frac{d\Theta}{dt} = \frac{V}{AKT} \left( \frac{dP}{dt} + \frac{S}{V} P \right) \quad (1.29)$$

where  $\Theta$  is the coverage of the analysed sample surface  $A$ ,  $T$  is the gas temperature,  $P$  is the background-subtracted pressure,  $V$  the tube volume and  $S$  the pumping speed. With low  $S$  the desorption rate would be proportional to the increase in pressure  $\frac{dP}{dt}$ . On the contrary, when  $S$  is high and the heating rate is low,  $-\frac{d\Theta}{dt}$  is proportional to  $P$ , so that the measured pressure is directly related to the desorption rate. This second regime is used in the present work.

The desorption rate is related to the coverage  $\Theta$  in terms of the Polanyi-Wigner equation [50, 52]:

$$r_d = -\frac{d\Theta}{dt} = \nu(\Theta) \Theta^{n(\Theta)} e^{-\frac{E_a(\Theta)}{k_B T}} \quad (1.30)$$

where  $\nu(\Theta)$  is the desorption rate constant,  $n(\Theta)$  the kinetic desorption order and  $E_a(\Theta)$  the desorption activation energy [20, 50]. Zero order occurs when the desorption rate is independent from coverage and characterises autocatalytic reactions; for order one atoms desorb directly, while for order two, desorption occurs through recombination of two adsorbed species. The major difficulty in solving equation 1.30 is that all variables  $\nu(\Theta)$ ,

$n(\Theta)$  and  $E_a(\Theta)$  depend on the coverage  $\Theta$ . Several TPD analysis methods have thus been developed to accurately estimate the activation energies, including the Redhead analysis, heating rate variation method, Monte Carlo simulations, Arrhenius plots and the leading edge method used in this work and detailed in section 4.2 [51, 52].

### 1.7.2 Experimental apparatus

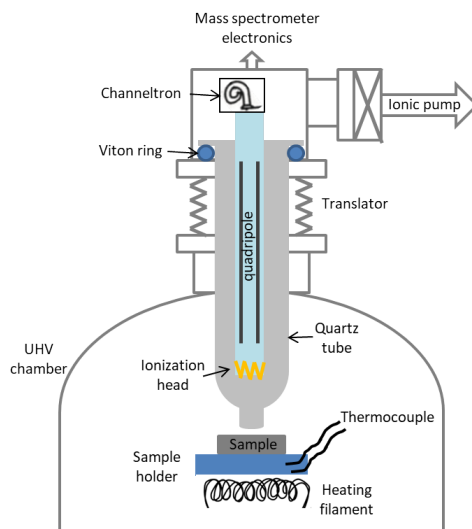


Figure 1.15: Schematic representation of the TPD setup.

The TPD setup used in this work is shown in figure 1.15 [21, 50]. A quadrupolar mass spectrometer (QMG 220 from PFEIFFER) is employed to detect the desorbed species. It is placed in a quartz tube, differentially pumped by an ionic pump, ending with a small cap pointing to the sample and whose entrance is smaller than the sample surface. During the experiments, the tube is approached close to the sample surface (at about 1 mm) to limit the detection of species to those desorbing from the sample and not from its surroundings. The desorbed species are first ionised by an ionisation source, *i.e.* a filament emitting electrons, and the so-formed ions are then sorted by electrostatic deviation according to their mass/charge ratio. The signal is finally amplified by a channeltron.

The sample placed on the manipulator is resistively heated by a metallic filament (up to 800 K in this work). A linear heating rate  $\alpha$  ( $T(t) = T_0 + \alpha t$  with  $\alpha = 0.5 \text{ K} \cdot \text{s}^{-1}$ ) is applied using a PID regulator while the temperature is measured by a thermocouple spot-welded near the sample on the manipulator.

## 1.8 Polarisation Modulation-Reflection Absorption InfraRed Spectroscopy

Infrared spectroscopy is a non-destructive vibrational technique in which the interaction of infrared light with matter is used to trigger molecular vibrations and gain information on chemical species, functional groups as well as on molecular orientation by means of the selection rules that apply for metal surfaces. It is therefore a well-suited and powerful technique in the study of molecular adsorption on metallic surfaces.



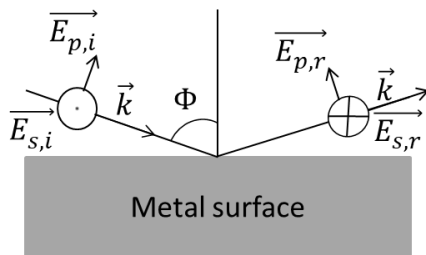


Figure 1.16: Reflection of the electric field, decomposed into the  $p$  and  $s$  components, at a metal surface at grazing incidence. The subscripts  $i$  and  $r$  stand for incident and reflected, respectively.

### 1.8.1 Basic principles of RAIRS

Infrared spectroscopy is based on the interaction between the incident electric field  $\mathbf{E}$  with the molecular dynamic dipole  $\boldsymbol{\mu}'$ . The absorbed infrared intensity is proportional to the square of the scalar product between  $\mathbf{E}$  and  $\boldsymbol{\mu}'$ :

$$I \propto [\mathbf{E} \cdot \boldsymbol{\mu}']^2 = |\mathbf{E}|^2 |\boldsymbol{\mu}'|^2 \cos^2 \theta \quad (1.31)$$

where  $\theta$  is the angle between vectors  $\mathbf{E}$  and  $\boldsymbol{\mu}'$ . Equation (1.31) implies that no absorption occurs when no change of the dipole moment is observed and for  $\theta = 90^\circ$ . Not every vibration is infrared active and specific selection rules apply for metal surfaces. To introduce them, we consider the specular reflection process of light at a metal surface, decomposed into  $p$  and  $s$  components (figure 1.16). As a reminder, the  $p$  ( $s$ ) component is parallel (perpendicular) to the plane of incidence. The process is studied using Fresnel's equations [53–55], giving the  $p$  and  $s$  reflected intensities  $R_p$  and  $R_s$  as well as the phase shifts  $d_p$  and  $d_s$ , which for metal surfaces are:

$$\begin{aligned} R_s &= \frac{(n - \cos \phi)^2 + k^2}{(n + \cos \phi)^2 + k^2} \\ R_p &= \frac{(n - \sec \phi)^2 + k^2}{(n + \sec \phi)^2 + k^2} \\ \tan \Delta &= \tan(d_p - d_s) = \frac{2k \tan \phi \sin \phi}{\tan^2 \phi - (n^2 + k^2)} \end{aligned} \quad (1.32)$$

where  $\phi$  is the incidence angle with respect to the surface normal,  $n$  and  $k$  are the real and imaginary part of the complex refractive index  $\tilde{n} = n + ik$  and  $n^2 + k^2 \gg 1$ . The phase shifts  $d_p$  and  $d_s$  are reported in figure 1.17 as a function of the angle of incidence  $\phi$ . Upon reflection,  $s$  polarised light undergoes a phase shift of  $180^\circ$  for all incident angles, resulting in a destructive interference between incident ( $E_{s,i}$ ) and reflected ( $E_{s,r}$ ) waves. Thus, the net electric field  $E_s = E_{s,i} + E_{s,r}$  vanishes at the metal surface. The phase change of the  $p$ -component is instead highly dependent on the incident angle. A constructive interference occurs between incident ( $E_{p,i}$ ) and reflected ( $E_{p,r}$ ) waves, with a strong exaltation of the resulting field  $E_p = E_{p,i} + E_{p,r}$  observed at grazing incidence, as shown in figure 1.17 for Cu ( $n=3$ ,  $k=30$ ). The interaction between incident light and surface dipoles at a metal surface is thus limited to  $p$ -polarised waves and strongly enhanced at grazing incidence. Moreover, from equation (1.31) only vibrational modes with a dynamic dipole moment component non parallel to the surface are probed [55, 56]. In the studies of molecular adsorption on metallic surfaces, the application of these selection rules may be used to obtain information on the orientation of molecular functional groups.

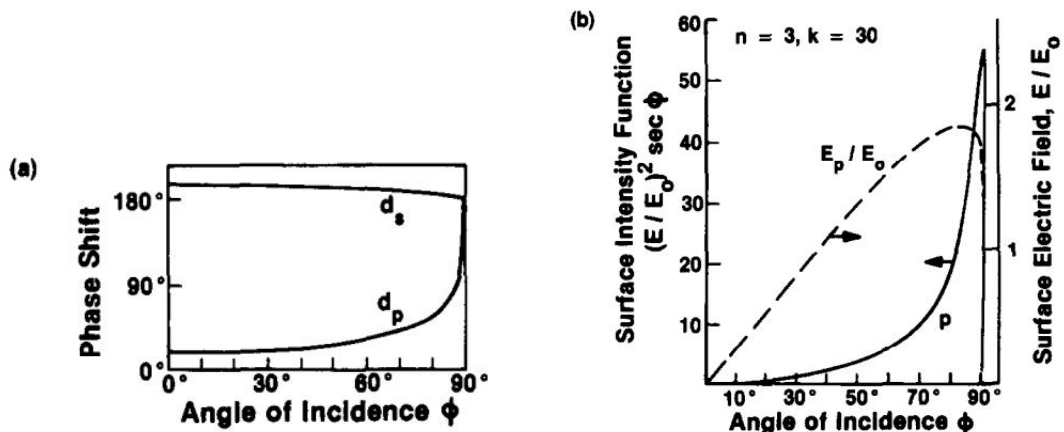


Figure 1.17: IR light reflection at a metal surface: (a) Phase shifts  $d_s$  and  $d_p$  as a function of the incident angle. (b) Electric field and intensity of the p-polarised component as a function of the incident angle.  $E_0$  and  $E$  are the incident and reflected electric fields, respectively [53].

From a practical point of view, a RAIRS experiment consists in recording the reflectivity spectrum of the substrate covered with adsorbates and normalising it with respect to the spectrum of the clean substrate, to remove contributions originating from the gas phase [54, 57].

### 1.8.2 PM-RAIRS

The necessity to record a reference spectrum is however one of the major drawback of RAIRS. In fact, even for efficient purging systems, changes in the environmental compositions and spectrometer instabilities always take place and record a reference spectrum in the same conditions as in the experimental one becomes a challenging task [54, 57]. This challenge is overcome using a differential technique known as Polarisation Modulation-Reflection Absorption InfraRed Spectroscopy (PM-RAIRS), based on a quick polarisation modulation of incident radiation between p and s states by means of a photoelastic modulator (PEM). The measured PM-RAIRS signal is the normalised differential reflectivity:

$$\frac{\Delta R}{R} = \frac{R_p - R_s}{R_p + R_s} \quad (1.33)$$

Since far from the surface s- and p-polarised light are equally absorbed, isotropic contributions from the environment are automatically filtered out. Moreover for s-polarised light the net electric field vanishes at the surface, thus yielding no absorption contributions to the signal [54].

### 1.8.3 Experimental setup

A typical PM-RAIRS setup is shown in figure 1.18. Incident light first passes through a FTIR spectrometer, which modulates the signal intensity at a low frequency  $\omega_i$  (between 100 and 1500 Hz). The beam is then p-polarised by means of a ZnSe polariser and modulated in polarisation using a photoelastic modulator ( $\omega_m=50$  kHz). After being reflected on the sample at grazing incidence, the beam is focused by a ZnSe lens on a liquid nitrogen-cooled mercury cadmium telluride (MCT) wide-band detector. The signal

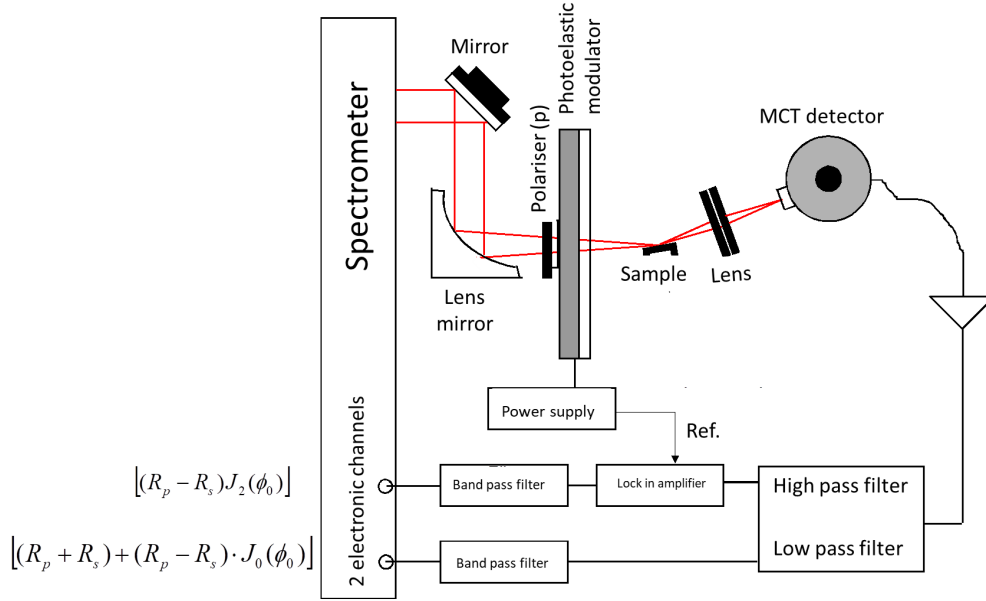


Figure 1.18: Schematic representation of a typical PM-RAIRS setup.

detected is written as:

$$I_d = \frac{1}{2} \cdot \underbrace{CI_0(\omega_i)[(R_p + R_s) + (R_p - R_s)J_0(\Phi_0)]}_A + \underbrace{CI_0(\omega_i)[(R_p - R_s)J_2(\Phi_0) \cos(2\omega_m t)]}_B \quad (1.34)$$

where  $C$  is a constant depending on the transmittance of the optical setup and on the detection yield,  $I_0(\omega_i)$  is the light intensity after the polariser,  $\Phi_0$  is the maximum dephasing of the PEM,  $J_0(\Phi_0)$  and  $J_2(\Phi_0)$  are the zero- and second-order Bessel functions. The first term A is modulated at the frequency  $\omega_i$  (between 100 and 1500 Hz), while the second component B undergoes a double modulation at  $\omega_i$  and at the higher frequency  $2\omega_m$ . The signal  $I_d$  is then filtered with a high-pass filter set at  $2\omega_m$  and a low-pass filter set at much lower frequency than  $2\omega_m$  [58], to split the two components A and B, collected in two separate channels. Since for a metal surface  $(R_p + R_s) \gg (R_p - R_s)$ , channel A returns a signal proportional to the  $(R_p + R_s)$  interferogram. Channel B is amplified and demodulated by a lock-in amplifier, by using a reference signal from the power supply of the PEM set at  $2\omega_m$  [57] and gives a signal proportional to the  $(R_p - R_s)J_2(\Phi_0)$  interferogram. The two interferograms are then treated simultaneously, Fourier transformed and their ratio is proportional to the normalised differential reflectivity multiplied by  $J_2(\Phi_0)$ :

$$\frac{\Delta R}{R} = \frac{R_p - R_s}{R_p + R_s} J_2(\Phi_0) \quad (1.35)$$

$J_2(\Phi_0)$  accounts for the fact that the modulation efficiency of the PEM depends on the light frequency. In practice, the modulation amplitude  $\Phi_0$  is adjusted to set the modulation yield in the region of interest [54]. When a quantitative analysis is needed or simply to avoid spectrum artifacts, the Bessel function  $J_2(\Phi_0)$  has to be suppressed. One easy method is to normalise the experimental spectrum by a reference one of the bare substrate acquired before the adsorbate deposition. If the optical and electronic set-ups are the same, this method allows the elimination of  $J_2(\Phi_0)$  and all experimental artifacts which do not

vary during the acquisition. Of course, normalisation to the bare substrate spectrum has a complete different origin with respect to RAIRS, since variations of the environmental composition are automatically filtered out in PM-RAIRS [54, 57, 58].

## 1.9 High Resolution Electron Energy Loss Spectroscopy

EELS (Electron Energy Loss Spectroscopy) is a powerful surface science technique used, among other things, for vibrational studies [59, 60]. It is based on the electron energy loss of low energy electrons interacting inelastically with the analysed sample surface. Depending on the energy loss, the inelastic scattering is used to probe different excitations including vibrations of phonons, plasmons, interband transitions and band gap states. High Resolution Electron Energy Loss Spectroscopy (HREELS) works on the same principle as EELS, using low energy electrons but with an increased resolution. It is used to probe excitations occurring at low energy losses (meV to a few eV), such as vibrations of surface atoms or adsorbates, for which an higher resolution is necessary to be distinguished from the elastic contribution.

### 1.9.1 Theoretical details

For primary electrons impinging on a sample, three scattering mechanisms are possible, known as *dipole scattering*, *impact scattering* and *resonance scattering* [60–62]. Each one of these interactions contributes to every scattering event, but depending on the scattering geometries one may dominate over the others, making the theoretical treatment more accessible. The dipole scattering, for example, dominates around the specular direction, in the so called dipole lobe. It arises from a long-range interaction between the incoming electrons and their related electric field with the electrostatic dipole field generated by any elementary excitation of the surface due to a charge density variation, such as phonons, plasmons, adsorbate vibrations, etc... On the other hand, when off-specular measurements are carried out, the dominant loss is represented by the impact scattering, *i.e.* when electrons lose energy directly by impact with the surface or adsorbate atoms. Contrary to the dipolar scattering, it is a short range interaction (of the order of 1 Å), whose theoretical description requires a quantum mechanical treatment. Lastly, resonance scattering is observed when the incident electron possesses the same energy as an electronic state of molecules adsorbed on the analysed surface; the electron becomes temporarily captured in an unoccupied adsorbate orbital forming a negative ion, increasing the loss probability and thus the intensity of the corresponding vibrational mode peaks [63]. Since most of the present measurements were carried out in a specular geometry, only the dipole scattering is detailed in the following.

### 1.9.2 Dipole scattering

The dipole scattering mechanism is the analogous of the photon interaction in RAIRS. In fact, the same physical quantity is at the base of both dipole scattering and RAIRS, *i.e.* the vibrating surface dipole; only vibrational modes associated to a change in dipole moment will thus be excited [14]. Moreover, the same selection rules as for the infrared counterpart apply for metal surfaces [61, 62]. Due to the long-range character of the dipolar scattering, the incoming electrons already start to feel the Coulomb potential associated to the elementary excitations on the sample when they are still far away from the surface, at about 100–200 Å, so that the dipolar interaction will last for about  $10^{-14}$  s [61, 62].

If we consider a surface excitation  $\Phi(x)$  of wave vector  $\mathbf{q}_{\parallel}$  with exponential decay in the direction  $z$  perpendicular to the surface, the corresponding potential is given by:

$$\Phi(x) = \Phi_0 e^{-q_{\parallel}|z|} e^{i\mathbf{q}_{\parallel}\mathbf{x}_{\parallel}} \quad (1.36)$$

Since the extension of the potential is proportional to the inverse of  $\mathbf{q}_{\parallel}$ , only those vibrations characterised by long wavelengths and thus small wave vectors (ca.  $10^{-2} \text{ \AA}^{-1}$ ) will be coupled for a long period to the electric field of the incoming electrons and therefore probed by dipole scattering [62].

The long interaction time characteristic of this scattering mechanism of ca.  $10^{-14} \text{ s}$  allows for a classical treatment of the dipole interaction, without necessarily having to recur to a quantum formulation. Over the years, several theoretical descriptions have been proposed [60–62], ranging from a **full-classical theory** [64], where the incoming electron follows a classical path and interacts with the classical electric field of elementary excitations in the sample, to a **semi-classical theory** (where the electrons still treated in a classical approximation, interact with the quantized boson field of the sample elementary excitations) [27, 65, 66] to a complete **quantum-mechanical formalism**, either considering multiple scattering events or not [65].

In this work the focus is placed on the first theoretical approach also known as dielectric theory, first developed by Lucas and Šunjić [62, 64] in the low energy case for simple crystalline materials and adjusted over the years for the description of more complex systems as anisotropic crystals, multilayered materials and non-planar surfaces. As already stated previously, the electron is treated as a classical particle, travelling along a classical path  $\mathbf{r}_e(t)$ , with some approximations. Firstly, the surface excitation energy  $\hbar\omega$  is small compared to the electron energy. Secondly, retardation effects, multiple scattering events, penetration of the electrons in the sample and effects of the image potential are not taken into account. The detailed calculations can be found elsewhere [27, 59, 60, 64–67], only the main results are reported here. The theory starts by considering an electron of mass  $m_e$  and charge  $-e$  approaching the sample with velocity  $\mathbf{v}_I = \hbar\mathbf{q}_I/m_e = (\mathbf{v}_{\parallel,I}, \mathbf{v}_{\perp,I})$  and energy  $E_I = \hbar^2 q_I^2/2m_e$ , where  $\mathbf{v}_{\parallel}$  and  $\mathbf{v}_{\perp}$  are the velocity component parallel and normal to the surface. When the electron is scattered by the surface, energy losses are described in terms of a classical loss function  $P_{cl}(\omega)$ , which corresponds to the probability for an electron to lose the energy  $\hbar\omega$  by creating one surface excitation at 0 K and it is given by [27, 59–62, 64–68]:

$$P_{cl}(\mathbf{q}_I, \omega) = \frac{4e^2}{v_{\perp}\hbar} \int_D \frac{d^2\mathbf{q}_{\parallel}}{\mathbf{q}_{\parallel}^2} \frac{(q_{\parallel}v_{\perp})^2}{[(\omega - \mathbf{q}_{\parallel}\mathbf{v}_{\parallel})^2 + q_{\parallel}^2 v_{\perp}^2]^2} \times \text{Im} \frac{-1}{\xi_0(\mathbf{q}_{\parallel}, \omega) + 1} = \int_D d^2\mathbf{q}_{\parallel} F(\mathbf{q}_I, \omega) G(q_{\parallel}, \omega) \quad (1.37)$$

$F(q_{\parallel}, \omega)$  represents the kinematic prefactor, which defines the angular behaviour of the HREEL cross section, *i.e.* a lobe of angular aperture  $\psi_E = \hbar\omega/2E_I$  peaked along the specular direction. The factor  $G(q_{\parallel}, \omega)$  contains the sample surface response, in terms of the effective dielectric function  $\xi_0(\mathbf{q}_{\parallel}, \omega)$ . When a semi-infinite homogeneous isotropic non dispersive sample is considered,  $\xi_0(\mathbf{q}_{\parallel}, \omega)$  corresponds to the material dielectric function  $\epsilon(\omega)$  which provides information on the solid-state excitations.  $D$ , the integration domain, is defined by the incident beam divergence and the analyser acceptance angle.

The dielectric tensor in uniaxial media such as TiO<sub>2</sub> rutile single crystals is anisotropic and diagonal in the main crystallographic axis; its two main components  $\epsilon_{\parallel}$  and  $\epsilon_{\perp}$  define the dielectric response of the media to electric fields parallel and perpendicular to the  $c$ -axis, respectively [69]. If the  $c$ -axis is in the  $xy$  plane oriented at an angle  $\theta$  with respect to the

surface normal axis  $z$ , the effective dielectric function  $\xi_0(\mathbf{q}_{\parallel}, \omega)$  becomes:

$$\xi_0(\mathbf{q}_{\parallel}, \omega) = \frac{\epsilon_{zz}(\omega)}{q_{\parallel}} \sqrt{\frac{\epsilon_{\parallel}(\omega)\epsilon_{\perp}(\omega)}{\epsilon_{zz}^2(\omega)} q_x^2 + \frac{\epsilon_{\perp}(\omega)}{\epsilon_{zz}(\omega)} q_y^2} \quad (1.38)$$

where  $q_x$  and  $q_y$  are the wave vector transfer components parallel to the surface, while  $\epsilon_{zz}(\omega) = \epsilon_{\parallel}(\omega) \cos^2(\theta) + \epsilon_{\perp}(\omega) \sin^2(\theta)$  is the dielectric tensor component normal to the surface. For  $\text{TiO}_2$  the  $c$ -axis is oriented in the  $x$  direction with  $\theta = 90^\circ$  and the effective dielectric function simplifies to

$$\xi_0(\mathbf{q}_{\parallel}, \omega) = \frac{1}{q_{\parallel}} \sqrt{\epsilon_{\parallel}(\omega)\epsilon_{\perp}(\omega)q_x^2 + \epsilon_{\perp}(\omega)^2q_y^2} \quad (1.39)$$

When scattering occurs in the  $yz$  plane,  $q_x \simeq 0$  and  $\xi_0(\mathbf{q}_{\parallel}, \omega) = \epsilon_{\perp}(\omega)$ ; otherwise, if it occurs in the  $xz$  plane where  $q_y \simeq 0$ ,  $\xi_0(\mathbf{q}_{\parallel}, \omega) = \sqrt{\epsilon_{\parallel}(\omega)\epsilon_{\perp}(\omega)}$ . These  $k$ -independent cases allow one to avoid the unwieldy integration in equation (1.37).

When incoming electrons strongly interact with the sample, there is a significant probability that successive scattering events will take place. Moreover, equation (1.37) strictly applies at 0 K, but at finite temperature energy gains arising from phonon deexcitations present at thermal equilibrium must be considered [42]. A HREEL spectrum recorded at finite temperature  $T$  thus consists in a rather complicated combination of gain and multiple loss peaks. Using a semi-classical treatment in which the incoming electron is considered as a classical particle acting as a time-dependent perturbation for the quantized field of elementary excitations [64, 68], the loss probability is:

$$P(\omega) = \frac{1}{2\pi} \int e^{-i\omega t} \mathcal{R}(t) e^{[\mathcal{P}(t) - \mathcal{P}(0)]} = e^{-\mathcal{P}(0)} R(\omega) \otimes \left\{ \delta(\omega) + \sum_{n=1}^{\infty} \frac{1}{n!} [\mathcal{P}(\omega)]^{n\otimes} \right\} \quad (1.40)$$

with

$$\mathcal{P}(t) = \int_0^{+\infty} d\omega' P_{cl}(\omega') \times [(n_{\omega'} + 1)(e^{i\omega't} + 1) + n_{\omega'}(e^{-i\omega't} - 1)] \quad (1.41)$$

The symbol  $\otimes$  denotes a convolution product between two functions, while  $n_{\omega} = [e^{\hbar\omega/k_B T} - 1]$  is the Bose-Einstein distribution. Moreover,  $\mathcal{P}(\omega)$  and  $\mathcal{R}(\omega)$  are the Fourier transforms of  $\mathcal{P}(t)$  and  $\mathcal{R}(t)$ , respectively. In practice,  $\mathcal{R}(t) = \int d\omega e^{-i\omega t} \mathcal{R}(\omega)$  represents the instrumental response function accounting for the finite resolution of the spectrometer. Looking at equation (1.40), we perceive that the HREEL spectrum  $P(\omega)$  is thus composed of an elastic peak, accounted for in the  $\delta(\omega)$  term, in addition to gain peaks, combinations between different transitions and multiple scattering events described as self-convolution products of the fundamental gain/loss function  $\mathcal{P}(\omega)$ . As checked both theoretically and experimentally, multiple losses follow a Poisson distribution. The Poisson statistics becomes extremely useful in the study of adsorbates, to remove the intense multiple excitation contributions which hinder molecular vibrations of much weaker oscillation strength [42, 70]. A method based on a Fourier log deconvolution technique, proposed by Cox and co-workers [71], has been developed and applied in this thesis to the case of TA adsorption on the rutile surface.

### 1.9.3 Experimental apparatus

HREEL spectra in this work were collected at room temperature using a LK2000 electrostatic spectrometer from LK-technologies. A schematic drawing of the apparatus is displayed in figure 1.19. Electrons emitted from the cathode, a  $\text{LaB}_6$  filament, pass through a

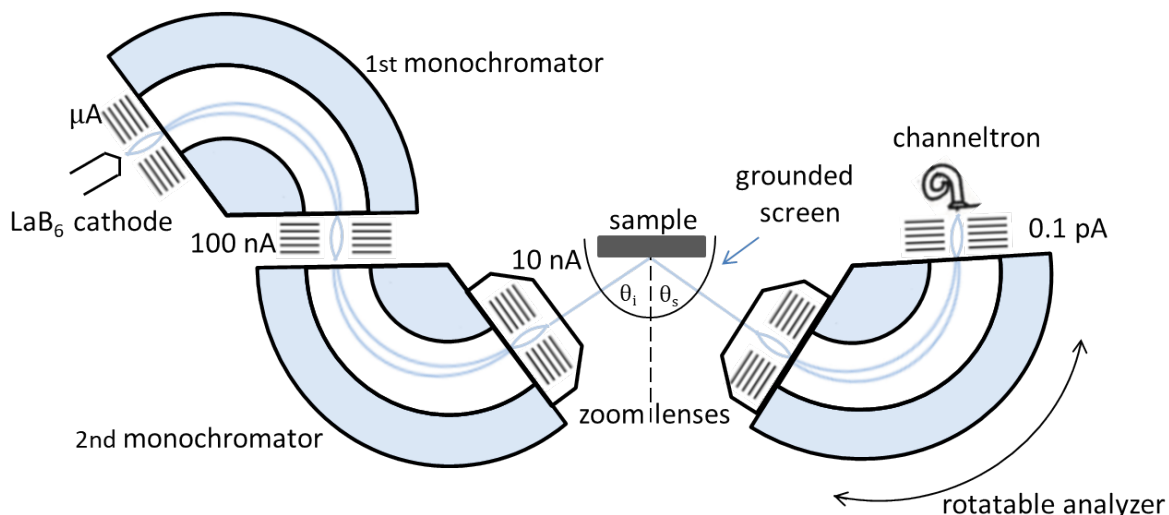


Figure 1.19: Schematic drawing of the HREEL spectrometer used in this work.

double stage 127° cylindrical monochromator. After they strike the sample, the scattered electrons are dispersed in energy by a rotatable 127° deflector analyser and the signal is finally amplified by an electron multiplier. The angle of the analyser can be varied from 20° to 70°, to perform off-specular measurements.

Most of HREEL data (unless explicitly specified otherwise) were acquired in specular geometry at an incident angle of 60° with respect to the surface normal. The primary electron beam energies (named  $E_b$  in the following) employed varied in the range of 3 to 18 eV. A resolution (FWHM) from 9 to 15 meV was obtained for the elastic peak at 8.8 eV.

## 1.10 Surface Differential Reflectivity Spectroscopy

Surface Differential Reflectivity Spectroscopy (SDRS) of UV-visible light is an optical technique in which relative variations of the sample surface reflectivity are monitored, for example during a thin film growth on a substrate. The relative change of reflectivity is defined as:

$$\frac{\Delta R}{R}(\omega, t) = \frac{R(\omega, t) - R(\omega, 0)}{R(\omega, 0)} \quad (1.42)$$

where  $\omega/2\pi$  is the light frequency, while  $R(\omega, 0)$  and  $R(\omega, t)$  are the sample reflectivities before and after an overlayer deposition of thickness  $t$ , respectively. The measured signal is normalised to the bare substrate reflectivity to remove the necessity to consider the detector response, lamp emission, optic transmission, which are unknown but need to remain constant all over the measurements. A good stability of the optical components is thus a pivotal requirement. Measurements are performed *in-situ* and in real time to gain information on dielectrical property variations and to probe the adlayer morphology. SDRS is indeed well-suited to investigate metallic film growth on oxide substrates with submonolayer sensitivity due to the strong contrast of their respective dielectric behaviours. More precisely, during metallic nanoparticle growth, the incident light excites surface plasmons. The induced dipole is damped by the imaginary part of the metal dielectric constant. The nanoparticle density, size and aspect ratio influence the resonance relative intensities and energy positions, thus enabling to probe particle morphology [72]. A more detailed description will be given in section 5.3.1.

### 1.10.1 Experimental apparatus

SDRS has been used in this work to monitor relative changes of the sample surface reflectivity during metal (Ni) depositions. The experimental set-up shown in figure 1.20 is mounted in the preparation chamber of 1.1a [73]. Light in the UV-visible range is emitted by a deuterium-halogen lamp and then splitted into two beams by passing into an optical fiber with a Y-branch structure. One beam is focused through a fused silica lens on the sample surface inside the UHV chamber passing through a silica window. The incidence angle is  $55^\circ$  with respect to the surface normal. The reflected signal travels towards a fused silica condenser and a barium borate Wollaston prism, which splits the incoming beam into two deviated beams of p and s polarisations. The separation angle equals  $25^\circ$  at 600nm wavelength and remains constant within the spectral range down to 300 nm, when it increases to  $45^\circ$ , causing a partial loss of UV light. The splitted beams are collected by lenses into optical fibers which transport light to the spectrometer entrance into two of its three available channels. The spectrometer (from Avantes) possesses indeed three fixed identical dispersing grating benches and CCD Si-array detectors. The optical beam from the other branch of the Y-shaped fiber passes through a diaphragm and it is fed into the remaining spectrometer entrance, to be used as reference to minimise the lamp drift in the other two channels. The UV transmittance is guaranteed along the optical path by the use of solarized silica optical fibers. The resolution, which depends on the spectrometer entrance slit and the grating groove density, is  $\sim 5$  nm. The measuring range extends from 1.4 to 6.2 eV (from 200 to 900 nm), being limited by the optical bench transmission and the detector response [73].

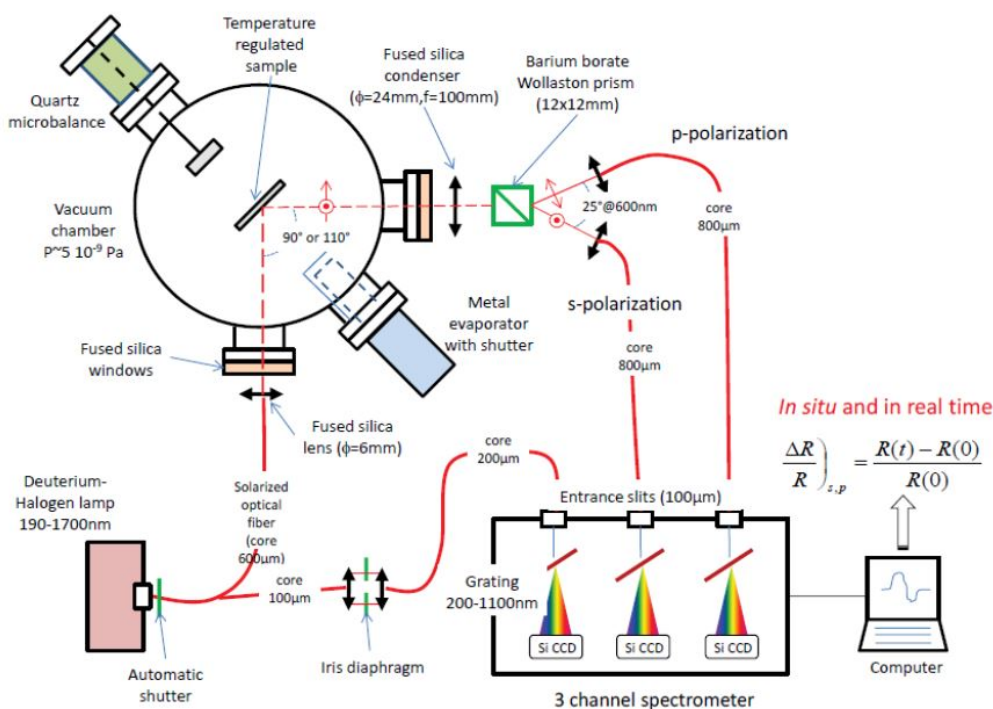


Figure 1.20: Schematic representation of the SDRS setup [73].





# CHAPTER 2

---

## State of the art

---

This chapter is a non exhaustive literature review of the rutile  $\text{TiO}_2(110)$  surface, its reactivity with carboxyl-containing but non chiral molecules as well as its interaction with Ni. Basic aspects of the concept of chirality and heterogeneous asymmetric catalysis are also reminded. All over the chapter, the attention is addressed to surface science studies.

*Ce chapitre est une revue non-exhaustive de la littérature sur la surface de rutile  $\text{TiO}_2(110)$ , sa réactivité avec des molécules carboxyliques mais non chirales et son interaction avec le Ni. Des aspects fondamentaux du concept de chiralité et de catalyse asymétrique hétérogène sont également rappelés. Tout au long de ce chapitre, l'attention est portée sur les études de science des surfaces.*

## 2.1 Chirality

The word *chirality* derives from the Greek  $\chi\epsilon\iota\rho$  (hand) and refers to objects, like our hands and feet, which cannot be superimposed on their mirror image through translation or rotation operations [4, 74]. When molecules are considered, chirality implies the lack of both mirror planes of symmetry and centres of inversion [74]. In organic compounds, chirality is often due to the presence of tetrahedral carbon atoms, *i.e.* carbon atoms linked to four different atomic entities. The two molecular mirror images are called *enantiomers* [4, 74]. Although possessing the same physical properties, e.g. density, boiling and melting points, differences arise when enantiomeric pairs interact with other chiral compounds or objects. Two enantiomers show a different optical activity when interacting with polarised light [74]. It was the chemist and biologist Louis Pasteur who first noticed the relationship between structure and optical activity of organic chiral molecules in 1848. He observed that when left and right-handed crystals of sodium ammonium tartrate interacted with plane polarised light, the plane of polarisation was rotated by an angle  $\alpha$  and  $-\alpha$ , respectively. Chiral compounds are thus often labelled after their optical activity: if the plane of polarisation is rotated in a clockwise direction, the chiral compound is called “dextrorotatory” and labelled with D or (+), while for an anticlockwise rotation the term “levorotatory” and the labels L or (-) are employed [74, 75]. Another alternative and common nomenclature is based on their absolute stereochemistry, using the Cahn-Ingold-Prelog (CIP) rules [76]. Within this convention, (R) and (S) labels are assigned in the following manner. Starting from a stereocenter, an order of priority is given to the

atomic substituents around it, in the order of decreasing atomic mass. When two atomic substituents are identical, priority is assigned by looking at atoms directly attached to the identical groups, until a difference is found. Once priority is assigned, the molecule is oriented so that the lowest priority group points away from the viewer, while the highest priority groups are oriented towards him (as in figure 2.1). If the curve going from the highest priority group (1) to the lowest one (3) is clockwise, the chiral centre is labelled (R) (from Latin “*rectus*”, meaning right), if anticlockwise, the chiral centre is name (S) (from “*sinister*”, meaning left). No direct link between the D,L and S,R nomenclature is observed [74].

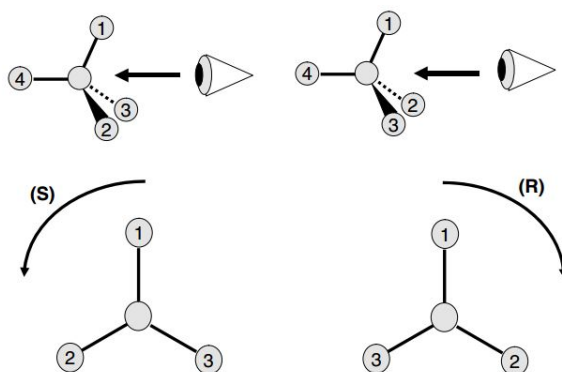


Figure 2.1: Schematic representation to label chiral compounds according to the Cahn-Ingold-Prelog (CIP) rules [74].

The synthesis of chiral compounds is of great interest in numerous fields, such as in the production of aromas, fragrances, pharmaceuticals and agrochemicals, but even more important is the ability to produce enantiomerically pure compounds, composed of only one enantiomer. The reason must be sought in the fact that many biomolecules in living systems (such as amino acids, enzymes, hormones and the DNA helix) are chiral and appear in nature in only one handedness. For example, aminoacids, the protein building blocks, only have the L configuration, sugars composing the DNA helix are exclusively in D form and olfactory receptors interact differently with opposite enantiomers. It is the case of the chiral molecule limonene whose R and S enantiomers smell as orange and turpentine, respectively [75, 77]. But the different biological response to opposite enantiomers may lead to more drastic and undesired effects than an odour perception, as in the case of thalidomide, used in the fifties as a sedative, hypnotic and anti-nausea drug especially indicated for pregnant women [77–79]. Unfortunately, it was sold as a racemic mixture and while the R enantiomer actually works as a sedative, the S one is teratogenic, causing malformations in the new-borns. This is a striking evidence of how the activity of pharmaceuticals, and not only that, strongly depends on which enantiomer is used, thus explaining why gaining a control of the enantioselectivity and producing enantiopure or at least enantioenriched compounds are of paramount importance in response to their increasing demand.

## 2.2 Heterogeneous asymmetric catalysis

From a practical point of view, the production of enantiomerically pure compounds is a tough task. When prochiral starting reagents are used, equal amounts of left- and right-handed enantiomers result at equilibrium, producing a *racemate*, since both enantiomers have the same Gibbs free energy [74]. A process of chiral resolution then follows to sepa-

rate enantiomerically pure compounds from the initial racemic mixture, but in which half of the initial product is thus wasted.

A different approach to the production of enantiopure chiral molecules is *asymmetric catalysis*. Asymmetric or enantioselective reactions refer to chemical processes in which the synthesis of one enantiomer of a chiral product is favoured with respect to the opposite one [80]. Asymmetric catalysis can be either homogeneous, if the catalysts, reactants and products are in the same phase, or heterogeneous, typically when a solid catalyst interacts with liquid or gaseous reactants. With homogeneous systems high selectivities and activities have been attained in a wide range of reactions; however, one of the major difficulty is related to catalyst separation from the reaction system, recovery and subsequent recycling, an essential requirement for industrial applications because of the high cost of chiral catalysts [3]. In this respect, heterogeneous asymmetric catalysis has recently received significant attention, as one possible solution to this problem, due to an easy separation of reactants, catalysts and reaction products. Two different strategies have been pursued to achieve heterogeneous asymmetric catalysis: the immobilisation of homogeneous asymmetric catalysts and the modification of an active metal surface by a chiral modifier, on which the focus of this work is laid [2, 75, 81–84]. In the latter, the strategy consists in combining the metal catalytic activity with the chiral modifier asymmetric induction during the reaction. Despite the significant potential in terms of catalyst separation, reuse and related economic advantages, successful systems with high enantiomeric product excess developed so far are mainly limited to the asymmetric hydrogenation of  $\alpha$ -keto esters over chincona alkaloid modified Pt catalysts [85–87] and the hydrogenation of  $\beta$ -keto esters over  $\alpha$ -hydroxy acid or  $\alpha$ -amino acid modified Ni catalysts [2, 75, 81–84, 88, 89]. Two examples are presented in figure 2.2, the asymmetric hydrogenation of methyl pyruvate over chinconidine modified Pt catalysts (top) and methylacetoacetate over (S)-glutamic acid modified Ni catalysts (bottom) [90]. Assuming that the reactant molecular plane is

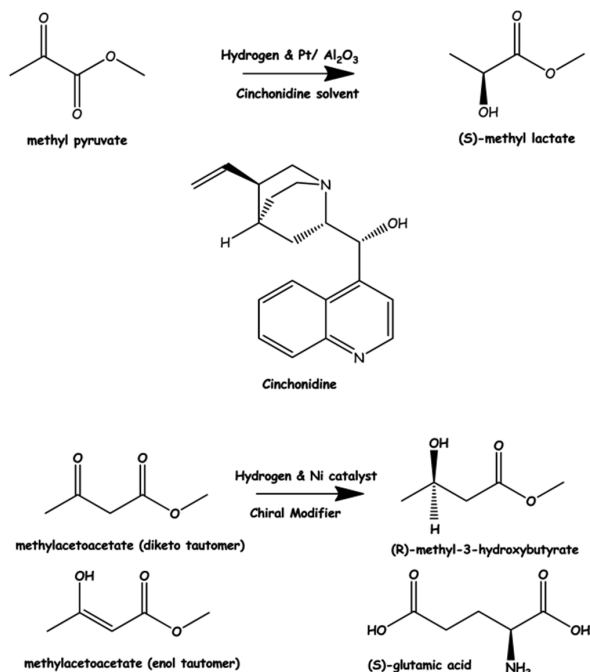


Figure 2.2: Scheme of the enantioselective hydrogenation reaction of methyl pyruvate over chinconidine modified Pt catalysts (top) and methylacetoacetate over (S)-glutamic acid modified Ni catalysts (bottom) [90].

parallel to the metallic surface, the molecule is adsorbed via one of its two enantiotopic faces (pro-(R) or pro-(S)). Upon hydrogenation, hydrogen atoms are thought to attack from beneath the reactant molecular plane and if no form of chirality is present at the surface, a racemic mixture is produced. If products in one single handedness are desired, reactant molecules must be forced to adsorb on the metal surface via one face only [90]. Various mechanisms have been suggested to be at the root of enantioselectivity [5]. In the Pt based catalytic systems, the Template model was first proposed by the Wells' group for the enantioselective hydrogenation of methyl pyruvate on cinchona-modified platinum [91]. The chiral molecules were thought to form ordered arrays upon adsorption on the metallic surface, leaving chiral shape sites accessible to the prochiral reactants. The chiral template formed at the surface would favour one specific reactant adsorption geometry and thus the production of one enantiomer over the other. However, later studies provided direct evidence against the Template model, since the adsorption of cinchonidine and similar molecules produced disordered structures. A second mechanism, known as the *active chiral site model* was therefore suggested, in which during the hydrogenation reactions, following protonation of either the N atom or the ketone O atom, enantioselectivity results from the formation of H-bonds between the N atom in the quinuclidine moiety and the reactant ketone group. For the Ni based systems, a 1:1 interaction between modifier and reactant was proposed as well. Another model based on the formation of an organometallic complex was also suggested by Petrov and Klabunovskii [5] and subsequently modified by Sachtler [92]. Within the proposed mechanism, a Ni-tartrate complex was thought to form upon tartaric acid adsorption.

## 2.3 Supported enantioselective catalysts

As shown previously, two enantioselective systems have been developed with success, namely cinchona alkaloid modified Pt catalysts and  $\alpha$ -hydroxy acid or  $\alpha$ -amino acid modified Ni catalysts. For Pt based catalysts, supported platinum is often used and common choices of supports are alumina, silica, carbon and sometimes zeolites [93]. For Ni based catalytic systems, Raney Ni, supported Ni catalysts as well as unsupported commercial Ni powders have been considered [79]. For supported Ni catalysts, silica [94, 95], alumina [94, 95], zeolites [94], carbon and graphite [96] have been tested as supports. Most studies have focused on the dependence of the catalyst activity and enantioselectivity on the choice of the metal catalyst, particle size and catalyst dispersion [97]. Moreover, the effect of solvents, modifier concentration and temperature have been investigated to obtain optimal activities and enantioselectivities [98–100]. In this respect, the optimal tartaric acid coverage on the Ni metal surface was estimated to be around 20% [98, 101]. Some studies have been carried out on the role of the support in supported catalysts. In some works, the choice of the support ( $\text{Al}_2\text{O}_3$ ,  $\text{SiO}_2$  or carbon) did not seem to have a major effect on the enantiomeric excess for the hydrogenation of ethyl pyruvate over Pt-cinchonidine catalysts [79, 102]. Conversely, in other studies differences were observed for cinchonidine adsorption on alumina and silica supports, suggesting a possible role of the support in the catalytic process [103]. For tartaric acid-modified nickel catalysts, it was shown that the activity and enantioselectivity of supported Ni catalysts may sometimes depend on the choice of the oxide support and catalyst preparation method [97]. While similar results were obtained for methyl acetoacetate hydrogenation on silica supported, unsupported and Raney nickel catalyst, a lower enantioselectivity was recorded on  $\gamma$ -alumina supported Ni catalysts [79, 92].

Catalytic systems are complex and our knowledge still lacks a detailed explanation of the

asymmetric catalytic process at a molecular level as well as of the role of the support. Understanding how the chiral modifier adsorbs, how chirality is conveyed to the surface and which are the active sites where catalysis takes place are the crucial preliminary steps in the conception of successful enantioselective systems. Different routes have been followed with the aim of understanding the origin of enantiodifferentiation. In this respect, surface science techniques have provided fundamental insights otherwise not accessible in the intrinsically complex more realistic systems. Most works have been focused on single crystal metal surfaces, while the role of the support has usually been overlooked. In the model surface science catalyst approach, chiral molecules are adsorbed on single crystals metal surfaces under controlled UHV conditions and studied by a variety of surface science techniques to gain information on the physics and chemistry behind [4, 5].

## 2.4 Chirality at surfaces

Heterogeneous asymmetric catalysis requires metal surfaces that are chiral at the atomic scale. Surfaces are either intrinsically chiral or they are made as such by the adsorption of either chiral or achiral molecules. Among the most common intrinsically chiral surfaces, there are the quartz crystals, named right-handed or left-handed based on the clockwise or anticlockwise helical disposition of its  $\text{SiO}_4$  tetrahedra. Another example is given by face-centred cubic (fcc) crystals, which although displaying high symmetry bulk structures, when cut along high Miller index directions expose kinked steps with different step lengths separated by low Miller index terraces. As an example, figure 2.3 shows the fcc  $(643)$  and the  $(\bar{6}\bar{4}\bar{3})$  mirror image surfaces, which are non-superimposable and therefore chiral [81]. The nomenclature of kinked metal surfaces is defined in analogy to the CIP rules. Looking from above at the kink site, an order of priority is assigned to the microfacets forming the kink in the order of decreasing atomic density ( $\{111\} > \{100\} > \{110\}$ ). If this sequence runs clockwise, the surface is labelled “R”, otherwise “S” [74, 104, 105]. Enantiospecific interactions of two enantiomers are observed on these kinked surfaces, as reported for example by Attard for D- and L-glucose electrooxidation on a  $\text{Pt}\{643\}$  surface studied by cyclic voltammetry [74, 106].

Another way of creating chiral surfaces, more interesting for the purpose of this work, is by the adsorption of either chiral or achiral molecules on initially achiral surfaces. In both cases, chirality may arise from the single molecular adsorption event and/or from the formation of chiral supramolecular assemblies. In this respect, a detailed classification for

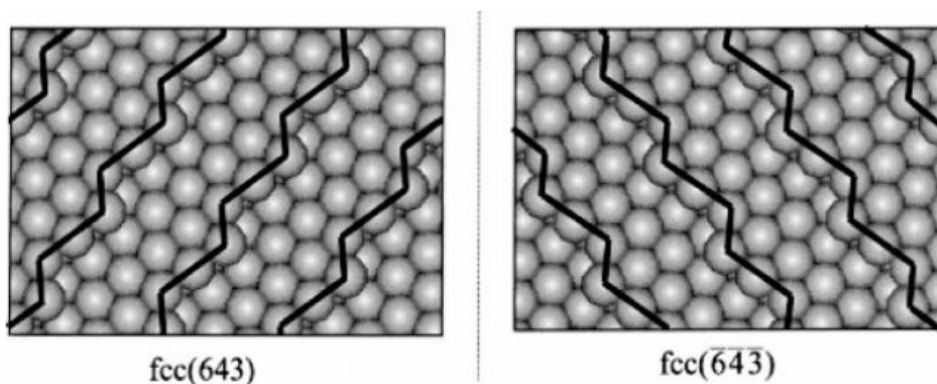


Figure 2.3: Ball model of the fcc  $(643)$  crystal and its mirror image  $(\bar{6}\bar{4}\bar{3})$ , where steps are indicated by the bold black line [81].

the various possible expressions of surface chirality was proposed by Barlow and Raval [4] and it is summarised in figure 2.4. The adsorption of non chiral molecules on non chiral surfaces is sometimes sufficient to create a chiral motif. The simplest example of surface chirality originates from a single adsorption event, when the adsorbed molecule is tilted away from any mirror planes of the substrate surface. Additionally, non-chiral molecules may organise in 2D chiral superstructures, oriented along non-symmetry directions of the

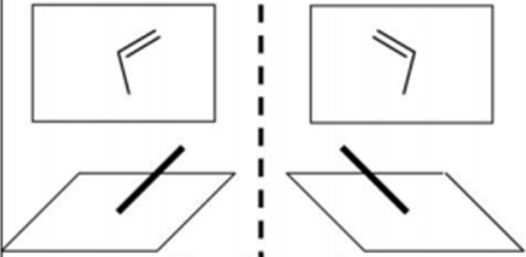
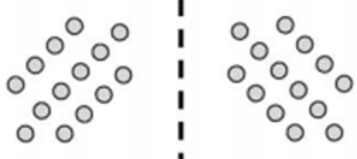

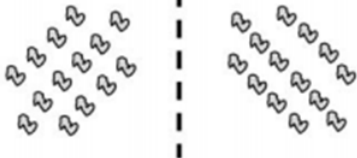

<b>Non-chiral molecules</b>	
<p>Adsorption induced chiral motifs.</p> <p><i>-alignment of molecule breaks the reflection symmetry axes of surface:</i>  <b>local point chirality</b>  <i>(i.e. belongs to a chiral point group).</i></p>	 <p>Overall racemic</p>
<p>Adsorption induced chiral arrangements (or domains).</p> <p><i>-the ordered domains possess a chiral space group:</i>  <b>local organisational chirality.</b></p>	 <p>Overall racemic</p>
<b>Chiral molecules</b>	
<p>Molecule induced chiral motifs.</p> <p><i>-intact preservation of chiral centre upon adsorption i.e. creates local chiral point group:</i>  <b>global point chirality.</b></p>	 <p>Overall chiral</p>
<p>Adsorption induced chiral arrangements.</p> <p><i>(i) asymmetric lateral interactions e.g. mediated by groups that are non-chiral - reflectional domains allowed:</i>  <b>global point and local organisational chirality.</b></p>	 <p><i>pseudo reflection</i> Overall chiral</p>
<p><i>(ii) chiral lateral interactions- no reflectional domains allowed:</i>  <b>global point and global organisational chirality</b></p>	 <p>Overall chiral</p>

Figure 2.4: Classification of the various types of chiral expressions following adsorption of non-chiral and chiral molecules on surfaces [4].

underlying surface. Nevertheless, in both cases, the intrinsic non-chiral nature of the adsorbed molecules ensures the presence in equal amounts of motifs or domains with opposite handedness. Chirality manifests only at a local level, while the surface is overall racemic [4]. The adsorption of chiral molecules always leads to some kind of chiral expression, if the chiral nature is retained in the adsorption process. As for non-chiral molecules, chirality is inferred by the adsorption of single molecules and their intrinsic molecular chirality prevents the formation of mirror chiral motifs, leading to a global point chirality. Moreover, they may assemble in ordered aggregates, either non-chiral or chiral. Among chiral arrangements, two different situations are identified:

- if lateral interactions retaining the aggregates are governed by non-chiral groups, sufficiently far from the chiral centres, reflectional domains are formed as well. However, when considering the intrinsic molecular chirality, image and mirror image assemblies are only pseudo-reflections of each other and the surface is overall chiral (see figure 2.4).
- if lateral interactions are mediated by chiral groups, reflectional domains are not observed on the surface. In this case chirality is imparted at a global point and global organisational level, leading to the highest form of chiral expression.

## 2.5 Tartaric acid adsorption on metal surfaces

Numerous surface science studies have been carried out on the deposition of chiral modifiers, such as hydroxy acids and amino acids, on metal surfaces to model the heterogeneous catalytic system and investigate how chirality is imparted upon adsorption. A great focus has been placed on tartaric acid, being one of the most efficient chiral modifier. Generally speaking, tartaric acid ( $C_4H_6O_6$ ) is a dicarboxylic acid, which appears in the form of a white odourless crystalline powder. It contains two asymmetric carbon atoms, namely the second and third ones, and three stereoisomeric TA exist: mesotartaric acid, in which the two asymmetric C atoms have opposite handedness, thus making it optically inactive, L-(+)-Tartaric acid (or (2R,3R)-(+)-Tartaric acid (RR-TA)) and D-(-)-Tartaric acid (or (2S,3S)-(-)-Tartaric acid (SS-TA)), which are enantiomers [107]. A schematic representation of RR-TA and SS-TA is presented in figure 2.5 [108].

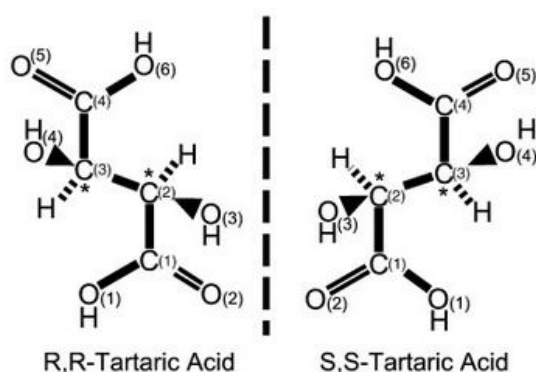


Figure 2.5: Schematic representation of RR-TA and SS-TA. The two chiral centers are marked by an asterisk [108].

Tartaric acid is found in nature in many plants like tamarinds, bananas and apples and it is commonly used in the food industry to confer a sour taste and as antioxidant [109].



In heterogeneous asymmetric catalysis, TA is one of the most efficient chiral modifier and most studies have focused on the R,R form, the naturally occurring one. RR-TA has proven to be highly versatile upon adsorption on metallic surface. Infact, at least three different chemical forms may appear upon adsorption (figure 2.6): the neutral bi-acid form, in which the molecule is adsorbed intact on the surface, the monotartrate and bitartrate forms in which one and both COOH groups deprotonate upon adsorption. Interesting for

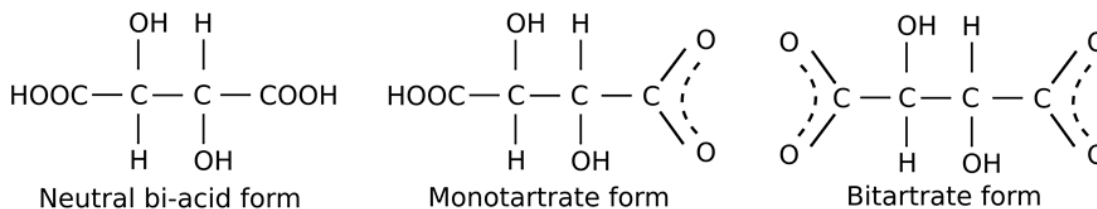


Figure 2.6: Different chemical forms of RR-TA upon adsorption.

the present study is its adsorption on Cu and Ni surfaces in the clean and controlled UHV conditions, initially investigated by the groups of Baddeley and Raval [4]. A combination of RAIRS, STM and LEED helped to unravel the chiral modifier chemical nature and organisation on such metal surfaces. One relevant conclusion is that TA adsorption and chemical nature strongly depends on the adsorption temperature, time and surface coverage, resulting in complicated adsorption phase diagrams, as shown for TA on Cu(110) (figure 2.7) [4, 110–112]. Without detailing all the specific adsorbate overlayer structures formed, we just focus on the  $\begin{pmatrix} 9 & 0 \\ 1 & 2 \end{pmatrix}^1$ , which is of particular interest for this work to understand how a metal surface is endowed with both local and global chirality. Bitartrate molecules bound to the Cu surface via the carboxylate O atoms of both deprotonated COOH groups (figure 2.7). Moreover, molecules assemble in rows of three along the  $[\bar{1}14]$  direction, due to lateral interactions between  $\alpha$ -hydroxy groups of neighbouring molecules (figure 2.8). Due to the inherent chirality of TA molecules, which is retained upon adsorp-

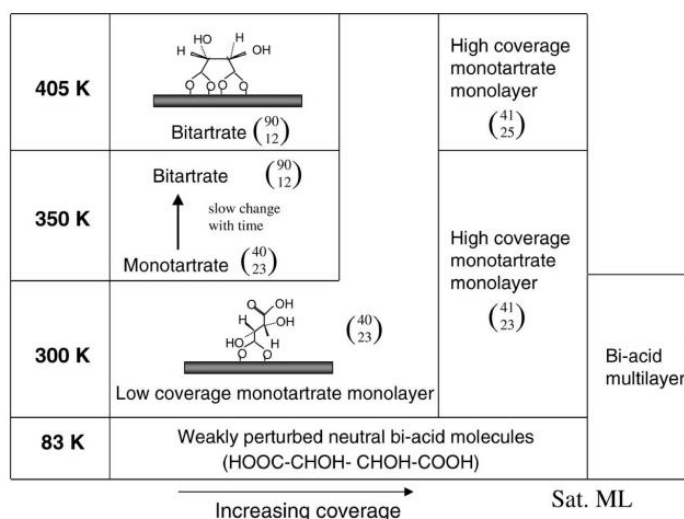


Figure 2.7: Adsorption phase diagram of TA adsorption on Cu(110) as a function of the adsorption temperature and coverage [4, 110].

<sup>1</sup>For the overlayer structure notation see section 1.6.

tion, the absence of any symmetry elements of reflection in the  $\begin{pmatrix} 9 & 0 \\ 1 & 2 \end{pmatrix}$  superstructure and the formation of molecular assemblies oriented along the same non-symmetry directions of the underlying surface, which are observed all over the Cu surface, lead to a global point and global organisational chirality [4]. Conversely, when the modifier with opposite handedness, namely SS-TA, is considered, a  $\begin{pmatrix} 9 & 0 \\ \bar{1} & 2 \end{pmatrix}$  superstructure is formed, which is the mirror image of the  $\begin{pmatrix} 9 & 0 \\ 1 & 2 \end{pmatrix}$  overlayer. Moreover, the triple molecular chains are oriented along the  $[1\bar{1}4]$  direction, which is the mirror growth direction of the RR-TA one, confirming that the adsorption geometry is enantiospecific. Following these studies, it was proposed that the formation of chiral channels leaves at the metal surface a chiral adsorption environment for the prochiral reactants, which thus dock to the modifier in one particular orientation, producing only one enantiomer of the product upon hydrogenation. When the opposite enantiomer is considered, channels with mirror growth directions are created, favouring the product with opposite handedness [5].

The adsorption of RR-TA has been intensively studied also on Ni, due to its higher efficiency in heterogeneous catalysis for hydrogenation compared to Cu. Ni(111) has been selected, since the  $\{111\}$  is the most thermodynamically stable face of fcc crystals and likely the most abundant facets of nanoscale-size Ni nanoparticles [114,115]. Similarly to Cu(110), the TA chemical nature strongly depends on the adsorption temperature and time. Ordered adlayer structures are formed, although with a lower order compared to Cu(110), possibly because of the greater reactivity of Ni [114]. In this case TA adsorption does not leave chiral channels, but ordered vacancies surrounded by chiral molecules on the Ni surface, which are thought to create a chiral adsorption environment for prochiral reactant molecules, in analogy to the Template model proposed for modified Pt systems. The adsorption of methylacetoacetate (MAA) on a RR-tartaric acid modified Ni(111) was studied as well to model the prochiral molecule behaviour. At intermediate TA coverage, ordered TA and MAA structures were formed, where MAA in specific conditions is adsorbed with the same orientation on the whole Ni surface. A different situation is reported

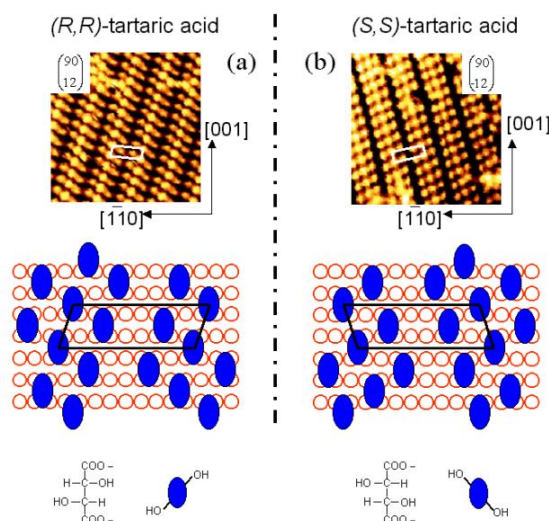


Figure 2.8: STM images of RR-TA (left) and SS-TA (right) on Cu(110) and corresponding schematic adsorption model [113].

for Ni(110), where TA molecules are randomly adsorbed on the surface, forming short 1D chains along the  $[1\bar{1}0]$ , a high symmetry direction for Ni(110), with no evidence of 2D ordered overlayers. Chirality is instead imparted to the metal surface by a local chiral reconstruction of the underlying Ni atoms induced by TA molecules.

## 2.6 The rutile $\text{TiO}_2$ structure

$\text{TiO}_2$  has attracted significant attention in the last decades for its proven or/and potential applications in many fields [116]. It is a widely employed white pigment in paints, inks, toothpastes and many more substances thanks to its high refractive index, non-toxicity and brightness [117]. Moreover, in sunscreens  $\text{TiO}_2$  acts as an ultra-violet blocker and it is employed in dental and orthopedic implants due to its biocompatibility and mechanical properties [118].  $\text{TiO}_2$  has recently gathered increasing scientific interest in photocatalysis [119] and as a heterogeneous catalyst support [120]. Besides, by virtue of the abundant availability of  $\text{TiO}_2$  single crystals, their low cost and the versatility of their characterisation by surface science techniques,  $\text{TiO}_2$  is often used as a prototypical model in the study of metal oxide materials [116,121].

### 2.6.1 Bulk structure

$\text{TiO}_2$  crystals exist in three crystallographic forms, rutile, anatase and brookite [116,122]. Among them, rutile is the most stable polymorph and it has attracted the most attention in the surface science field, for the high availability of rutile single crystals and their easy and reproducible preparation and characterisation under UHV conditions. Bulk rutile presents a tetragonal lattice structure. Its tetragonal unit cell, which contains 2  $\text{TiO}_2$  molecules, has dimensions  $a=b=4.587 \text{ \AA}$  and  $c=2.953 \text{ \AA}$  [116]. The rutile bulk structure is often described in terms of slightly distorted  $\text{TiO}_6$  octahedra, which are stacked by alternating the long axis by  $90^\circ$  as illustrated in figure 2.9.

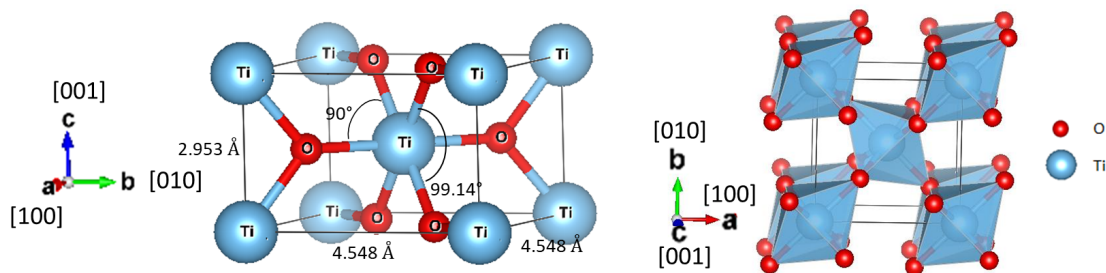


Figure 2.9: Ball and stick model of the rutile bulk structure: the unit cell (left) and the stacking of the  $\text{TiO}_6$  octahedra.

As shown in figure 2.10, the phase diagram of a Ti-O system is quite complex, with a multitude of possible stable phases [116,123]. The reduction of  $\text{TiO}_2$  single crystals is readily done, for example following a standard UHV cleaning preparation, and involves the formation of oxygen vacancies and titanium interstitials and the change in the oxidation degree from  $\text{Ti}^{4+}$  to  $\text{Ti}^{3+}$ . The presence of these bulk defects changes the single crystal colour (from transparent to dark blue in heavily reduced oxides) and its electronic properties. The excess electrons resulting from the bulk defects occupy the Ti 3d orbitals and give rise to a defect state located at about 0.8-1 eV below the Fermi level  $E_F$ , the so-called band gap state, observed for example by XPS and EELS [69,116]. Reduced  $\text{TiO}_{2-x}$

crystals are n-type semiconductors.

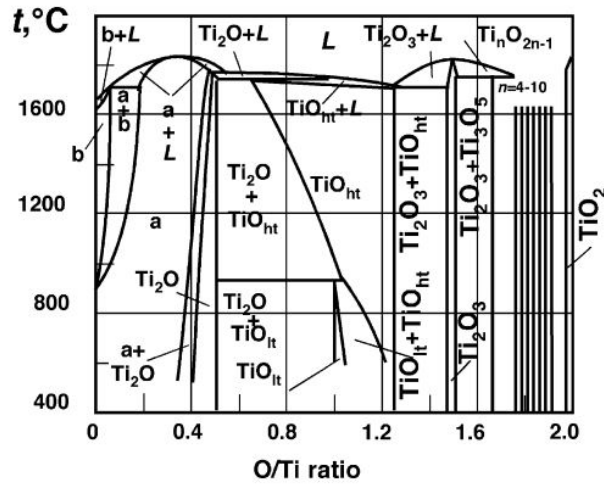


Figure 2.10: Phase diagram of a Ti-O system [116, 123].

### 2.6.2 The rutile $TiO_2(110)$ surface

A rutile crystal typically exhibits (110) and (001) surfaces [124]. Among them, the most focused upon surface is the (110), which is the thermodynamically most stable one. It consists of alternating rows of five-fold coordinated Ti atoms ( $Ti_{5c}$ ), three-fold O atoms ( $O_{3c}$ ) and six-fold Ti atoms ( $Ti_{6c}$ ) (figure 2.11). On top of the  $Ti_{6c}$  atoms, rows of two-

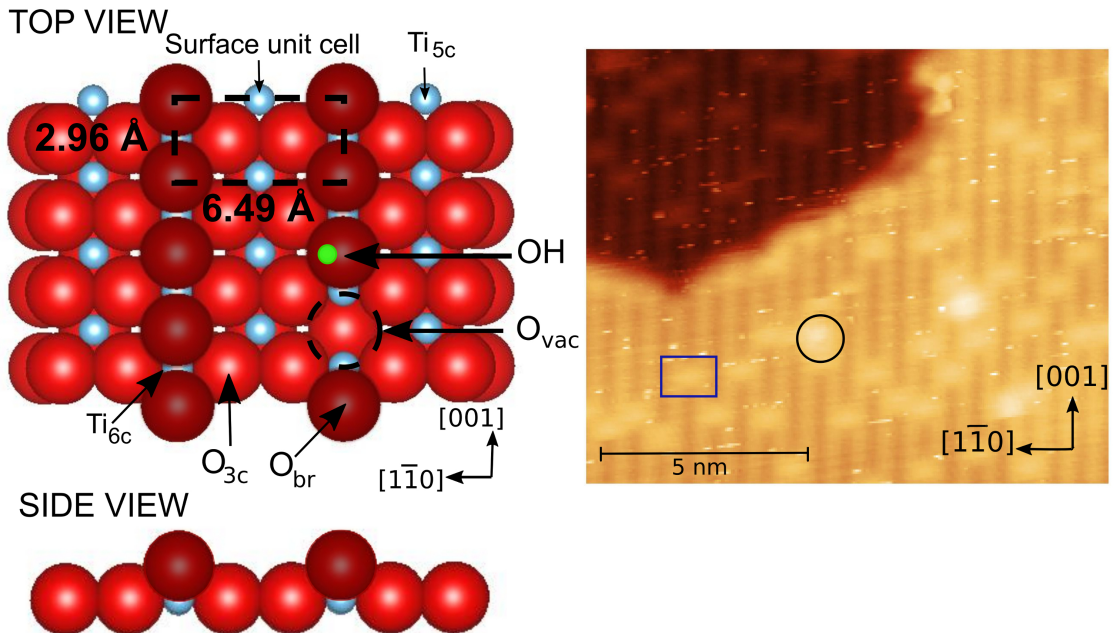


Figure 2.11: Left: Ball model of the rutile  $TiO_2(110)$  surface (top and side view). Ti,  $O_{3c}$ ,  $O_{br}$  and H atoms are represented in blue, red, dark red and green, respectively. The black rectangle corresponds to the  $(1 \times 1)$  surface unit cell. Right: STM image of the clean rutile  $TiO_2(110)$  surface (0.9 V, 100 pA). Examples of  $O_{vac}$  and OH group are marked with a blue rectangle and a black circle, respectively.

fold O atoms, also called bridging oxygen ( $O_{br}$ ) protrude out of the surface layer. The  $(1 \times 1)$  surface unit cell is rectangular, with parameters of  $2.96\text{\AA}$  and  $6.49\text{\AA}$  in the  $[001]$  and the  $[\bar{1}\bar{1}0]$  directions, respectively. Among the most common defects there are oxygen vacancies ( $O_{vac}$ ), *i.e.* the lack of an  $O_{br}$  atom, and surface hydroxyls (OH). A great focus has been placed on the reactivity of  $O_{vac}$  with  $O_2$  and  $H_2O$ . It has been shown that  $H_2O$  molecules can dissociate, fill the vacancies and form hydroxyl groups everywhere on the  $O_{br}$  rows [116,121]. The standard UHV cleaning preparation of  $TiO_2(110)$  single crystals is known to lead to an amount of  $O_{vac}$  between 5 and 10%. The presence of defects is confirmed by the appearance of a shoulder in the XPS Ti 2p peak shifted by  $\sim 1.7$  eV to lower binding energy with respect to the  $Ti^{4+}$  main peak at 459 eV and attributed to a reduced  $Ti^{3+}$  component (figure 2.12) [116]. Figure 2.12 also shows the effect of  $Ar^+$  bombardment, with a preferential O sputtering with respect to Ti. Following annealing, samples are reoxidised and the excess Ti atom flow towards the bulk [125].

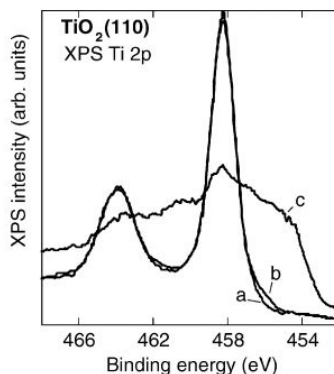


Figure 2.12: Ti 2p XPS peak of rutile  $TiO_2(110)$ : (a) stoichiometric surface, (b) after UHV annealing and (c) after sputtering [116].

The increasing attention directed at rutile  $TiO_2(110)$  in surface science stems from the possibility of increasing the crystal conductivity by reducing the samples under UHV conditions and thus allowing its characterisation by surface science methods. In this respect, STM is a powerful method to image the surface as well as the presence of defects which play an important role in the reactivity of metal oxides. Following a standard UHV cleaning procedure with an annealing temperature around 1000 K, terraces are generally between 5 and 20 nm wide [126]. Steps are preferentially oriented along the  $\langle 1\bar{1}1 \rangle$  and  $\langle 001 \rangle$  directions, with a step height  $\sim 3$  Å. The clean  $TiO_2(110)$  surface is imaged in STM as alternate parallel bright and dark rows running along the  $[001]$  direction (figure 2.11, right panel). In the case of  $TiO_2$ , a positive bias is applied to the sample for imaging, *i.e.* electrons flow from the occupied states of the tip into the empty states of the sample. The bright rows imaged in STM thus correspond to surface  $Ti_{5c}$  rows, while the dark ones to bridging O atoms, in contrast to the surface topography ( $O_{br}$  protrude out by 1 Å) [116,121]. Surface defects ( $O_{vac}$  and OH groups) appear then as bright protrusions on the dark  $O_{br}$  rows (figure 2.11). Wendt *et al.* and Bikondoa *et al.* investigated the STM imaging difference between  $O_{vac}$ , surface hydroxyls and water molecules on the  $TiO_2(110)$  surface [127,128]. The experimental results shown in figure 2.13 suggest that these different surface defects can be distinguished in STM images mainly by their profile and contrast compared to the  $Ti_{5c}$  rows. Compared to  $O_{vac}$ , OH groups appear brighter, as shown in figure 2.13. Part of the  $O_{vac}$  have already reacted with the residual water in the UHV chamber before the STM analysis, giving rise to surface hydroxyl groups. Moreover, paired hydroxyls are found on the  $TiO_2$  surface as well, which are formed by water adsorption at

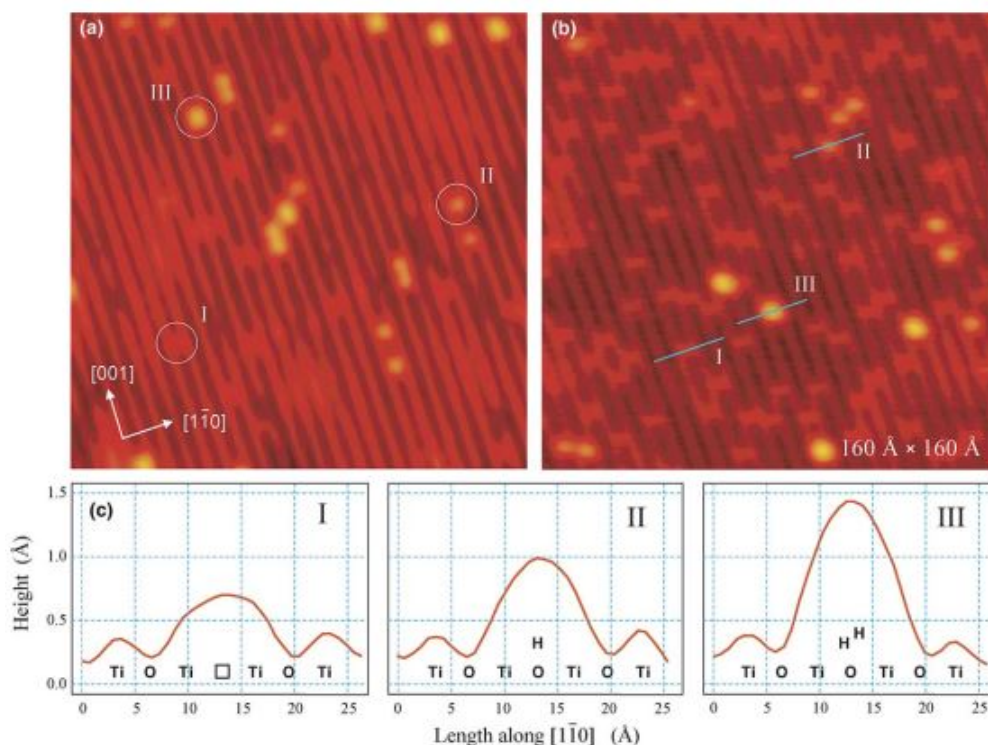


Figure 2.13: STM images of clean reduced TiO<sub>2</sub>(110) surfaces: (a) slightly reduced sample; (b) stronger reduced sample. Details on the sample preparation are found in ref. [127]. (c) STM height-profiles along the [1 $\bar{1}$ 0] direction of the surface defects in (b). Defects named I, II and III refer to oxygen vacancies, bridging hydroxyls and pairs of bridging hydroxyls, respectively [127].

$O_{vac}$  and which are easily distinguished because of their even greater brightness compared to OH groups.

## 2.7 Carboxylic acid adsorption on TiO<sub>2</sub>(110)

The adsorption of non-chiral carboxylic acid molecules on the rutile TiO<sub>2</sub>(110) surface has received considerable attention due to the number of potential applications and current devices. Grätzel solar cells, self-assembled monolayers, dental implants, gas sensors, heterogeneous catalysis are just a few examples. Research has focused both on simple molecules, such as formic and acetic acid, and larger and more complex ones, containing two or more COOH groups.

### 2.7.1 Formic acid adsorption on rutile TiO<sub>2</sub>(110)

Being the simplest carboxylic acid, the adsorption of formic acid (FA) (HCOOH) on TiO<sub>2</sub> surfaces has been intensively investigated and held as a prototype model to understand the adsorption mechanism of more complex molecules [121]. Several rutile TiO<sub>2</sub> surface orientations have been chosen as supports, such as TiO<sub>2</sub>(100) [129], TiO<sub>2</sub>(001) [130] and TiO<sub>2</sub>(110). However most studies have focused on TiO<sub>2</sub>(110) and quite a wide range of techniques have been employed, including LEED [131, 132], Fourier-Transform Reflection-Absorption InfraRed Spectroscopy (FT-RAIRS) [132, 133], STM [134, 135], XPS [131, 132, 136, 137], UPS [137], TPD [131, 138], HREELS [131, 138], Photoelectron Diffraction

tion (PhD) [139], Near Edge X-ray Absorption Fine Structure (NEXAFS) [140] as well as Density Functional Theory (DFT) calculations [133]. It is nowadays well-known that FA dissociatively adsorbs on  $\text{TiO}_2(110)$  into a formate anion and a proton [121, 136, 138]:



The adsorbed formate is arranged in a  $(2 \times 1)$  overlayer at saturation coverage, which correspond to 0.5 ML as determined by XPS (1 ML = 1 formate per  $\text{Ti}_{5c}$ , *i.e.*  $\sim 5.20 \times 10^{14} \text{ cm}^{-2}$ ) [134–136]. There is a general agreement that formate adsorbs normal to the surface, with both carboxylate O atoms bound to two adjacent  $\text{Ti}_{5c}$  atoms and with the molecular plane aligned along the  $[001]$  direction. Based on HREELS studies, it was proposed that the acidic H binds to a bridging O anion giving rise to a surface hydroxyl [131, 138, 141]. FA adsorption geometry and the substrate relaxations have been obtained both by means of PhD [139] and later by a quantitative LEED-IV study [142]. The structural parameters resulting from the two studies are in good agreement, as schematically illustrated in figure 2.14. The distance between two adjacent  $\text{Ti}_{5c}$  is suitable to accommodate the adsorption of carboxylate groups.

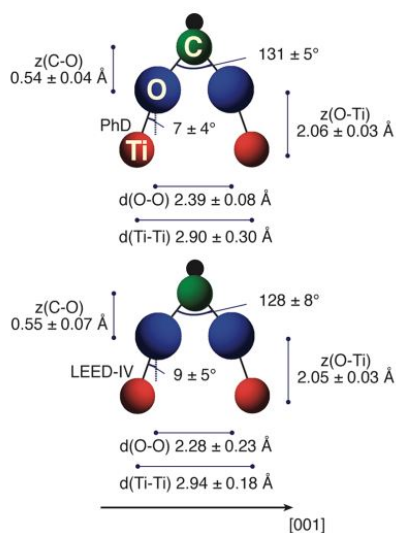


Figure 2.14: Schematic representations of the formate adsorption geometry on  $\text{TiO}_2(110)$ , as determined by PhD (top) [121, 139] and LEED-IV (bottom) [121, 142]. The geometrical parameters obtained from the two independent studies are in perfect agreement [121].

Over the years, other groups found evidence of a second formate species adsorbed on the rutile surface [132, 137, 140, 141, 143]. Using a combination of XPS and FT-RAIRS, Hayden *et al.* [132] demonstrated the coexistence of two formate species adsorbed orthogonally to each other on the surface. Species denoted with A in figure 2.15 are the above mentioned ones, with their molecular plane along the  $[001]$  direction. Species B are instead aligned along the  $[1\bar{1}0]$  direction, with one  $[\text{HCOO}]^-$  oxygen atom bound to a  $\text{Ti}_{5c}$  atom and the other one filling a bridging O vacancy on the  $\text{TiO}_2(110)$  surface. The coverage for species A and B was estimated to be 0.4 and 0.2 ML, respectively, confirming that species A are the ones responsible for the  $(2 \times 1)$  ordered overlayer observed at saturation coverage. STM images recorded by Bowker (figure 2.16), confirmed the existence of formate in a different bonding site, most likely species B as previously denoted. However, contrary to what was stated by Hayden, these molecules were rarely detected on the surface, less than 1% for FA deposited at room temperature. Different experimental conditions and specifically a different substrate temperature may account for such discrepancies. In this respect, STM images recorded for FA deposited at room temperature on  $\text{TiO}_2(110)$  and subsequently annealed at 350 K revealed that 35% of formate species are oriented along the  $[1\bar{1}0]$  direction. In the PhD study of Sayago *et al.* [144], no evidence for a significant presence of species B was instead reported; again this may be explained on the basis of

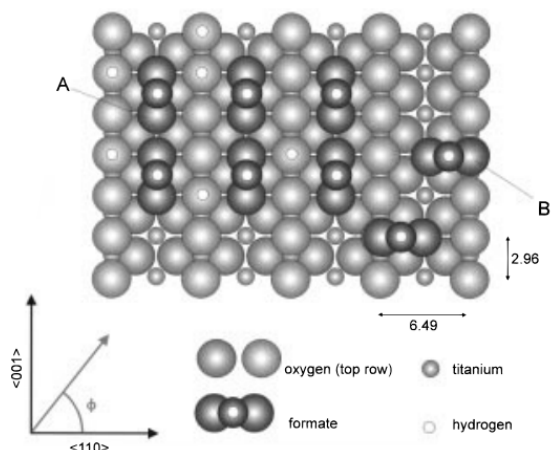


Figure 2.15: Ball model for formate species on  $\text{TiO}_2(110)$ . Species A and B are described in the text [132].

different substrate temperature used or the presence of OH groups due to dissociation of  $\text{H}_2\text{O}$ .

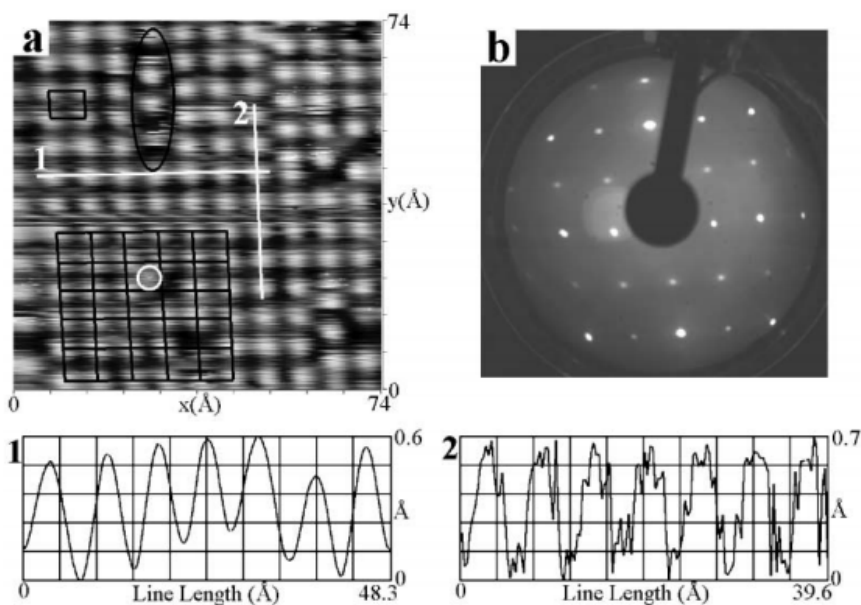


Figure 2.16: (a) STM image of formic acid on rutile  $\text{TiO}_2(110)$  for a near-saturation coverage at room temperature. The  $(2 \times 1)$  overlayer is evidenced by the grid. This assignment is confirmed by the line profiles at the bottom of the image. A different formate species is marked with a white circle. (b) Corresponding LEED pattern (beam energy = 67 eV) [143].

The peculiar adsorption geometry of species B, which fill bridging O vacancies on the  $\text{TiO}_2(110)$  surface, suggested that surface defects may actually play a role on FA adsorption. In this respect, Wang and co-workers [137] investigated the interaction of formic acid with both stoichiometric and defective  $\text{TiO}_2(110)$  surfaces. On the nearly defect-free surface, the saturation coverage was estimated to be  $\sim 0.5$  ML, while when additional surface defects were created by electron and  $\text{Ar}^+$  ion bombardment, the saturation coverage increased up to 0.77 and 0.92 ML, respectively. For electron-beam surface defects, one additional molecule adsorbs for every two defect  $\text{Ti}^{3+}$  sites; on the other hand, for  $\text{Ar}^+$  bombarded surfaces, a quantitative analysis was more difficult to obtain, due to the variety of defects created. Unlike the case of an  $\text{Ar}^+$  bombarded surface (figure 2.17(a)), exposure



of the formate saturated - Ar<sup>+</sup> bombarded surface did not show any defect healing when exposed to an O<sub>2</sub> atmosphere, as shown in the ultra-violet photoemission spectra in figure 2.17(b), suggesting that FA also blocks Ti<sup>3+</sup> available sites. The strong interaction of formate species with Ti sites of both stoichiometric and defective surfaces was also supported by ab initio calculations.

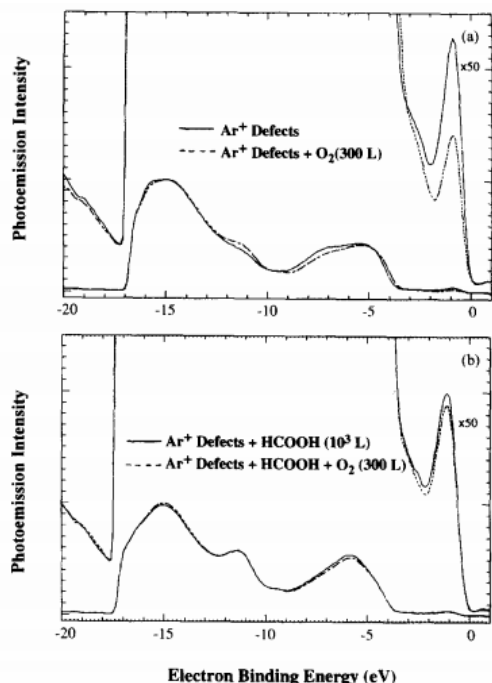


Figure 2.17: UPS spectra for (a) an Ar<sup>+</sup> bombarded surface before and after 300 L O<sub>2</sub> exposure and (b) a Ar<sup>+</sup> bombarded surface after 10<sup>3</sup> L of FA and after additional 300 L of O<sub>2</sub> [137].

### 2.7.2 Other carboxyl-containing molecules on TiO<sub>2</sub>(110)

The adsorption of other simple monocarboxylic acids, such as acetic acid (CH<sub>3</sub>COOH) [145], trimethylacetic acid ((CH<sub>3</sub>)<sub>3</sub>CCOOH) [146] and amino acids containing one carboxylic acid group, such as glycine (NH<sub>2</sub>CH<sub>2</sub>COOH) [145, 147, 148], has been investigated as well on the TiO<sub>2</sub> (110) surface. When deposited at room temperature, they all follow the same dissociative adsorption behaviour, giving rise to a well-ordered (2 × 1) structure, with both carboxylate O atoms bound to a pair of 5-fold coordinated Ti atoms along the [001] direction. Other more complex monocarboxylic acids adsorb in a similar manner (C<sub>6</sub>H<sub>5</sub>COOH, benzoic acid) [149–151] and pyridine-carboxylic acid isomers (C<sub>5</sub>H<sub>4</sub>NCOOH; isonicotinic acid, nicotinic acid and picolinic acid) [151, 152]), but the presence of intermolecular interactions between neighbouring molecules leads sometimes to irregular (2 × 1) overlayers. As an example, STM showed that benzoate molecules form T-shaped dimers at saturation coverage, which are aligned along the [1 $\bar{1}$ 0] direction across bridging O rows [149]. A second example is given by pyridine-carboxylic acid monomers, whose monolayer and multilayer deposition on TiO<sub>2</sub> (110) has been investigated by means of XPS, XAS and STM. In analogy to benzoate, all molecules adsorb via deprotonation of the carboxylic group and tend to assemble in dimer structures on the surface [151, 152]. Such dimerization arises from attractive intermolecular interactions between adjacent molecules.

The adsorption of more complex molecules on rutile TiO<sub>2</sub>(110), such as bi-isonicotinic acid [153–155] and terephthalic acid (TPA) [150, 156–158], which contain more than one COOH group, has been extensively studied as well. Being the ligand of several dye

molecules, the investigation of bi-isonicotinic acid adsorption on semiconductors is of fundamental importance for the understanding and development of photovoltaic devices, as dye-sensitized solar cells, where dyes bind to  $\text{TiO}_2$  nanoparticles. In this respect, a combination of several experimental techniques and theoretical calculations were used to analyse bi-isonicotinic acid molecular geometry and orientation on rutile  $\text{TiO}_2(110)$ . In the sub-monolayer regime, the molecule is found to adsorb on the surface via both deprotonated carboxyl groups, with a tilt angle of  $25^\circ$  with respect to the surface normal (figure 2.18).

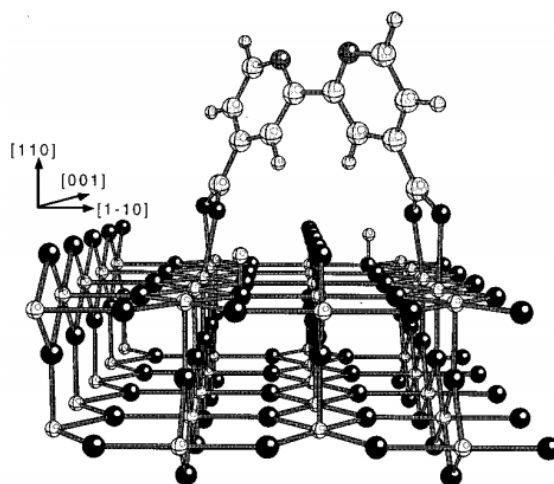


Figure 2.18: Ball and stick model for bi-isonicotinic acid adsorption on  $\text{TiO}_2(110)$ . For the rutile substrate, dark and light atoms represent O and Ti, respectively [153].

Concerning the adsorption mechanism of TPA, a combination of STM, non-contact AFM and NEXAFS spectroscopy has evidenced different molecular geometries depending on the coverage [157]. At low coverage (up to 0.3 ML), a disordered structure is observed, consisting of single molecules lying flat on the surface (figure 2.19). However, as the coverage increases, a transition from flat to upright geometry takes place. In the range between 0.3 and 0.8 ML, a well-ordered  $(2 \times 1)$  pattern appears, similarly to monoacids, suggesting

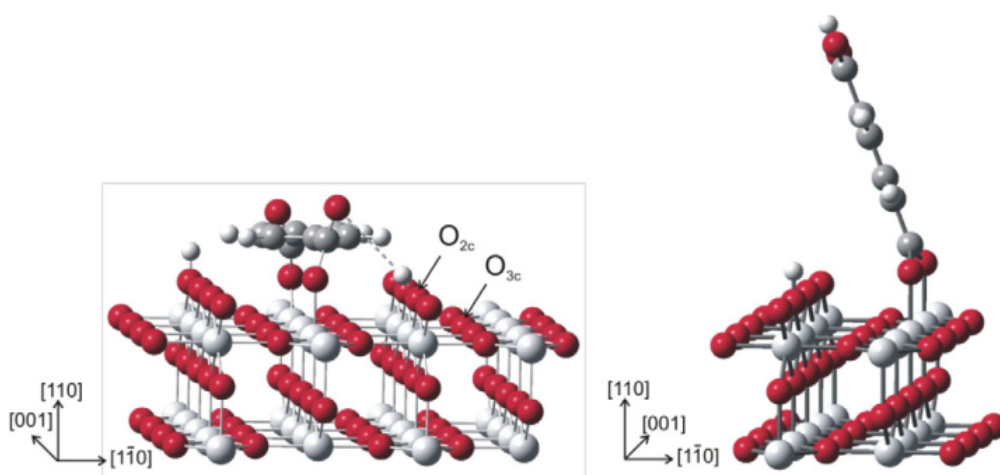


Figure 2.19: Ball and stick models for TPA adsorption on  $\text{TiO}_2(110)$ : flat-lying geometry on the left, upright geometry on the right. C, O, H and Ti atoms are represented in grey, red, white and light grey respectively [150].

that only one carboxylic group per molecule deprotonates. TPA was therefore assumed to adsorb in a monodentate fashion, with the deprotonated group bridge bonding across two adjacent  $\text{Ti}_{5c}$  atoms and the remaining one held away from the surface (figure 2.19). As shown in figure 2.20, at higher coverage (from 0.8 to 1 ML coverage) a stripline pattern of dark lines oriented along the  $[001]$  direction coexists with the  $(2 \times 1)$  pattern, resulting in a  $(2 \times 3)$  superstructure. Such striped structures have also been previously observed by Tiekel and attributed to alternating single and double rows of TPA molecules [156]. The presence of double rows probably arises from hydrogen bonding interactions between carboxylic acid groups of two adjacent molecules. A considerable agreement between experimental and simulated STM images supports the dimerization hypothesis [158].

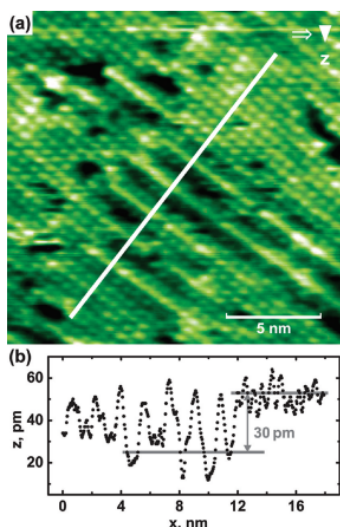


Figure 2.20: (a) Atomic force microscopy image of the striped structure consisting of single and double molecular rows of TPA/ $\text{TiO}_2(110)$  along the  $[001]$  direction. (b) Corresponding line scan at the position indicated in panel (a) [157].

Complementary IR investigations confirmed the adsorption model proposed [150]. It is interesting to note that this study is one of the few which report IR spectra on oxide surfaces. When IR spectroscopy is applied to oxide surfaces, which is considered in more detail in section 3.1, IR bands may be either positive or negative, as opposed to metallic surfaces. In this specific case, for the submonolayer regime (spectra A and B in figure 2.21), two bands are observed at  $1412$  and  $1635\text{ cm}^{-1}$ , attributed to the OCO symmetric and asymmetric stretching, respectively, suggesting that TPA molecules undergo a complete deprotonation. When a full monolayer regime is reached (spectra C and D), new bands appear, whose peak assignment is reported in figure 2.21. The presence of bands associated both to the carboxylic ( $1760\text{ cm}^{-1}$ ) and carboxylate functionalities ( $1427$  and  $1498\text{ cm}^{-1}$ ) confirms that only one carboxylic acid group is deprotonated, in agreement with what was previously suggested by STM. Moreover, one can notice that the frequency of the C=O vibration is down-shifted by  $70\text{ cm}^{-1}$  (from  $1760$  to  $1690\text{ cm}^{-1}$ ), consistent with the formation of H bonds between dimers. When the coverage is further increased, new bands characteristic of multilayer deposition appear.

Overall, carboxyl containing molecules display a common propensity to deprotonate at least one COOH upon adsorption on the rutile  $\text{TiO}_2(110)$ , with the  $\text{Ti}_{5c}$  providing the anchoring points for the carboxylate O atoms. When only one COOH group is deprotonated, a  $(2 \times 1)$  overlayer is observed at saturation coverage, otherwise different structures may be observed. Depending on the molecule being investigated, several chemical structures may appear as a function of the molecular coverage, indicating the great versatility of this class of molecules.

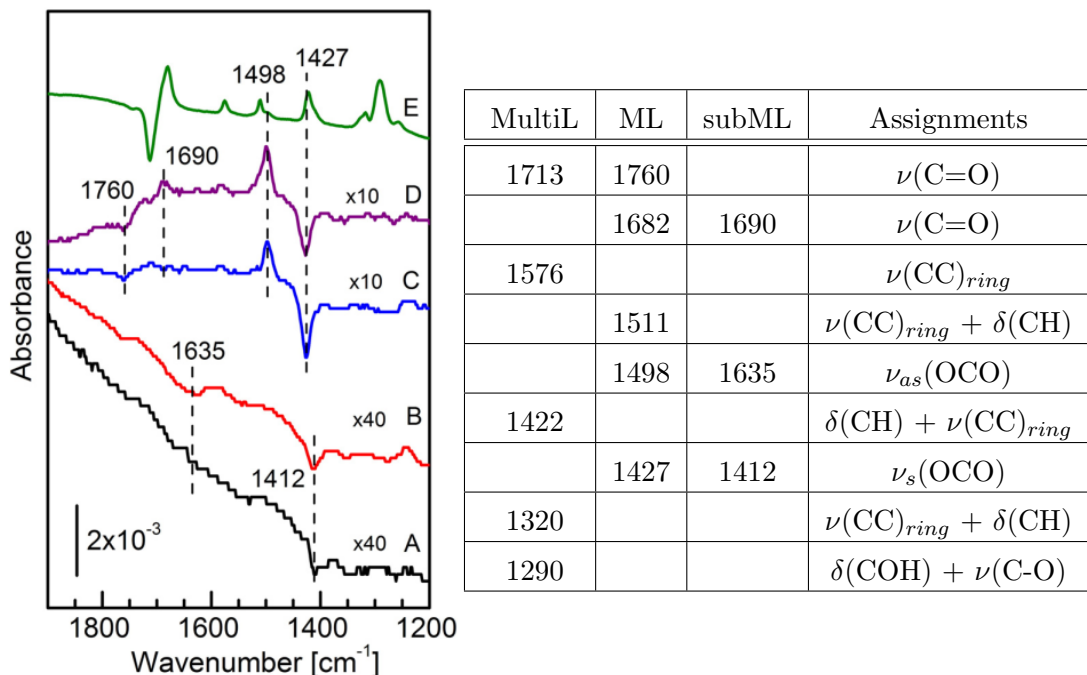


Figure 2.21: Left panel: IRRAS spectra recorded for terephthalic acid adsorption on  $\text{TiO}_2(110)$  at different coverages: A,B: submonolayer; C,D: monolayer and E: multilayer. Right panel: Corresponding vibrational frequencies and peak assignment for multilayer (MultiL), monolayer (ML) and submonolayer (subML) deposition of TPA molecules on  $\text{TiO}_2(110)$  [150].

## 2.8 Chiral molecule adsorption on rutile $\text{TiO}_2(110)$

Compared to the metal counterpart, surface science investigations of chiral molecules on oxide single crystals are scarce [159] and mainly involve only the use of XPS, DFT and NEXAFS [159]. One of the few examples on the  $\text{TiO}_2(110)$  surface involves the adsorption of *L*-cysteine. The carboxylic groups are mainly found to deprotonate upon adsorption and bound to two  $\text{Ti}_{5c}$  atoms, in analogy with the other aforementioned carboxyl containing molecules. Moreover, an additional dissociative interaction occurs between the molecular thiol groups and the oxide surface, more precisely with a bond forming between the thiolates and the bridging oxygen vacancies [159,160].

## 2.9 Nickel growth on rutile $\text{TiO}_2(110)$

Understanding the underlying mechanisms of metal particle or film deposition on oxide surfaces is of paramount importance in a variety of fields, including gas sensors, electronics, photovoltaic devices and heterogeneous catalysis [116,121,161,162]. In supported-metal catalysts, the active phase is dispersed on an oxide surface in the form of small metal particles [163]. The catalytic performance of such systems is directly related to the number of active sites, which in turn depends on the surface area exposed and thus on the metal growth mechanism [164,165].

The complexity of real catalytic systems often hinders the understanding of the detailed catalyst structure and of the catalytic process at a microscopic level. This challenge has led to the development of model approaches aimed at simulating the complex oxide-supported catalytic systems and understanding the metal-oxide interactions. One of the

most common strategies involves the use of surface science techniques [166, 167]. The oxide supports are usually modelled by planar oxide single crystals or by oxide thin film on conductive supports, when the oxide has an insulating character, which would create problems, for example, in the use of electron spectroscopies. In most studies the metal component is deposited by evaporation. In this section we give a brief overview of the surface science studies of Ni on the rutile  $\text{TiO}_2(110)$  surface.

### 2.9.1 Growth modes

Generally speaking, depending on the interaction between the adatoms of the deposited material and the substrate, under equilibrium conditions three main different growth modes are commonly identified, which owe their names to their original researchers (figure 2.22) [20, 161]:

- the Frank-van der Merwe (FM) or layer-by-layer growth mode, in which metal atoms are more tightly bound to the substrate than to each other, leading to the formation of metallic layers, one above the other;
- the Volmer-Weber (VW) or island growth mode, in which the interactions between metal atoms are stronger than with those to the substrate, resulting in the formation of 3D islands or clusters, with bare substrate regions in between;
- the Stranski-Krastanov (SK) or layer + island growth mode, where after the creation of a complete 2D layer, further deposition of metal results in the formation of islands.

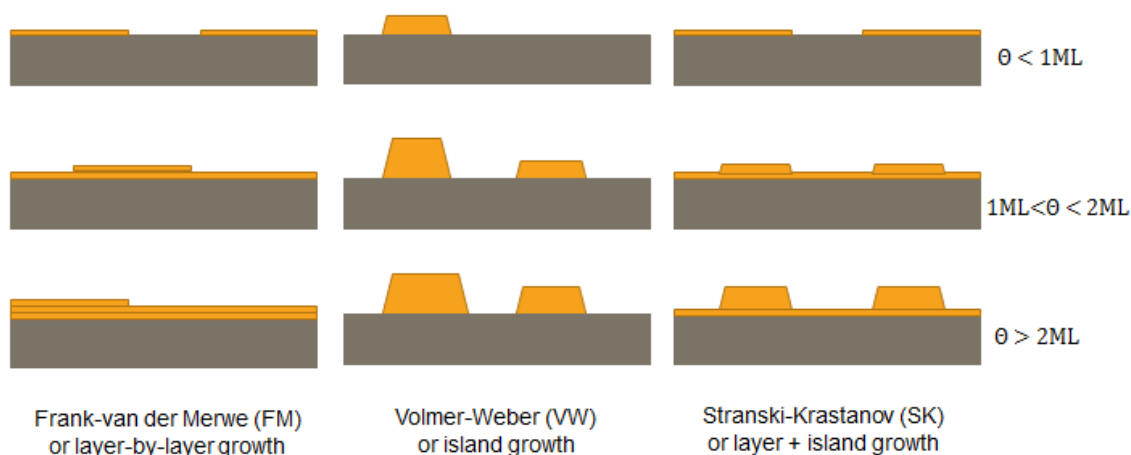


Figure 2.22: Different growth modes as a function of thickness  $\theta$ .

The occurrence of one of these three modes is determined by the competition between the metal and oxide surface free energies in vacuum ( $\gamma_{mv}$  and  $\gamma_{ov}$ , respectively) and the metal/oxide interfacial free energies  $\gamma_{m/o}$  involved. When:

$$\gamma_{ov} < \gamma_{mv} + \gamma_{m/o} \quad (2.1)$$

the metal does not wet the oxide surfaces and a VW growth occurs; otherwise if:

$$\gamma_{ov} \geq \gamma_{mv} + \gamma_{m/o} \quad (2.2)$$

the metal wets the oxide and either FM or SK growth mode are observed. Another way of determining the wetting of the substrate by the overlayer is based on the adhesion energy, the work necessary to separate in vacuum the metal/oxide interface:

$$W_{adh} = \gamma_{mv} + \gamma_{ov} - \gamma_{m/o} \quad (2.3)$$

VW growth mode is thus observed when  $W_{adh} < 2\gamma_{mv}$ , while FM and SK when  $W_{adh} > 2\gamma_{mv}$  and  $W_{adh} \sim 2\gamma_{mv}$ , respectively. The metal surface free energy is generally greater than or comparable to that of oxide materials. In the specific case of  $\text{TiO}_2$ , the surface energy  $\gamma_{ov}$  is reported to be between 0.7-1.1 J/m<sup>2</sup> [168–170], considerably lower than the surface energy of most metals (1.7-2 J/m<sup>2</sup> for Ni [161, 170]), so that a VW or cluster growth is the main growth mechanism expected for metals on  $\text{TiO}_2$  from thermodynamic considerations. A VW growth is indeed reported for several transition metals, such as Au, Fe, Cu, Pt, Pd and Ni [162, 171]. Thorough reviews by Diebold [116] and more recently by Pang *et al.* [121] of metal growth on the rutile  $\text{TiO}_2$  (110) surface are found in literature.

### 2.9.2 Previous studies on Ni nucleation and growth

Most experimental works reported here involve the deposition of Ni from the vapour phase and subsequent characterisation by surface science techniques. In early studies, a layer + island growth mechanism was suggested, based on XPS and EXAFS (Extended X-ray Absorption Fine Structure) [172–174]. Similar 2D growth models were suggested, with Ni atoms forming wavy chains between the bridging oxygen rows.

More recent investigations suggested a quite different growth mechanism, with the formation of metallic clusters already from very low coverage, in line with thermodynamic considerations. There is evidence that Ni clusters grow quite flat in the first stages of growth, with a height of one or two atomic layers [121, 175, 176], in analogy with the behaviour of other metals on  $\text{TiO}_2(110)$ , such as Pd and Pt [121]. In this respect, by evaporating nickel on a rutile  $\text{TiO}_2$  sample with a low step density, Fujikawa *et al.* reported by means of STM the formation of oval clusters, with the long axis oriented along the [001] direction (figure 2.23), and whose average dimensions are summarised in figure 2.23 as a function of Ni surface density. Ni clusters initially measure 1.8 nm and 1.4 nm along the [001] and the  $[1\bar{1}0]$  directions, respectively, while they appear quite flat, with height of one or two atomic layers. The cluster size and shape seemed not to be affected by variations in coverage up to 1 atoms nm<sup>-2</sup> (see figure 2.23), while an increase in the cluster density was simultaneously recorded. However, above 1 atoms nm<sup>-2</sup> (coverage  $\sim$  5%), a vertical growth and consequently the formation of more 3D islands began, while the density increase rate lessened [175]. Furthermore, concerning the nucleation sites, Ni islands were found to nucleate mostly on terraces and only occasionally at step edges (figure 2.23).

Tanner and co-workers investigated as well the growth and the morphology of nickel islands by STM and Reflection High-Energy Electron Diffraction (RHEED) [177]. Differently from Fujikawa, 3D clusters were found to nucleate preferentially at step edges (see figure 2.24). At low coverage, Ni islands were found to grow as hemispheres, with average diameter of  $\sim$  1.6 nm. Upon further deposition, more faceted nanocrystals were obtained, elongated along the [001] direction. As seen in figure 2.25, such nanocrystals resemble an array of roof and for this reason they are usually referred as “hut-clusters”. From RHEED, the long cluster facets are found to be inclined at about 35° with respect to the surface and are therefore attributed to {111} type-facets, while the short ones are of {100} type (see figure 2.25). The orientation of the nanocrystals was found to change with the deposition time: while randomly oriented at low coverage, as the Ni dose increases the following orientations are established with the substrate:  $(110)_{\text{Ni}} \parallel (110)_{\text{TiO}_2}$ ,  $[\bar{1}10]_{\text{Ni}} \parallel [001]_{\text{TiO}_2}$ . This

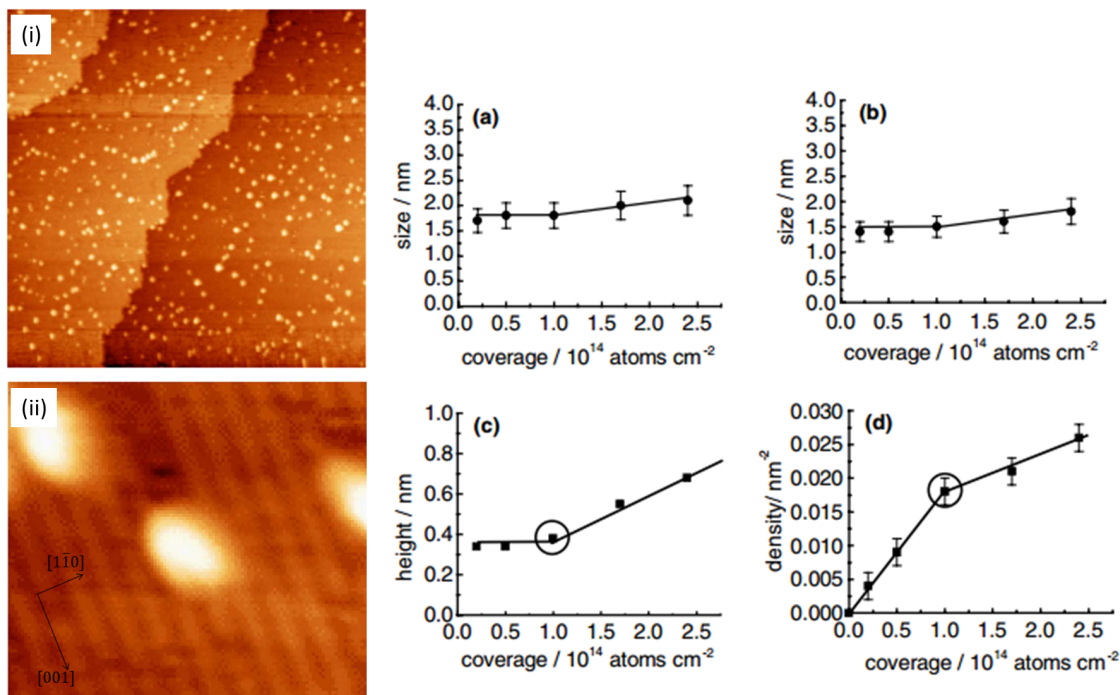


Figure 2.23: Left: (i) STM image of Ni clusters on TiO<sub>2</sub> at the coverage of 1 atoms nm<sup>-2</sup>. The area is 150 nm × 150 nm. (ii) A narrow scan STM image. The area is 7.2 nm × 6.4 nm. Right: Dependence of average lateral size, height and cluster density on the Ni coverage on TiO<sub>2</sub>(110): (a) parallel to the [001] direction; (b) parallel to the [110] direction; (c) average height (parallel to [110]); and (d) cluster density [175].

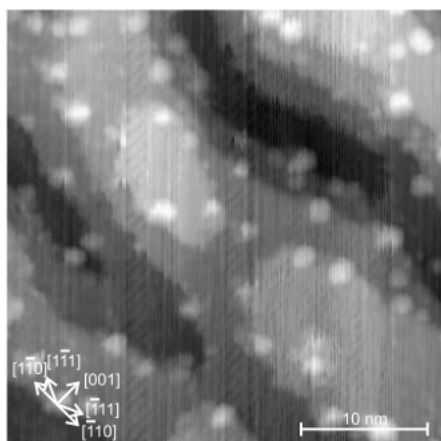


Figure 2.24: STM image of Ni nanoislands on TiO<sub>2</sub>(110) after the exposure to Ni at 375 K [177].

relationship presents one of the highest match with the substrate, if an average mismatch in the two perpendicular surface directions [001] and [110] is considered. Before the work of Tanner, different epitaxial orientation relationships of Ni nanoparticles with respect to the TiO<sub>2</sub>(110) surface were reported by Wu *et al.* by means of Low Energy Electron Diffraction (LEED) and Auger Electron Spectroscopy (AES):

$$\begin{aligned} (111)_{\text{Ni}} \parallel (110)_{\text{TiO}_2}, [10\bar{1}]_{\text{Ni}} \parallel [001]_{\text{TiO}_2} \\ (131)_{\text{Ni}} \parallel (110)_{\text{TiO}_2}, [10\bar{1}]_{\text{Ni}} \parallel [001]_{\text{TiO}_2} \end{aligned}$$

The epitaxial mismatch values for coherent Ni growth in various orientations on TiO<sub>2</sub>(110) are shown in Table 2.1. The epitaxial mismatch with the substrate for the orientations

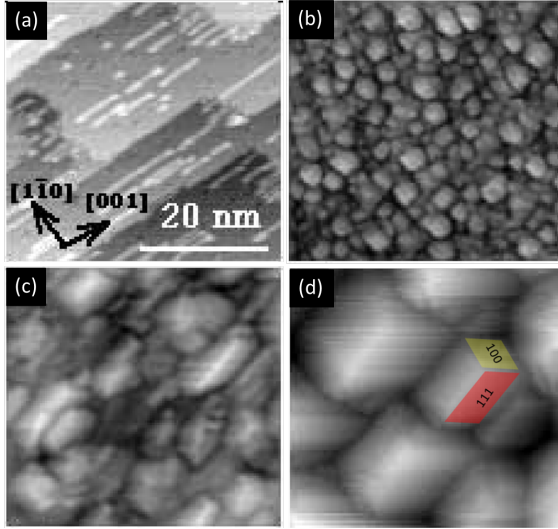


Figure 2.25: STM images for Ni/TiO<sub>2</sub>(110) as a function of Ni coverage: (a) clean TiO<sub>2</sub> surface; (b) Ni deposition of 20 s; (c) Ni deposition of 50 s and (d) Ni deposition of 110 s (adapted from [177]). In image (d), the {100} and {111}-type facets are indicated in yellow and red, respectively. All images are 43 nm x 43 nm in size.

proposed by Wu is quite high and these relationships were proposed computationally assuming a Ni(111) growth. This implies that a fully coherent growth is not expected, at least not without a considerable surface-induced strain.

Table 2.1: Epitaxial mismatch values for coherent Ni growth in various orientations on TiO<sub>2</sub>(110). In each column a different Ni plane lying parallel to the TiO<sub>2</sub>(110) surface is reported. The first and fourth rows represent Ni surface unit cell vectors lying along the [001]<sub>TiO<sub>2</sub></sub> and [1 $\bar{1}$ 0]<sub>TiO<sub>2</sub></sub>, respectively. The coincidence  $n_x$  (rows two and five) gives the number of  $d_{hkl}$  spacings in direction  $x$  that lead to the mismatch value  $\epsilon_x$  (rows three and six) [177].

		Ni(001)	Ni(001)	Ni(111)	Ni(131)	Ni(110)
TiO <sub>2</sub> [001]	Ni direction	Ni[100]	Ni[1 $\bar{1}$ 0]	Ni[10 $\bar{1}$ ]	Ni[10 $\bar{1}$ ]	Ni[ $\bar{1}$ 10]
	$n_1$	1	1	1	1	1
	$\epsilon_1$	+19.0%	-15.8%	-15.8%	-15.8%	-15.8%
TiO <sub>2</sub> [1 $\bar{1}$ 0]	Ni direction	Ni[010]	Ni[110]	Ni[1 $\bar{2}$ 1]	Ni[ $\bar{3}$ 2 $\bar{3}$ ]	Ni[001]
	$n_2$	2	3	1	1	2
	$\epsilon_2$	+8.5%	+15.1%	-33.6%	+27.2%	+8.5%

Both the effects of annealing and oxidation have been considered as well by Tanner. The same orientation-relations were found after annealing the sample up to 1065 K in UHV. Moreover, although preserving the “hut-clusters” shape, the cluster size increased as a function of annealing temperature, reaching  $\sim 25$  nm in length and  $\sim 35$  nm in height at 880 K; upon annealing up to 1065 K, the Ni clusters did not grow any further. Upon oxidation, a new epitaxial relation was found between the substrate and the metal adsorbate, consistent with the formation of NiO: (110)<sub>Ni</sub> || (110)<sub>TiO<sub>2</sub></sub>, [1 $\bar{1}$ 0]<sub>Ni</sub> || [001]<sub>TiO<sub>2</sub></sub>. When reduced again, the lattice parameters of Ni metal were restored, but the oxide overlayer orientation was maintained.

The presence of 3D clusters and their preferential growth at step edges, the highest coordination sites, were found also in STM experiments performed by Zhou *et al.* [169]. A particular focus was placed on the effect of the diffusion (D) and flux (F) on the cluster growth. In details, by decreasing the deposition flux or increasing the temperature, and hence the diffusion rate, larger island sizes and lower island densities were obtained, as seen in figure 2.26 for a given coverage deposited with different flux and temperature ex-



perimental conditions.

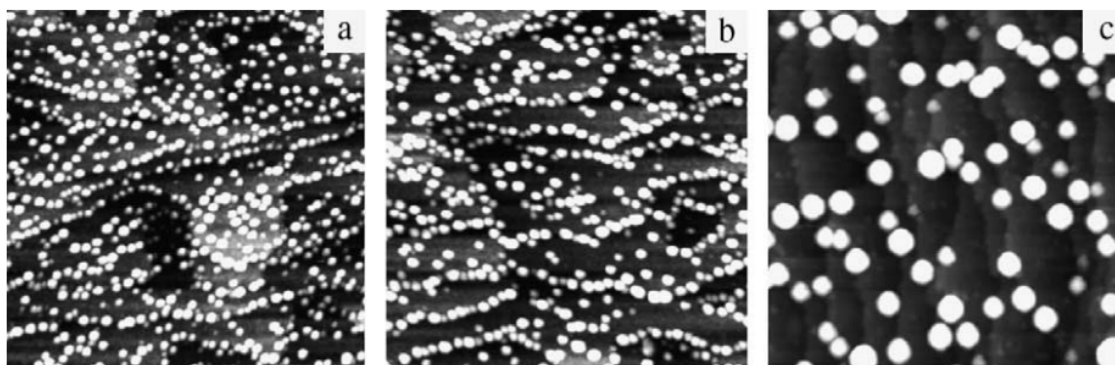


Figure 2.26: STM images for a 1 ML coverage of Ni deposited on rutile  $\text{TiO}_2(110)$  at different temperatures and fluxes: (a) 0.16 ML/min at 295 K; (b) 0.02 ML/min at 295 K; and (c) 0.02 ML/min at 500 K. All images are  $1000 \text{ \AA} \times 1000 \text{ \AA}$ , collected with a tunnelling current of 0.2 nA and sample bias of 1.7 V [169].

The apparent conflicting results and the differences observed between the works of Tanner and Zhou [169,177] and the one of Fujikawa in terms of nucleation sites and cluster size are attributed to the experimental parameters used, in particular the flux rate (the flux used by Fujikawa is almost equivalent to those of Tanner’s work, but one order of magnitude faster than in Zhou’s work), the deposition temperature (room temperature for Zhou and Fujikawa, 375 K for Tanner) and the step density. If the density of Ni adatoms is low and their diffusion rate is high enough, Ni adatoms can reach the step edges and stably adsorb, becoming a nucleation site for Ni islands. However, when the density increases, Ni adatoms can form dimer on terraces, which eventually grow into clusters. These dimers and clusters decay by losing Ni atoms, which are easily trapped by step edges, if the step density is high enough. Such clusters are often referred as “subcritical clusters” since their process of decay is faster than their growth, finally resulting in their disappearance, as reported in the works of Tanner and Zhou [169,177]. On the contrary, if the step density and/or D/F ratio are low enough, subcritical clusters have a higher probability to catch Ni adatoms, reaching a critical size and growing into stable clusters. The latter situation is indeed the one reported by Fujikawa, where terraces also become nucleation sites for the formation of Ni clusters. Lower step density and higher fluxes thus favour the collision between Ni adatoms and consequently nucleation on terraces.

Concerning the possible charge transfer between Ni and  $\text{TiO}_2$ , an electron transfer from  $\text{TiO}_2$  to Ni was predicted in an early study by Kao *et al.* [178]. The measure of the energy shift of the Ni  $2p_{3/2}$  core level as a function of Ni coverage indicated that the Ni atoms at the Ni/ $\text{TiO}_2$  interface are negatively charged and the corresponding amount of charge transfer was estimated to be  $0.13 e^-/\text{Ni atom}$ . More recently, Onishi and coworkers measured by UPS a decrease in the work function and an electron transfer from Ni to the substrate equal to  $0.1 e^-$  per Ni adatom [172]. Recent Kelvin Probe Force Microscopy (KPFM) measurements have confirmed the existence of an electron transfer from Ni atoms to the oxide surface [176].

More recently, the group of Chen *et al.* has studied the nucleation and growth of Ni in comparison with other metals (Au, Co and Pt) on both reduced and oxidised  $\text{TiO}_2$  surfaces [165,179,180]. Ni was found to diffuse slightly less readily compared to Au, forming clusters of smaller sizes but with a larger nucleation density when similar coverages are considered. Moreover, a preferential nucleation at step edges was remarked, suggesting a

diffusion length larger than the  $\text{TiO}_2$  step distance. A similar tendency has been observed for room temperature deposition of several other metals on  $\text{TiO}_2(110)$ , including Au, Cu and Ag [180]. The differences observed were explained on the bases of binding energy calculations of one single metal atom with the  $\text{TiO}_2$  surface by DFT. It was evidenced that the higher the binding energy, the higher the nucleation density and the smaller the cluster dimensions. The binding energy values found were thus in accord with the diffusion rate of the different metals, more precisely the strongest binding corresponded to the shorter diffusion lengths.

The possible role of defects was also investigated, by considering the metal deposition on both oxidised and reduced  $\text{TiO}_2$  surfaces (figure 2.27). It was shown that on oxidised surfaces, for all the metals considered and for a given coverage, the cluster density increases while the height decreases compared to the reduced surfaces, suggesting a lower mobility due to a stronger interaction between the metal and the oxide surface. Higher metal- $\text{TiO}_2$  binding energies were found by DFT calculations on the oxidised surfaces than on the vacuum-annealed ones, consistently with the experimental observations (table 2.2).

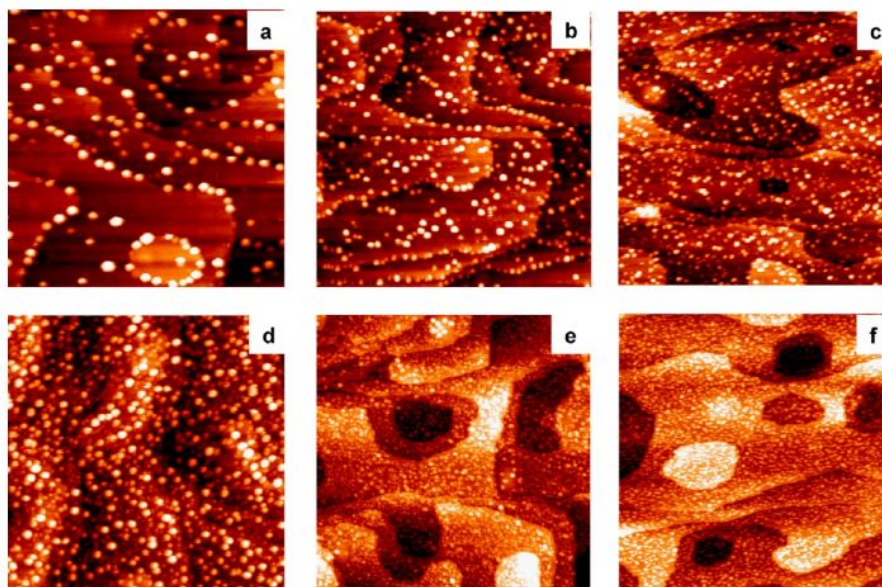


Figure 2.27: Top: STM images ( $1000\text{\AA} \times 1000\text{\AA}$ ) of 0.05 ML of a) Au, b) Ni and c) Co on a vacuum-annealed rutile  $\text{TiO}_2(110)$  surface. Bottom: STM images ( $1000\text{\AA} \times 1000\text{\AA}$ ) of 0.05 ML of d) Au, e) Ni and f) Co on a rutile  $\text{TiO}_2(110)$  surface exposed to  $\text{O}_2$  at 295 K. All metal depositions were performed at room temperature. [165].

Table 2.2: BE values calculated by DFT on a reduced  $\text{TiO}_2(110)$  surface and on an oxidised  $\text{TiO}_2(110)$  surface [165].

metal	metal BE on reduced $\text{TiO}_2$ [eV]	metal BE on oxidised $\text{TiO}_2$ [eV]
Au	-1.54	-3.89
Ni	-1.61	-7.23
Pt	-2.28	-6.05
Co	-3.07	-8.70

Further investigations were carried out on the nature of the Ni-TiO<sub>2</sub> interaction and recently a great focus has been placed on the effect of heating on the Ni/TiO<sub>2</sub> system and the occurrence of sintering and possible encapsulation. The process of annealing is indeed of particular importance since it may lead sometimes to a drastic change in the catalytic behaviour and activity of oxide supported metal catalysts, as in the case of CO and H<sub>2</sub> adsorption on metal/TiO<sub>2</sub> systems where the activity is strongly diminished after annealing in H<sub>2</sub> atmosphere or above 725 K in UHV conditions [121, 177, 181]. Such common effect is called strong metal-support interaction (SMSI) and it has been reported for many metals (Ni, Pt, Pd, Ir, Co, Fe, etc.) on TiO<sub>2</sub> and other reducible oxide materials, such as MnO and V<sub>2</sub>O<sub>3</sub> [121, 177]. The SMSI is explained on the basis of encapsulation of the metal catalyst by the oxide which thus blocks the catalyst active sites [121, 181]. Many studies have reported that Ni clusters are encapsulated by TiO<sub>2</sub> (both single crystals and powders) upon annealing in a reducing environment (as UHV) [181, 182] or H<sub>2</sub> atmosphere [165, 170, 179, 183]. By means of Low Energy Ion Scattering (LEIS), Chen *et al.* reported a significant drop of the Ni signal after heating to 800 K. Since Ni does not desorb from the TiO<sub>2</sub> surface at this temperature and the effect of sintering observed was minor, the reduction of Ni signal was attributed to Ni cluster encapsulation from the TiO<sub>2</sub> support [180]. Chen *et al.* also showed that TiO<sub>2</sub> becomes reduced after annealing 8 ML Ni on TiO<sub>2</sub>(110) at 850 K, from the analysis of the XPS Ti 2p peak (a shoulder assigned to Ti<sup>3+</sup> was recorded). It is important to note that no changes in the Ti 2p peak were observed before and after Ni deposition at room temperature [181]. By means of transmission electron microscopy it was evidenced that following annealing in H<sub>2</sub> atmosphere at 1000 K, Ni clusters deposited on TiO<sub>2</sub> films were covered by Ti<sub>4</sub>O<sub>7</sub> species [181, 183]. Similarly, for Ni deposited on TiO<sub>2</sub> powders, encapsulation of Ni by TiO<sub>x</sub> species was reported following H<sub>2</sub> treatment at 773 K [181, 184].

## 2.10 Conclusion

This chapter reviewed the state of the art of different topics treated in the following chapters. Some important aspects of chirality and heterogeneous asymmetric catalysis were first reviewed. Despite having been addressed in some studies, a clear understanding of the role of the oxide support is still lacking. A particular attention was devoted on how chirality may be imparted to surfaces by the adsorption of either non-chiral or chiral molecules, giving rise to a complex hierarchy of possible chiral manifestations. The attention was then focused on RR-TA, selected as model chiral modifier in the present work, and its adsorption on single crystal metal surfaces, such as Cu(110), Ni(111) and Ni(110). One of the major conclusions was that TA adsorption on such surfaces often leads to complex adsorption phase diagrams, which depend on the substrate considered and experimental conditions used. Moreover, different chiral expressions were evidenced: chirality was found to be imparted on Cu(110) and Ni(111) both to a local and global 2D level. Conversely, on Ni(110), no evidence of long-range organised structures was remarked, but chirality was instead bestowed to the metal surface via a local chiral reconstruction of the underlying metal Ni atoms.

After presenting the rutile TiO<sub>2</sub> structure, the reactivity of the (110) surface with non-chiral carboxyl-containing molecules was reviewed, ranging from simple carboxylic acids to larger and more complex ones. Despite being non chiral, their adsorption is a useful starting point for the study of RR-TA molecules on TiO<sub>2</sub>. All the carboxyl-containing molecules reviewed displayed a general common tendency to deprotonate one or more COOH groups, with the carboxylate O atoms binding to an adjacent pair of Ti<sub>5c</sub> atoms

along the [001] direction and the parted H atoms possibly forming surface hydroxyls. In the case of formic acid, some groups suggested the existence of a minority formate species over the years, which was adsorbed in a different site involving O vacancies. Studies on the adsorption of chiral molecules on oxide surfaces are instead scarce, showing the interest of the present work about chirality induced at oxide  $\text{TiO}_2$  surfaces towards enantiospecific heterogeneous catalysis.

Previous results on Ni growth on  $\text{TiO}_2(110)$  were then presented. The attention was mainly focused on the early stages of nucleation and growth. STM investigation showed that Ni deposition follows a Volmer-Weber mechanism with the formation of nanoparticles. Apparent conflicting results between different studies in terms of nucleation and cluster size were explained on the basis of different experimental parameters used, thus suggesting the importance to characterise the systems, as reported in the following. The charge transfer between Ni and  $\text{TiO}_2$ , the epitaxy and the possible role of  $\text{TiO}_2$  surface defects were also explored in some studies. Finally, the effect of annealing  $\text{TiO}_2$  supported Ni nanoparticles showed evidence of encapsulation of Ni clusters from the oxide support.



# CHAPTER 3

---

## Tartaric acid adsorption on $\text{TiO}_2(110)$

---

In this chapter we explore tartaric acid (RR-TA) adsorption on the rutile  $\text{TiO}_2(110)$  surface, to model the interaction between the oxide support and the chiral modifier, whose comprehension is essential for the conception and development of new oxide supported catalytic systems. A combination of X-ray Photoemission Spectroscopy (XPS), High Resolution Electron Energy Loss Spectroscopy (HREELS) and Polarisation Modulation Reflection Absorption InfraRed Spectroscopy (PM-RAIRS) is used to understand the molecular chemical nature of RR-TA upon adsorption. To do so, the chiral modifier is deposited in parallel on two model metal surfaces, namely Au(111) and Cu(110), on which TA chemical form is well understood. The XPS spectra obtained are used as references to shed light on the TA adsorption behaviour on the oxide surface. Furthermore, Scanning Tunnelling Microscopy (STM) and Low-Energy Electron Diffraction (LEED) are employed to study the 2D molecular layer ordering and identify the adsorption sites for TA molecules on  $\text{TiO}_2(110)$ . Additional UPS experiments are also performed to investigate the possible formation of a surface dipole upon TA adsorption.

*Dans ce chapitre, nous explorons l'adsorption de l'acide tartrique (RR-AT) sur la surface de rutile  $\text{TiO}_2(110)$ , afin de modéliser l'interaction entre le support oxyde et l'inducteur chiral, dont la compréhension est essentielle pour la conception et le développement de nouveaux systèmes catalytiques supportés sur oxyde. Une combinaison de diverses techniques, photoémission X (XPS), spectroscopie de perte d'énergie d'électrons lents à haute résolution (HREELS) et spectroscopie infrarouge de réflexion-absorption par modulation de polarisation (PM-RAIRS), est utilisée pour comprendre la nature chimique moléculaire lors de l'adsorption. Pour ce faire, l'inducteur chiral est déposé en parallèle sur deux surfaces métalliques modèles, à savoir Au(111) et Cu(110), sur lesquelles la forme chimique de l'AT est bien comprise. Les spectres XPS obtenus servent de référence pour éclairer le comportement d'adsorption de l'AT à la surface de l'oxyde. En outre, la microscopie à effet tunnel (STM) et la diffraction d'électrons lents (LEED) sont utilisés pour étudier l'organisation de la couche moléculaire et identifier les sites d'adsorption des molécules d'AT sur le  $\text{TiO}_2(110)$ . Des expériences UPS supplémentaires sont également effectuées pour étudier la formation possible d'un dipôle de surface lors de l'adsorption de l'AT.*

### 3.1 Infrared spectroscopy on oxide surfaces

When studying TA deposition on surfaces, its molecular versatility brings up the question of determining in which chemical form TA is adsorbed, namely biacid, monotartrate or bitartrate (figure 2.6). In this respect, vibrational spectroscopies are powerful methods to discriminate between different molecular forms, since each functional group possesses specific vibrational frequencies. For example, when molecules contain carboxylic acid groups,  $\nu(\text{C-O})$  and  $\nu(\text{C=O})$  vibrations at about 1200 and 1750  $\text{cm}^{-1}$  are observed, respectively, while the presence of carboxylate functionalities is characterised by the  $\text{COO}^-$  symmetric and asymmetric stretching at 1400 and 1600  $\text{cm}^{-1}$ , respectively. Infrared spectroscopy is thus one of the most well-suited techniques to determine the chemical structure of adsorbates.

As shown in section 1.8, RAIRS spectroscopy performed on metal surfaces is ruled by the dipole selection rule (from equation 1.31), which implies that no absorption occurs when no change of the adsorbate dipole moment is observed, and the surface selection rule, which states that only vibrational modes with a dynamic dipole moment component non-parallel to the metal surface are probed by p-polarised light giving rise to positive adsorbate bands in a typical absorbance spectrum (reflected intensity attenuation) [185]. The application of RAIRS to metal oxide surfaces, and more generally to non-metallic ones, is much more challenging. Because of the oxide optical properties, measurements are affected by the oxide lower reflectivity and sensitivities are consistently attenuated by one or two order of magnitude with respect to metal surfaces [185, 186]. This explains why the number of successful studies is extremely limited compared to the metallic counterpart. To overcome this problem, one first solution has involved the deposition of thin metal oxide layers on metallic supports, to exploit the strong metal reflectivity of the substrate. However reasonable questions have been raised concerning the influence of the metallic support on the oxide thin film physical properties (the thin film thickness is usually limited to 10 nm) which may differ from that of bulk single crystal oxides [185]. Therefore, to overcome the lower sensitivity and to be able to measure low absorbances, *i.e.* below  $5 \times 10^{-6}$  at grazing incidence, most recent studies reported in literature have been carried out on optimised RAIRS set-ups [186]. In contrast to the metallic case, vibrations of the adsorbate couple to both s and p incident light components, thus allowing to detect vibrations both parallel and perpendicular to the surface, and in addition to this, surface selection rules are not valid [185]. Changes of reflectivity at an oxide surface is explained using the three-phase model developed by Hansen *et al.* [187–189] and Yoon and Mielezarski [189, 190], where the three layers correspond to 1) vacuum or air, 2) adsorbate and 3) substrate. Within this model,  $\Delta R = R_0 - R_a$ , the difference between the clean oxide surface reflectivity and the adsorbate-covered one, is calculated for s and p incident components and complicated behaviours are observed. As a reminder (figure 3.1a), for s polarised light the electric field is perpendicular to the plane of incidence and parallel to the surface ( $E_s$ ), while for p one the electric field is in the plane of incidence and has components both tangential ( $E_{p,t}$ ) and normal to the surface ( $E_{p,n}$ ) [70, 150]. In the specific case of TiO<sub>2</sub>(110), depending on the orientation of the incident light along the  $[1\bar{1}0]$  or the  $[001]$  crystallographic directions (figure 3.1), both  $E_s$  and  $E_{p,t}$  couple to adsorbate vibrational modes with dynamic dipole moment component parallel to the surface, while  $E_{p,n}$  only with those having dynamic dipole moment components perpendicular to the surface. For s-polarised light a negative value of  $\Delta R$  is always found, thus giving rise to negative absorbance bands in the RAIRS spectrum. On the opposite, both positive and negative vibrational bands can be excited by p-polarised light, depending on the substrate refractive index and the light incident angle

$\Theta$ . As an example, figure 3.1b reports  $\Delta R$  calculated between the clean rutile  $\text{TiO}_2(110)$  surface and after deposition of carboxylic benzoic acid. For  $\Theta = 80^\circ$ , at which measurements were performed in this specific work,  $\Delta R$  is positive for  $E_{p,t}$ , but negative for  $E_s$  and  $E_{p,n}$ . When trying to probe the carboxylate stretching modes,  $\nu_{asym}$  (OCO), which has a dynamic dipole moment parallel to the surface, couples to  $E_{p,t}$ , thus giving rise to a positive band in the RAIRS spectrum, while  $\nu_{sym}$  (OCO) is excited by  $E_{p,n}$ , resulting in a negative adsorption band, as effectively reported in the work. Despite the great effective potential of RAIRS in the studies of adsorbate deposition on oxide surfaces, to gain information on the chemical structure, geometry and orientation

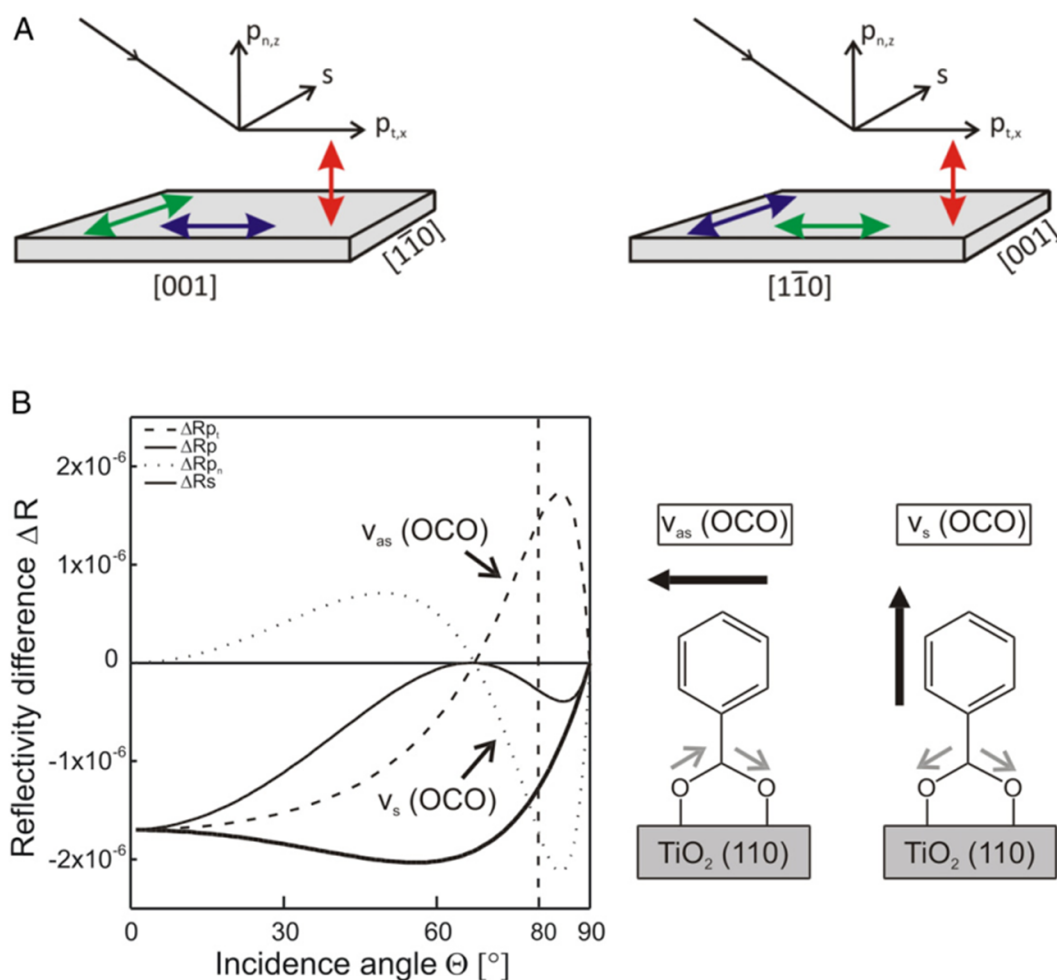


Figure 3.1: A) S- and p-polarised light component orientation with respect to the [001] (left) and [110] azimuth (right) of the sample. The s polarised light is perpendicular to the plane of incidence and parallel to the surface (s), while for p one the electric field has components both tangential ( $p_{t,x}$ ) and normal to the surface ( $p_{n,z}$ ). Green, blue and red arrows are oriented along the [110] direction, the [001] direction and perpendicular to the surface, respectively. B) Left panel: Calculated reflectivity differences ( $\Delta R = R_0 - R_a$ ) between the clean rutile  $\text{TiO}_2(110)$  surface ( $R_0$ ) and after benzoic acid deposition ( $R_a$ ) as a function of incidence angle for p-polarised light (x- and z-component (dashed lines) and sum (solid line)) and for s-polarised light (bold solid line) at  $1425 \text{ cm}^{-1}$ . Right panel: Asymmetric and symmetric  $\text{COO}^-$  vibrations and corresponding transition dipole moment vectors.



of adsorbed molecules, adapted RAIRS set-ups are mandatory to overcome the problems due to low signals. As an example, in the successful works reported in literature the spectrometer was placed inside the UHV chamber which resulted in a signal to noise ratio (S/N) in absorbance of the order of  $10^{-6}$ . In our work, several tests were done both by means of conventional RAIRS and PM-RAIRS, but S/N was approximately one order of magnitude lower, which may explain why no workable signal was obtained (figure 3.2). As an alternative, TA chemical nature is deciphered by means of HREELS and XPS, more precisely by making use of XPS reference spectra recorded on model metal surfaces, more precisely Au(111) and Cu(110), on which the TA chemical nature is well known.

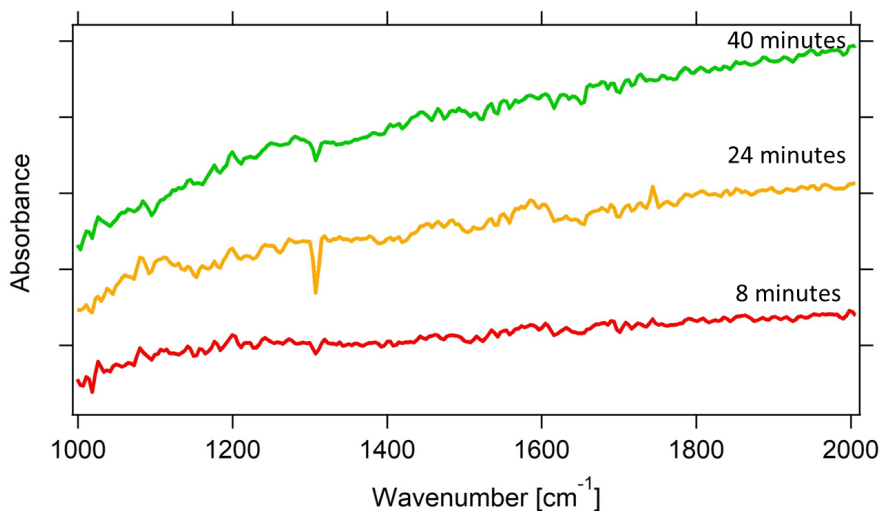


Figure 3.2: RAIRS spectra acquired for increasing dosing times of TA on TiO<sub>2</sub>(110). As explained in the text, no workable signal could be obtained.

## 3.2 RR-TA adsorption on Au(111) and Cu(110): PM-RAIRS and XPS results

While RR-TA deposition on Cu(110) has been intensively investigated by Raval's group [110–112], to our knowledge no previous studies of TA adsorption on Au(111) have been reported. In both cases, TA chemical nature is first verified by a combination of XPS and PM-RAIRS and the results are reported in details in the present section.

### 3.2.1 RR-TA adsorption on Au(111)

Figure 3.3 shows the PM-RAIRS spectra recorded on Au(111) following increasing doses of RR-TA at room temperature. The dominant peaks at 1137 and 1737  $\text{cm}^{-1}$  are attributed to the OH bending ( $\delta^{acid}(\text{OH})$ ) and the C=O stretching ( $\nu(\text{C}=\text{O})$ ) of the acid group, suggesting that at least one carboxylic acid group is intact (*i.e.* non deprotonated). The adsorption bands observed at 1090 and 1273  $\text{cm}^{-1}$  are assigned to the stretching of the alcohol groups  $\nu^{alc}(\text{C}-\text{OH})$  and the bending mode  $\delta^{alc}(\text{OH})+\delta(\text{CH})$ , respectively. Overall, no adsorption bands appear at 1400 and 1600  $\text{cm}^{-1}$ , where the symmetric and asymmetric stretching of carboxylate functionalities are expected, thus suggesting that TA molecules are adsorbed in a biacid form on Au(111).

The XPS spectra recorded further confirm this finding. In this respect, figure 3.4 displays

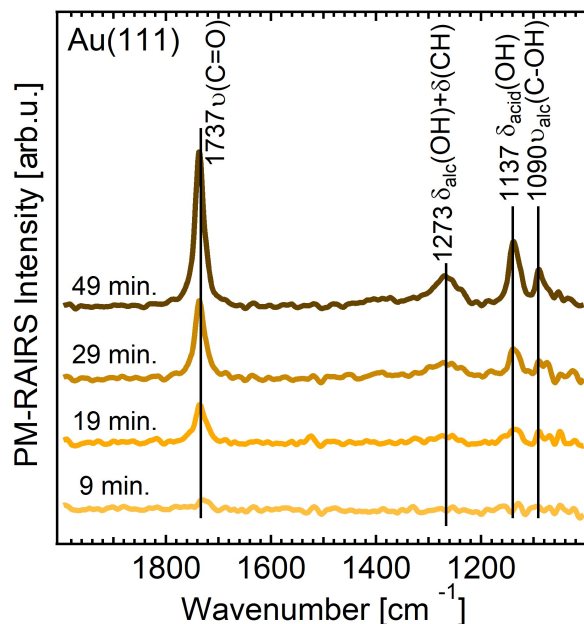


Figure 3.3: PM-RAIRS spectra acquired at increasing dosing times of TA on Au(111).

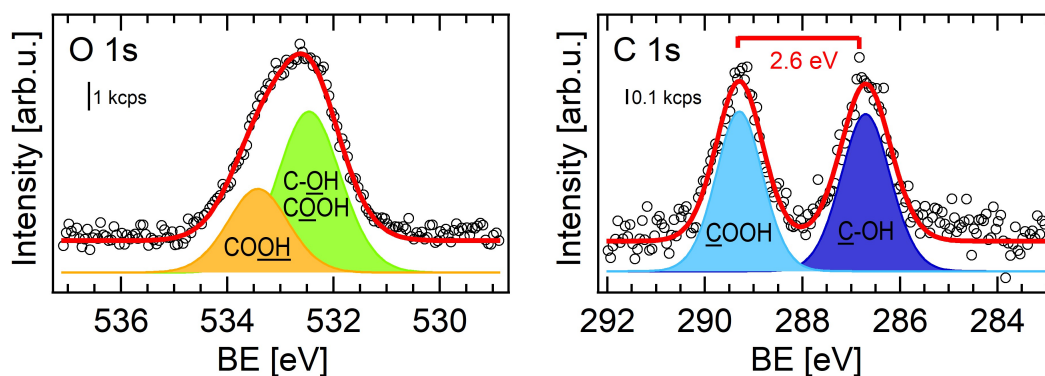


Figure 3.4: O 1s and C 1s XPS spectra acquired after a TA dose of  $\sim 2.5$  Å on Au(111). RR-TA coverage is estimated from the Au 4f/C 1s XPS intensity ratio, assuming a homogeneous molecular film. Spectra are recorded using a monochromatised Al K $\alpha$  X-ray source (photon energy  $h\nu = 1486.6$  eV). The fit is carried out with CasaXPS Software.

the O 1s and C 1s XPS peaks acquired after a TA dose on the Au surface (estimated thickness  $\sim 2.5$  Å). All along this chapter, molecular dosing has been performed at room temperature, while samples have been subsequently cooled down with liquid nitrogen for the XPS analysis, to prevent molecular desorption. In the O 1s region two molecular contributions appear: a dominant peak at  $532.5 \pm 0.1$  eV, assigned to the OH alcohol groups together with the C=O oxygen atoms from the carboxylic group and a weaker contribution at  $533.5 \pm 0.1$  eV from the OH acid groups. The energy position and the peak assignment are in good accord with the values reported for RR-TA deposition on Cu(111) [191]. On Cu(111) the C-OH and the C=O contributions were separated in the fit proposed and set at  $532.3 \pm 0.1$  eV and  $532.7 \pm 0.1$  eV in binding energy, respectively.

However, because of their relative small energy splitting, a unique feature set at  $532.5 \pm 0.1$  eV is taken into account in our fitting procedure. A (C-OH + COOH):(COOH) ratio of  $\sim 2 : 1$  is found, in agreement with the molecular expected stoichiometry.

In line with the O 1s analysis, in the C 1s region two main molecular peaks are identified at  $286.7 \pm 0.1$  eV and  $289.3 \pm 0.1$  eV, ascribed to the central (C(2),C(3)) and to the carboxylic C atoms, respectively. The two peaks appear to have equal intensities, consistent with the stoichiometry expected for biacid molecules.

### 3.2.2 RR-TA adsorption on Cu(110)

Previous investigations by STM and RAIRS of RR-TA on Cu(110) surface carried out by Ortega Lorenzo *et al.* showed that TA molecules are adsorbed in a monotartrate form at room temperature [110–112]. With that in mind, the same analysis as the one on the Au surface is performed on Cu(110). The PM-RAIRS spectra recorded at increasing deposition times are reported in figure 3.5. Several molecular adsorption bands appear, whose corresponding peak assignment in figure 3.5 is in good agreement with the work of Ortega Lorenzo *et al.* At the highest coverages, the  $\nu(\text{C}=\text{O})$  peak at  $1711 \text{ cm}^{-1}$  is replaced by two distinct bands at  $1683$  and  $1759 \text{ cm}^{-1}$ , suggesting that two types of carboxylic acid groups are found on the surface: they were attributed to the presence of H-bonded cyclic acid dimers and monomer acid groups, respectively [110]. The main result from the PM-RAIRS analysis is that a coexistence of peaks associated to carboxylic groups ( $\nu(\text{C}=\text{O})$  at  $1711 \text{ cm}^{-1}$ ) and carboxylate functionalities ( $\nu_{\text{sym}}(\text{COO})$  at  $1436 \text{ cm}^{-1}$ ) is observed, thus confirming that TA molecules are adsorbed in a monotartrate form. The absence of the corresponding ( $\nu_{\text{asym}}(\text{COO})$ ) at  $1600 \text{ cm}^{-1}$  implies that the carboxylate O atoms are equidistant from the surface, by application of the infrared selection rules valid for metal surfaces since no dynamic dipole moment perpendicular to the surface is observed [110–112].

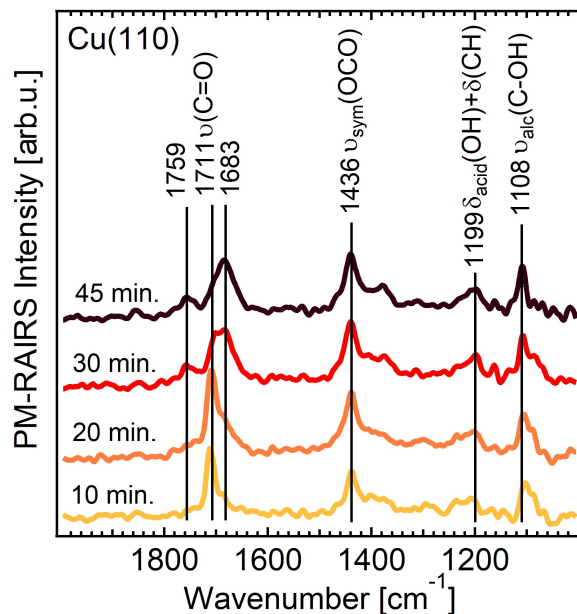


Figure 3.5: PM-RAIRS spectra acquired for increasing dosing times of TA on Cu(110).

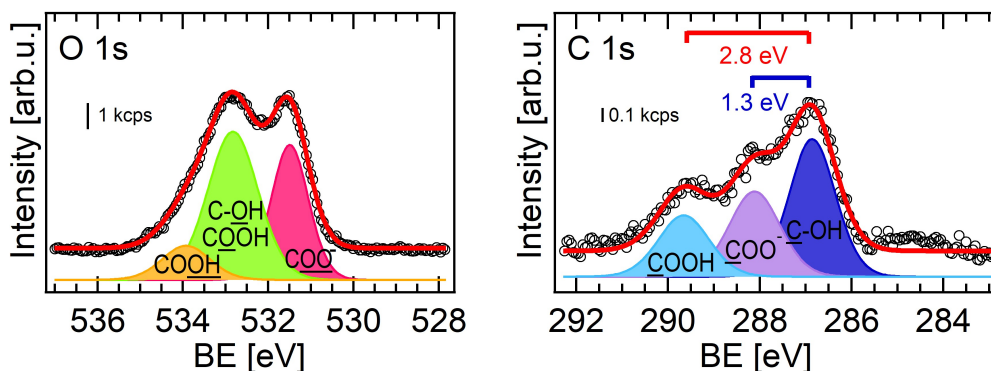


Figure 3.6: O 1s and C 1s XPS spectra acquired after a TA dose of  $\sim 2.4 \text{ \AA}$  on Cu(110). RR-TA coverage is estimated from the Cu 2p/C 1s XPS intensity ratio, assuming a homogeneous molecular film. Spectra are recorded using a monochromatised Al  $K\alpha$  X-ray source (photon energy  $h\nu = 1486.6 \text{ eV}$ ). The fit is carried out with CasaXPS Software.

As for the XPS analysis (figure 3.6), in the O 1s region one additional contribution is found at  $531.5 \pm 0.1 \text{ eV}$  with respect to Au(111), which is ascribed to the carboxylate O atoms. In line with the monotartrate molecular nature expected, an extra peak in the C 1s region arising from C atoms in the carboxylate groups is detected at  $288.1 \pm 0.1 \text{ eV}$ . The energy splitting between the main molecular peaks is consistent with the values reported by Rieger *et al.* on Cu(111) [191]. Peak ratios of  $\sim 3:1$  (O 1s) and  $\sim 1.5:1$  (C 1s) are obtained from the fit for  $\text{COO}^-/\text{COOH}$  and  $\text{COO}^-/\text{COOH}$ , respectively, which deviate from 2:1 and 1:1, expected from the stoichiometry of monotartrate species. Similar stoichiometric divergences, which suggest that a fraction of molecules is completely deprotonated, were observed for RR- and SS-TA on Cu(531) [192], for racemic mixtures of RR-TA and SS-TA on Cu(111) [191] as well as for malic acid ( $\text{HOOC-CH}_2\text{-HCOH-COOH}$ ) on Cu(110) [193]. A weak contribution appears at  $\sim 285.0 \text{ eV}$  which is likely due to contaminations or dissociation products as previously reported for the adsorption of the RR and SS enantiomers of TA on the intrinsically chiral Cu(531) surface [192].

### 3.3 RR-TA adsorption on rutile $\text{TiO}_2(110)$

#### 3.3.1 Chemical analysis

The XPS peaks recorded for TA on Au(111) and Cu(110) are used as references to decipher TA adsorption on the rutile  $\text{TiO}_2(110)$  surface. The main analysis focuses on the C 1s peaks, since for the  $\text{TiO}_2$  surface the molecular features in the O 1s region are partially covered by the intrinsic rutile contributions from the lattice O atoms and surface hydroxyls groups. Nevertheless, this fact does not prevent to perform a subsequent analysis of the O 1s region. The C 1s spectra for increasing RR-TA dosing times on  $\text{TiO}_2(110)$  are reported in figure 3.7. RR-TA coverage is estimated from the Ti 2p/C 1s XPS intensity ratio, assuming a homogeneous molecular film. A saturated monolayer coverage is obtained after approximately 30 minutes of dose<sup>1</sup>. Two equivalent contributions are found

<sup>1</sup>The coverage of 1 ML is estimated from STM and XPS *a posteriori* as half of  $\text{Ti}_{5c}$  density of the exposed surface ( $5.2 \times 10^{14} \text{ cm}^{-2}$  [136], knowing that upright RR-TA molecules are in a monotartrate form with one RR-TA molecule every two surface  $\text{Ti}_{5c}$  atoms), which corresponds to an equivalent film thickness of about 6 – 7  $\text{ \AA}$ .

at  $289.3 \pm 0.1$  eV and  $287.1 \pm 0.1$ , the latter attributed to central  $\text{C-OH}$  atoms. To decipher the TA chemical nature and in particular the origin of the high BE component, the energy separation between the molecular C 1s peaks is considered and compared to the values found on Au and Cu. In this respect, on Au(111) and Cu(110) the carboxylic acid contribution is shifted by 2.6 and 2.8 eV to higher BE with respect to the central C-OH carbon atoms, respectively. In addition to this, on Cu, where monotartrate species are found, the carboxylate peak appears at 1.3 eV higher binding energy with respect to the central C-OH carbon atoms (figure 3.6). On the rutile surface no evolution in the energy splitting between the two components occurs, which remains invariable at about 2.2 eV for the various dosing times, suggesting that on this surface the TA chemical nature is not subject to important chemical modifications as the molecular surface coverage increases. Moreover, the energy splitting value of 2.2 eV falls in between the values found for the  $\text{COOH}$  and  $\text{COO}^-$  groups on the reference metal substrates, which at a rough estimate may suggest that carboxylic acid groups and carboxylate functionalities coexist on the rutile surface and thus that TA adsorption takes place in a monotartrate form. The partial deprotonation would imply that, differently from the metallic cases, the  $\text{COOH}$  and  $\text{COO}^-$  contributions are not resolved on  $\text{TiO}_2$ , as previously evidenced for terephthalic acid (TPA) adsorption on the same rutile surface [194], thus both contributing to the high BE peak located at  $289.3 \pm 0.1$  eV. A possible explanation would be a different charge transfer between metals and  $\text{TiO}_2$ , where the  $\text{COO}^-$  charge is less screened by the oxide than by the metal, thus leading to a higher BE shift compared to Au and Cu. A contribution of two different species (carboxylate and carboxylic C atoms) to the high BE peak is also supported by the fit and in particular by the broadened width of the peak located at  $289.3 \pm 0.1$  eV, compared to the one at  $287.1 \pm 0.1$  eV, which despite being moderate (fwhm=1.5 eV *vs* 1.35 eV for 30 minutes of dose) is in line with the values reported by Zhang *et al.* for TPA adsorption on  $\text{TiO}_2(110)$  [194].

The O 1s spectra of the clean  $\text{TiO}_2$  (110) and of a saturated dose (30 minutes) of RR-TA on the same surface are presented in figure 3.8. As previously mentioned, the O 1s region

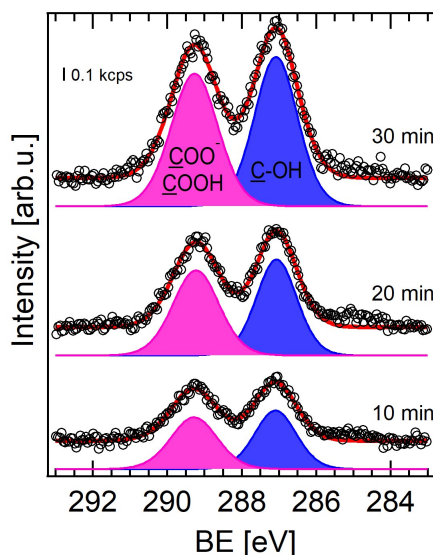


Figure 3.7: C 1s XPS spectra acquired at TA increasing dosing times on  $\text{TiO}_2(110)$ . Spectra are recorded using a monochromatised Al  $K\alpha$  X-ray source (photon energy  $h\nu = 1486.6$  eV). The fit is carried out with CasaXPS Software.

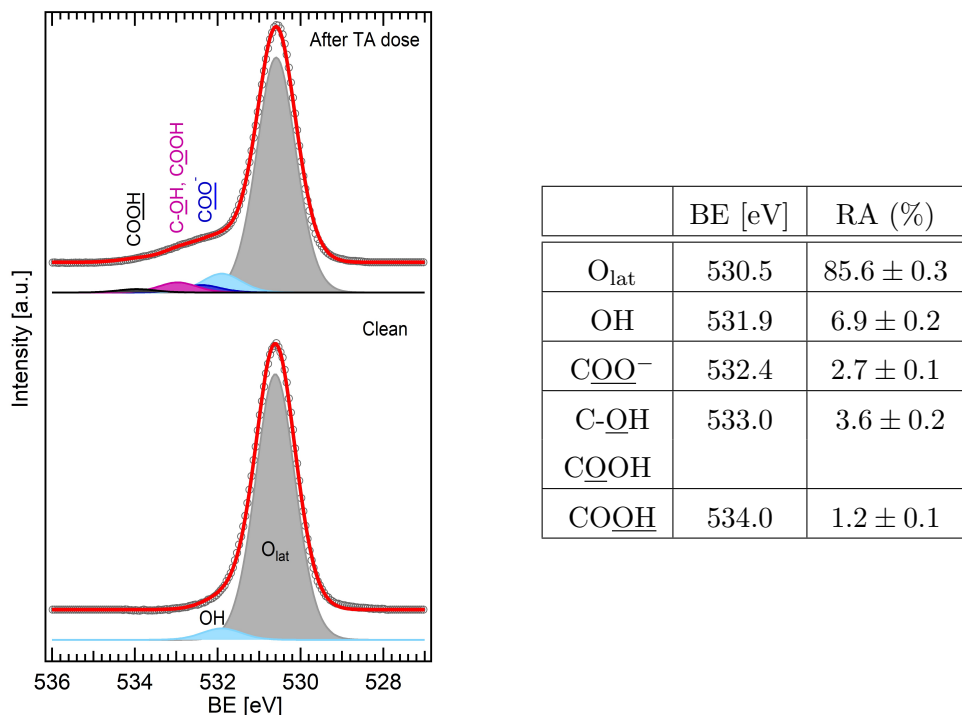


Figure 3.8: Left panel: O 1s spectra and corresponding fit of the clean rutile TiO<sub>2</sub> (110) surface (bottom) and after a saturated TA dose/TiO<sub>2</sub> (110) (top). Spectra are recorded using a monochromatised Al K $\alpha$  X-ray source (photon energy  $h\nu = 1486.6$  eV). The fit is carried out with CasaXPS Software. The red line and black dots represent the sum of the fitted components and the raw data, respectively. For the peak fitting attribution refer to the text. Right panel: Fit parameters for TA/TiO<sub>2</sub>(110): binding energy BE [eV] and relative area RA (%). A Gaussian/Lorentzian ratio equal to 70/30 has been used. Error bars on BE are of the order of 0.1 eV.

analysis is not as straightforward as in the C 1s case, due to the presence of intrinsic TiO<sub>2</sub> contributions from O lattice (O<sub>lat</sub> at  $530.5 \pm 0.1$  eV) and surface hydroxyls (OH at  $531.8 \pm 0.1$  eV) which partially overlap with the molecular peaks. The BE difference between O<sub>lat</sub> and OH peaks is 1.3 eV, in good agreement with previous works [194,195]. Following TA dose, a shoulder appears on the high BE energy side of the O 1s peak. Despite these complications, a fit is proposed with the support of the chemical information provided by the C 1s analysis. The intensity of the molecular contributions is far weaker than the intrinsic TiO<sub>2</sub> components so that performing a fit was possible only fixing all the fit parameters. The result is presented in figure 3.8 together with the fit parameters used in the analysis (peak BE, peak area ratio, FWHM). Three molecular contributions are found at 532.4 eV, at 533.0 eV and at 534.0 eV, attributed to COO<sup>-</sup>, (C-OH+ COOH) and COOH, respectively. COO<sup>-</sup>/COOH and (C-OH+ COOH)/COOH peak area ratios are set to  $\sim 2$  and  $\sim 3$ , respectively, consistent with the stoichiometry of monotartrate molecular species. The BE difference between the COO<sup>-</sup> and (C-OH+ COOH) contributions is about 0.6 eV in good agreement with what was reported for TPA molecules [194] and for carboxylic dye [196] on the same rutile TiO<sub>2</sub>(110). According to the decomposition proposed, upon TA adsorption the OH peak intensity increases, since the acidic H of the deprotonated COOH groups adsorb at bridging O sites forming additional surface hydroxyls. Overall, what comes out from the fitting procedure used is that the simultaneous presence of carboxylic and carboxylate groups deduced from the C 1s analysis, is coherent with the peak

shape.

### 3.3.2 Vibrational measurements

#### 3.3.2.1 General considerations: HR spectra of oxide surfaces, deconvolution method

HREELS measurements are carried out to confirm the hypothesis on the adsorbed RR-TA chemical nature on the rutile surface suggested by the XPS analysis. Figure 3.9 shows a typical HREEL spectrum of the clean rutile TiO<sub>2</sub>(110) surface. Starting from the lowest energies, some weak gain peaks due to the annihilation of excitation quanta are visible, followed by the intense elastic peak. Moving to the positive energy loss side, the HREEL spectra of oxide surfaces are dominated by intense optical phonon losses; for the rutile TiO<sub>2</sub>(110) surface, three fundamental surface optical phonon losses are detected at 365, 445 and 755 cm<sup>-1</sup> [116]. At about 3690 cm<sup>-1</sup> a weak band associated to surface hydroxyls appears. As reported in section 1.9, under specular scattering geometry, the incoming electrons interact with the dipolar field of the induced surface excitations. The most strongly excited phonons are characterised by long penetration depths and small wave vectors parallel to the surface, since they will be coupled for a long period to the electric field of the incoming electrons [62, 71]. Surface adsorbate molecular contributions will thus have a much lower oscillator strength, with a probability of being excited generally two orders of magnitude lower with respect to surface phonons [197]. In addition to this, the coupling between the incoming electrons and the dipolar field of surface excitations is so strong that electrons may subsequently exchange multiple quanta of energy. This gives rise to the series of weaker peaks observed at higher loss energies, which thus are due to combinations and sequential excitations of more than one phonon by one single electron scattered from the surface. More precisely, in the energy range up to 4000 cm<sup>-1</sup> the multiple phonon peaks observed arise from 1 to 4 multiple scattering events [198].

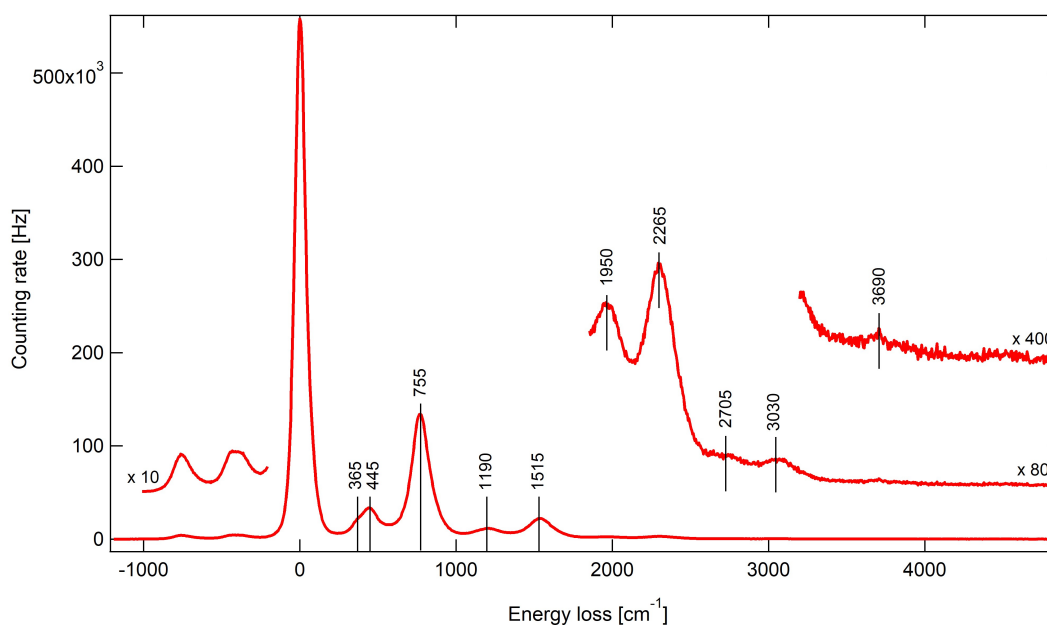


Figure 3.9: HREELS spectrum of the clean rutile TiO<sub>2</sub> (110) surface, recorded with an electron beam energy of 12.8 eV.

These strong vibrational features intrinsic to metal oxide surfaces lie in the energy loss region where the much weaker molecular contributions are expected, thereby substantially complicating the analysis of HREELS spectra [197]. This problem has thus inspired the development of solutions to try to eliminate completely or at least the majority of the multiple phonon contributions [42]. In this work, a Fourier log deconvolution technique first developed by Cox and co-workers has been used [71, 197]. The starting point is that multiple phonon losses follow a Poisson distribution, as demonstrated both theoretically and experimentally. The experimental HREEL spectrum  $s(\omega)$  is thus mathematically described as:

$$s(\omega) = i(\omega) \otimes \left[ \underbrace{\delta(0)}_{\text{elastic peak}} + \underbrace{p(\omega)}_{\text{single loss}} + \underbrace{\frac{1}{2!}p(\omega) \otimes p(\omega) + \frac{1}{3!}p(\omega) \otimes p(\omega) \otimes p(\omega) + \dots}_{\text{multiple losses}} \right] + \underbrace{N(\omega)}_{\text{noise}} \quad (3.1)$$

where  $i(\omega)$  represents the instrumental response,  $\otimes$  defines a convolution product and  $N(\omega)$  is an additional term of noise describing the random arrival of the electrons at the detector [199].  $p(\omega)$  is the single-loss phonon intensity and the multiple losses are written as an infinite series of  $p(\omega)$  self-convolution terms [71, 197, 199]. The Fourier transform of  $s(\omega)$  is written as:

$$S(\tau) = I(\tau) \left[ 1 + P(\tau) + \frac{1}{2!}P(\tau)^2 + \frac{1}{3!}P(\tau)^3 + \dots \right] + N(\tau) = I(\tau) \exp(P(\tau)) + N(\tau) \quad (3.2)$$

Thus yielding to:

$$P(\tau) = \ln \left[ \frac{S(\tau)}{I(\tau)} - \frac{N(\tau)}{I(\tau)} \right] \quad (3.3)$$

$p(\omega)$  cannot be obtained directly by back-Fourier transforming  $P(\tau)$  since the exact resolution is unknown and its Fourier components  $N(\tau)$  decay much slower with  $\tau$  than that of the signal. When trying to eliminate the instrumental broadening, high frequency Fourier ripples will thus be introduced in the deconvoluted spectrum [71, 199]. Equation (3.3) is thus smoothed with a function  $I'(\tau)$  generally with broadening greater than  $I(\tau)$ , to suppress the Fourier ripples from the deconvoluted spectrum [197], and the noise component is neglected leading to the spectrum free from multiple phonon losses:

$$s'(\omega) = p(\omega) \otimes i'(\omega) = F^{-1} I'(\tau) \ln \left[ \frac{S(\tau)}{I(\tau)} \right] \quad (3.4)$$

From a practical point of view,  $S(\tau)$  is the Fourier transform of the HREEL spectrum, while  $i(\omega)$  and  $i'(\omega)$  are estimated from the fit of the elastic peak which is a fair estimate of the apparatus function. For adsorbates on an oxide substrate, the application of the Fourier deconvolution method is extremely powerful since it allows the removal of phonon-phonon, phonon-adsorbate and in principle also adsorbate-adsorbate combination peaks. This technique has been successfully employed in the study of adsorbed species on metal oxide surfaces, such as ZnO, NiO, SrTiO<sub>3</sub> and TiO<sub>2</sub>, just to name a few [42, 71, 131, 138, 197, 198].

In this work, a Gaussian-Lorentzian profile is used to fit the elastic peak and used to model the instrumental response function. This latter is then folded by a Gaussian of FWHM of the order of meV to obtain  $i'(\omega)$ . The fundamental phonon losses cannot be suppressed from the spectrum, but the molecular contributions we are interested in lie in the multiple losses region [42]. The deconvoluted spectrum is shown in figure 3.10. Most of the multiple phonon losses above the three fundamental surface optical phonons of TiO<sub>2</sub>



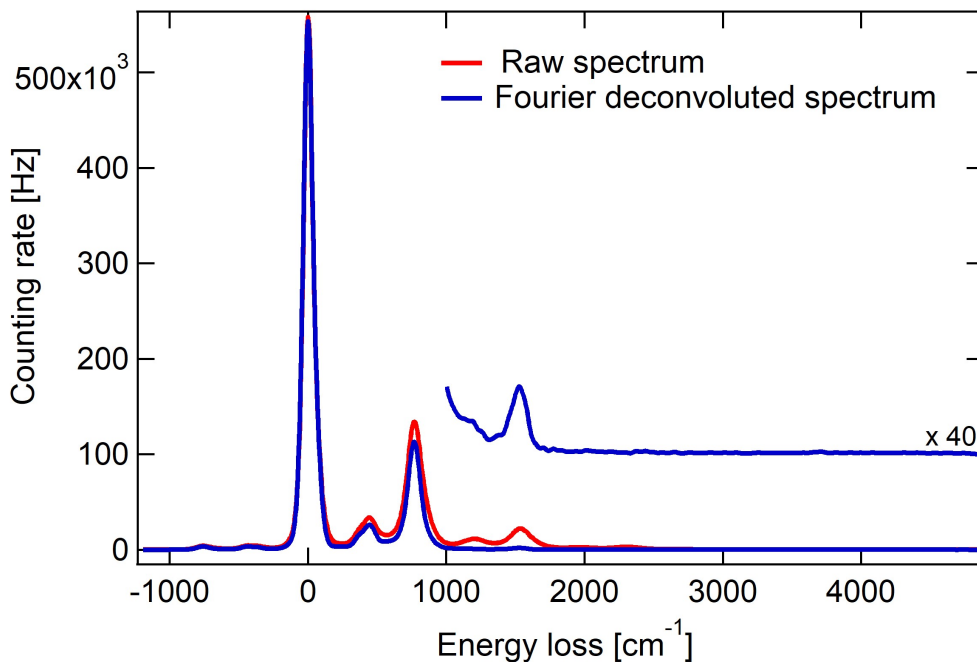


Figure 3.10: HREELS spectra of the clean rutile TiO<sub>2</sub> (110) surface as recorded (in red) and after the application of the Fourier log deconvolution method (in blue).

have successfully been removed. However, a contribution is still observed at about 1500  $\text{cm}^{-1}$ , which is not accounted for in the deconvolution process and whose origin is still debated [198]. One hypothesis is that this contribution would arise from an overtone of the 755  $\text{cm}^{-1}$  fundamental phonon loss [198]. Differently from combination features, which are due to sequential excitations of one or various surface vibrational modes from the ground state to the first excited state, overtones occur when the surface vibrational mode excitation is from the ground state to the second excited state in one single scattering event [197]. In the former case a loss equal to twice the fundamental excitation energy appears, while in the latter because of anharmonic effects the loss occurs at an energy less than twice the fundamental one [197, 198]. Since the deconvolution method used here successfully removes only combination features, overtone modes will still be observed in the Fourier deconvoluted spectrum. The remnant peak at 1500  $\text{cm}^{-1}$  partially hampers the observation of the less intense molecular contributions expected in this region, but information on TA chemical nature is still accessible.

### 3.3.2.2 Results

Figure 3.11 displays the HREELS spectra obtained after application of the Fourier deconvolution method for the clean TiO<sub>2</sub>(110) surface in red and plotted in black for TA exposures of 10 minutes (traces labelled a) and 5 minutes (traces labelled b), where 10 minutes correspond to 1 ML on the basis of previous calibrations. Although the counting rate was high on the clean surface, the elastic peak intensity drastically decreased following TA deposition, suggesting a variation of the surface electron reflectivity upon molecular deposition, as already previously observed [138, 198]. To allow a direct comparison of spectra for the clean and adsorbate-covered surfaces, but without any physical reason, the HREELS spectra are normalised to the peak at 1500  $\text{cm}^{-1}$ . Several molecular peaks

appear. The loss at 1380 cm<sup>-1</sup> arises from  $\delta_{alc}(\text{OH})$  bending, while the peak at 1460 cm<sup>-1</sup> is assigned to the COO symmetric stretching mode  $\nu_{sym}(\text{COO})$ , in perfect accord with the value of 1465 cm<sup>-1</sup> reported for acetic acid adsorption on the same rutile TiO<sub>2</sub>(110) [200]. The corresponding asymmetric vibrational mode  $\nu_{asym}(\text{COO})$  expected between 1500 and 1600 cm<sup>-1</sup> is not observed, probably hindered by the residual contribution at 1500 cm<sup>-1</sup>, as suggested in previous studies [197, 200]. The  $\nu_{asym}(\text{COO})$  was indeed reported at 1536 cm<sup>-1</sup> for formic acid and 1498 cm<sup>-1</sup> for benzoic and terephthalic acid deposited on TiO<sub>2</sub> and probed by RAIRS [132, 150]. The loss appearing at 1740 cm<sup>-1</sup> is assigned to the carboxylic C=O stretching mode ( $\nu(\text{C}=\text{O})$ ). A higher molecular dose reported in traces b results in the downshift of  $\nu(\text{C}=\text{O})$  to 1680 cm<sup>-1</sup>. The displacement to lower frequency is consistent with what was reported for RR-TA on Cu(110) and Ni(110), explained on the basis of H-bonding formation between the intact carboxylic acid groups of adjacent molecules. Finally, the loss at 2920 cm<sup>-1</sup> arises from to C-H vibration ( $\nu(\text{CH})$ ). No conclusions on the OH variations can be drawn since these weak modes at 3690 cm<sup>-1</sup> are comparable to the noise level. Overall, the simultaneous presence of carboxylic and carboxylate related peaks establishes that monotartrate species are adsorbed on the rutile surface, thus corroborating the hypothesis suggested by the XPS analysis.

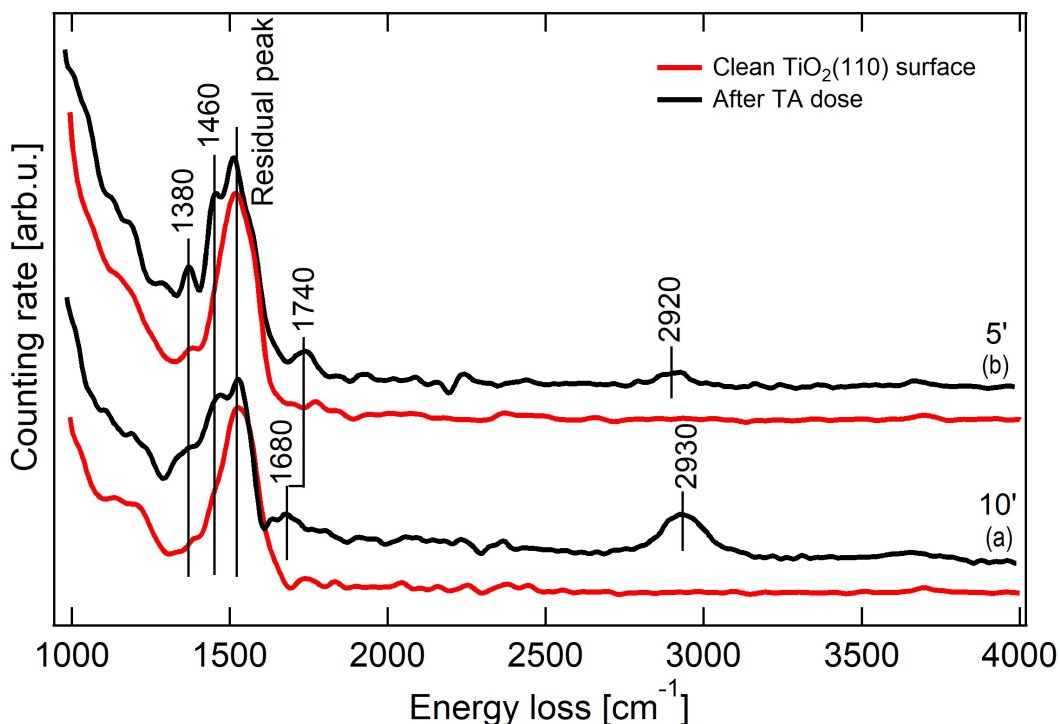


Figure 3.11: (a) Fourier deconvoluted HREEL spectrum for the clean TiO<sub>2</sub>(110) surface recorded at an impact energy of 8.8 eV. (b) Zoom of Fourier deconvoluted HREEL spectra for the clean TiO<sub>2</sub>(110) surface (red) and after a TA dose of 5 minutes (black) at 12.8 eV. (c) Zoom of Fourier deconvoluted HREEL spectra for the clean TiO<sub>2</sub>(110) surface (red) and after a TA dose of 10 minutes (black) at a beam energy of 8.8 eV.

### 3.3.3 Structural results

STM and LEED experiments are carried out to understand the adlayer geometry and anchoring points of TA molecules on the rutile  $\text{TiO}_2$  surface. In figure 3.12 a STM image for a low molecular coverage is reported. RR-TA molecules are imaged as bright spots with a random distribution all over the surface. To determine and locate TA anchoring points, the discernible underlying bright  $\text{Ti}_{5c}$  rows are identified with red lines, while molecules are marked by blue circles. In this way RR-TA molecules appear to be anchored on top of  $\text{Ti}_{5c}$  atoms, while no molecules are observed on the dark  $\text{O}_{br}$  rows in between. The bright large patches probably arise either from contamination or from the formation of localised molecular multilayers.

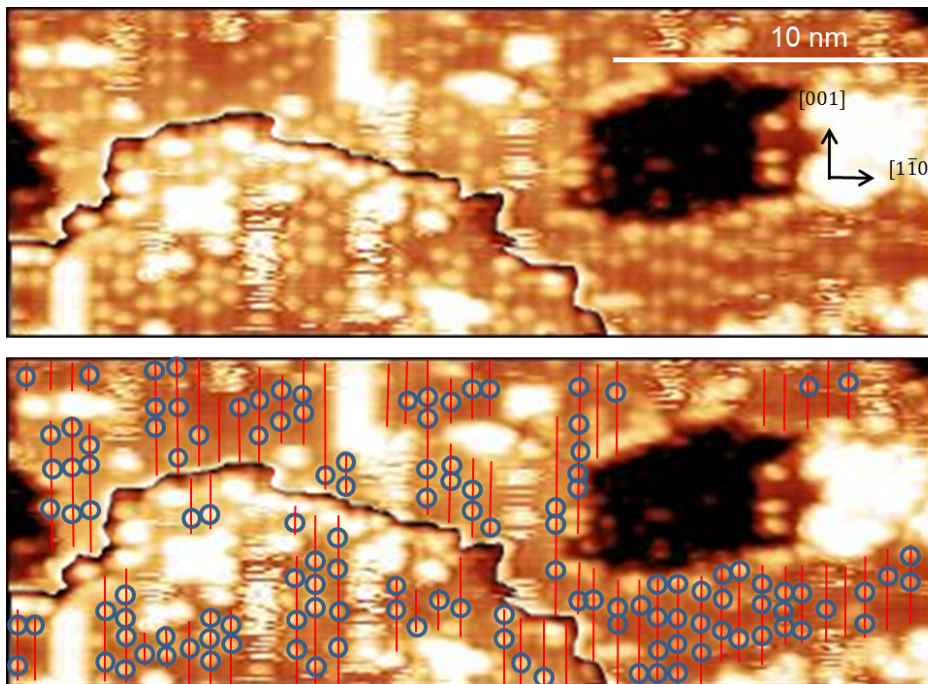


Figure 3.12: Top: STM image for a submonolayer dose of RR-TA on rutile  $\text{TiO}_2(110)$  (1.9 V, 130 pA). The image was calibrated setting the distance between adjacent  $\text{Ti}_{5c}$  rows to 6.49 Å as expected. Bottom: Same STM image where the bright  $\text{Ti}_{5c}$  rows are evidenced with red lines while TA positions are marked with blue circles. The two terraces have been analysed separately to optimise the contrast.

Figure 3.13a shows a STM image recorded for a saturated monolayer coverage, used to understand the 2D adlayer geometry and estimate the intermolecular spacing between neighbouring RR-TA molecules. From a statistical analysis distances between neighbouring molecules amount, on average, to  $6.3 \pm 0.7$  Å in the  $[001]$  direction and  $6.8 \pm 0.8$  Å in the  $[1\bar{1}0]$  direction. Knowing that the surface  $\text{TiO}_2(110)$  unit-cell dimensions are  $2.96$  Å  $\times$   $6.49$  Å, the values measured for the molecular adlayer correspond to  $\sim 2$  and  $\sim 1$  surface unit cell parameters of  $\text{TiO}_2$  in the  $[001]$  and  $[1\bar{1}0]$  directions, respectively. The slight deviation arises from the lack of drift compensation in the considered image. The measured intermolecular distances thus suggest that TA molecules assemble at saturation coverage in a  $(2 \times 1)$  adlayer, as further confirmed by LEED. A TA dose of about 1 ML leads indeed to the appearance of additional spots which correspond to a clear  $(2 \times 1)$  LEED pattern (evidenced in green) with respect to the  $(1 \times 1)$  of the clean  $\text{TiO}_2(110)$  surface (in blue), in consistence with the STM results. The  $(2 \times 1)$  pattern is observed simultaneously, but

disappears with time, because of electron beam damage during exposure. Electron beam effects were also observed for TA on Ni(111) [114].

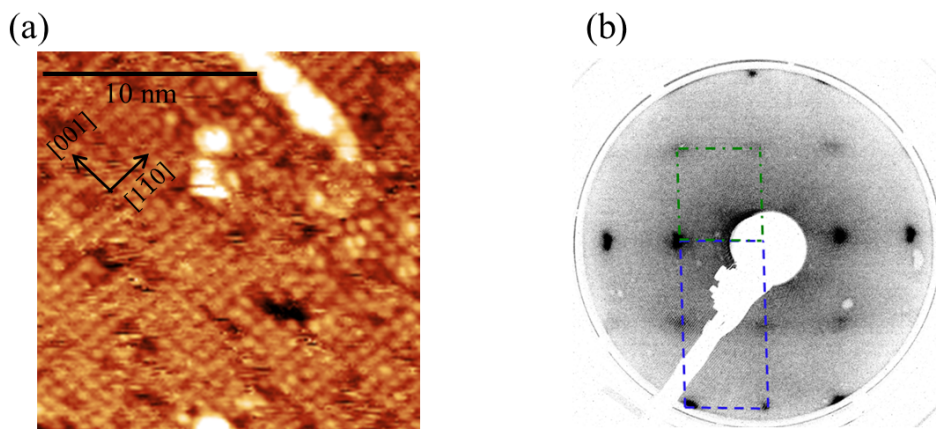


Figure 3.13: (a) STM image recorded for a TA monolayer saturated coverage on the rutile  $\text{TiO}_2(110)$  surface (1.7 V, 150 pA). (b) LEED pattern for a 1 ML TA dose on the same rutile  $\text{TiO}_2(110)$  surface (electron beam energy = 45 eV). The  $(1 \times 1)$  and the  $(2 \times 1)$  patterns of the clean rutile surface and after TA dose are evidenced in blue and green, respectively.

### 3.3.4 Proposed adsorption model

Gathering together the chemical and vibrational information provided by XPS and HREELS and the morphological analysis from STM and LEED, a model of TA molecular arrangement on the  $\text{TiO}_2(110)$  is presented in figure 3.14. Within the proposed adsorption model, TA molecules adopt an upright position and bind to the  $\text{TiO}_2$  surface via the carboxylate O atoms, adsorbed in a bridging bidentate configuration on two adjacent  $\text{Ti}_{5c}$  sites, with the molecular plane aligned along the [001] direction. The remaining carboxylic acid group is instead intact and protrude outwardly from the  $\text{TiO}_2$  surface. By schematically depicting the molecule by a black segment, placed in between to adjacent  $\text{Ti}_{5c}$  atoms to mimic the carboxylate O bonding sites, the formation of the  $(2 \times 1)$  overlayer observed by STM and LEED is evidenced (green rectangle in figure 3.14), with respect to the  $(1 \times 1)$  unit cell of the underlying rutile surface (in blue in figure 3.14). The occurrence of a bidentate bonding is consistent with the distance between adjacent  $\text{Ti}_{5c}$  rows, as already shown for formic acid (figure 2.14) [121, 142, 144].

As presented in section 2.4, adsorbates may form 2D chiral structures, whose growth directions are oriented along non-symmetric directions of the substrate surface, as shown for RR-TA deposition on Cu(110) and Ni(111). On both surfaces, chirality manifests at a local point level and global organisational level. On the contrary, in this work STM images reveal a different behaviour for TA adsorption on  $\text{TiO}_2(110)$ , with no formation of extended chiral domains, similarly to what was observed on Ni(110) [201]. The chiral expression on  $\text{TiO}_2(110)$  is not imparted globally to the surface, but it is thus limited only to a local level, which is nevertheless at the heart of the most successful real enantioselective catalysts.

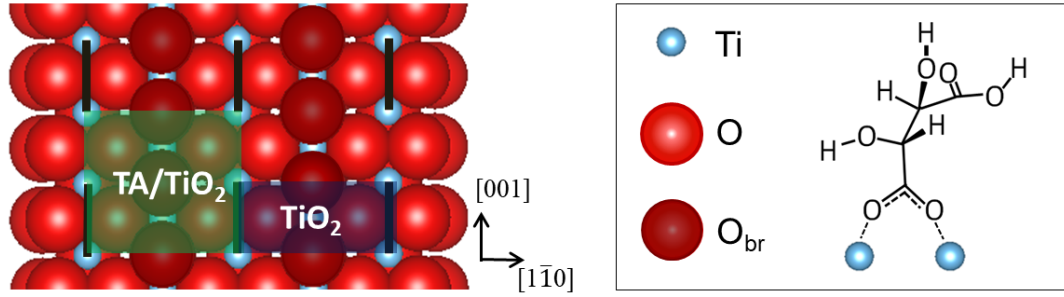


Figure 3.14: Proposed adsorption model of TA on  $\text{TiO}_2(110)$ . Ti atoms, in plane O and bridging O atoms are represented in blue, red and dark red, respectively. Molecules are adsorbed in the monotartrate form and anchoring to the rutile surface occurs via both carboxylate O atoms schematically represented by a black segment aligned along the  $[001]$  direction and corresponding to the  $\text{COO}^-$  plane. The  $(2 \times 1)$  overlayer formed by TA molecules and the  $(1 \times 1)$  unit cell of the underlying rutile surface are evidenced by a green and a blue rectangle, respectively.

### 3.4 UPS measurements

#### 3.4.1 Adsorbate-induced work function variations

Generally speaking, for a semiconductor the work function is written as the sum of three terms (figure 3.15):

$$e\Phi = I + eV_S - (E_F - E_V) = \chi + eV_S + (E_C - E_F) \quad (3.5)$$

where  $E_F$  is the Fermi level,  $E_V$  is the position of the valence band,  $I$  is the ionisation energy (*i.e.* the energy difference between the valence band and the vacuum level),  $V_S$  is the band bending,  $\chi$  is the electron affinity and  $E_C$  is the position of the conduction band [21, 50, 202].

When atoms or molecules are chemisorbed on a surface, a charge transfer between the adsorbate and the substrate takes place. Even when adsorbates are simply physisorbed, screening effects of the underlying substrate create image charges. In both cases the dipole moment created results in variations of the electron affinity and thus the work function. Moreover, when dealing with semiconductors, a band bending change must be accounted

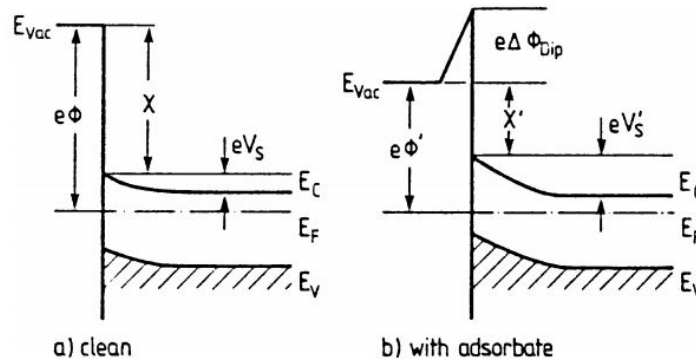


Figure 3.15: Schematic band diagram of a clean semiconductor surface (a) and after adsorbate deposition on the same surface (b) [21].

for, due to charge transfer (figure 3.15). Therefore, upon adsorbate deposition, the work function variation is overall expressed as:

$$e\Delta\Phi = e\Delta\Phi_{dip} + e\Delta V_S = \Delta\chi + e\Delta V_S = \Delta I + e\Delta V_S \quad (3.6)$$

where  $e\Delta V_S$  corresponds to contribution due to the band bending [21], while  $e\Delta\Phi_{dip}$  includes variations due to the surface dipole, which may be related to a variation of the electron affinity  $\chi$  or the ionization energy  $\Delta I$ . These two terms are directly estimated by UPS, as schematically represented in figure 3.16. As described in section 1.4.2 and shown in figure 3.16, the work function variation is determined by the variations of the total width of the UPS spectrum, while band bending contributions are estimated by measuring the shift of the high energy VB flank, with respect to  $E_F$ , if no new molecular states appear in the gap.

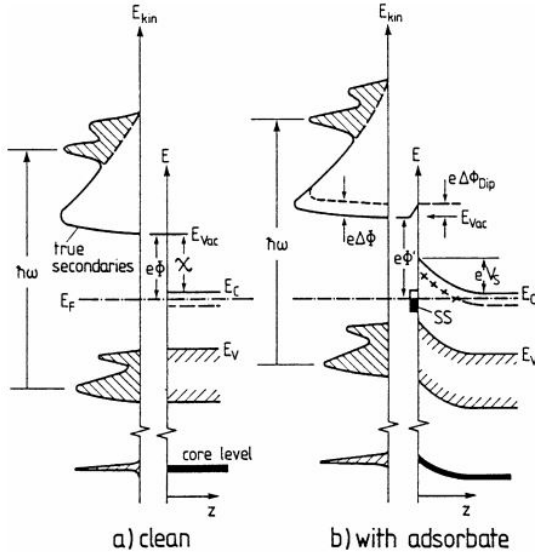


Figure 3.16: Changes induced in a typical UPS spectrum of a semiconductor (a) after adsorbate deposition (b) [21].

In a simplistic model, the presence of dipoles of the adsorbed molecules is schematised in terms of a parallel plate capacitor, with positive and negative charges separated by a distance  $d$  (figure 3.17). The potential difference across the capacitor is assumed to be equal to the work function variation induced by the dipole presence [21, 202, 203]:

$$\Delta I = \frac{en_{dip}p_{\perp}(\theta)}{\epsilon_0} \quad (3.7)$$

where  $n_{dip}$  is the dipole surface density,  $\theta$  is the surface coverage and  $p_{\perp}(\theta)$  is the dipole moment perpendicular to the surface of the adsorbed molecules.  $p_{\perp}$  may vary with the coverage, due to the interaction between neighbouring dipoles [21, 202].

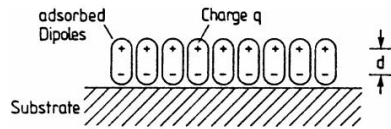


Figure 3.17: Schematic representation of adsorbed molecules in terms of a parallel plate capacitor with positive and negative charges separated by a distance  $d$  [21].

### 3.4.2 Results

Figure 3.18(a) displays the evolution of the valence band (VB) for the clean TiO<sub>2</sub> (110) (red trace) and at increasing TA coverage. TA thickness is estimated from previous XPS

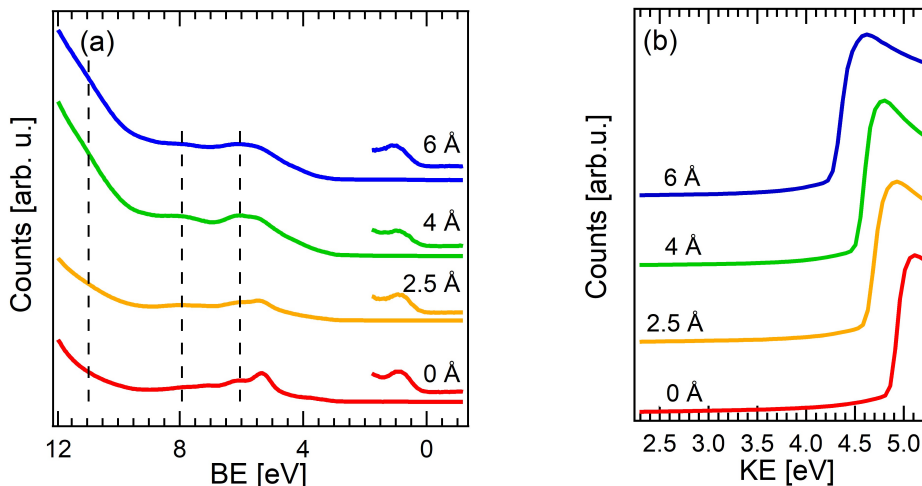


Figure 3.18: (a) Evolution of the UPS spectra as a function of TA coverage on the rutile  $\text{TiO}_2(110)$  surface, together with a zoom of the band gap state region. (b) Zoom on the secondary cut-off region as a function of TA dose. The spectra presented are normalized to the maximum.

calibrations from the C 1s/Ti 2p core level peak area ratio. All UPS spectra presented are recorded in normal emission using a He I excitation source (21.2 eV). As previously mentioned, the dominant contribution to the  $\text{TiO}_2$  valence band which appears between 4 and 9 eV originates from the O 2p states with some Ti 3d and Ti 4sp character which follows from hybridization between the empty Ti 3d and Ti 4sp states with O 2p [204,205]. The VB spectrum of the pristine  $\text{TiO}_2$  surface resembles those reported by Thornton *et al.* [206] and Aika *et al.* [207], with an intense peak at about 5.5 eV and a shoulder at 7.0 eV, arising from the non-bonding and bonding O 2p states, respectively [208,209]. Since the rutile crystal is partially reduced from the preparation procedure, at 0.9 eV below  $E_F$  (zoom in figure 3.18(a)) a small contribution arising from the Ti 3d occupied states is observed, whose intensity is enhanced when performing grazing emission experiments and whose origin is associated to the presence of surface defects [116,194,206,207,209]. Upon increasing TA coverage, new molecular states appear at about 6, 8 and 11 eV and partially damp the substrate contributions. For TPA molecules on  $\text{TiO}_2(110)$ , depending on the coverage, molecular electronic states were observed at  $\sim 14.0$  eV,  $\sim 11.5$  eV,  $\sim 10.0$  eV,  $\sim 7.9$  eV and  $\sim 6.7$  eV [194]. For acetic acid deposition on the same rutile surface, states appearing at  $\sim 14.0$  eV,  $\sim 11.0$  eV were ascribed to the presence of carboxylate species [194,210]. Based on these attributions, the contribution observed in this work at  $\sim 11$  eV may be ascribed to carboxylate groups. However, in the absence of a support from theoretical calculation, an unambiguous assignment of this peak and the other molecular contributions is not possible. No interface states seem to appear in band gap upon TA adsorption, in agreement with what was observed for water and other carboxylic acids, such as acetic acid, benzoic acid and TPA molecules on metal oxide surfaces (MgO, ZnO and  $\text{TiO}_2$ ) [194,211]. As for the band gap state (BGS), no direct conclusions can be drawn on its intensity variation, since overall UPS peak intensities vary with TA coverage and a spectrum normalization thus becomes difficult to perform. Moreover, TA spectra could not be sequentially recorded since the TA doser is not placed in the same chamber where UPS analysis is carried out, thus making it difficult to compare the BGS intensity from one spectrum to another. However, efforts are done as far as possible to place the sample

in the same position while performing UPS.

Figure 3.18(b) shows an enlarged view of the secondary cut-off (SCO) region at increasing TA coverage. Figures 3.18(a) and (b) have been used to estimate the work function and band-bending variations following molecular deposition. To be able to record the SCO, *i.e.* the electrons having low kinetic energies, the sample is biased at  $-10$  V. The valence band maximum (VBM) and the work function (WF) values are measured using a tangent method, more precisely from the intersection of the linear extrapolation of the background and the tangent in the inflexion point of the edge of the considered spectrum [202], as shown in figure 3.19. The inflection point is determined from the maximum in the derivative spectrum.

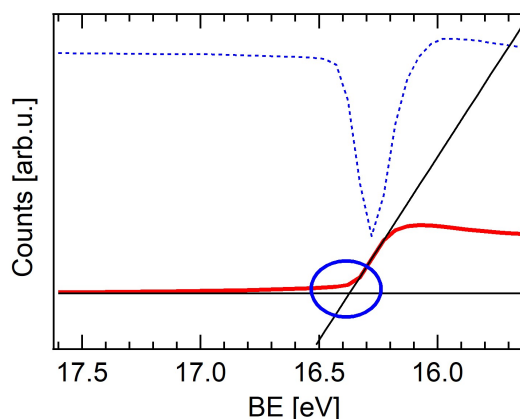


Figure 3.19: Example of the use of the tangent method to determine the WF (shown here) and VBM values. The original spectrum is represented in red, while the derivative spectrum with a dotted blue line. The intersection between the linear extrapolation of the background and the tangent in the inflexion point of the edge of the considered spectrum is marked with a blue circle. The inflection point is determined from the maximum of the derivative spectrum. The accuracy is estimated to about 0.1 eV.

For the clean TiO<sub>2</sub> surface, the VBM is located at 2.8 eV. The band gap of rutile is about 3 eV, so that the Fermi level is close to the conduction band minimum, which is an evidence of the n-type doping caused by intrinsic defects in reduced TiO<sub>2</sub> single crystals [116,194]. From the SCO spectrum, the WF of the clean TiO<sub>2</sub> (110) is 4.8 eV, in accordance with values reported in literature which vary between 3.9 and 6.2 eV, according to the sample preparation [116,194]. The work function and band bending variations upon RR-TA increasing doses are reported in figure 3.20. As the TiO<sub>2</sub> surface is covered with TA molecules, a gradual decrease of the WF is observed to 4.2 eV at about 1 ML of TA. The same trend was reported for TPA molecules, but the WF reduction was more intense (around 1.2 eV) at one monolayer coverage. As for the band-bending contribution, the variation observed is not significant and remains within the tangent method accuracy, in accordance with the XPS core level peaks, where no significant shift occurs. From the difference  $e\Delta\phi - e\Delta V_S$ , which is equal to  $\Delta I$ , it is possible to estimate the local surface dipole per atom  $p_{\perp}(\theta)$ , whose trend is reported in figure 3.20 as a function of the molecular coverage. An inward dipole of  $\sim 0.5$  debye per molecule is required to reduce the work function by 0.6 eV at about 1 ML of RR-TA. Overall the formation of an inward dipole may suggest as well that one carboxylic group is deprotonated.



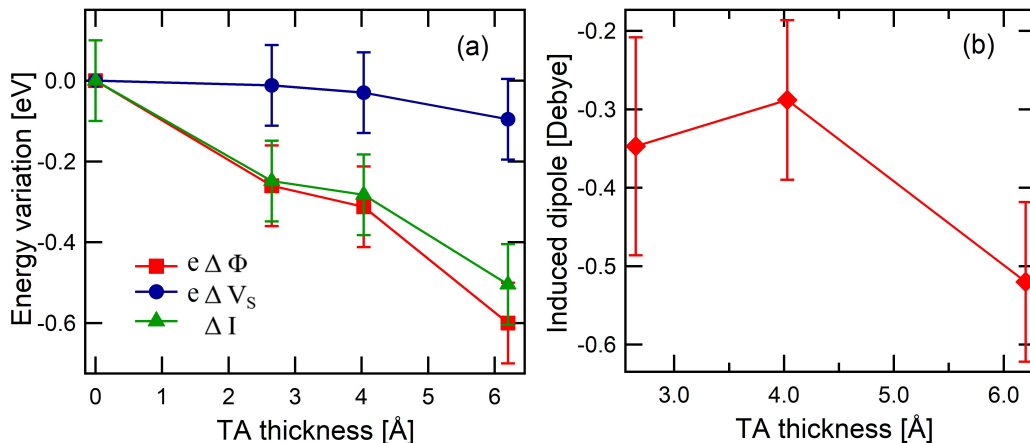


Figure 3.20: Left panel: Work function, band bending and ionization energy variations as a function of TA thickness on the  $\text{TiO}_2(110)$  surface represented by red squares, blue circles and green triangles, respectively. Right panel: Variation of the surface induced dipole per atom  $p_{\perp}(\theta)$  as a function of TA thickness on the  $\text{TiO}_2(110)$  surface. Error bars are estimated assuming that of  $\Delta I$  equal to 0.1 eV.

### 3.5 Conclusion

Several surface science techniques have been combined to tackle the questions of RR-TA chemical state, layer structure and anchoring sites on rutile  $\text{TiO}_2(110)$ . The investigation of molecular adsorption on  $\text{TiO}_2$  is fairly complex to perform because of the issues associated with doing infrared measurements and electron spectroscopy on oxide surfaces. Studies of chiral molecule adsorption on the  $\text{TiO}_2(110)$  surface are scarce. Nevertheless, understanding the interaction between a chiral modifier and an oxide support is of central concern for the rational design of oxide-supported enantioselective metal catalysts.

The analysis of the XPS spectra recorded on  $\text{TiO}_2$  and the comparison with those recorded on Cu and Au single crystals have suggested that monotartrate species are adsorbed on  $\text{TiO}_2(110)$ . This hypothesis was confirmed by HREELS experiments, which allowed to evidence the coexistence of peaks attributed to carboxylic and carboxylate groups. STM imaging and LEED showed that molecules are bound to  $\text{Ti}_{5c}$  atoms and that a  $(2 \times 1)$  overlayer is formed at saturation coverage. This set of results allowed to propose an adsorption model for RR-TA molecules on  $\text{TiO}_2(110)$ , with both carboxylate O atoms bound to two adjacent  $\text{Ti}_{5c}$  atoms, while the remaining carboxylic acid group is intact and protrudes out of the surface layer. UPS data revealed a decrease in the work function and the formation of an inward dipole following TA doses, which may confirm the deprotonation of a COOH group upon adsorption. Overall, the dissociative adsorption mechanism via deprotonation of one (or more) carboxylic acid groups is in line with what was observed for carboxylic-containing molecules on  $\text{TiO}_2(110)$ , as presented in chapter 2. The lack of extended chiral domains suggests that TA behaviour on  $\text{TiO}_2(110)$  substantially differs from what was observed on Cu(110) or Ni(111), revealing instead an adsorption geometry closer to that of TA on Ni(110). Chirality on the oxide surface is not induced to a global level through the formation of extended chiral domains, but only locally due to the intrinsic chiral character of TA molecules, which is retained upon adsorption.

# CHAPTER 4

---

## Chemical nature and thermal decomposition behaviour of RR-TA multilayers on rutile TiO<sub>2</sub>(110)

---

In the previous chapter, we investigated RR-TA sub-monolayer and monolayer deposition on the rutile TiO<sub>2</sub>(110) surface by combining several surface science techniques. Here we extend the study to the RR-TA thermal stability and decomposition on TiO<sub>2</sub>(110) by Temperature Programmed Desorption (TPD) as well as its adsorption behaviour in the multilayer regime investigated by X-Ray Photoemission Spectroscopy (XPS). It has already been observed experimentally that protruding carboxylic groups favor the formation of physisorbed multilayers [212]. Hence, the interface layer formed by monotartrate species and leaving one carboxylic group available at the surface should lead to a multilayer formation via H-bond interactions.

*Dans le chapitre précédent, nous avons étudié le dépôt de l'acide tartrique (RR-AT) sur la surface du rutile TiO<sub>2</sub>(110) dans le domaine de la sous-monocouche et monocouche en combinant plusieurs techniques de sciences des surfaces. Nous étendons ici l'étude à la stabilité thermique et au comportement de décomposition de l'AT sur TiO<sub>2</sub>(110) suivi par désorption thermique (TPD) ainsi que son absorption dans le régime de la multicouche étudié par photoémission X (XPS). Il a déjà été observé expérimentalement que des groupes carboxyliques disponibles à la surface d'une monocouche favorisent la formation de multicouches physisorbées [212]. Par conséquent, la couche d'interface formée par des espèces monotartrates et laissant un groupe carboxylique libre à la surface devrait conduire à la formation de multicouches via formation de liaisons hydrogène.*

### 4.1 Experimental aspects

RR-TA multilayer growth is undertaken using longer deposition times with the same experimental deposition conditions employed for sub-monolayer and monolayer doses. RR-TA coverage is then estimated as usual by XPS, from the Ti 2p/C 1s XPS intensity ratio, assuming a homogeneous molecular film.

When performing XPS or more generally analysis techniques which employ electrons or X-ray and UV radiation in the study of organic molecules, one common issue is the occurrence of molecular beam damage, which may affect the recorded spectra. Beam damage effects may arise from the direct interaction with the incident beam, such as in the case of LEED or photolysis in XPS, but also from the interaction with secondary electrons emit-

ted. In both cases, molecular desorption and/or decomposition of the sensitive analysed samples may occur. In the analysis, a particular attention has thus to be paid to recognise the signatures of beam damage and avoid misleading data interpretations. In some cases, understanding the stability of certain molecules under X-ray and UV light may be useful in applications such as solar cell development, where the exposition to sunlight may cause degradation of the device over time [193].

Beam damage or desorption may be monitored for example in XPS by recording scans of the same region (for example C 1s for organic molecules) periodically all over the analysis, to check the appearances of new species or the evolution in the intensity of the considered peaks. Beam effects have been observed both with synchrotron radiation and conventional laboratory sources. Occurrence of beam damage is indeed quite common and some examples are reported here. It has been previously observed, for instance, that malonic acid molecules both decompose and desorb under soft X-ray beam [193]. Similarly, as a result of X-ray damage, bi-isonicotinic acid molecules adsorbed on rutile TiO<sub>2</sub>(110) have been found to decompose into two isonicotinic acid fragments [213]. Beam damage and desorption due to synchrotron radiation have been observed as well on glycine multilayers adsorbed on TiO<sub>2</sub>(110) [214]. Electron stimulated decomposition and disorder following LEED was observed for RR-TA deposition on Ni(111) [114] and after longer exposure times also on Cu(110) [110].

In general we observed that under prolonged XPS and UPS analysis, RR-TA molecules are not stable and tend to desorb from the surface, more intensely in the multilayer regime. In this respect, figure 4.1 shows the effect of long time X-ray irradiation (at least two hours) at room temperature on RR-TA molecules adsorbed on TiO<sub>2</sub>(110). After prolonged XPS analysis time, considerable desorption of the molecular film is observed, especially in the multilayer regime, so that a plateau is reached and apparently no multilayer formation is observed.

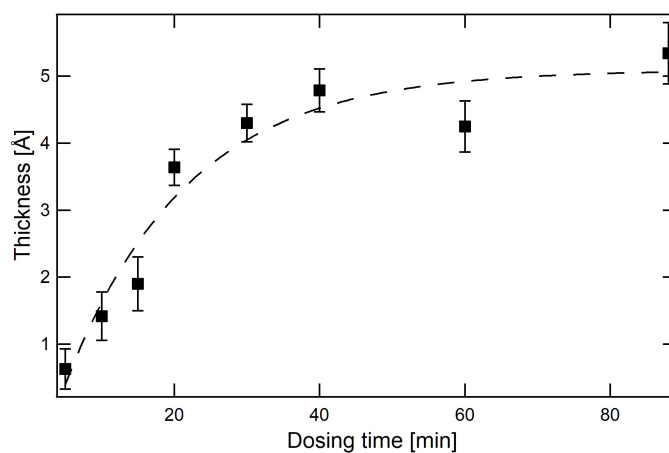


Figure 4.1: RR-TA layer thicknesses as a function of the dosing time, as estimated from the Ti 2p and the C 1s XPS peaks after prolonged analysis times (at least two hours).

To avoid the problem of beam damage, one solution is to limit in time the molecular exposure to the beam. This was done for example in the XPS study of bi-isonicotinic acid on several different substrates, such as TiO<sub>2</sub> and Au(111) [213]. The sample was continuously swept across the beam under the synchrotron radiation, to limit in time the molecular exposure to the beam and no evidence of beam damage was seen in the recorded spectra [215]. When longer acquisition times are required to obtain good spectrum reso-

lution, cooling the sample temperature down to liquid nitrogen may limit the damage.

This was done for the photoemission spectra recorded in the present work in the monolayer regime (chapter 3), where, after dosing RR-TA at room temperature, the sample temperature has been cooled down with liquid nitrogen. XPS spectra recorded at low temperature were then stable even after prolonged exposure times, thus ensuring the integrity of the molecules.

In the multilayer regime presented here, the molecular signal is strong enough that no long analysis times are necessary to obtain a sufficient spectrum resolution. Hence, to avoid molecular desorption rapid XPS scans (less than a minute) were recorded.

## 4.2 Thermal stability of RR-TA on rutile TiO<sub>2</sub>(110)

### 4.2.1 Introduction

The question of RR-TA thermal decomposition mechanism has been addressed for several surfaces, such as Cu [112, 191, 192, 216], Ni [114, 201, 217–219] and Pd [220] and it has been found to strongly depend on the surface structure. On some surfaces, such as Cu(110) [216, 221–223] and Ni(110) [201], TPD experiments have evidenced an explosive decomposition behaviour for RR-TA by tracing the molecular decomposition products H<sub>2</sub>, H<sub>2</sub>O, CO and CO<sub>2</sub>. The term explosive decomposition designates an autocatalytic increase in the reaction rate in thermally induced surface reactions [224]. The desorption of the decomposition products are found to occur in a narrow range of temperature (between 1-5 K) and the reaction rate is found to accelerate with time or extent of the reaction during isothermal heating [222].

However, the same desorption mechanism was not observed on other metal surfaces such as Pd(111) [220] and Ni(111) [114]. Different surface structures, surface roughness, contaminations and experimental conditions (mainly the adsorption temperature) have been proposed as possible explanations for the different observed behaviours [192].

### 4.2.2 Temperature programmed desorption results

In this context, TPD experiments are carried out to gain information on RR-TA thermal stability and decomposition behaviour on TiO<sub>2</sub>(110). Based on the mass spectrum of RR-TA from the NIST database (figure 4.2), the main fragments observed correspond to mass to charge ratios ( $m/z$ ) of 58 (fragment HOC-COH<sup>+</sup>) and 76 (fragment C<sub>2</sub>O<sub>3</sub>H<sub>4</sub><sup>+</sup>) with relative intensities of 40 and 100, respectively. Hence, these fragments of the molecule are tracked in the present TPD experiments. Moreover,  $m/z$  2 (H<sub>2</sub><sup>+</sup>), 18 (H<sub>2</sub>O<sup>+</sup>), 28 (CO<sup>+</sup>) and 44 (CO<sub>2</sub><sup>+</sup>) are also monitored.

TPD spectra are recorded for the clean TiO<sub>2</sub>(110) surface as a blank and following increasing doses of RR-TA at room temperature. The results obtained are displayed in figure 4.3 for  $m/z$  58 (HOC-COH<sup>+</sup>) and 76 (C<sub>2</sub>O<sub>3</sub>H<sub>4</sub><sup>+</sup>) corresponding to the main two fragments ascribed to the molecular form and in figure 4.4 for  $m/z$  2 (H<sub>2</sub><sup>+</sup>), 18 (H<sub>2</sub>O<sup>+</sup>), 28 (CO<sup>+</sup>) and 44 (CO<sub>2</sub><sup>+</sup>). A particular attention has to be paid when considering H<sub>2</sub><sup>+</sup>, H<sub>2</sub>O<sup>+</sup>, CO<sup>+</sup> and CO<sub>2</sub><sup>+</sup> fragments since they usually are the dominant residual gases in UHV chambers and their presence is inevitable when heating something in UHV conditions. To be sure that H<sub>2</sub><sup>+</sup>, H<sub>2</sub>O<sup>+</sup>, CO<sup>+</sup> and CO<sub>2</sub><sup>+</sup> contributions truly arise from RR-TA molecular desorption and not simply due to desorption of common vacuum contaminants, TPD spectra at increasing RR-TA coverage are compared to those recorded on the clean TiO<sub>2</sub> surface.

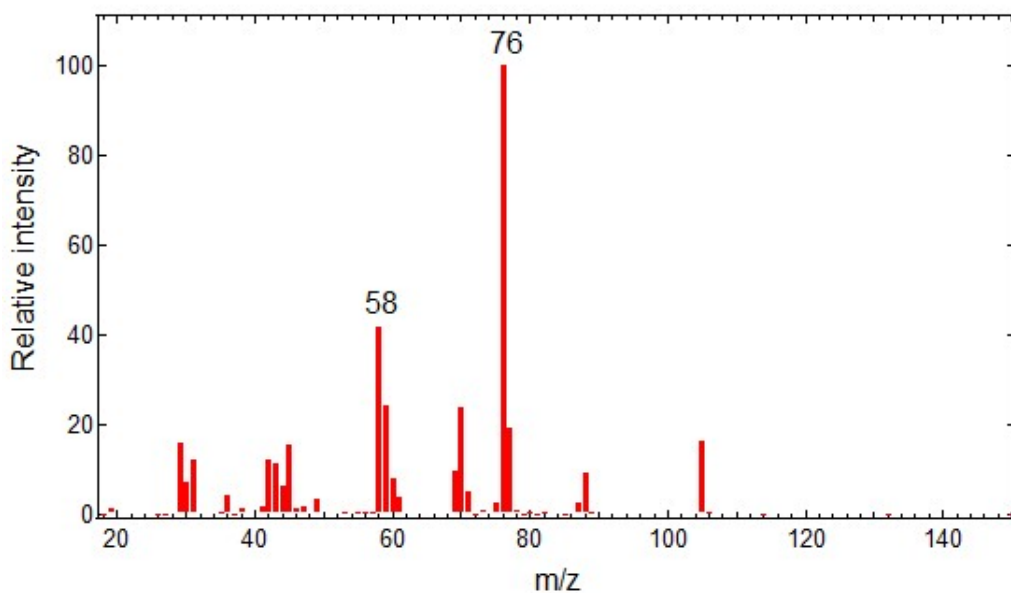


Figure 4.2: Mass spectrum of RR-TA from the NIST database (retraced from [225]).

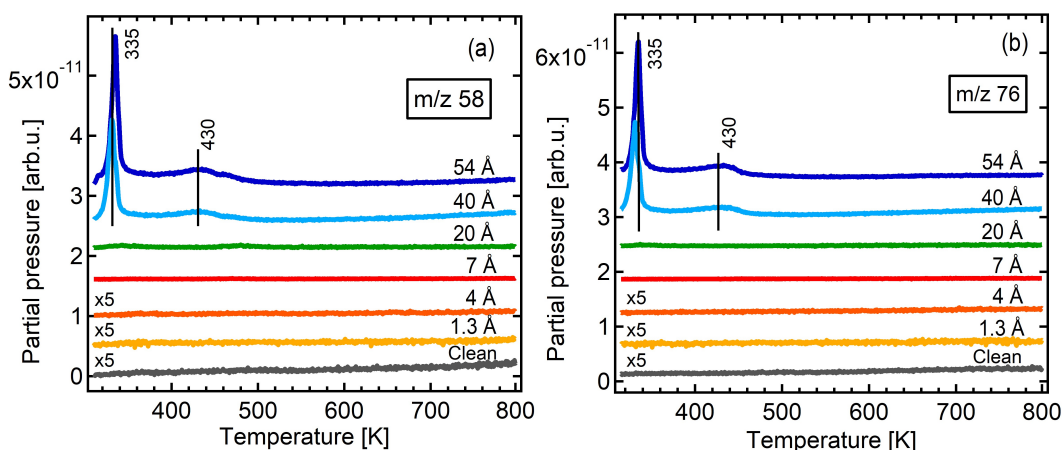


Figure 4.3: TPD spectra of relative  $m/z$  58 and 76 for increasing doses of RR-TA on TiO<sub>2</sub>(110) at room temperature. The recorded spectra are vertically shifted for the sake of clarity. Scale factors are specified near the corresponding spectra.

After RR-TA doses, two main features are identified at about 335-340 K and 430-480 K. The peak at low temperature (335-340 K) appears very intense at high RR-TA doses for  $m/z$  58 and 76 (fig. 4.3), which are specific to RR-TA molecules, and does not saturate as the molecular dose increases. In analogy to previous findings for RR-TA on Cu(531) [192] and on Pd(111) [220], it is thus attributed to multilayer desorption. Desorption of the second molecular layer was found to occur around 330 K on Pd(111), in reasonable agreement with the present work. This peak at 335-340 K is also far weaker for the molecular decomposition fragments  $H_2^+$ ,  $H_2O^+$ ,  $CO^+$  and  $CO_2^+$ , again suggesting intact molecular desorption at low temperature of multilayer TA molecules.

Hence, the desorption peak at higher temperature, between 430 and 480 K, is expected to arise from monolayer desorption. This feature appears much more intense in the  $H_2^+$ ,

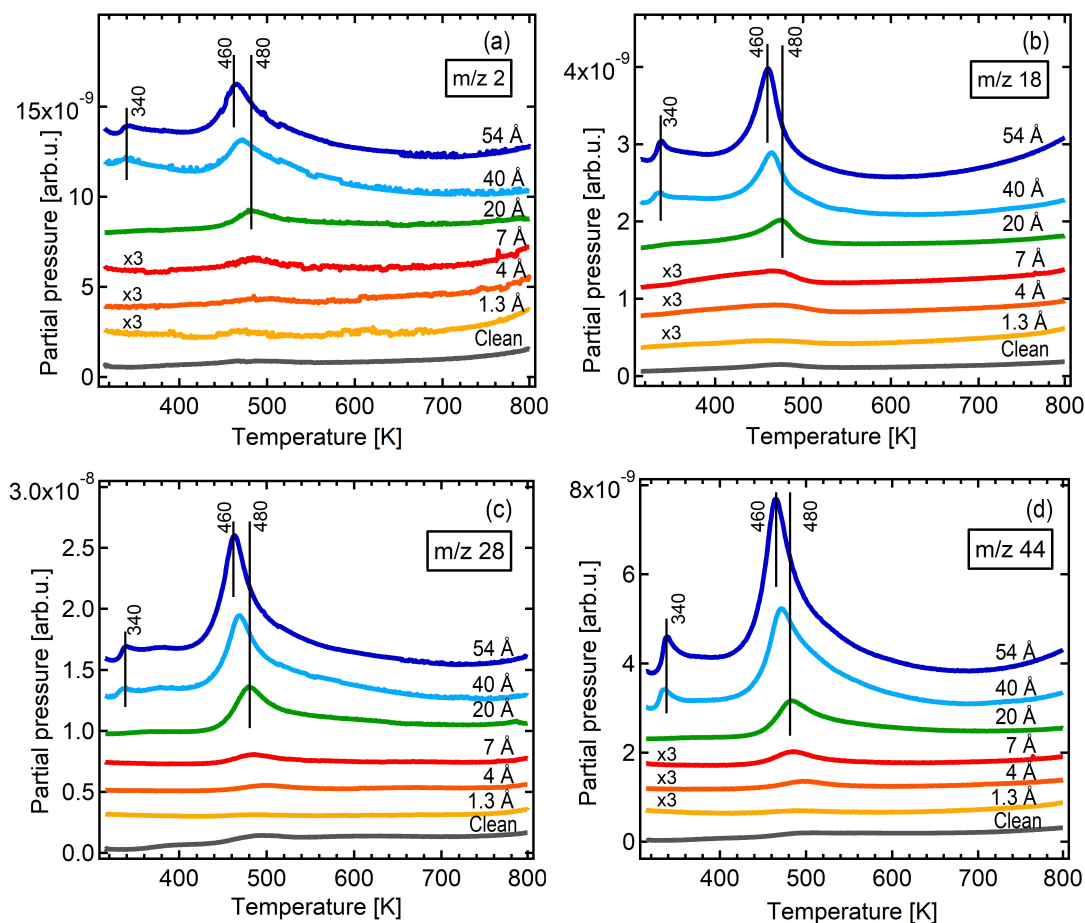


Figure 4.4: TPD spectra of relative  $m/z$  2 ( $\text{H}_2^+$ ), 18 ( $\text{H}_2\text{O}^+$ ), 28 ( $\text{CO}^+$ ) and 44 ( $\text{CO}_2^+$ ) for increasing doses of RR-TA on TiO<sub>2</sub>(110) at room temperature. The recorded spectra are vertically shifted for the sake of clarity. Scale factors are specified near the corresponding spectra.

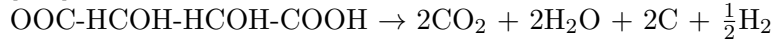
$\text{H}_2\text{O}^+$ ,  $\text{CO}^+$  and  $\text{CO}_2^+$  spectra, and far less for the  $m/z$  specific to the desorption of intact RR-TA molecules. The intensity of this feature does not completely saturate and continues to slightly increase even for the higher doses; this fact may be partially explained by the formation of multilayers before the complete saturation of the first chemisorbed layer, as previously observed in the case of RR-TA on Cu(531) [192] or from an incomplete multilayer desorption at 340 K. Moreover, a shift to lower temperature is observed at increasing molecular doses. The intensity of the desorption features observed in  $\text{H}_2^+$ ,  $\text{H}_2\text{O}^+$ ,  $\text{CO}^+$  and  $\text{CO}_2^+$  spectra increases for increasing RR-TA doses, thus ruling out the attribution of their origin only to desorption of vacuum residuals. Moreover, in the corresponding  $m/z$  58 and 76 spectra, no desorption features are observed between 430 and 480 K for the lowest molecular coverages, confirming that the desorption peak comes from molecular desorption for the highest coverages.

Overall in the multilayer regime, large fragments of RR-TA molecules are detected suggesting desorption of intact molecular RR-TA, while RR-TA decomposes into smaller fragments when desorbed from a monolayer coverage. This observation is indicative of a strong interaction between the molecule and the TiO<sub>2</sub> surface, stronger than the intramolecular bonds. A rough estimate of the desorption temperature can be given by the Readhead

formula, which provides a simple relation between the activation energy  $E_a$  and the temperature of the desorption peak maximum  $T_m$  for a first order and coverage independent desorption [226]:

$$E_a = kT_m \left[ \ln \left( \frac{\nu T_m}{\alpha} \right) - 3.46 \right] \quad (4.1)$$

The error of this estimate is less than 1.5% for  $10^8 < \nu/\alpha < 10^{13} \text{ K}^{-1}$ . Having an estimate of  $\nu$  of  $\sim 10^{13} \text{ s}^{-1}$  in the classical case,  $E_a$  is thus obtained. In the case of a C-C bond (90 kcal/mol), the expected temperature required to break the bond is enormous, *i.e.*  $\sim 1300 \text{ K}$ . The process of RR-TA decomposition is thus probably a two-step process with an adsorbed intermediate. As previously reported, decomposition of RR-TA from the chemisorbed layer has been evidenced on other surfaces, such as Cu(110), Cu(531), Ni(110) and Pd(111), with the main decomposition products being hydrogen, carbon dioxide and water as observed herein and where different decomposition pathways have been proposed [75, 114, 192, 220]. In the case of Cu(110), the following decomposition reaction was suggested [223]:



However, the presence of CO from the TPD cannot be ascribed to CO<sub>2</sub> decomposition in the mass spectrometer. Indeed the relative ion currents for CO<sub>2</sub> are 100 and 13 for  $m/z$  44 and 28 respectively, at an impact energy of 90 eV. In our case the  $m/z$  28 signal is stronger and thus cannot come from CO<sub>2</sub> ionization only. This might be explained by another decomposition pathway, supported by the presence of C ( $\sim 285 \text{ eV}$ ) at the end of TPD experiments, as described later by XPS experiments.

### 4.2.3 Activation energy for RR-TA desorption in the multilayer regime

In the multilayer regime, RR-TA molecules are expected to form H bonds. A good way to verify it is from the estimation of the molecular activation energy from the peaks associated to multilayer desorption. To do so, the more accurate leading edge analysis has been preferred to the Redhead method [51, 52, 227]. We start from the Ansatz of desorption rate of Polanyi and Wigner for the desorption rate (equation 1.30), reminded here:

$$r_d = -\frac{d\Theta}{dt} = \nu(\Theta)\Theta^{n(\Theta)} e^{\left[-\frac{E_a(\Theta)}{k_B T}\right]} \quad (4.2)$$

As previously mentioned, the major difficulty is that the desorption rate constant  $\nu(\Theta)$ , the kinetic desorption order  $n(\Theta)$  and the desorption activation energy  $E_a(\Theta)$  depend on the coverage  $\Theta$ . The problem is overcome by considering the desorption threshold, where the adsorption coverage has not changed significantly yet, so that  $n$  and  $E_a$  can be considered as constants. If the sample is linearly heated and with an efficient differential pumping, the ion current detected (named  $i_d(T)$ ), which is proportional to the partial pressure, is considered to be proportional to  $-\frac{d\Theta}{dt}$ . Equation 4.2 can be thus rearranged as:

$$i_d(T) \propto \left( \int_T^\infty i_d(T') dT' \right)^n e^{\left[-\frac{E_a}{k_B T}\right]} \quad (4.3)$$

Taking the logarithm of equation 4.4, defined as  $I_d(n, T)$ , the previous equation can be linearised as:

$$I_d(n, T) = \ln[i_d(T)] - n \ln \left[ \int_T^\infty i_d(T') dT' \right] = K - \frac{E_a}{k_B T} \quad (4.4)$$

Based on these considerations,  $I_d(n, T)$  should have a linear dependence on  $1/T$  with a slope equal to  $E_a$ . By tracing  $I_d(T)$  vs  $1/T$  for different values of  $n$ , as shown in figure 4.5(a), the best value that linearises the signal at the onset of desorption can be obtained. This analysis is applied here for the highest RR-TA doses (namely 40 Å and 54 Å) and for the multilayer desorption peaks (at 335 K) of  $m/z$  58 and 76, to evaluate the molecular activation energy in the multilayer regime. As shown in figure 4.5, an order  $n = 0$  is found

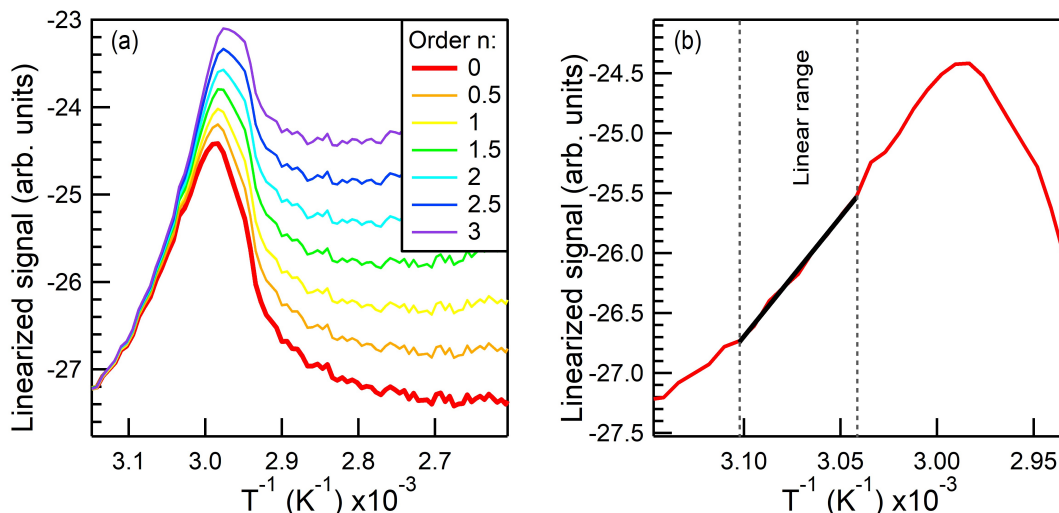


Figure 4.5: (a)  $I_d(n, T)$  linearised spectra plotted for different values of the desorption order  $n$ .  $M/z$  58 for 54 Å of TA have been used here as an example. (b) Zoom on the trace  $I_d(n = 0, T)$ . The linear fit of  $I_d(n = 0, T)$  at the edge of the desorption is represented by a black line.

to linearise at best the signal leading to an activation energy in the range 37 – 39 kcal/mol. The zero order is typical for autocatalytic desorption as in the case of water ice and agrees with a peak shift to higher temperatures with increasing doses (figure 4.3). Assuming that layers of RR-TA molecules are hydrogen bonded through carboxylic dimer rings, a value of 18.5 – 19.5 kcal/mol is found per hydrogen bond, an order of magnitude in agreement with previous findings (14 – 15 kcal/mol) [228].

### 4.3 Chemical nature of RR-TA multilayers on rutile $\text{TiO}_2(110)$

The TPD analysis has shown that RR-TA multilayer formation occurs via H-bond interactions, suggesting that intact biacid molecules form the multilayers. Complementary information on the chemical state of RR-TA molecules in the multilayer regime is here gained by XPS. In this respect, the O 1s and C 1s spectra recorded for multilayer doses of RR-TA are presented in figure 4.6 and compared to the spectra obtained for the clean surface and for a monolayer dose. A saturated monolayer coverage corresponds to an equivalent film thickness of about 6 – 7 Å. Moreover, the spectra recorded after a typical TPD experiment are also presented. The corresponding fit parameters are summarised in table 4.1 and 4.2. The fit performed is based on the previous considerations for RR-TA adsorption on rutile in the monolayer regime presented in chapter 3, where monotartrate molecules are observed. As reported in chapter 3, the O 1s region of the clean rutile surface displays two contributions A and B, attributed to the  $\text{TiO}_2$  O lattice atoms and the surface hydroxyl groups, respectively. Following RR-TA deposition, three molecu-



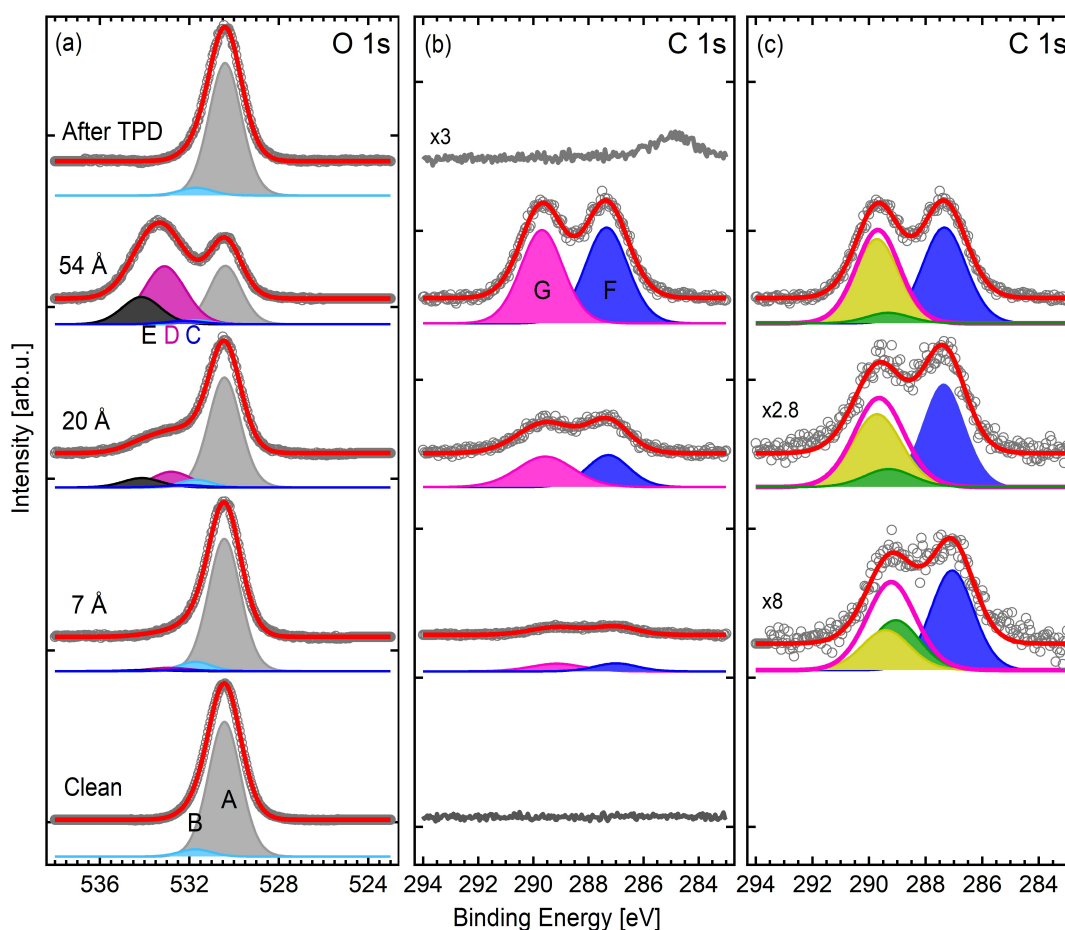


Figure 4.6: Evolution of O 1s (a) and C 1s (b) peaks for RR-TA increasing doses on the rutile  $\text{TiO}_2(110)$  surface and after a TPD experiment; (c) same as (b) where the  $\text{COO}^-$  and  $\text{COOH}$  contribution are represented by the green and the yellow peaks, respectively. Spectra are recorded using a non-monochromatic dual anode Al/Mg  $K\alpha$  X-ray source ( $h\nu = 1486.6$  eV). Spectra are vertically shifted for sake of clarity and normalized to the peak height. Raw data and fitted component sums are represented by grey dots and a red line, respectively. The peak fitting attribution is detailed in the text.

lar contributions are identified, C, D and E. Component C is related to the carboxylate functionality  $\text{COO}^-$ , D to a superposition of  $\text{COOH}$  and  $\text{C-OH}$ , while E to the  $\text{COOH}$  contribution. To substantiate this decomposition, the fit of the spectra is first performed on the highest coverage spectrum ( $54 \text{ \AA}$ ), where the molecular contributions prevail over the  $\text{TiO}_2$  substrate ones. The full-width at half-maximum (FWHM) and the peak binding energies determined are then kept fixed to fit the lower RR-TA dose spectra, where the presence of RR-TA results only in O 1s peak shouldering at high binding energies. Some constraints on the peak areas are also used; for a  $7 \text{ \AA}$  layer, close to the monolayer saturation, the analysis is consistent with a majority presence of monotartrate species. As the RR-TA dose increases, the intensities of peaks D and E, predominantly associated to the presence of protonated  $\text{COOH}$  groups, largely increases, suggesting the presence of fully protonated RR-TA molecules in the stacking of multilayers. Finally, following TPD, the O 1s spectrum recovers its initial line shape.

As shown in chapter 3, for the C 1s region two contributions are identified at  $\sim 287$  and

Table 4.1: O 1s peak parameters (binding energy (BE) and relative area (RA), respectively) used for the fit presented in figure 4.6. For components A and B the FWHM is 1.7 eV, while for peak C, D and E the FWHM is 2.0 eV. Error bars on BE are of the order of 0.1 eV.

Dose	<b>A</b> O <sub>lat</sub>		<b>B</b> OH		<b>C</b> COO <sup>-</sup>		<b>D</b> COOH, C-OH		<b>E</b> COOH	
	BE[eV]	RA %	BE[eV]	RA %	BE[eV]	RA %	BE[eV]	RA %	BE[eV]	RA %
Clean	530.4	94.9 ± 0.2	531.7	5.1 ± 0.2						
7Å	530.4	89.0 ± 0.6	531.7	5.7 ± 0.1	532.3	1.7 ± 0.1	532.9	2.7 ± 0.4	533.9	0.9 ± 0.2
20Å	530.4	73.1 ± 3.5	531.7	5.1 ± 0.3	532.2	1.8 ± 0.3	532.9	12.5 ± 1.9	534.1	7.5 ± 2.5
54Å	530.4	33.6 ± 1.8	531.7	2.4 ± 1.9	532.3	3.4 ± 2.4	533.1	40.6 ± 3.4	533.9	20.2 ± 2.9
After TPD	530.4	94.4 ± 2.1	531.7	5.6 ± 2.1						

Table 4.2: C 1s peak parameters (binding energy BE [eV], FWHM [eV] and relative area RA, respectively) used for the spectra presented in figure 4.6. The binding energy difference between peaks B and A,  $\Delta(B - A)$  [eV], is also reported. Error bars on BE are of the order of 0.1 eV.

Dose	<b>F</b> C-OH			<b>G</b> COO <sup>-</sup> , COOH			$\Delta$ F-G (COO <sup>-</sup> , COOH) - (C-OH)
	BE [eV]	FWHM [eV]	RA %	BE [eV]	FWHM [eV]	RA %	
Clean	0			0			0
7Å	287.1	1.8	50.0 ± 9.0	289.2	2.1	50.0 ± 9.0	2.1
20Å	287.4	1.8	50.0 ± 7.0	289.6	2.1	50.0 ± 7.0	2.2
54Å	287.3	1.8	50.0 ± 7.0	289.7	1.8	50.0 ± 7.0	2.4

~ 289 eV. The low binding energy peak (herein named F) was attributed to the central C-OH carbon atoms, while the one at higher BE (herein named G) to a superposition of COO<sup>-</sup> and COOH groups. Despite the superposition of COO<sup>-</sup> and COOH contributions on TiO<sub>2</sub>(110), information on the evolution of RR-TA chemical form may still be gained by considering the energy splitting between peaks F and G and the relative variation of their FWHM. Some constraints are used for the fit, namely the intensity ratio F/G=1, according to the molecular stoichiometry, and the FWHM of peak F, since no variation is expected for this peak which is related to the central C-OH carbon atoms.

The fit is first performed for the highest coverage of 54 Å, where the two peaks F and G are clearly discerned, to estimate the width of peak F and to use it for the fit of the lower coverage spectra. In the multilayer regime, upon increasing RR-TA doses, the energy splitting between G and F increases progressively from 2.1 eV to 2.4 eV. For the highest RR-TA dose, peak G is found at 289.7 eV, in agreement with what was found for the carboxylic contribution of monotartrate RR-TA molecules on Cu(110) in section 3.2.2. At the same time, the width of the high binding energy peak reduces by 0.2 eV. These considerations overall suggest the prevalence of one species (COO<sup>-</sup> vs. COOH) over the other, and more precisely, the dominant contribution of carboxylic acid groups, as expected in the formation of multilayers of fully protonated RR-TA molecules. This conclusion matches what is observed for other carboxyl-containing molecules on the same rutile surface [194] and on other metallic surfaces [229, 230]. To evidence the increasing contribution of the carboxylic component over the carboxylate one, two components are discerned in peak G (figure 4.6(c)). In the decomposition proposed the area ratio between COO<sup>-</sup> and COOH peaks is fixed to the one obtained from the O 1s analysis. It is clear how at coverages near the first layer saturation, the COO<sup>-</sup> and COOH components are almost

equivalent, while at increasing doses the  $\text{COOH}$  prevails, as expected in non-deprotonated RR-TA multilayers. At last, a graphitic-like C 1s component at 285 eV (figure 4.6(b)) remains at the surface after the thermal decomposition of the molecule.

#### 4.4 Conclusion

The investigation of RR-TA adsorption on rutile TiO<sub>2</sub>(110) was further extended here to the multilayer regime. The questions of desorption and decomposition behaviour of RR-TA molecules have been addressed by TPD, while XPS mainly helped to decipher the molecular chemical state. It was shown that while molecules desorb more or less intact from the multilayer, they decompose in the monolayer regime, which points at a strong interaction with the oxide substrate. From the analysis of the XPS O 1s region in the multilayer regime, a dominant contribution of carboxylic acid groups was evidenced. At the same time, in the C 1s region, an increase of the energy splitting between the two molecular peaks was observed at increasing molecular coverage, accompanied by a reduction of the high BE peak width. Overall, these observations pinpointed a majority presence of intact bi-acid molecules upon TA deposition onto the first monolayer. The dominant presence of non-deprotonated molecules in the multilayer regime suggests that the carboxylate species up to 1 ML adsorbed at the TiO<sub>2</sub>(110) surface leave one carboxylic group available at the surface, which favours the formation of molecular multilayers via H-bond interactions, as observed in previous studies for other carboxylic acid molecules [194,212]. The estimation of the multilayer desorption activation energy further confirmed this point, since the values obtained were in good agreement with typical values found in literature for hydrogen-bonded molecules.

# CHAPTER 5

---

## Ni adsorption on TiO<sub>2</sub>(110)

---

This chapter deals with Ni deposition on the TiO<sub>2</sub>(110) surface as a function of Ni coverage. The question of Ni morphology in the first stages of growth is tackled through Scanning Tunnelling Microscopy (STM) imaging and information on the cluster size and density is gained. X-ray Photoemission Spectroscopy (XPS) analysis performed in parallel allows to gain insight into the chemical nature of Ni clusters and possible charge transfer between Ni and TiO<sub>2</sub>. Information on the cluster shape is possible through modelling of the XPS core level peak intensities. Two models are compared, which describe flat and hemisphere clusters. Being sensitive to changes in the cluster morphology, Surface Differential Reflectivity Spectroscopy (SDRS) is then used to probe the evolution of Ni cluster aspect ratio through the plasmonic response up to thicknesses of 10 ML. The different growth phases are followed through the integrated SDRS signals in s-polarisation. This analysis further allows to gain insight into a possible anisotropic growth of Ni clusters due to the easiest diffusion in the [001] substrate direction with respect to the [1 $\bar{1}$ 0].

*Ce chapitre traite des dépôts de Ni sur une surface de rutile TiO<sub>2</sub>(110) en fonction du taux de couverture. La question de la morphologie des nanoparticules de Ni lors des premiers stades de la croissance est abordée à travers la microscopie à effet tunnel (STM), permettant d'obtenir des informations sur la taille et la densité des particules. Les analyses en photoémission X (XPS) réalisées en parallèle permettent de mieux comprendre la nature chimique des particules de Ni et le possible transfert de charge entre Ni et TiO<sub>2</sub>. Des informations sur la morphologie des particules sont obtenues grâce à la modélisation des intensités en XPS. Deux modèles sont ici comparés, décrivant des nanoparticules plates ou hémisphériques. Étant sensible aux modifications de la morphologie des nanoparticules, la technique de réflectivité différentielle de surface (SDRS) est ensuite utilisée pour sonder l'évolution du rapport d'aspect par le biais de leur réponse plasmonique jusqu'à une épaisseur de 10 ML. L'apparition des stades successifs de croissance du film est suivie par l'examen des signaux SDRS intégrés, en polarisation s. Cette analyse permet également de mieux comprendre la possible croissance anisotrope des nanoparticules de Ni en raison de la diffusion plus facile dans la direction du substrat [001] par rapport à la [1 $\bar{1}$ 0].*

## 5.1 Morphologic study of Ni clusters

### 5.1.1 Technical aspects of Ni cluster size measurement

STM images are recorded to gain information on Ni cluster size and geometry. Different sample regions are recorded for the analysis, which are averaged over all the analysed images. STM data are analysed using the Gwyddion software [231]. To obtain good statistics of the cluster properties, at least 300 clusters are considered in the analysis for each Ni coverage investigated. Firstly, a mean plane subtraction is performed and the substrate surface is put to zero height. Secondly, to select Ni clusters both a grain marking function based on height thresholding and manual selection are used. Then, the number of Ni clusters and their sizes are obtained using specific functions provided by the software. To estimate the radii, a mean radius is calculated for each selected cluster. Histograms of cluster radii and heights are reported and the average values are obtained by fitting the histograms with Gaussian functions. The error bar is defined from the relative standard deviation.

### 5.1.2 Ni cluster growth

STM images recorded for different coverages of Ni deposited at room temperature on TiO<sub>2</sub>(110) are presented in figure 5.1. Ni coverage is given in units of equivalent monolayer, where one monolayer (1 ML) is defined as  $1.6 \times 10^{15}$  atoms/cm<sup>2</sup>, *i.e.* the Ni(111) packing density [165,180,181]. Looking at figure 5.1, a considerable fraction of Ni clusters are located on TiO<sub>2</sub> terraces. The presence of large TiO<sub>2</sub> terraces increases the probability of collision between Ni adatoms and thus nucleation on terraces. Moreover, some Ni clusters straddle the substrate step edges, which probably arises from the formation of these clusters from diffusion of metal adatoms both from the upper and lower terraces. The same tendency was reported in previous studies, such as for Cu islands on TiO<sub>2</sub> (110) [232]. Histograms of heights and radii are reported as well in figure 5.1 for the corresponding Ni coverage investigated. The average height, radius and cluster density values are reported in figure 5.2 as a function of Ni coverage. At the lowest Ni coverage, Ni clusters measure on average  $(5.7 \pm 1.5)$  Å in height and  $(9.7 \pm 3.0)$  Å in radius. Assuming a Ni atomic diameter equal to  $\sim 2.5$  Å [175], clusters are therefore initially on average two atomic layers high. As the coverage increases, the average height and radius slightly increase reaching  $\sim 8.5$  Å and 13 Å at 0.3 ML, suggesting the formation of more 3D clusters. Looking at the histograms of figure 5.2, the radius distribution slightly seems to broaden as the coverage increases. This can be explained on the bases that at increasing coverage Ni atom arrival cause either the existing Ni clusters to grow larger or an increase in density.

The cluster dimensions found in this work are thus globally in line with those reported in previous works, in which the average values of radius cluster range between 10 and 25 Å for Ni coverages up to 1 ML [169,175,177]. For example, Fujikawa determined average cluster radii of about 9 Å and heights of 4 Å, which increased to 10 Å and 7 Å at about 0.2 ML, respectively.

The cluster density slightly increases over the considered Ni coverages, reaching  $4.3 \times 10^{12}$  clusters/cm<sup>2</sup>. Such values are globally in accord with what was reported in previous studies, where cluster density values were around  $3 \times 10^{12}$  clusters/cm<sup>2</sup> [175].

When Ni cluster sizes are estimated from STM imaging, the values obtained are known to be considerably affected and overestimated by STM tip convolution effects, more importantly for the radii than the heights. Cluster heights more than their radii have to be retained as indication of the cluster size and for this reason, in the following, only

the height values will be used and compared to the cluster analysis performed with other techniques. Nevertheless, the radius values remain important to give a trend of the Ni cluster size evolution, thus allowing at least a qualitative track of the cluster growth for increasing doses.

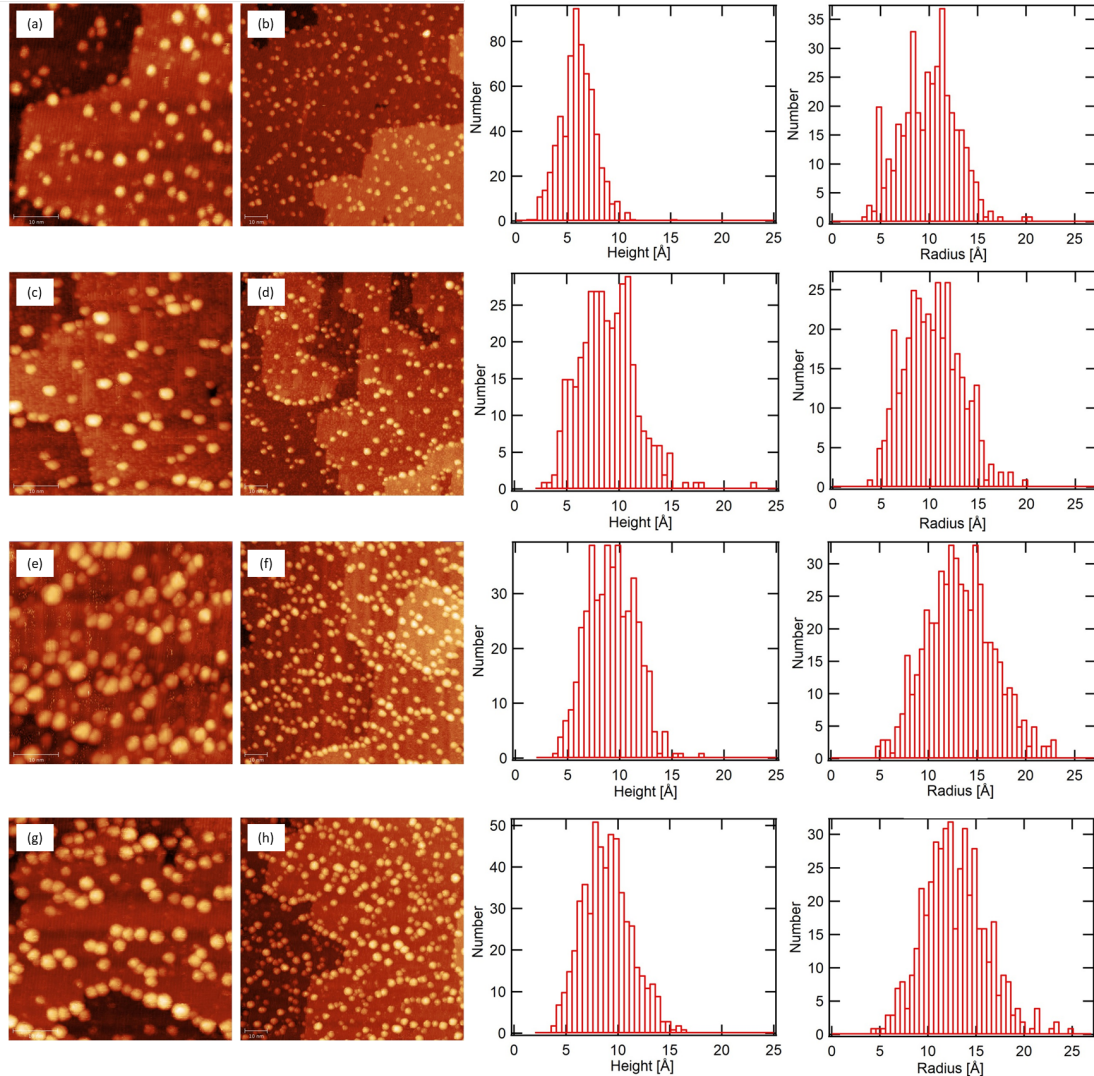


Figure 5.1: Left: STM images recorded at increasing Ni coverage on rutile TiO<sub>2</sub>(110). (a) and (b): 0.06 ML; (c) and (d): 0.1 ML; (e) and (f): 0.2 ML; (g) and (h): 0.3 ML. Dimensions of STM images are 50 nm × 50 nm for images (a), (c), (e) and (g), while 100 nm × 100 nm for images (b), (d), (f) and (h). The Ni evaporation parameters used are: filament current  $I_{fil} = 1.8$  A, emission current  $I_{em} = 22$  mA, flux  $\Phi = 20$  nA. Right: Corresponding height and radius histograms.

## 5.2 XPS analysis of Ni cluster growth

### 5.2.1 Chemical analysis

In parallel to the morphologic study, XPS spectra are recorded for increasing Ni coverage. A typical survey spectrum following Ni deposition on the clean rutile TiO<sub>2</sub>(110) surface using a non-monochromatised Al K $\alpha$  source is shown in figure 5.3. In addition to all the

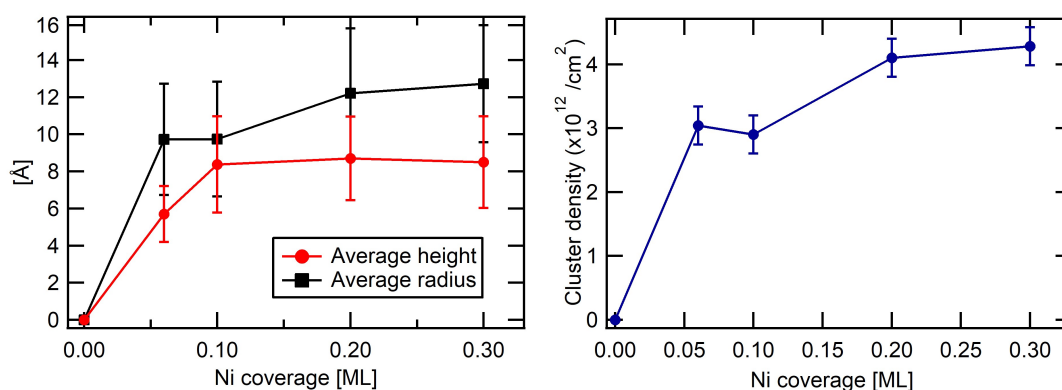


Figure 5.2: Left: average height and radius trend of Ni clusters on rutile TiO<sub>2</sub>(110) for increasing Ni coverage. Right: average cluster density for increasing Ni coverage.

peaks specific to the TiO<sub>2</sub> surface (detailed in section 1.3.3), the survey spectrum features the characteristic peaks of Ni, whose binding energy values are reported in table 5.1. The most intense ones, namely the Ni 2p core level and the Ni LMM Auger line, are evidenced in figure 5.3. No presence of carbon contamination appears after Ni dosing at the XPS sensitivity (a few % of monolayer). For the record, the Al K $\alpha$  source has been chosen since using a Mg K $\alpha$  source leads to a superposition between the Ni LMM Auger peaks ( $\sim 390$ - $550$  eV) with the Ti 2p ( $\sim 459$  eV) and O 1s ( $\sim 531$  eV) core level peaks, thus preventing the analysis.

Ti 2p and O 1s peaks are systematically recorded as reference for the TiO<sub>2</sub> substrate, while

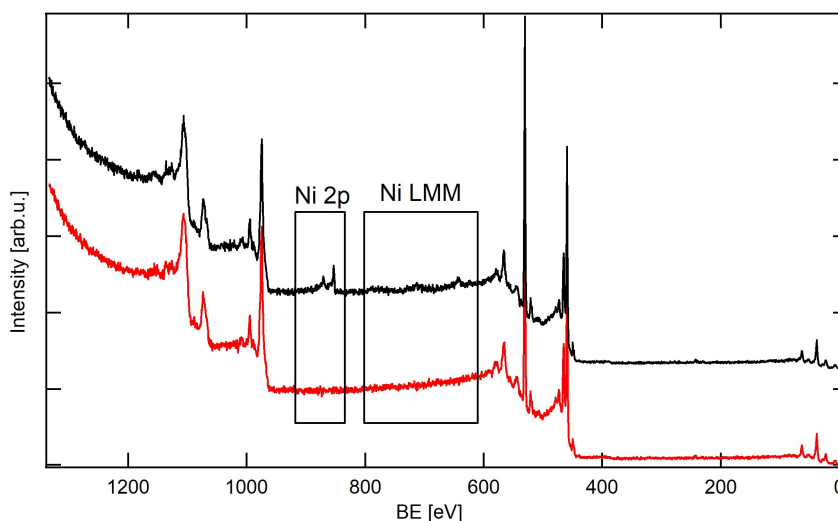


Figure 5.3: Survey spectra (pass energy = 50 eV) recorded on the clean rutile TiO<sub>2</sub>(110) surface (in red) and after a Ni dose (in black thickness = 0.3 ML) using a non-monochromatised Al K $\alpha$  source. The most intense Ni peaks are evidenced. Spectra are vertically shifted for clarity.

Table 5.1: Ni XPS core level peak positions [eV].

2s	2p <sub>1/2</sub>	2p <sub>3/2</sub>	3s	3p
1009	870	853	111	67

Ni 2p is measured for the adsorbate. Figure 5.4(a) displays the Ni 2p region for increasing Ni coverage. Ni 2p<sub>1/2</sub> and Ni 2p<sub>3/2</sub> appear at 869.8 and 852.5 eV for the thickest deposit probed. The spectrum has a complex structure, with large shoulders appearing at around 858.2 eV and 875.4 eV. Overall, the Ni 2p region presents some metallic features: the spin orbit splitting between Ni 2p<sub>3/2</sub> and Ni 2p<sub>1/2</sub> (17.2 eV) and the satellite structure at around 858.2 eV are indeed in accord with what is expected for metallic Ni [233]. This suggests that Ni clusters are mainly deposited in the metallic form. For comparison, the Ni 2p spectrum of a Ni(111) single crystal is shown in figure 5.4(b). The main Ni 2p<sub>3/2</sub> line

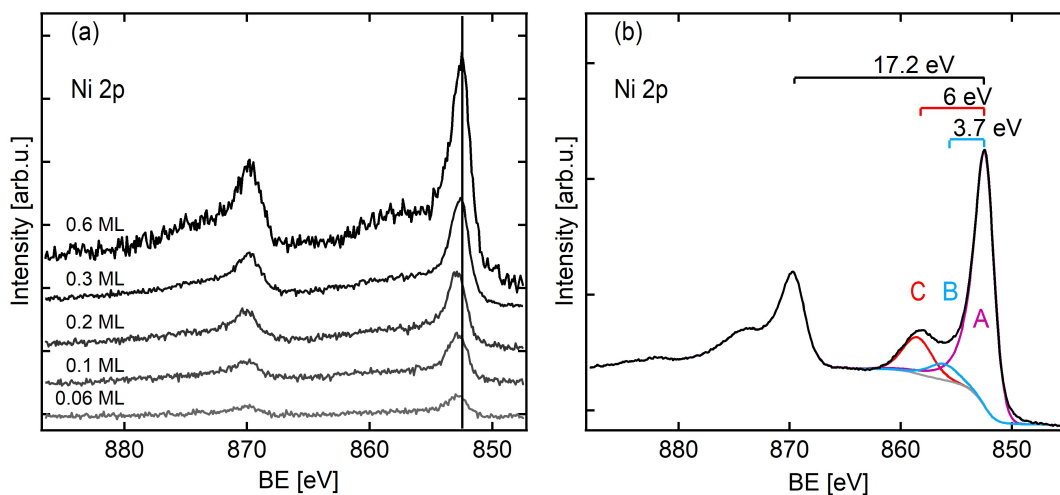


Figure 5.4: (a) Evolution of the Ni 2p peak at increasing Ni dosing on TiO<sub>2</sub> (110). To allow a direct comparison of the peak intensities, spectra are normalised to the background intensity at the low BE side of the peak. (b) Ni 2p spectrum of a Ni(111) single crystal. The fit proposed is taken from ref. [234, 235]. The attribution of components A, B and C is detailed in the text.

is located at 852.6 eV (peak A), in accord with the value reported in literature ( $852.7 \pm 0.4$  eV) [235]. The satellite appearing at around 6 eV above the main Ni 2p contribution has been previously assigned to plasmon losses [234, 235]. A fit was also proposed and reported here for Ni 2p<sub>3/2</sub>. The broad shoulder is fitted by two contributions (peaks B and C) set at 3.7 and 6 eV above the main line, which do not mean to represent specific processes, but rather a combination of shake up and plasmon losses, as reported in ref. [234]. The parameters used for the fit are taken from ref. [234, 235]. Overall, the main metallic character of Ni clusters was also evidenced in previous studies in which, following deposition in UHV, Ni does not react with the TiO<sub>2</sub> substrate forming metallic clusters [169, 171, 236]. With increasing Ni dosing, although moderate, a shift of the spectrum positions towards lower binding energies is remarked. A combination of different effects may affect the binding energy position of metallic clusters and its origin for Ni clusters deposited on TiO<sub>2</sub> (110) has been previously discussed [237]. A possible interfacial reaction between Ni and the oxide support, *i.e.* Ni oxidation at the interface, was excluded as the main reason for the energy shift. Since the heat of formation at room temperature for TiO<sub>2</sub> ( $-472$  kJ/mol<sup>-1</sup>) is higher compared to NiO ( $-240.6$  kJ/mol<sup>-1</sup>), the observed energy shifts were thus mainly attributed to cluster size effects. In small clusters, contributions to the binding energy shift have been observed from both initial and final state effects due to the photoemission process [179, 237]. Among initial state effects, both the interaction with the substrate and surface core level shifts have been found to play an important role. For the record, surface core level shifts are related to the lower coordination number of sur-



face atoms, compared to the those in the bulk. Generally, a decrease in the coordination number goes with a decrease in the binding energy of surface atoms. Due to the high ratio of surface atoms in nanometric clusters, their binding energy values are normally reduced with respect to the bulk samples. Moreover, a charge transfer of 0.1 eV from Ni to TiO<sub>2</sub> has been calculated for small Ni clusters. On the opposite, final state effects are due to the lower core hole screening felt by metallic clusters compared to bulk samples after the photoemission process and they shift the binding energy towards higher values. As the cluster size decreases, initial state effects lower Ni 2p binding energy, while the final ones tend to increase it.

Moreover, as the Ni cluster character becomes more bulk like, Ni 2p peaks narrow. One possible reason is related to the shortened corehole lifetime in small clusters which arises from faster relaxation, thus resulting in broader peaks [237,238]. Another reason is that for broad size distributions of small clusters, initial and final state effects have a different impact on clusters depending on their size, thus enlarging XPS peaks [237,238].

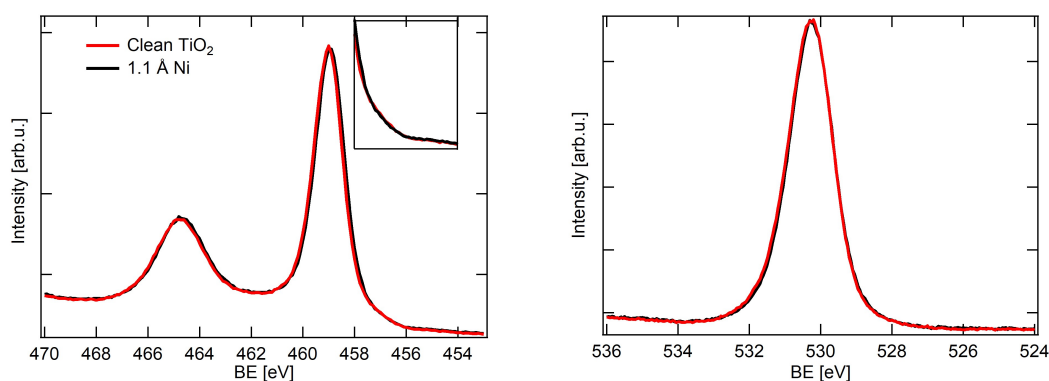


Figure 5.5: Comparison between Ti 2p (left) and O 1s (right) spectra for the clean rutile TiO<sub>2</sub>(110) in red and after a Ni dose of 1.1 Å in black. To allow a direct comparison of the spectral shapes, peaks are normalised to the maximum.

Looking at the O 1s and Ti 2p regions, no changes in the spectrum shapes and no sizeable core level shift are observed here at these coverages. This confirms that Ti is not reduced upon Ni dosing [171,181]. Conversely, other studies have evidenced a reduction of Ti<sup>4+</sup> to Ti<sup>3+</sup> and even Ti<sup>2+</sup> upon Ni deposition at room temperature. When considering such apparent conflicting results, one aspect has to be considered. In all these works, Ni evaporation has been performed using an evaporator, which works by electron bombardment of the evaporant. A fraction of the evaporant is thus always ionised and while the majority of the ions goes to the flux monitor electrode, a part of them may reach the sample. This induces defects on the substrate surface and thus plays a role in the sample reduction. To eliminate this problem, an upgrade of the evaporator is available, which is provided with a suppressor electrode. In the present study, very low fluxes are used for Ni depositions investigated in STM images, so that sample reduction does not occur, as confirmed by the absence of variation of the Ti<sup>3+</sup> component in the Ti 2p spectrum. However, we will come back to this issue later in this chapter, when presenting the SDRS measurements, where sample bombardment effects are remarked, since higher fluxes are used to be able to probe a wide range of Ni coverages.

### 5.2.2 XPS modelling of Ni clusters

Depending on the experimental conditions used, Ni clusters have been found to grow both as hemisphere or flat clusters in the first stages of growth [121]. The STM images recorded here suggests that Ni clusters initially are two atomic layers high, while at increasing coverage a 3D growth is more pronounced, in accord with the work of Fujikawa [175]. Some information on the cluster size and shape may be gathered also from the XPS analysis and more specifically from the intensity ratio of substrate to adsorbate signals. For this reason, two geometries are used here to model the cluster shape in the first stages of growth: pancake and hemisphere models, schematically sketched in figure 5.6. The main

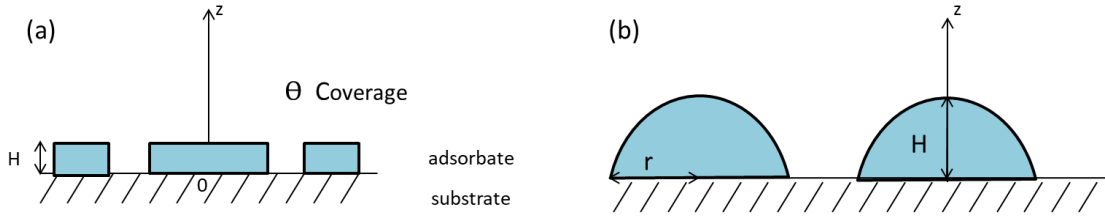


Figure 5.6: Schematic representation of the (a) pancake and (b) hemisphere geometries used to model the Ni cluster shapes from the XPS analysis.

assumption in the calculations for both models is the homogeneous height distribution of the clusters. In the pancake model, flat clusters of constant thickness  $H$  have a partial surface coverage  $\Theta$  over the substrate surface (total thickness  $\Theta H$ ). In the hemisphere model, hemispheres of height  $H = R$  which cover a fraction  $\Theta$  of the substrate surface are considered. The substrate and adsorbate intensities are derived by integrating equation 1.10 and their ratios are equal to:

$$\frac{I_s}{I_a} = \frac{n_s T_s \sigma_s \lambda_{ss}}{n_a T_a \sigma_a \lambda_{aa}} \frac{\Theta \exp(-H/\lambda_{sa}) + 1 - \Theta}{\Theta [1 - \exp(-H/\lambda_{aa})]} \quad (5.1)$$

in the pancake model, and

$$\frac{I_s}{I_a} = \frac{n_s T_s \sigma_s \lambda_{ss}}{n_a T_a \sigma_a \lambda_{aa}} \frac{1 - \Theta + \Theta \frac{2\lambda_{sa}^2}{H^2} [1 - (1 + \frac{H}{\lambda_{sa}}) \exp(-H/\lambda_{sa})]}{\Theta [1 - 2\frac{\lambda_{aa}^2}{H^2} + 2\frac{\lambda_{aa}(H+\lambda_{aa})}{H^2} \exp(-H/\lambda_{aa})]} \quad (5.2)$$

in the hemisphere model. In equations 5.1 and 5.2, the substrate is denoted “s”, while the adsorbate is denoted “a”. Definitions of the quantities used were given in section 1.3.4.2. Knowing the coverage  $\Theta$ , it is possible to solve equations 5.1 and 5.2 by dichotomy to obtain the height  $H$  in both models. The coverage  $\Theta$  can be estimated here only from the STM images. However, since the cluster radius is known to be overestimated due to tip convolution effects, the Ni surface coverage from the STM images will be overestimated as well. To obtain a more realistic value, which is necessary in the XPS modelling, a correction factor needs to be estimated. Such a correction factor is determined by the comparison between the overestimated total Ni quantity deposited derived from STM images and the “true” value estimated by XPS (table 5.2). In details, on one side, the equivalent total Ni quantity is calculated from the cluster volumes and densities measured from the STM images assuming a truncated sphere shape. On the other side, it is estimated from the XPS analysis within the continuous film hypothesis. From the XPS equivalent total thickness

it is possible to obtain a corrected value of the radius (hereafter named  $R_{\text{corr}}$ ), assuming truncated sphere nanoparticles with heights corresponding to the ones measured directly from STM ( $H_{\text{STM}}$ ). From  $R_{\text{corr}}$ , a corrected Ni coverage ( $\Theta_{\text{corr}}$ ) is then obtained and compared to the experimental ones from the STM analysis ( $\Theta_{\text{STM}}$ ).

Table 5.2: Comparison between the radius and coverage values estimated from XPS and from the STM images for increasing Ni coverage on TiO<sub>2</sub>(110).

Total thickness (XPS) [ML]	$H_{\text{STM}}$ [Å]	$R_{\text{STM}}$ [Å]	$R_{\text{corr}}$ [Å]	$\Theta_{\text{STM}}$ [%]	$\Theta_{\text{corr}}$ [%]
0.06	5.7	10.0	5.2	12.0	3
0.1	8.3	9.6	5.8	12.6	5
0.2	8.7	12.1	7.0	23.5	8
0.3	8.5	12.6	7.9	28.0	12

One first conclusion can be drawn by comparing the  $R_{\text{corr}}$  values with the mean heights obtained by STM and reported in figure 5.2. At increasing Ni coverage, the mean height values ( $\sim 8$  Å at 0.2 and 0.3 ML of Ni) approach the radius ones ( $\sim 7$  and 8 Å at 0.2 and 0.3 ML of Ni, respectively), which suggests the formation of more hemispheric clusters. As for the XPS modelling, in figure 5.7 the experimental height values from STM are compared to those obtained from the XPS modelling using pancake and hemisphere shapes by solving equations 5.1 and 5.2. Although the average experimental values seem to better agree with those obtained using the hemisphere model, differences are not so marked and remain within the error bar of both models. This is probably due to the major simplifications used in the analysis. One of the major approximations used in the model which surely affects the results is that we suppose Ni clusters to have the same size all over the surface, which is not the case as seen in the STM images. Therefore, modelling from the XPS analysis is not a suitable replacement. More convincing results and a better discrimination between different cluster shapes would probably be obtained for more homogeneous cluster size distributions. Information on cluster shapes is thus acquired by SDRS.

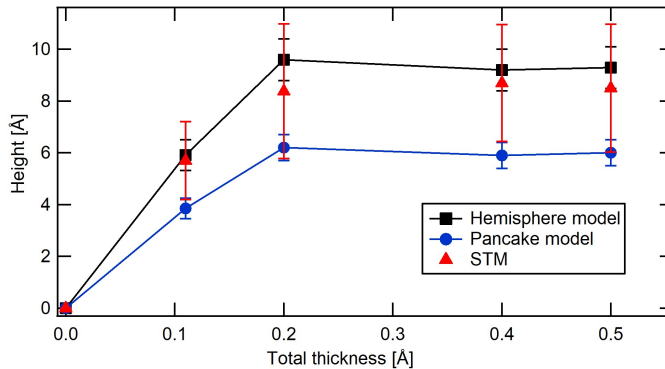


Figure 5.7: Comparison between the average cluster height from the STM images and those obtained using pancake and hemisphere models.

### 5.3 Morphology of Ni clusters as seen by differential reflectivity

SDRS is a well suited technique for the study of metal growth on oxide substrates, since it allows a real-time and *in-situ* characterisation. Moreover, an easy monitoring of metal growth over a large range of coverages is possible, which is instead more demanding and time-consuming by means of microscopic techniques. In the following, before presenting the results obtained on Ni growth on rutile TiO<sub>2</sub>(110), a quick overview of the main theory behind the technique is reported.

#### 5.3.1 Theory behind SDRS

The Bedeaux-Vlioger model, developed since the 1970s by D. Bedeaux and J. Vlioger, describes the optical behaviour of a boundary layer (such as thin film islands and rough surfaces) growing between two homogeneous bulk media with dielectric functions  $\epsilon_1$  and  $\epsilon_2$ , based on the concept of excess fields [239–244]. The excess fields are defined as the difference between the real fields in the presence of the interfacial perturbation and those of the bulk regions extrapolated to the surface. For example, if the electric field is considered, the excess field is defined as:

$$\mathbf{E}_{ex}(\mathbf{r}, t) = \mathbf{E}(\mathbf{r}, t) - \mathbf{E}_1(\mathbf{r}, t)\theta(z) - \mathbf{E}_2(\mathbf{r}, t)\theta(z) \quad (5.3)$$

where  $\theta(z)$  is the Heaviside function ( $\theta(z) = 1$  for  $z > 0$  and  $\theta(z) = 0$  for  $z < 0$ ) and the subscripts 1 and 2 refer to the ambient medium (often vacuum) and the substrate, respectively [245]. The introduction of the excess field notion avoids the detailed knowledge of the surface structure, since all the main physical quantities turn out to be independent from it [246]. The main restriction used in the model is that the geometrical parameters of the interfacial layer (such as the layer thickness, nanoparticle size and spacing, etc.) are small compared to the wavelength of the incident light. Maxwell's equations are then rewritten in terms of excess fields and boundary conditions at the surface are expressed in terms of excess field integrals in the direction perpendicular to the surface. The integrated excess fields are linked to a first order to the bulk electric fields extrapolated to the surface by two coefficients  $\gamma$  and  $\beta$ , respectively [245].  $\gamma$  and  $\beta$  are called interfacial susceptibilities and they describe the optical response of the considered surface. They have the meaning of dielectric length. More precisely,  $\gamma$  and  $\beta$  represent the tendency of the layer to be polarised in the directions parallel and perpendicular to the surface, respectively [245]. In the simple case of a thin continuous layer of thickness  $d$ ,  $\gamma$  and  $\beta$  are found to be equal to:

$$\gamma = d(\epsilon_2 - \epsilon_1) \quad (5.4)$$

$$\beta = d(1/\epsilon_1 - 1/\epsilon_2) \quad (5.5)$$

From Maxwell's equations, Fresnel coefficients are then written in terms of the susceptibilities  $\gamma$  and  $\beta$  [239, 244, 247] and the reflection coefficients, in which we are most interested in, are reported here:

$$r_s = \frac{n_1 \cos \theta_i - n_2 \cos \theta_t + i(\omega/c)\gamma}{n_1 \cos \theta_i + n_2 \cos \theta_t - i(\omega/c)\gamma} \quad (5.6)$$

$$r_p = \frac{(n_2 \cos \theta_i - n_1 \cos \theta_t)[1 - (\omega/2c)^2 \epsilon_1 \gamma \beta \sin^2 \theta_i] - i(\omega/c)\gamma \cos \theta_i \cos \theta_t + i(\omega/c)n_1 n_2 \epsilon_1 \beta \sin^2 \theta_i}{(n_2 \cos \theta_i + n_1 \cos \theta_t)[1 - (\omega/2c)^2 \epsilon_1 \gamma \beta \sin^2 \theta_i] - i(\omega/c)\gamma \cos \theta_i \cos \theta_t - i(\omega/c)n_1 n_2 \epsilon_1 \beta \sin^2 \theta_i} \quad (5.7)$$

where  $\theta_i$  and  $\theta_t$  are the angles of incidence and transmittance, respectively,  $n_{1,2} = \sqrt{\epsilon_{1,2}}$  are the refractive indices of the ambient medium (often vacuum) and the substrate, respectively. From equation 5.6 and 5.7,  $r_s$  depends only on  $\gamma$ , while  $r_p$  both on  $\gamma$  and  $\beta$ . This means that while p-polarised light can probe modes both parallel and perpendicular to the substrate surface, with s-polarised light only modes parallel to the surface will be probed. Up to now, the equations found are valid for any perturbed zones smaller than the incident light wavelength, since no hypothesis have been made regarding the layer geometry. In the limit of large incident wavelength ( $2\pi/\lambda|\gamma|$  and  $2\pi/\lambda|\beta| \ll 1$ ) and for a non-absorbing substrate, differential reflectivity equations for p and s components read:

$$\frac{\Delta R_s}{R_s} = \frac{8\pi}{\lambda} \frac{n_1 \cos \theta_i}{\epsilon_2 - \epsilon_1} \text{Im}[\gamma] \quad (5.8)$$

$$\frac{\Delta R_p}{R_p} = \frac{8\pi}{\lambda} \frac{n_1 \cos \theta_i}{(\epsilon_2 - \epsilon_1)(\epsilon_2 \cos^2 \theta_i - \epsilon_1 \sin^2 \theta_i)} [(\epsilon_2 - \epsilon_1 \sin^2 \theta_i) \text{Im}(\gamma) - \epsilon_2^2 \epsilon_1 \sin^2 \theta_i \text{Im}(\beta)] \quad (5.9)$$

$\frac{\Delta R_s}{R_s}$  depends on the imaginary part of  $\gamma$ ,  $\frac{\Delta R_p}{R_p}$  on the imaginary part of both  $\gamma$  and  $\beta$ . In both cases,  $\Delta R/R$  involves the imaginary part of the susceptibilities, hence it is proportional to the absorption in the layer.

The next step thus consists in calculating the exact susceptibilities in the case of an overlayer composed of nanoparticles, whose dimensions are smaller compared to  $\lambda$ .  $\gamma$  and  $\beta$  are related to the average island polarisabilities in the directions parallel and perpendicular to the surface, respectively:

$$\gamma(\omega) = \rho \langle \alpha_{\parallel}(\omega) \rangle \quad (5.10)$$

$$\beta(\omega) = \rho \langle \alpha_{\perp}(\omega) \rangle \quad (5.11)$$

in which  $\rho$  is the particle density. Polarisabilities are proportional to the particle volume, so that  $\gamma$  and  $\beta$  are proportional to the film thickness. Equations 5.10 and 5.11 show that the film optical response depends on the average island polarisabilities, which thus have to be computed exactly for nanoparticles of a given shape supported on a substrate. Two cases of particle geometries are found in the literature, namely truncated spheres and spheroidal particles [243, 244, 248–250]. The truncated sphere geometry has been chosen since it represents the Wulff construction equilibrium shape of isotropic surface energy materials, while truncated spheroidal geometries have been selected to describe a wider range of wetting conditions. A quasi-static approximation is considered, in which retardation effects are neglected and non-magnetic particles are taken into account, so that only the incident electric field is considered. The Laplace equation  $\nabla^2 \Psi(r)$  for the electrostatic potential  $\Psi(r)$  is solved by using a multipole expansion for the potential using spherical or spheroidal coordinates according to the considered particle shape [245]. The expansion is located at the centre of the particle and at the image charge position, *i.e.* symmetrically with respect to the object below the substrate surface, to take into account the presence of the substrate. By imposing boundary conditions at the interface (continuity of electrostatic potential and normal component of displacement field), two infinite linear systems of infinite order are obtained for the expansion coefficients. The first terms correspond to the polarisabilities sought. The systems are solved numerically for each energy by fixing an upper limit for the multipolar order  $M$ .  $M=24$  is often sufficient to obtain a good convergence.

When particles are not isolated, interactions between neighbouring clusters have to be accounted for in the model. This is done in the quasi-static approximation by applying an electrostatic correction to the polarisabilities at the dipolar or quadrupolar order. A

quadrupolar correction turned out to be enough for coverages up to 50% [245,246,251]. At the dipolar order, a blue shift in frequency results for the resonances for the perpendicular component  $\beta(\omega)$ , while towards the red for the parallel one  $\gamma(\omega)$ . Different particle arrangements on the substrate surface have been considered, namely square and hexagonal networks (as shown in figure 5.8), since marginal differences in the optical response were found compared to randomly-dispersed particles [243].

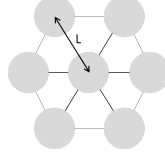


Figure 5.8: The hexagonal lattice used to model the particle arrangement on the substrate surface.

Besides the interaction between neighbouring particles, inhomogeneous broadening due to aspect ratio and size distribution effects is taken into account by a convolution method [72]. Polarizabilities  $\alpha_{\parallel,\perp}$  are convoluted with gaussian functions of width  $\sigma_{\parallel,\perp}$  over the energy range considered ( $\omega_2 - \omega_1$ ):

$$\langle \alpha_{\parallel,\perp}(\omega) \rangle = \frac{1}{\sqrt{2\pi}\sigma_{\parallel,\perp}} \int_{\omega_1}^{\omega_2} d\omega' \alpha_{\parallel,\perp}(\omega') \exp \left[ -\frac{(\omega - \omega')^2}{2\sigma_{\parallel,\perp}^2} \right] \quad (5.12)$$

This procedure to calculate the Fresnel coefficient of thin-layer particle films has been implemented in the freely available software called GRANFILM, developed by R. Lazzari and I. Simonsen [245,252] and written in Fortran 90. The software allows to choose between different film geometries (film, rough film, truncated sphere, truncate spheroid) and both dielectric simulations and fit of experimental data can be performed.

To go further, besides providing information on the cluster shape, SDRS spectrum analysis allows to evidence the transition between the stages of cluster growth. To do so, the integrated signal of the differential reflectivity spectrum in s-polarisation

$$\mathcal{A}_s(t) = \frac{1}{t} \int_0^\infty \frac{1}{\omega} \frac{\Delta R_s}{R_s}(\omega) d\omega \quad (5.13)$$

is considered, where  $t$  is the film thickness.  $\mathcal{A}_s$  is proportional to the parallel plasmon mode oscillation strength divided by its mass. It depends to a first approximation on the particle aspect ratio, in which an increase in  $\mathcal{A}_s$  corresponds to an increase of the aspect ratio. Only the s-polarisation is considered because for p-polarisation the dependence is less direct since the signal depends on both terms  $\text{Im}[\gamma]$  and  $\text{Im}[\beta]$ . The different stages of Volmer-Weber growth can thus be monitored by SDRS since they entail changes in the particle shape and aspect ratios. Higher metal amounts lead to the coalescence/percolation stage which corresponds to an increase of the particle aspect ratio, *i.e.* to flatter clusters. The growth behaviour described is typical of a Volmer-Weber growth and does not depend on the metal or substrate considered. It has been indeed used to characterise the different stages of growth for a variety of metal/substrate combinations, including Au, Ag, Cr and Zn on Al<sub>2</sub>O<sub>3</sub> and Ag on ZnO [253,254].

### 5.3.2 Optical dielectric functions of Ni and TiO<sub>2</sub>

As shown in equations 5.4 and 5.5, in the case of a continuous thin film of thickness  $d$ , the optical properties of the layer depends on  $d$  and the dielectric function  $\epsilon(\omega)$  and loss

function  $1/\epsilon(\omega)$ . The dielectric constants of Ni and TiO<sub>2</sub> used in the dielectric simulations are taken from the Palik's handbook of bulk optical constants [255], without applying finite-size correction. The dielectric functions  $\epsilon(\omega)$  used and the loss functions  $1/\epsilon(\omega)$  are plotted in figure 5.9.

One aspect that has to be considered when performing optical experiments on TiO<sub>2</sub> is that TiO<sub>2</sub> is an uniaxial material with optical anisotropy. The dielectric tensor  $\epsilon_{ij}$  of uniaxial materials is diagonal in the principal axis, and two values of the principal permittivity tensor are equal. One of them is parallel, while the other one is perpendicular to the *c*-axis and they are referred as  $\epsilon_{\parallel}$  and  $\epsilon_{\perp}$ , respectively. In the case of rutile TiO<sub>2</sub>, the *c*-axis corresponds to the [001] direction and thus lies in the surface plane.

The optical model presented so far does not take into account the anisotropy of the substrate. In this respect, the parallel and perpendicular values of the dielectric constant and loss function are plotted in figure 5.9. The anisotropy of the TiO<sub>2</sub> substrate dielectric constant is sufficiently low to allow the use of this optical model [245]. For this reason, TiO<sub>2</sub> is thus considered as optically isotropic by averaging the parallel and perpendicular values of the dielectric constants and the mean values of the dielectric constant and loss function used in the simulations are reported in figure 5.9 as well.

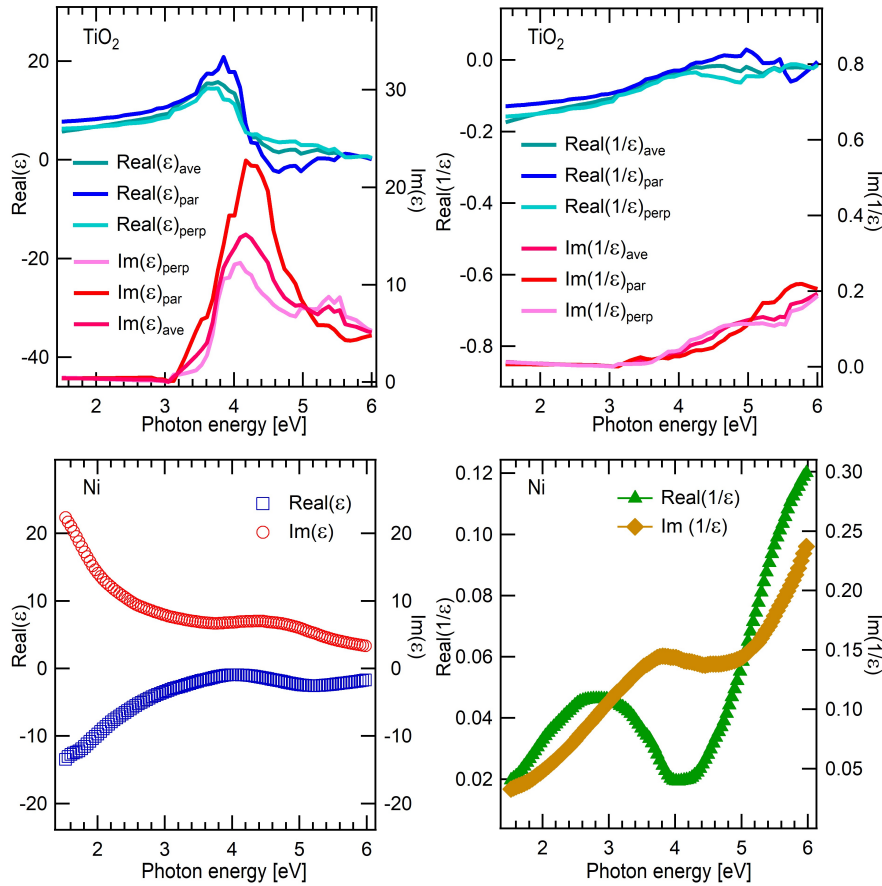


Figure 5.9: Bulk dielectric constants  $\epsilon(\omega)$  and loss function  $1/\epsilon(\omega)$  of TiO<sub>2</sub> (top) and Ni (bottom) as a function of the photon energy. Real parts are plotted on the left axes, while imaginary parts on the right one. Data are taken from ref. [255].

The optical dielectric function of metals,  $\epsilon(\omega)$ , can be written as the sum of two terms:

$$\epsilon(\omega) = \epsilon_D + \epsilon_{IB} = \epsilon_\infty - \frac{\omega_p^2}{\omega^2 + i\omega\Gamma} + \epsilon_{IB} \quad (5.14)$$

the first term  $\epsilon_D$  takes into account the free carrier response and it is described by the Drude model, where  $\omega_p$  is the bulk plasma frequency and  $\Gamma$  the relaxation rate. The second contribution  $\epsilon_{IB}$  refers instead to the additional interband transitions. The experimental values of  $\epsilon(\omega)$  for Ni taken from the collection of Palik [255] are compared to the values calculated from the Drude model in figure 5.10. In the calculations values of 11.7 eV and 1.4 eV have been used for  $\omega_p$  and  $\Gamma$ , respectively. Interband transitions occurring at high energies are not taken into account in the Drude model, as expected.

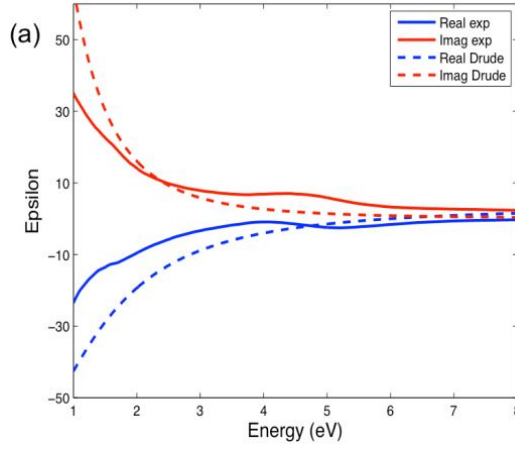


Figure 5.10: Comparison of the real and imaginary part of the optical dielectric function  $\epsilon(\omega)$  obtained from experimental data and calculations based on the Drude model [256].

### 5.3.3 Dielectric simulations

Since cluster aspect ratio ( $A_r$ ) and density have a strong influence on plasmonic resonances in terms of energy position and intensities, dielectric simulations have been performed using the GRANFILM software. Two geometries have been used to model the Ni cluster shape (figure 5.11), namely truncated spheres and truncated hemi-spheroids. Truncated spheres are described in terms of the diameter  $D_{\parallel}$ , height  $H$  and contact angle  $\theta_C$ . Truncated hemi-spheroids are instead described by the diameters  $D_{\parallel} = 2R$  and  $R_{\perp} = H$ , parallel and perpendicular to the substrate surface, respectively. Truncated hemispheroid

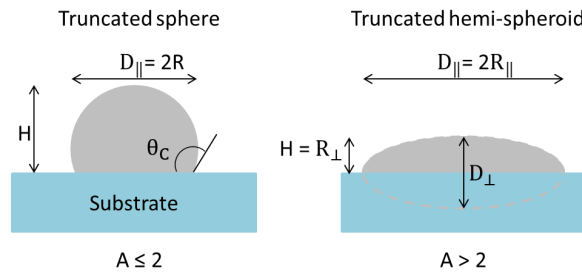


Figure 5.11: Geometries used in the dielectric simulations: truncated sphere and hemi-spheroid.



models have been assumed for  $A_r = D_{\parallel}/H > 2$ , while truncated spheres for  $A_r \leq 2$ . No interactions between neighbouring particles and no inhomogeneous broadening effects have been taken into account at this level to focus only on the effect of the particle shape. The total equivalent film thickness has been maintained constant at 0.6 ML in all the simulations performed. The choice of this value is arbitrary since the position of the plasmon resonances only depends on the morphology of the film and on the cluster aspect ratio, and not on the total equivalent film thickness used. Thickness will only scale up the intensities. A multipole order  $M=24$  has been used.

The results of the dielectric simulations are presented in figure 5.12 for s- and p-polarisations at increasing values of  $A_r$ . The simulated spectra for a continuous film geometry are reported as well, shown by a grey curve. It becomes evident that the optical response of the clusters is strongly influenced by the aspect ratio in both models and that 3D clusters and continuous film growths can be easily distinguished. For Ni, a plasmon resonance appears in the UV-visible region probed (1.5-4.5 eV), whose energy position and intensity depends on the cluster aspect ratio. The broad bump shifts from  $\sim 3$  eV to 1.7 eV for the highest simulated  $A_r$ , thus making it possible to probe different wetting conditions. Differences between the two polarisations are marginal, except for the intensities of the  $\Delta R/R$  spectra, higher in p-polarisation than in s.

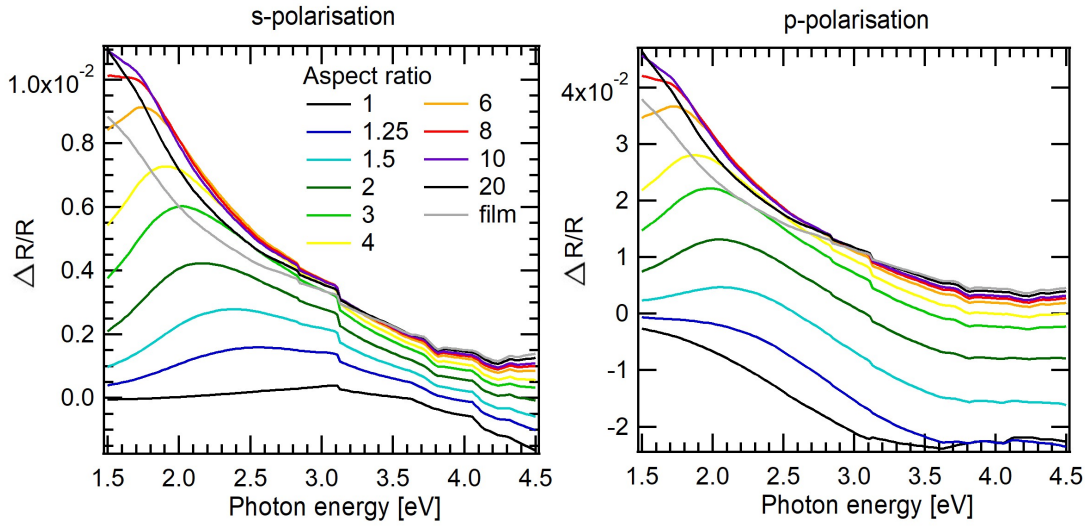


Figure 5.12: Simulations of the differential reflectivity spectra for Ni clusters on TiO<sub>2</sub>(110) for increasing values of  $A_r$  and for a continuous film in s- (left) and p-polarisation (right). The film thickness is kept constant at 0.6 ML.

In a second part, the effect of the interactions between neighbouring particles is introduced. Both dipolar and quadrupolar orders are considered for coverages not exceeding 50%. A hemi-spheroid geometry has been used, with  $R_{\parallel} = 5$  nm,  $A_r = 4$  and  $\Theta = 30\%$ . A hexagonal lattice has been selected with lattice constant 17.3 nm. The results of the simulations are presented in figure 5.13, where the interactions at dipolar and quadrupolar orders are compared with the case of no particle-particle interactions. When interactions are considered, the intensity of the resonance slightly increases, but differences remain negligible, also between dipolar and quadrupolar orders. Similar results are obtained for different values of  $A_r$  as well (not shown here). This implies that particle-particle interactions will have a minor effect on SDRS spectra and thus the simulations presented in figure 5.12 are retained as a model of the dependence of the optical response on the cluster

geometry.

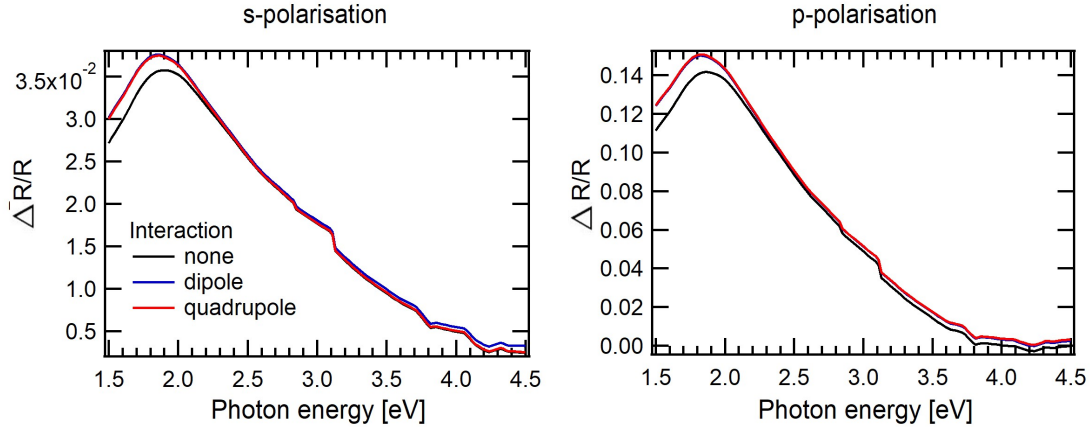


Figure 5.13: Differential reflectivity simulations for Ni clusters on TiO<sub>2</sub>(110). Interactions between particles are taken into account at dipolar and quadrupolar orders and compared with the case of no particle-particle interactions. A hemi-spheroid geometry has been used, with  $R_{\parallel} = 5$  nm,  $A_r = 4$  and  $\Theta = 30\%$ . A hexagonal lattice has been selected with lattice constant 17.3 nm.

### 5.3.4 SDRS experimental spectra

A major asset of SDRS is that this technique allows an *in-situ* real-time monitoring of metal growth on a substrate. Moreover, thanks to dielectric simulations performed in parallel, information on the cluster shape in terms of aspect ratio and size may be gained. It has been applied here to follow Ni deposition on rutile TiO<sub>2</sub>(110) up to  $\sim 10$  ML. Compared to the evaporation conditions used in the STM images, higher fluxes (filament current  $I=1.35$  A, emission current  $I_{em}=37$  mA, flux  $\Phi=900$  nA) have been used for the SDRS analysis, to be able to study a larger range of Ni coverages. SDRS spectra acquired in s- and p-polarisations are reported in figure 5.14. The spectra have been recorded both with the incident light directed along the [001] direction and the [1 $\bar{1}$ 0] direction of the TiO<sub>2</sub>(110) surface, to gain information on a possible anisotropic growth of Ni clusters. For the record, the [001] direction corresponds to the  $O_{br}$  row direction. Previous studies have evidenced an elongation of Ni clusters along the  $O_{br}$  channels due to the easiest diffusion in the [001] direction [175, 177].

Qualitative information on the cluster shape is gained by looking at the energy position of the plasmon resonances. Spectra recorded in s-polarisation are quite noisy, while in p-polarisation a clear appearance of a large plasmon resonance is observed at about 2 eV at increasing Ni coverage. The energy position of the resonance is indicative of 3D cluster growth, with aspect ratio close to 2 (see figure 5.12), which correspond to a hemisphere, in good accord with what suggested from the combined STM and XPS analysis in the first stages of growth.

At increasing Ni dosing, a negative optical feature appears at about 4.2 eV. This feature is absent in the optical simulations presented in figure 5.12, suggesting that its origin is not due to a plasmon resonance contribution. It falls indeed in the energy region expected for the rutile band gap and it was already observed in the SDRS spectra recorded for Au deposition on the same TiO<sub>2</sub>(110) substrate [73]. This would imply a strong interaction between Ni and the substrate that modifies its dielectric properties. A likely explanation is the Ti reduction upon Ni deposition, which is confirmed by the increase of

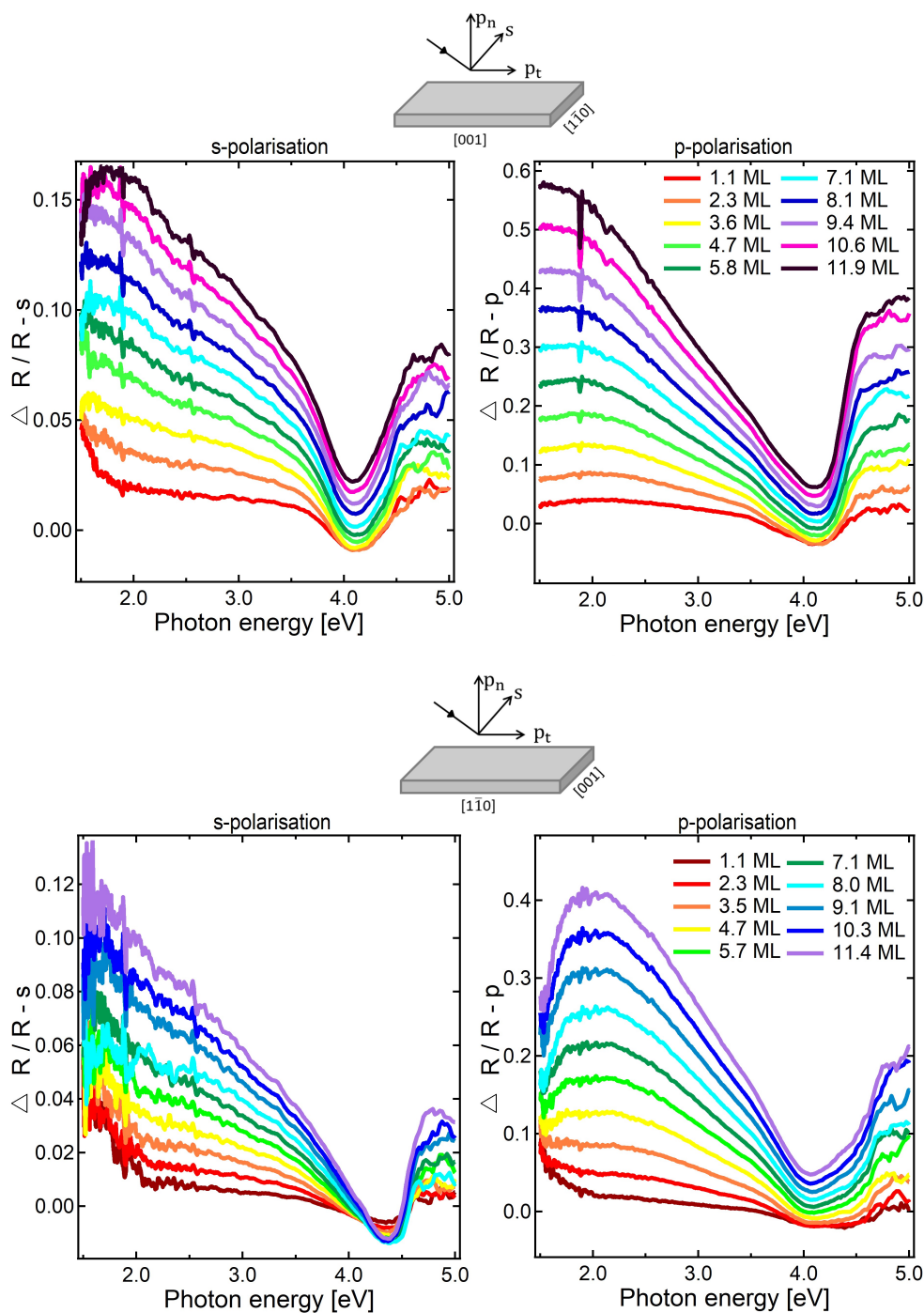


Figure 5.14: Experimental SDRS spectra recorded for increasing Ni coverage on rutile TiO<sub>2</sub>(110) at room temperature with incident light oriented along the [001] (top) and  $[1\bar{1}0]$  (bottom) directions, as schematically depicted. Both s- and p-polarisations are reported. Ni coverage has been estimated from XPS quantification.

the Ti<sup>3+</sup> contribution in the Ti 2p photoemission spectrum recorded at the end of SDRS experiments, as shown in figure 5.15 (despite the less than optimal resolution). Again, it is not possible to conclude if Ti reduction is due intrinsically to the presence of Ni and/or the effect of ion bombardment of the substrate when using electron beam evaporators. The

Ni 2p signal has a metallic character, as evidenced in figure 5.15 by the comparison with Ni 2p recorded on a Ni(111) single crystal. Nevertheless due to the high Ni coverage, XPS is most probably not sensitive enough to evidence the presence of an oxide component at the interface.

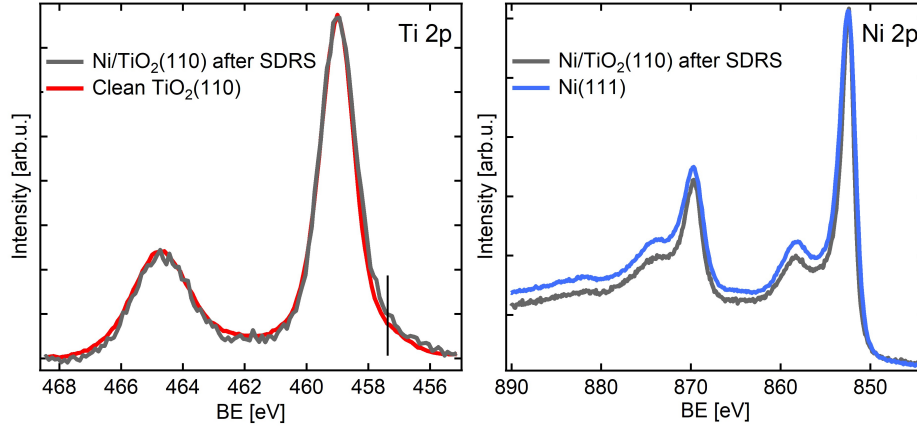


Figure 5.15: Left: Ti 2p spectra of the clean rutile  $\text{TiO}_2(110)$  surface and after Ni deposition (2 nm). Right: Comparison of the Ni 2p signal recorded after SDRS Ni dosing on the rutile  $\text{TiO}_2(110)$  and for a Ni(111) monocrystal.

### 5.3.5 Film growth stages: the evolution of SDRS integrated intensity

By considering the evolution of the normalised integrated intensity of the SDRS signal  $\mathcal{A}_s$  as a function of deposited metal thickness, it is possible to identify transitions between stages of cluster growth. The evolution of the normalised integrated intensity in s-polarisation as a function of Ni thickness is presented in figure 5.16. The plateau ob-

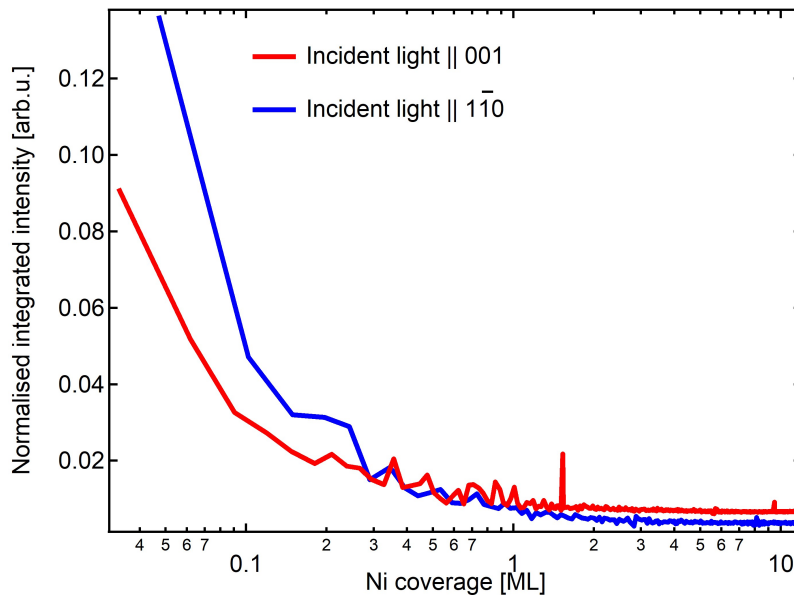


Figure 5.16: Evolution of the normalised integrated intensity as a function of Ni thickness. Only the polarisation s is shown.

served corresponds to the growth of clusters of constant aspect ratio. An increase of  $\mathcal{A}_s$  at higher thicknesses beyond the ones probed in the present work is in principle expected, which is related to the transition from the growth to coalescence regime. The origin of the increase of  $\mathcal{A}_s$  at low thicknesses, in the submonolayer regime, is still under debate. It could be instead due to stress effects in the nanoparticles.

Differences in the intensity of the normalised integrated signals along the [001] and [1 $\bar{1}$ 0] directions are observed and they are due to the anisotropic growth of Ni clusters in the two crystallographic directions. In a first approximation,  $\mathcal{A}_s$  is proportional to the cluster aspect ratio. More precisely, a stronger  $\mathcal{A}_s$  signal corresponds to a higher aspect ratio and thus to more elongated clusters. It is worth to remember that in s-polarisation the electric field is perpendicular to the plane of incidence and parallel to the surface, so that when incident light is oriented along the [001] ([1 $\bar{1}$ 0]) direction, the s-polarised component will be oriented along the [1 $\bar{1}$ 0] ([001]). In the first stage of growth,  $\mathcal{A}_s$  is more intense when the incident light is oriented along the [1 $\bar{1}$ 0], thus implying that Ni clusters are more elongated along the [001] direction. This is consistent with the expected easiest diffusion along the  $O_{br}$  channels, as evidenced in previous studies [175, 177].

## 5.4 Conclusion

This chapter was dedicated to the adsorption of Ni on the TiO<sub>2</sub>(110) surface. By probing the early stages of the overlayer growth by STM, it was confirmed that Ni deposition occurs through a Volmer-Weber island growth. While clusters were initially on average two atomic layers high, further Ni deposition led to a more pronounced 3D growth. Cluster dimension and density values obtained were of the same order of those reported in previous studies. A combined STM and XPS approach suggested that Ni clusters grow as hemispheres. Moreover, photoemission evidenced that Ni clusters are mainly metallic.

Previous studies reported for Ni growth on the TiO<sub>2</sub>(110) surface mainly focussed on local microscopic approach by means of STM to probe the initial stages of growth. In this respect, to extend Ni investigation over a larger range of coverage and at the same time to overcome the problems of size overestimation due to tip convolution effects, Ni growth was additionally probed by SDRS. SDRS is a less popular technique well-suited to probe *in situ* and in real-time metal depositions on dielectric substrates. After a quick introduction on the underlying theory based on the notions of excess fields and surface susceptibilities, dielectric simulations were performed to demonstrate the dependence of the optical response of the nanoparticles on their morphology. Simulations were compared to the experimental spectra recorded, which showed that hemispherical Ni clusters (aspect ratio around 2) grow on the TiO<sub>2</sub> surface. No unequivocal information on titania reduction upon Ni dosing could be gained by XPS, due to the effect of substrate ion bombardment when using electron beam evaporators. The normalised integrated differential reflectivity signals were then used to follow the evolution of the Ni cluster growth stages and no beginning of coalescence was observed for the thicknesses probed. The differences observed in the normalised integrated intensity along the [001] and [1 $\bar{1}$ 0] directions pointed to an anisotropic growth of Ni nanoparticles, which appeared to be more elongated along the [001] direction due to the easiest diffusion along the  $O_{br}$  channels, confirming what was suggested in previous studies [175, 177].

# CHAPTER 6

---

## Modelling the complete catalytic system: perspectives on TA adsorption on Ni-covered TiO<sub>2</sub>(110)

---

In this chapter we combine RR-TA and Ni adsorption on the rutile TiO<sub>2</sub>(110) surface, whose adsorptions have been studied separately in the previous chapters, with the aim of exploring some aspects of the complete catalytic model system, TA/Ni/TiO<sub>2</sub>(110). The isolated systems TA/TiO<sub>2</sub> and Ni/TiO<sub>2</sub> are already quite complex so that the additional presence of Ni and the absence of vibrational studies make the interpretation of TA adsorption difficult. Nevertheless, some information on a possible preferential TA adsorption on either the metal catalyst or the oxide support can be gathered by means of XPS. Additional TPD studies are carried out to probe the decomposition of RR-TA molecules for different Ni coverages. RR-TA decomposition is studied in parallel on Ni(111), the {111} facets being the main facets found in Ni nanoparticles.

*Après avoir étudié l'adsorption sur rutile TiO<sub>2</sub>(110) des molécules de RR-AT et des nanoparticules de Ni séparément, on étudie à présent dans ce chapitre leur adsorption combinée sur la même surface, dans le but d'explorer certains aspects du système catalytique modèle complet, AT/Ni/TiO<sub>2</sub>(110). Les systèmes isolés AT/TiO<sub>2</sub> et Ni/TiO<sub>2</sub> sont déjà assez complexes de sorte que la présence supplémentaire de Ni et l'absence d'études vibrationnelles rendent difficile l'étude de l'adsorption de l'AT sur Ni/TiO<sub>2</sub>. Néanmoins, certaines informations sur une éventuelle adsorption préférentielle des molécules chirales soit sur le catalyseur métallique ou sur le support oxyde peuvent être recueillies au moyen de l'XPS. D'autres études de TPD sont menées pour étudier la décomposition des molécules de RR-AT pour différents taux de recouvrement de Ni. La décomposition de RR-AT est étudiée en parallèle sur le Ni(111), les faces {111} étant les principales facettes trouvées dans les nanoparticules de Ni.*

### 6.1 Chemical analysis

To gain some insights on TA adsorption on the Ni/TiO<sub>2</sub>(110) system, some tests were made by means of *in-situ* PM-RAIRS. To try to overcome the difficulties encountered in the study of RR-TA/TiO<sub>2</sub> mainly due to the lower oxide reflectivity and attenuated sensitivities with respect to metal surfaces, a high Ni dose was first deposited on TiO<sub>2</sub>(110). Nevertheless, no workable signal was obtained, thus ruling out again the possibility of using infrared spectroscopy to characterise the complete model catalytic system. Again

the insertion of the entire IR light path in vacuum is necessary to gain a factor of 10 in the S/N ratio.

The influence of Ni on the adsorption of RR-TA molecules on TiO<sub>2</sub>(110) is thus considered by means of XPS. The presence of Ni clusters on the oxide surface could indeed provide additional adsorption sites for TA molecules compared to the bare TiO<sub>2</sub>(110) surface. To investigate this aspect, equivalent TA doses are deposited both on the clean TiO<sub>2</sub>(110) surface and on a Ni covered one (0.2 ML), in which about 10% of the TiO<sub>2</sub> surface is covered by Ni. The adsorption curves are plotted in figure 6.1, in which the quantity of RR-TA adsorbates against the evaporation time is compared for the two systems. RR-TA coverage on the clean TiO<sub>2</sub>(110) surface is estimated, as usual, from the Ti 2p/C 1s XPS intensity ratio, assuming a homogeneous molecular film. For the Ni/TiO<sub>2</sub> system an additional damping factor of the substrate signal through the intermediate Ni layer of equivalent thickness of 0.2 ML is taken into account (with respect to the thickness estimation procedure presented in section 1.3.4). As shown in figure 6.1 the differences observed between TA dosing on the TiO<sub>2</sub>(110) and on Ni/TiO<sub>2</sub>(110) systems remain within the experimental uncertainty and the presence of Ni clusters on the TiO<sub>2</sub>(110) surface seems to minorly influence RR-TA adsorption at this dose as far as quantity is concerned.

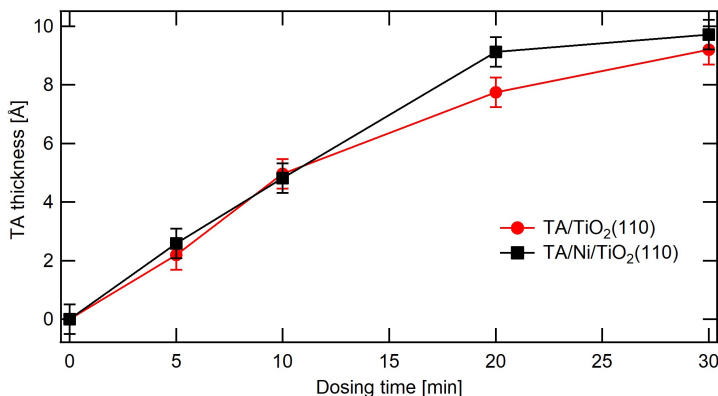


Figure 6.1: Comparison of equivalent RR-TA dosing times on the clean TiO<sub>2</sub>(110) surface and on a Ni covered one (equivalent Ni thickness = 0.2 ML.)

Figure 6.2 shows the evolution of the Ni 2p (a) and C 1s (b) for 1 ML of RR-TA (dosing time 20 min) on increasing Ni coverages on TiO<sub>2</sub>(110). In the C 1s region, two main contributions are identified, with an energy splitting of 2.2 eV which slightly decreases at 2.1 eV for the highest Ni dose. Peaks are initially 1.3 and 1.6 eV large, which are not far from the values obtained for TA deposition on the clean TiO<sub>2</sub> surface (1.35 eV and 1.5 eV, respectively). At increasing Ni dosing, the high BE contributions gets larger, reaching a FWHM = 1.9 eV, possibly suggesting that a higher fraction of RR-TA molecules are adsorbed on Ni clusters and that the corresponding carboxylate and/or carboxylic contributions become more important in the C 1s region. At the same time, a contribution develops at about 284.5 eV, possibly due to a decomposition products, as observed in previous studies [192].

The adsorption of RR-TA molecules on Ni is further confirmed by looking at the Ni 2p spectra (6.2(a)). For comparison, the Ni 2p spectrum before TA deposition is also shown in red for the highest Ni coverage probed (0.6 ML). After TA dosing, a new component develops at about 856 eV, suggesting that Ni clusters are oxidised. This confirms that RR-TA molecules effectively adsorb on Ni, possibly by deprotonation of a carboxylic group. To investigate in more details the evolution of the Ni 2p peak upon molecular adsorption,

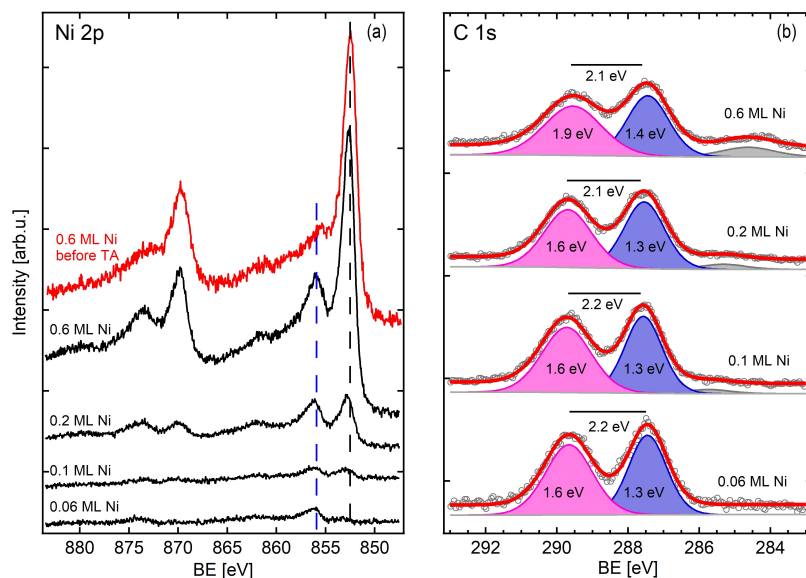


Figure 6.2: Evolution of the (a) Ni 2p and (b) C 1s spectra for the same RR-TA dose (1 ML) on increasing Ni coverages on TiO<sub>2</sub>(110). In panel (a), the corresponding Ni 2p spectrum for 0.6 ML of Ni before RR-TA dose is shown in red. The energy splitting between the C 1s components is marked as well as the FWHM on the corresponding peaks. Spectra are recorded using a monochromatised Al K $\alpha$  X-ray source (photon energy  $h\nu = 1486.6$  eV)

submonolayer ( $3 \text{ \AA} \sim 0.5$  ML) and monolayer ( $6 \text{ \AA} \sim 1$  ML) RR-TA doses have been deposited on a 0.06 ML Ni/TiO<sub>2</sub> and a 0.2 ML Ni/TiO<sub>2</sub>. The corresponding Ni 2p spectra are reported in figure 6.3. For clarity, the metallic and oxide Ni component positions are marked with dotted black and blue vertical lines, respectively. By looking at figure 6.3(a) it is clear that following a submonolayer TA deposition of  $3 \text{ \AA}$  on 0.06 ML of Ni, only part of Ni is oxidised, while after dosing  $6 \text{ \AA}$  ( $\sim 1$  ML) of TA, Ni is almost completely oxidised.

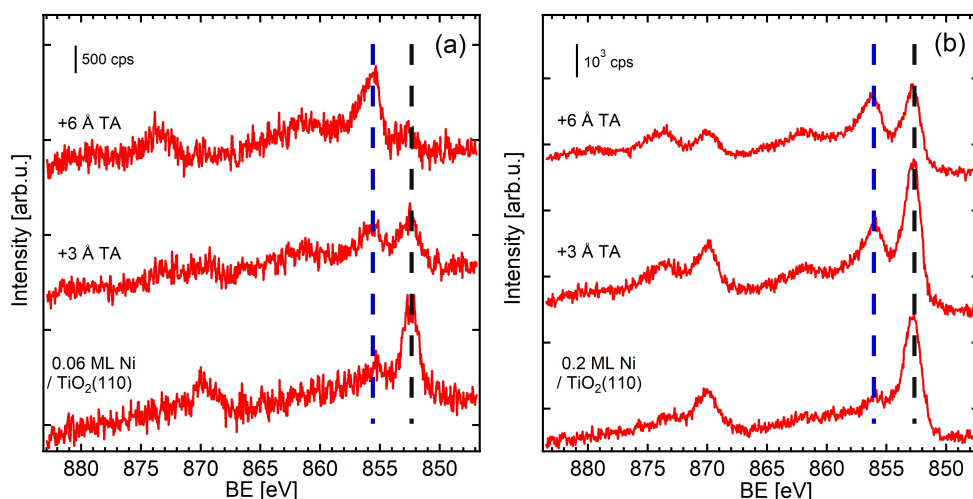


Figure 6.3: Evolution of the Ni 2p region for (a) 0.06 ML of Ni and (b) 0.2 ML of Ni, at increasing doses of RR-TA. Spectra are recorded using a monochromatised Al K $\alpha$  X-ray source (photon energy  $h\nu = 1486.6$  eV)



For 0.06 ML of Ni, a low fraction of the TiO<sub>2</sub> surface (about 3%) is expected to be covered by Ni from STM imaging. Since nearly half of Ni remains metallic after deposition of the lowest TA dose, this fact suggests that there is no preferential adsorption of TA on Ni clusters. Moreover, at this low Ni dose, the ratio (surface area)/volume is high since Ni clusters are almost completely oxidised for the highest RR-TA dose. Conversely, for 0.2 ML of Ni (figure 6.3(b)), Ni clusters have a more bulky character so that Ni oxidation takes place at the surface, while the bulk remains metallic upon a monolayer TA deposition. Globally, photoemission has helped to elucidate some aspects of the chiral modifier adsorption on the complete Ni/TiO<sub>2</sub> system. The analysis of the Ni 2p region has suggested that TA adsorbs on the metal nanoparticles (oxidation of Ni). However, the similarity of the kinetics of RR-TA adsorption on the clean oxide surface and on a Ni-covered one seems to suggest that molecules adsorb both on the Ni catalyst and on the TiO<sub>2</sub> substrate.

## 6.2 Thermal stability of RR-TA

### 6.2.1 Thermal stability of RR-TA on Ni(111)

Being the main facets found in Ni clusters, the decomposition behaviour of RR-TA molecules is first studied on Ni(111). The adsorption of RR-TA molecules on Ni(111) has already been investigated in literature and has revealed the presence of monotartrate species at room temperature [114]. However, the desorption behaviour is here reproduced mainly to obtain a reference of RR-TA desorption temperatures in our system and be able to directly compare them to those recorded on TiO<sub>2</sub>(110). Being more interested in the monolayer adsorption regime, low RR-TA doses are mainly studied. Nevertheless, a high RR-TA multilayer coverage is considered as well, to have a reference of the multilayer desorption peak temperature. Figure 6.4 displays the spectra obtained on the clean surface as a blank and following RR-TA adsorption on Ni(111) at room temperature for the main two fragments ascribed to the molecular form,  $m/z$  58 (HOC-COH<sup>+</sup>) and 76 (C<sub>2</sub>O<sub>3</sub>H<sub>4</sub><sup>+</sup>). Figure 6.5 reports the TPD spectra for the fragments  $m/z$  2, 18, 28 and 44 for the same RR-TA doses.

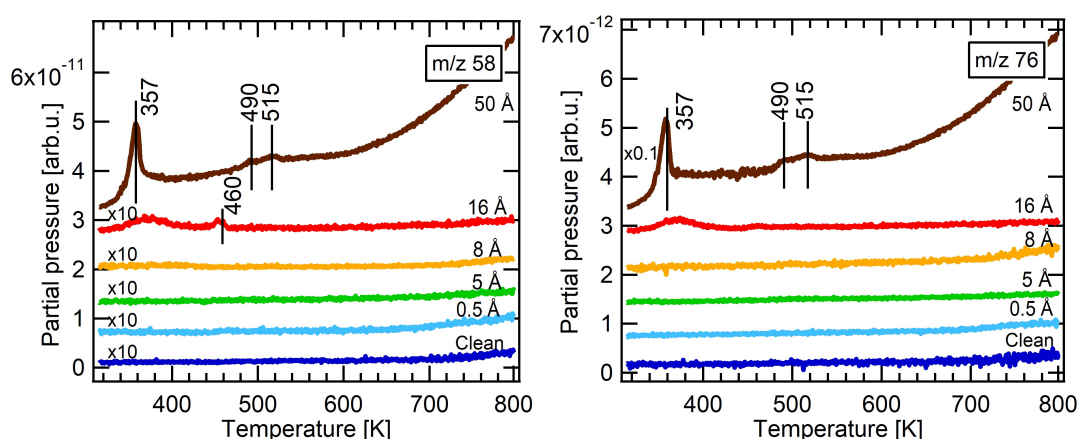


Figure 6.4: TPD spectra of  $m/z$  58 and 76 for increasing doses of RR-TA on Ni(111) at room temperature. The recorded spectra are vertically shifted arbitrarily for the sake of clarity.

First of all, no workable signal is obtained for fragments 58 and 76, except for the highest

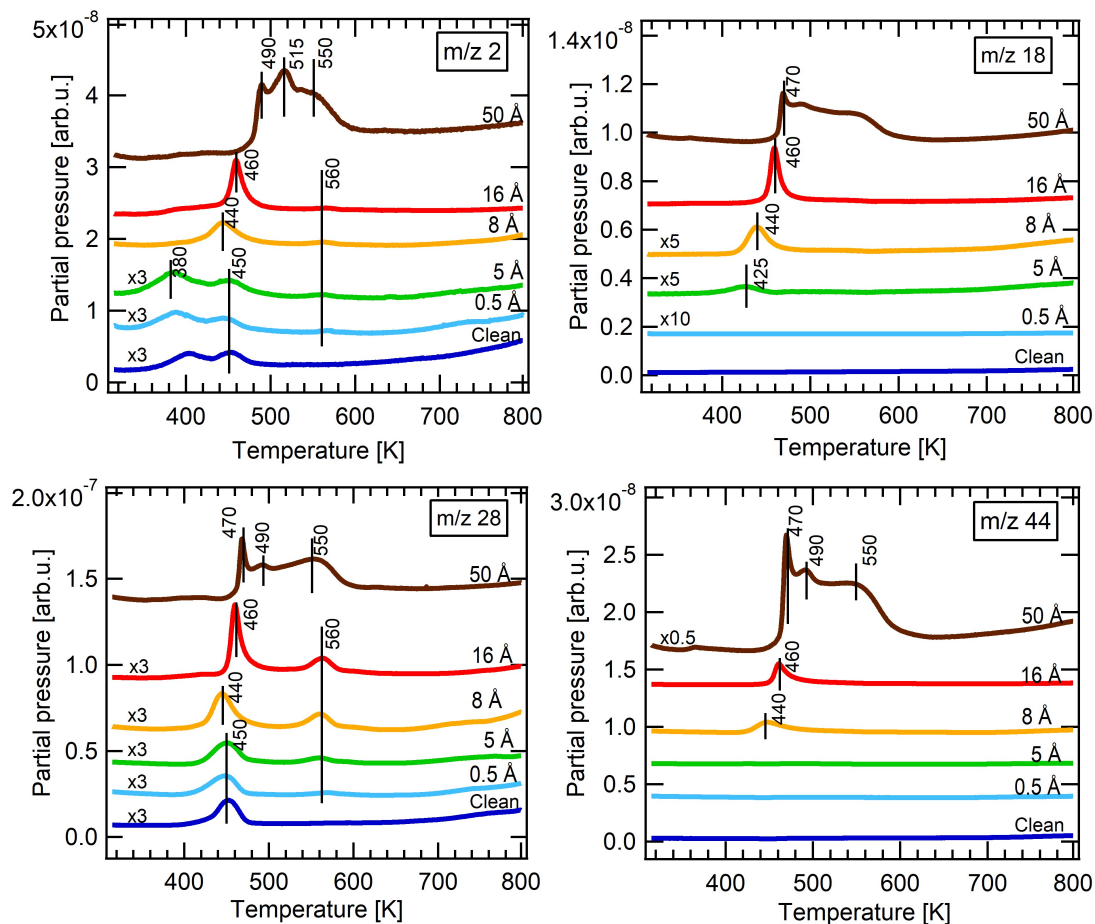


Figure 6.5: TPD spectra of  $m/z$  2 ( $\text{H}_2^+$ ), 18 ( $\text{H}_2\text{O}^+$ ), 28 ( $\text{CO}^+$ ) and 44 ( $\text{CO}_2^+$ ) for increasing doses of RR-TA on Ni(111) at room temperature. The recorded spectra are vertically shifted arbitrarily for the sake of clarity.

multilayer doses, suggesting that desorption of RR-TA molecules from the multilayer occurs at  $\sim 357$  K. Less intense desorption peaks are also found at 460 K, 490 K and 515 K. From these spectra, we observe that monolayer coverage probably occurs after 8 Å, due to the absence of multilayer contributions for this dose.

We focus the main analysis on figure 6.5. Starting from the blank spectra, we observe that both CO ( $\sim 450$  K) and  $\text{H}_2$  are already present on the clean surface. They are adsorbed on the surface or manipulator, before TA deposition and subsequent TPD experiments. However, it was shown in previous studies by coupling TPD and RAIRS experiments that, at increasing molecular depositions, RR-TA molecules are capable of displacing CO from the surface, so that at the highest doses the surface is effectively free from CO [114]. Following a 8 Å dose, in all spectra a peak is observed at about 450 K, which gradually shifts to higher temperature as the molecular dose increases. Moreover, at higher doses, a new peak appears at 560 K in the CO spectra, attributed by Jones and Baddeley to C+O recombination on the Ni surface [114], which may arise from decomposition of a limited amount of molecules adsorbed at step edges. In the highest dose spectra, three features are observed at about 470 K, 490 K and 540-550 K in  $\text{H}_2\text{O}$ , CO and  $\text{CO}_2$  traces. In  $\text{H}_2$  spectra, three peaks appear at about 490 K, 515 K and 550 K. The appearance of new

desorption peaks at increasing temperature was explained in the work of Jones and Baddeley [114], hypothesizing that TA desorption occurs in a stepwise manner: the desorption of RR-TA molecules at lower temperature would create space for the remaining ones to assume a more stable configuration, in such a way that their desorption actually occurs at higher temperatures.

Overall, the peak shapes recorded are in good agreement with the work of Jones and Baddeley [114], shown in figure 6.6. RR-TA coverages probed are probably limited to the monolayer regime, even if a clear correspondence between the dosing times and the coverage is not given in the text. A systematic shift in the desorption temperature of  $\sim 40$  K towards higher temperature is observed in the present study compared to spectra presented in figure 6.6, probably due to different temperature measurements.

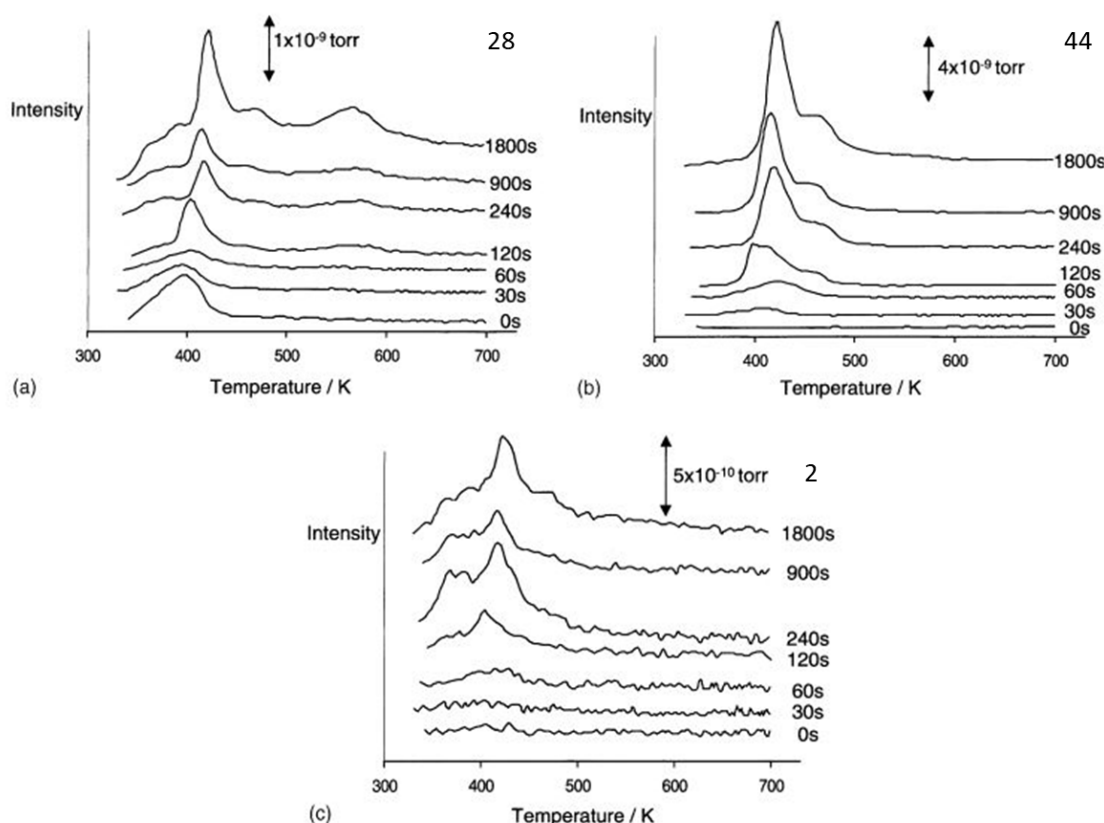


Figure 6.6: TPD spectra following RR-TA adsorption on Ni(111) at room temperature.  $m/z$  (a) 28, (b) 44 and (c) 2 are shown for RR-TA increasing dosing times.

## 6.2.2 Thermal stability of RR-TA on Ni/TiO<sub>2</sub>(110)

With the desorption references obtained for RR-TA on TiO<sub>2</sub>(110) (chapter 4) and Ni(111), the thermal stability of RR-TA molecules is then investigated on the Ni/TiO<sub>2</sub>(110) system. Two different Ni doses have been tested, namely 0.3 ML and 1.7 ML. For the first low Ni dose, Ni coverage is estimated to be around 12% by taking into account the STM tip overestimation effects, while for the highest dose we do not have the corresponding STM images. Nevertheless, we expect that  $\sim 60\%$  of the TiO<sub>2</sub> surface will be covered by Ni from the linear extrapolation of corrected coverage *vs* total thickness values in table 5.2. The TPD spectra recorded for  $m/z$  2, 18, 28 and 44 and for increasing TA doses are shown

in figures 6.7 and 6.8 for the 0.3 ML Ni/TiO<sub>2</sub>(110) and for the 1.7 ML Ni/TiO<sub>2</sub>(110) systems, respectively.  $m/z$  58 and 76 have also been recorded but they are not shown here, since no workable signals have been obtained, except for the highest dose (50 Å), where a multilayer desorption peak is found at about 335 K, in good accord with what found for RR-TA desorption on the TiO<sub>2</sub>(110) surface.

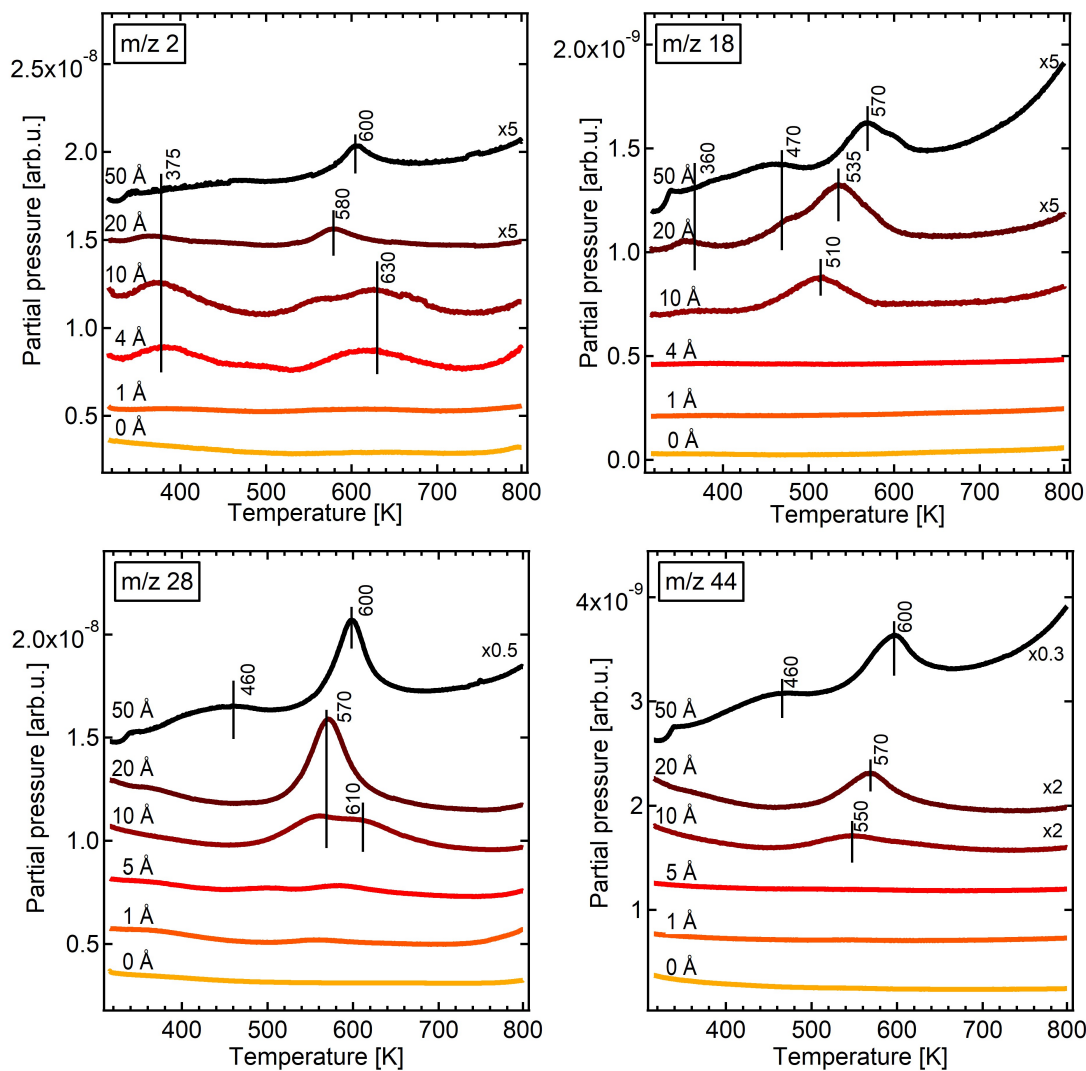


Figure 6.7: TPD spectra of  $m/z$  2 ( $\text{H}_2^+$ ), 18 ( $\text{H}_2\text{O}^+$ ), 28 ( $\text{CO}^+$ ) and 44 ( $\text{CO}_2^+$ ) for increasing doses of RR-TA on 0.3 ML Ni/TiO<sub>2</sub>(110). The recorded spectra are vertically shifted arbitrarily for the sake of clarity.

We start by considering the desorption spectra recorded for the 0.3 ML Ni/TiO<sub>2</sub>(110) system. Desorption of  $m/z$  2 produces peaks at 375 K and a large feature around 630 K for low coverages. At higher multilayer TA depositions, besides the feature at 375 K, an additional peak is observed at  $\sim$  600 K, which seems to shift to higher temperature as TA dose increases. In the  $m/z$  18 spectra, no desorption features are observed for TA submonolayer depositions. In the multilayer regime, a desorption peak appears at 510 K for 10 Å of TA, while peaks are found at 360 K, 470 K, 535 K and 570 K at higher molecular doses. In the  $m/z$  28 spectra, for a 10 Å TA dose, desorption peaks are observed

at 570 K and 610 K. The spectrum for 20 Å of TA exhibits a unique feature at 570 K for, while peaks are observed at 460 K and 600 K, following TA deposition of 50 Å. Finally, the m/z 44 spectra globally follow the same trend of the m/z 28 ones.

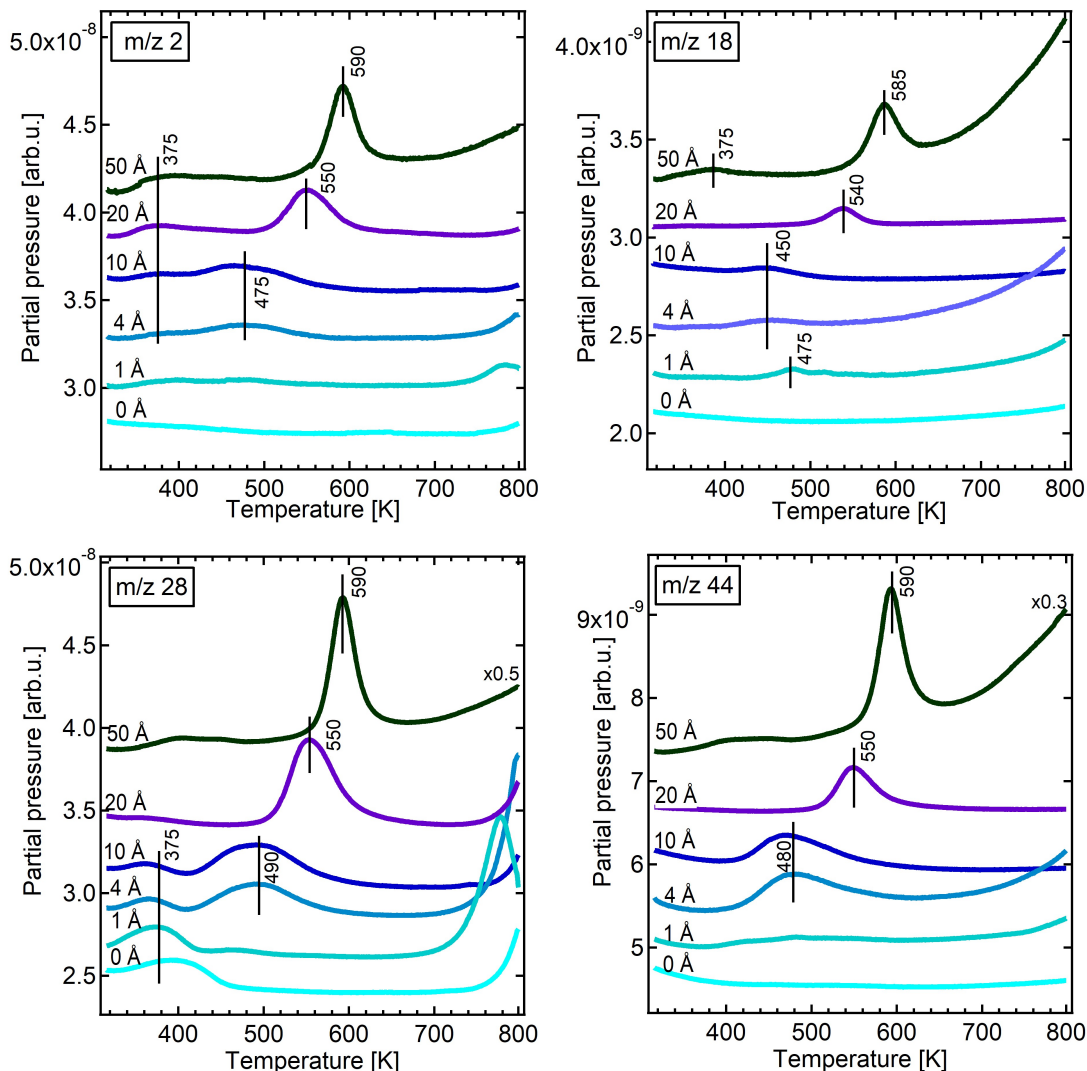


Figure 6.8: TPD spectra of m/z 2 ( $\text{H}_2^+$ ), 18 ( $\text{H}_2\text{O}^+$ ), 28 ( $\text{CO}^+$ ) and 44 ( $\text{CO}_2^+$ ) for increasing doses of RR-TA on 1.7 ML Ni/TiO<sub>2</sub>(110). The recorded spectra are vertically shifted arbitrarily for the sake of clarity.

We now consider the highest Ni dose of 1.7 ML and the relative desorption spectra presented in figure 6.8. In the m/z 2 spectra, desorption features appear at 375 K for both submonolayer and multilayer doses, in analogy to the low Ni dose system. For the 4 Å and 10 Å TA doses, an additional peak appears around 475 K, while for higher molecular doses, desorption peaks are recorded at 550 K and 590 K. In the m/z 18 spectra, up to TA doses of 10 Å, peaks appear at 475 K and 450 K. As TA coverage further increases, new peaks are recorded at 540 K for 20 Å of TA, while at 375 K and 585 K for 50 Å of TA. By looking at the m/z 28 spectra, it is clear that CO is already present in the blank spectrum and gives rise to a desorption feature at about 375 K. For increasing RR-TA coverages, the intensity of the peak at 375 K decreases, possibly suggesting that RR-TA

molecules are capable of displacing the coadsorbed CO, in analogy to what is reported in the previous section for the Ni(111) surface. For submonolayer molecular depositions, a desorption peak appears at  $\sim 800$  K. A peak is also observed at 490 K, which seems to shift at higher temperatures at increasing RR-TA multilayer doses, reaching 590 K for 50 Å of TA. The  $m/z$  44 spectra globally follow the same trend of  $m/z$  28, but no evidence of a desorption feature at 370 K is remarked, possibly confirming its attribution to coadsorbed CO molecules.

In general, by comparing the desorption spectra for the two Ni doses, the 1.7 ML Ni/TiO<sub>2</sub> system seems more reactive than the clean TiO<sub>2</sub> surface and the 0.3 ML Ni/TiO<sub>2</sub> system, as evidenced by the presence of CO already in the blank spectra. Moreover, for the same TA coverage, desorption for low and high Ni coverage results in the same products, but with lower yields of H<sub>2</sub>, H<sub>2</sub>O and CO for small Ni clusters. In this respect, to allow a more direct comparison, some of the TPD spectra for TA adsorption on the TiO<sub>2</sub> surface, on the Ni-covered one and on Ni(111) are compared in figure 6.9.  $M/z$  44 has been selected as exemplary case since, as shown previously in the chapter, H<sub>2</sub> and CO contributions may be already present on Ni surfaces before TA adsorption. Only one dose has been selected for each system, to be able to compare, as far as possible, similar equivalent TA depositions.

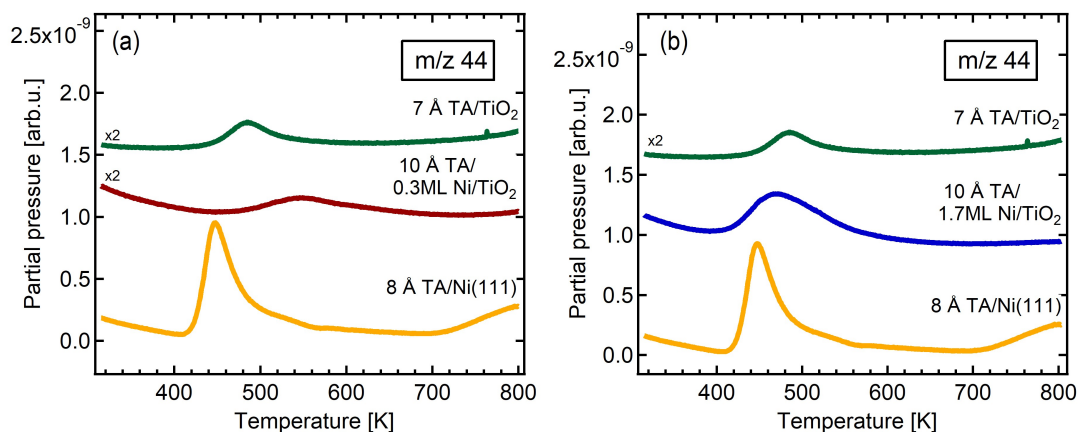


Figure 6.9: (a) Comparison of the TPD spectra of  $m/z$  44 ( $\text{CO}_2^+$ ) for 7 Å TA/TiO<sub>2</sub>, 8 Å TA/Ni(111) and 10 Å TA/0.3 ML Ni/TiO<sub>2</sub>. (b) Comparison of the TPD spectra of  $m/z$  44 ( $\text{CO}_2^+$ ) for 7 Å TA/TiO<sub>2</sub>, 8 Å TA/Ni(111) and 10 Å TA/1.7 ML Ni/TiO<sub>2</sub>. The recorded spectra are vertically shifted arbitrarily for the sake of clarity.

One first aspect that can be remarked is that for an equivalent Ni thickness of 0.3 ML, the desorption traces of TA/Ni/TiO<sub>2</sub> deviate from those for TA/TiO<sub>2</sub>(110). At the same time the shape of the spectrum recorded for TA on 1.7 ML Ni/TiO<sub>2</sub>(110) appears quite different from that of TA on Ni(111). One possible reason is that Ni clusters described in chapter 5 does not seem to present ordered structures. It is possible that the resolution achieved with the STM tip does not allow to resolve small details in the nanoscale on Ni clusters. Nevertheless, it is however certain that Ni clusters in our work appear very different from the hut-clusters reported by Tanner with very defined shapes and lateral facets, which were attributed to {111} and {100} facets. Hence, the {111} facets are probably not the dominant ones in our system.

More precise comparisons between the desorption traces of TA recorded for TiO<sub>2</sub>, for a Ni-covered one and for Ni(111) are difficult to perform for several reasons. Drawing con-

clusions in terms of the exact desorption temperature peak positions is complicated by the fact that the temperatures are recorded by means of a thermocouple spot-welded on the sample holder and not directly on the sample surface. This may be an issue when comparing desorption traces of metal and oxide samples, since the metal surface temperature is expected to be greater due to its higher thermal conductivity. Another issue that comes out when performing desorption studies on supported Ni clusters is that heating results in diffusion and partial encapsulation of Ni clusters. If sintering problems could in principle be ruled out by annealing the systems a first time before RR-TA exposure, encapsulation is always present. Previous studies showed that heating Ni clusters up to 550 K does not result in changes in the cluster morphology, while sintering and encapsulation were observed after heating up to 850 K [181].

Globally, even if a detailed analysis of TPD is complex due to both technical or intrinsic issues, some conclusions can be drawn on the global system. TPD traces recorded for Ni-covered TiO<sub>2</sub> have appeared quite different from those recorded on the TiO<sub>2</sub> surface as well as on Ni(111), suggesting that TA molecules are adsorbed on Ni nanoparticles, which possibly do not show dominant {111} facets.

One unresolved issue remains the lack of desorption feature for TA on 0.3 ML Ni/TiO<sub>2</sub>(110) at the desorption temperature observed for TA on TiO<sub>2</sub> in figure 6.9a. For a Ni dose of 0.3 ML, about 12% of the surface is covered by Ni, so that upon a high dose of TA of 10 Å, which exceeds the monolayer dose, the TiO<sub>2</sub> surface is in principle expected to be completely covered by TA molecules. As a matter of fact, both the comparison of the kinetics of TA adsorption on the TiO<sub>2</sub> surface and of a Ni covered one (figure 6.1) and the evolution of Ni 2p spectra (figure 6.3a) have suggested that TA effectively adsorbs on the TiO<sub>2</sub> substrate. It may be hypothesized that desorption of TA adsorbed on the TiO<sub>2</sub> surface is more complexed on Ni-containing surfaces due to desorption-readsorption phenomena of TA from the TiO<sub>2</sub> surface to Ni nanoparticles which explains the lack of clear desorption peak assigned to TA on TiO<sub>2</sub>.

### 6.3 Conclusion

After having considered Ni and TA depositions separately on the rutile TiO<sub>2</sub>(110) surface in the previous chapters, their combined adsorption was here addressed. The study of the complete catalytic system is a tricky challenge, further complicated because of the issues associated with doing infrared measurements on oxide surfaces. A complete understanding of the TA/Ni/TiO<sub>2</sub> system could not be reached only by means of XPS and TPD, nevertheless some interesting insights were gained. Photoemission data evidenced that Ni nanoparticles oxidise upon TA deposition, confirming the presence of the chiral modifier on the metal catalyst. However, the comparison of the kinetics of RR-TA adsorption on the clean TiO<sub>2</sub> surface and on a Ni-covered one evidenced minor differences, which could suggest that the chiral modifier adsorb both on the Ni catalyst and on the TiO<sub>2</sub> substrate. TPD spectra recorded for the TA/Ni/TiO<sub>2</sub> system appeared quite different from those recorded of TA on both TiO<sub>2</sub> and Ni(111) surfaces, suggesting that TA adsorb as well as on the oxide and metal catalyst and that Ni nanoparticles, which do not seem to be dominated by {111} facets. Overall, the combined XPS and TPD analysis pointed to the adsorption of TA molecules without a preferential adsorption on the metal catalyst with respect to the oxide surface.







---

## Conclusion

---

Heterogeneous enantioselective reactions are at the center of the production of useful chiral molecules in enantiomerically pure forms. Their fundamental importance in various fields, including pharmaceutical and agrochemical industries, stems from the fact that two enantiomers of a chiral compound may have opposite and possibly drastic physiological effects in living organisms. One successful approach involves the modification of a metal surface by the adsorption of a chiral modifier, responsible for inducing the asymmetry during the reaction. Despite its great potential and economic advantages, only a small number of successful heterogeneous supported systems have been developed so far. Moreover, most of fundamental works have been devoted to model systems based on single crystal metal surfaces while little is known on the role of the oxide support in supported metal catalysts. To date, fundamental questions remain on the role of the oxide support on the chiral induction during the reaction.

In this context, the present thesis aimed at gaining new insight on the interactions at the molecular level between the different actors of an enantioselective catalytic system, namely chiral modifier, oxide support and metal catalyst. A surface science approach has been used, in which the chiral modifier and the metal catalyst have been deposited by evaporation onto planar oxide supports in the clean and controlled conditions of ultrahigh vacuum. By means of a combination of several surface science techniques, the as-prepared systems have been subsequently characterised in details, to provide fundamental insights into the physics and chemistry. Rutile  $\text{TiO}_2(110)$  single crystals, (R,R)-Tartaric Acid (RR-TA) molecules and Ni nanoparticles (Ni NPs) have been selected as model components to mimic the catalytic system. This choice owes to the possible characterisation of  $\text{TiO}_2$  surfaces by surface science techniques on one side and the efficiency of RR-TA molecules and Ni NPs as chiral modifier and metal catalyst, respectively, on the other.

The attention has been initially paid to a thorough surface-science study on the monolayer adsorption of (RR-TA) molecules on rutile  $\text{TiO}_2(110)$  single crystals. A comprehensive knowledge of the interaction between the chiral modifier and the oxide support is indeed at the heart of the conception of efficient oxide-supported enantioselective metal catalysts. The chemical state was obtained through a comparison of the X-ray Photoemission Spectroscopy (XPS) data for RR-TA adsorption on  $\text{TiO}_2(110)$  with those recorded for RR-TA on Au(111) and Cu(110), the adsorption on the two latter being well understood. From the XPS analysis of the energy splitting between the C 1s molecular components, RR-TA molecules are found to adsorb in a monotartrate form (only one carboxylic group is deprotonated), an adsorption state confirmed as well by High Resolution Electron Energy Loss Spectroscopy experiments. Moreover, Ultraviolet Photoemission Spectroscopy has evidenced the formation of an inward dipole upon RR-TA adsorption. The use of Scanning Tunnelling Microscopy (STM) imaging has shown that the molecular bonding sites are the  $\text{Ti}_{5c}$  atoms. Moreover, STM combined with Low Energy Electron Diffraction

(LEED) studies indicated the formation of a  $(2 \times 1)$  superstructure at saturation coverage. No extended chiral domains are formed suggesting that the TA behaviour on  $\text{TiO}_2(110)$  substantially differs from what is observed on  $\text{Cu}(110)$  or  $\text{Ni}(111)$ , revealing instead an adsorption geometry closer to that of TA on  $\text{Ni}(110)$ . Chirality is thus not induced at a global level, but only locally due to the inherent TA chiral behaviour. Gathering together all this information, a structural adsorption model is proposed, in which RR-TA molecules bound to two adjacent  $\text{Ti}_{5c}$  sites on the  $\text{TiO}_2(110)$  surface through both carboxylate O atoms, while the remaining carboxylic acid group is intact and protrudes above the surface layer.

RR-TA adsorption investigation on rutile  $\text{TiO}_2(110)$  is then extended to its molecular desorption, thermal decomposition behaviour and chemical bonding mechanism in the multilayer regime by Thermal Programmed Desorption (TPD) and XPS. TPD data evidence that molecules desorb more or less intact from the multilayer, while they decompose in the monolayer regime, which therefore implies a strong interaction with the oxide substrate. By means of both TPD and XPS, it is shown that further deposition of RR-TA molecules on the first saturated monolayer results in a multilayer growth regime where TA molecules are adsorbed intact, in the bi-acid form. Hence, the interface layer formed by monotartrate species leaves one available carboxylic group to form physisorbed multilayers via H-bond interactions, as confirmed by the estimation of the activation energy of desorption from TPD.

One major conclusion to be drawn from this first part of the study is that since RR-TA molecules adsorb on the  $\text{TiO}_2$  surface, enantioselective induction may not be limited to metallic surfaces but might be driven as well by the oxide support. Moreover, the formation at high coverages of an achiral unit cell by the adsorbed RR-TA molecules implies that any enantiospecificity to other species adsorbing on the  $\text{TA}/\text{TiO}_2$  surface must thus derive from short range molecular interactions.

The attention has been then turned to the adsorption of Ni on the  $\text{TiO}_2(110)$  surface alone. The first stages of Ni growth have been described with a local microscopic approach using STM. Ni is found to grow on the  $\text{TiO}_2(110)$  surface through a Volmer-Weber growth mode, as expected from thermodynamic considerations and previous works, forming clusters of nanometric size. Clusters are initially on average two atomic layers high, while at increasing coverage a 3D growth is more pronounced. In parallel to the morphologic study, XPS experiments have evidenced the prevailing metallic character of Ni clusters. Moreover, the modelling of XPS intensity has tentatively suggested that a hemisphere model seems to be in better accord with the experimental results. To overcome problems due to the STM tip convolution effects, Surface Differential Reflectivity Spectroscopy (SDRS) provided the opportunity to follow *in situ* and in real-time Ni growth on  $\text{TiO}_2(110)$  over a large range of coverage. Combined with dielectric simulations, qualitative information on the cluster shape has been gained by looking at the energy position of the plasmon resonances. This analysis led to the conclusion that 3D Ni clusters grow on the  $\text{TiO}_2$  surface, with an aspect ratio close to 2, which corresponds to a hemisphere. At last, by considering the evolution of the normalised integrated intensity of the SDRS signal at increasing Ni thickness, the different stages of the film formation were followed through the changes in the cluster aspect ratio and no beginning of coalescence was observed. Moreover, the differences observed in the normalised integrated intensity along the  $[001]$  and  $[1\bar{1}0]$  directions suggested an anisotropic growth of Ni nanoparticles, which appeared to be more elongated along the  $[001]$  direction due to the easiest diffusion along the  $\text{O}_{br}$  channels.

In the last part of the present work, the adsorption of both RR-TA molecules and Ni on the rutile  $\text{TiO}_2(110)$  surface has been considered, with the aim of exploring some aspects of the complete catalytic model system. Despite the great complexity of the system, further worsened by the absence of vibrational information, some insight is gained by means of XPS and TPD experiments. One first point that has been addressed by means of XPS concerns the possible preferential TA adsorption on either the metal catalyst or the oxide support. In principle, the presence of Ni nanoparticles provides a greater surface area and additional adsorption sites for TA molecules compared to the bare  $\text{TiO}_2(110)$  surface. In this respect, a comparison of the kinetics of RR-TA adsorption on the bare rutile surface and on a Ni covered one has evidenced minor differences between the two systems. Such variations, which remain within the experimental uncertainty, may suggest that RR-TA molecules adsorb as well as on the  $\text{TiO}_2$  substrate and the Ni catalyst. Nevertheless, TPD studies carried out to probe the decomposition of RR-TA molecules for a low Ni coverage have shown desorption traces quite different from those on the  $\text{TiO}_2$  and Ni(111) surfaces alone, suggesting that part of the molecules are effectively adsorbed on Ni that do not expose predominant  $\{111\}$  facets. This has been confirmed by XPS which has shown that Ni clusters become oxidised upon TA deposition. Overall, the adsorption of RR-TA molecules seem to take place on both the rutile surface and the Ni nanoparticles, apparently without preferential adsorption on the metal catalyst.

On a more applied perspective, enantioselective hydrogenation occurs on the metallic nanoparticles that will dissociate hydrogen. If a significant part of the chiral modifier adsorbs on the oxide support instead of the metal, it will be lost for the enantioselective catalytic reaction. The results presented here are thus a first step to tune the metal/modifier ratio in order to optimise the Ni decoration.

With respect to the conception of enantioselective catalytic systems, the present surface science investigation is a first but important step which opens up to several perceived prospects in different scientific directions. Despite the inherent difficulty of the system, it would be useful to complement this study with STM imaging to gain deeper knowledge on the anchoring mode of the chiral modifier on the Ni covered  $\text{TiO}_2(110)$  surface. It would be interesting to address the role of the oxide substrate in terms of different  $\text{TiO}_2$  polymorphs and surface structures (anatase *vs.* rutile), of surface defects density and hydration state of the surface which can be controlled at will through the sample preparation in UHV. An interesting aspect to tackle would be performing RR-TA deposition from aqueous solution, for example by means of an electrospray device. This different adsorption method will allow to bridge the gap between the model catalyst preparation used in the present work and one in a liquid state, more realistic from an industrial point of view.

Once completely characterised, the additional presence of a prochiral target molecule, ethyl pyruvate, on a model TA-modified Ni/ $\text{TiO}_2$  system could be considered, in order to determine the specific interactions of the target reactant with one of the surface components (oxide support, metal nanoparticle, chiral modifier), if any. Longer term prospects could involve testing the model catalytic system for a specific reaction, namely the enantioselective hydrogenation of ethyl pyruvate to ethyl lactate and gain a deeper insight into the reaction mechanisms.



---

## Bibliography

---

- [1] D. G. Blackmond. The origin of biological homochirality. *Cold Spring Harb Perspect Biol.*, 2(5):a002147, 2010.
- [2] C. J. Baddeley, T. E. Jones, A. G. Trant, K. E. Wilson. Fundamental investigations of enantioselective heterogeneous catalysis. *Top. Catal.*, 54(19-20):1348–1356, 2011.
- [3] Z. Wang, K. Ding, Y. Uozumi. An overview of heterogeneous asymmetric catalysis. In *Handbook of Asymmetric Heterogeneous Catalysis*, pages 1–24. Wiley-VCH Verlag GmbH & Co. KGaA, 2008.
- [4] S. M. Barlow, R. Raval. Complex organic molecules at metal surfaces: bonding, organisation and chirality. *Surf. Sci. Rep.*, 50(6-8):201–341, 2003.
- [5] C. J. Baddeley. Fundamental investigations of enantioselective heterogeneous catalysis. *Top. Catal.*, 25(1-4):17–28, 2003.
- [6] G. C. Bond, D. T. Thompson. Gold-catalysed oxidation of carbon monoxide. *Gold Bull.*, 33(2):41–50, 2000.
- [7] R. Meyer, C. Lemire, S. K. Shaikhutdinov, H.-J. Freund. Surface chemistry of catalysis by gold. *Gold Bull.*, 37(1-2):72–124, 2004.
- [8] I. Laoufi, M.-C. Saint-Lager, R. Lazzari, J. Jupille, O. Robach, S. Garaudée, G. Cabailh, P. Dolle, H. Cruguel, A. Bailly. Size and catalytic activity of supported gold nanoparticles: An in operando study during CO oxidation. *J. Phys. Chem. C*, 115(11):4673–4679, 2011.
- [9] G.C. Bond. The modification of catalytic properties by metal-support interactions. *Stud. Surf. Sci. Catal.*, 11:1–10, 1982.
- [10] C.-J. Pan, M.-C. Tsai, W.-N. Su, J. Rick, N. G. Akalework, A. K. Agegnehu, S.-Y. Cheng, B.-J. Hwang. Tuning/exploiting strong metal-support interaction (SMSI) in heterogeneous catalysis. *J. Taiwan Inst. Chem. E.*, 74:154–186, 2017.
- [11] A. Einstein. Concerning an heuristic point of view toward the emission and transformation of light. *Annalen Phys.*, 17:132–148, 1905.
- [12] K. Siegbahn. Electron spectroscopy for chemical analysis (E.S.C.A.). *Phil. Trans. R. Soc. Lond. A*, 268(1184):33–57, 1970.
- [13] C. D. Wagner, W. M. Riggs, L. E. Davis, J. F. Moulder, G. E. Muilenberg. *Handbook of X-ray photoelectron spectroscopy*. Perkin-Elmer Corporation, 1979.
- [14] D. P. Woodruff, T. A. Delchar. *Modern Techniques of Surface Science*. Cambridge University Press, 1994.

- [15] J. F. Watts, J. Wolstenholme. *An Introduction to Surface Analysis by XPS and AES*. John Wiley & Sons, Ltd, 2003.
- [16] S. Tanuma, C. J. Powell, D. R. Penn. Calculations of electron inelastic mean free paths. II. Data for 27 elements over the 50-2000 eV range. *Surf. Interface Anal.*, 17(13):911–926, 1991.
- [17] C. S. Fadley, D. A. Shirley. Electronic densities of states from X-ray photoemission spectroscopy. *Journal of research of the National Bureau of Standards - A. Physics and Chemistry*, 74A:543–558, 1970.
- [18] D. R. Vij. *Handbook of Applied Solid State Spectroscopy*. Springer U.S., 2006.
- [19] D. Briggs, M. P. Seah. *Practical Surface Analysis: Auger and X-ray photoelectron spectroscopy*. Practical Surface Analysis. Wiley, 1990.
- [20] K. Oura, M. Katayama, A. V. Zotov, V. G. Lifshits, A. A. Saranin. *Surface Science*. Springer Berlin Heidelberg, 2003.
- [21] H. Lüth. *Surfaces and Interfaces of Solids*. Springer Berlin Heidelberg, 1993.
- [22] J. M. Walls, R. Smith. *Surface science techniques*. Oxford, England; New York: Pergamon, 1994.
- [23] K. Prabhakaran, Y. Kobayashi, T. Ogino. Interference of Ag L radiation in the XPS of Si and Au using an Al/Mg twin anode. *Journal of Electron Spectroscopy and Related Phenomena*, 63(3):283–288, 1993.
- [24] D. A. Shirley. High-resolution X-ray photoemission spectrum of the valence bands of gold. *Phys. Rev. B*, 5(12):4709, 1972.
- [25] S. Tougaard. Quantitative analysis of the inelastic background in surface electron spectroscopy. *Surf. Interface Anal.*, 11(9):453–472, 1988.
- [26] M. R. Guascito, E. Mesto, C. Malitesta, R. A. Picca, F. Scordari. The effect of XPS background removing method on the appraisal of Ti and Fe: The case of phlogopites and brookite. *American Mineralogist*, 99(1):139–148, 2014.
- [27] S. Evans. Curve synthesis and optimization procedures for X-ray photoelectron spectroscopy. *Surf. Interface Anal.*, 17(2):85–93, 1991.
- [28] S. Hüfner. *Photoelectron Spectroscopy*. Springer Berlin Heidelberg, 2003.
- [29] S. Hofmann. *Auger- and X-Ray Photoelectron Spectroscopy in Materials Science*. Springer Berlin Heidelberg, 2013.
- [30] P. Ruffieux, P. Schwaller, O. Gröning, L. Schlapbach, P. Gröning, Q. Herd, D. Funemann, J. Westermann. Experimental determination of the transmission factor for the Omicron EA125 electron analyzer. *Review of Scientific Instruments*, 71:3634–3639, 2000.
- [31] J. J. Yeh, I. Lindau. Atomic subshell photoionization cross sections and asymmetry parameters:  $1 \leq z \leq 103$ . *Atomic Data and Nuclear Data Tables*, 32(1):1–155, 1985.
- [32] S. Tougaard. Quases-imfp-tpp2m software, <http://www.quases.com7products/quasesimfp-tpp2m/>.

- [33] S. Tanuma, C. J. Powell, D. R. Penn. Calculations of electron inelastic mean free paths for 31 materials. *Surf. Interface Anal.*, 11(11):577–589, 1988.
- [34] S. Tanuma, C. J. Powell, D. R. Penn. Calculations of electron inelastic mean free paths. III. Data for 15 inorganic compounds over the 50-2000 eV range. *Surf. Interface Anal.*, 17(13):927–939, 1991.
- [35] S. Tanuma, C. J. Powell, D. R. Penn. Calculations of electron inelastic mean free paths (IMFPPs). IV. Evaluation of calculated IMFPPs and of the predictive IMFPP formula TPP-2 for electron energies between 50 and 2000 eV. *Surf. Interface Anal.*, 20(1):77–89, 1993.
- [36] S. Tanuma, C. J. Powell, D. R. Penn. Calculations of electron inelastic mean free paths. V. Data for 14 organic compounds over the 50-2000 eV range. *Surf. Interface Anal.*, 21(3):165–176, 1994.
- [37] S. Tanuma, C. J. Powell, D. R. Penn. Calculations of electron inelastic mean free paths (IMFPPs) VI. Analysis of the Gries inelastic scattering model and predictive IMFPP equation. *Surf. Interface Anal.*, 25(1):25–35, 1997.
- [38] S. Tanuma, C. J. Powell, D. R. Penn. Calculation of electron inelastic mean free paths (IMFPPs) VII. Reliability of the TPP-2M IMFPP predictive equation. *Surf. Interface Anal.*, 35(3):268–275, 2003.
- [39] S. Tanuma, C. J. Powell, D. R. Penn. Calculations of electron inelastic mean free paths. *Surf. Interface Anal.*, 37(1):1–14, 2005.
- [40] W. F. Egelhoff, D. L. Perry, J. W. Linnett. UPS studies of the adsorption and decomposition of methanol and formaldehyde on a tungsten(100) surface. *J. Electron. Spectrosc. Relat. Phenom.*, 5(1):339–350, 1974.
- [41] B. Caglar, A. C. Kizilkaya, J. W. H. Niemantsverdriet, C. J. K.-J. Weststrate. Application of work function measurements in the study of surface catalyzed reactions on Rh(100). *Catal. Struct. React.*, 4(1):1–11, 2018.
- [42] V. E. Henrich, P. A. Cox. *The Surface Science of Metal Oxides*. Cambridge University Press, 1996.
- [43] A. Wieckowski. *Interfacial Electrochemistry: Theory, Experiment, and Applications*. CRC Press, 1999.
- [44] K. Besocke. An easily operable scanning tunneling microscope. *Surf. Sci.*, 181(1-2):145–153, 1987.
- [45] H. B. Michaelson. The work function of the elements and its periodicity. *J. Appl. Phys.*, 48(11):4729–4733, 1977.
- [46] C. J. Chen. *Introduction to scanning tunneling microscopy*. Oxford University Press New York, 1993.
- [47] J. Bardeen. Tunnelling from a many-particle point of view. *Phys. Rev. Lett.*, 6:57–59, 1961.
- [48] I. Giaever. Energy gap in superconductors measured by electron tunneling. *Phys. Rev. Lett.*, 5:147–148, 1960.



- [49] J. P. Ibe, P. P. Bey, S. L. Brandow, R. A. Brizzolara, N. A. Burnham, D. P. DiLella, K. P. Lee, C. R. K. Marrian, R. J. Colton. On the electrochemical etching of tips for scanning tunneling microscopy. *J. Vac. Sci. Technol. A*, 8(4):3570–3575, 1990.
- [50] H. Ibach. *Physics of Surfaces and Interfaces*. Springer Berlin Heidelberg, 2006.
- [51] P.A. Redhead. Thermal desorption of gases. *Vacuum*, 12:203–211, 1962.
- [52] D. A. King. Thermal desorption from metal surfaces: a review. *Surf. Sci.*, 47:384–402, 1975.
- [53] F. Hoffmann. Infrared reflection-absorption spectroscopy of adsorbed molecules. *Surf. Sci. Rep.*, 3(2-3):107, 1983.
- [54] M. Che, J. C. Védrine, editor. *Characterization of Solid Materials and Heterogeneous Catalysts*. Wiley-VCH Verlag GmbH & Co. KGaA, 2012.
- [55] J. T. Yates, T. E. Madey, editor. *Vibrational Spectroscopy of Molecules on Surfaces*. Springer US, 1987.
- [56] R. G. Greenler. Infrared study of adsorbed molecules on metal surfaces by reflection techniques. *J. Chem. Phys.*, 44(1):310–315, 1966.
- [57] T. Buffeteau, B. Desbat, J. M. Turelet. Polarization modulation FT-IR spectroscopy of surfaces and ultra-thin films: Experimental procedure and quantitative analysis. *Appl. Spectrosc.*, 45(3):380–389, 1991.
- [58] E. A. Monyoncho, V. Zamlyunny, T. K. Woo, E. A. Baranova. The utility of polarization modulation infrared reflection absorption spectroscopy (PM-IRRAS) in surface and in situ studies: new data processing and presentation approach. *Analyst*, 143(11):2563–2573, 2018.
- [59] A. A. Lucas, M. Šunjić. Fast-electron spectroscopy of collective excitations in solids. *Prog. Surf. Sci.*, 2:75–137, 1972.
- [60] H. Ibach. *Electron Energy Loss Spectroscopy and Surface Vibrations*. Elsevier, 1982.
- [61] G. Bracco, B. Holst, editor. *Surface Science Techniques*. Springer Berlin Heidelberg, 2013.
- [62] P. A. Thiry, M. Liehr, J. J. Pireaux, R. Caudano. Electron interaction mechanisms in high resolution electron energy loss spectroscopy. *Phys. Scr.*, 35(3):368–379, 1987.
- [63] R. E. Palmer, P. J. Rous. Resonances in electron scattering by molecules on surfaces. *Rev. Mod. Phys.*, 64(2):383–440, 1992.
- [64] A. A. Lucas, M. Šunjić. Fast-electron spectroscopy of surface excitations. *Phys. Rev. Lett.*, 26(5):229–232, 1971.
- [65] E. Evans, D. L. Mills. Theory of inelastic scattering of slow electrons by long-wavelength surface of optical phonons: Multiphonon processes. *Phys. Rev. B*, 7(2):853–868, 1973.
- [66] D. L. Mills. The scattering of low energy electrons by electric field fluctuations near crystal surfaces. *Surf. Sci.*, 48(1):59–79, 1975.

- [67] A. A. Lucas, J.P. Vigneron. Theory of electron energy loss spectroscopy from surfaces of anisotropic materials. *Solid State Commun.*, 49(4):327–330, 1984.
- [68] R. Lazzari, J. Li, J. Jupille. Dielectric study of the interplay between charge carriers and electron energy losses in reduced titanium dioxide. *Phys. Rev. B*, 98(7), 2018.
- [69] J. Li. *Origin, location and transport of excess electrons in titanium dioxide*. Ph.D. thesis, Université Pierre et Marie Curie - Paris VI, 2016.
- [70] B. E. Hayden. Vibrational spectroscopy of oxide surfaces. In D.P. Woodruff, editor, *Oxide Surfaces*, volume 9, pages 514–546. Elsevier Science, 2001. Chapter 13.
- [71] P. A. Cox, W. R. Flavell, A. A. Williams, R. G. Egdell. Application of Fourier transform techniques to deconvolution of HREEL spectra. *Surf. Sci.*, 152-153:784–790, 1985.
- [72] R. Lazzari, J. Jupille. Quantitative analysis of nanoparticle growth through plasmonics. *Nanotechnology*, 22(44):445703, 2011.
- [73] R. Lazzari, J. Jupille, R. Cavallotti, I. Simonsen. Model-free unraveling of supported nanoparticles plasmon resonance modes. *J. Phys. Chem. C*, 118(13):7032–7048, 2014.
- [74] C. J. Baddeley, N. V. Richardson. Chirality at metal surfaces. In *Scanning Tunneling Microscopy in Surface Science*, pages 1–27. Wiley-VCH Verlag GmbH & Co. KGaA, 2010.
- [75] K. H. Ernst. Molecular chirality at surfaces. *Phys. Status Solidi B*, 249(11):2057–2088, 2012.
- [76] R. S. Cahn, C. Ingold, V. Prelog. Specification of molecular chirality. *Angew. Chem. Int. Ed.*, 5(4):385–415, 1966.
- [77] F. Zaera. Chiral modification of solid surfaces: A molecular view. *J. Phys. Chem. C*, 112(42):16196–16203, 2008.
- [78] ACS. Molecule of the week archive. Thalidomide, <https://www.acs.org/content/acs/en/molecule-of-the-week/archive/t/thalidomine.html>.
- [79] D. Y. Murzin, P. Mäki-Arvela, E. Toukoniitty, T. Salmi. Asymmetric heterogeneous catalysis: Science and engineering. *Cat. Rev.*, 47(2):175–256, 2005.
- [80] A. J. Gellman, W. T. Tysoe, F. Zaera. Surface chemistry for enantioselective catalysis. *Catal. Lett.*, 145(1):220–232, 2014.
- [81] T. Mallat, E. Orglmeister, A. Baiker. Asymmetric catalysis at chiral metal surfaces. *Chem. Rev.*, 107(11):4863–4890, 2007.
- [82] G. Webb, P.B. Wells. Asymmetric hydrogenation. *Catal. Today*, 12(2-3):319–337, 1992.
- [83] A. Baiker. Chiral catalysis on solids. *Curr. Opin. Solid State Mater. Sci.*, 3(1):86–93, 1998.
- [84] M. Heitbaum, F. Glorius, I. Escher. Asymmetric heterogeneous catalysis. *Angew. Chem. Int. Ed.*, 45(29):4732–4762, 2006.

- [85] Y. Orito, S. Imai, S. Niwa, G.-H. Nguyen. *J. of Synth. Org. Chem. Jpn.*, 37(2):173–174, 1979.
- [86] Y. Orito, S. Imai, S. Niwa. *J. Chem. Soc. Jpn.*, (8):1118–1120, 1979.
- [87] Y. Orito, S. Imai, S. Niwa. *J. Chem. Soc. Jpn.*, (4):670–672, 1980.
- [88] Y. Izumi. Modified Raney Nickel (MRNi) catalyst: Heterogeneous enantio-differentiating (asymmetric) catalyst. In *Adv. Catal.*, pages 215–271. Elsevier, 1983.
- [89] H. U. Blaser. Enantioselective synthesis using chiral heterogeneous catalysts. *Tetrahedron: Asymmetry*, 2(9):843–866, 1991.
- [90] A. G. Trant, C. J. Baddeley. Surface chemistry underpinning enantioselective heterogeneous catalysis: Supramolecular self-assembly of chiral modifiers and pro-chiral reagents on Ni{111}. *J. Phys. Chem. C*, 115(4):1025–1030, 2010.
- [91] G. Bond, P. A. Meheux, A. Ibbotson, P. B. Wells. Origin of enhanced rate in the platinum-catalysed enantioselective hydrogenation of methyl pyruvate. *Catal. Today*, 10(3):371–378, 1991.
- [92] A. Hoek, W. M. H. Sachtler. Enantioselectivity of nickel catalysts modified with tartaric acid or nickel tartrate complexes. *J. Catal.*, 58(2):276–286, 1979.
- [93] A. Baiker. Progress in asymmetric heterogeneous catalysis: Design of novel chirally modified platinum metal catalysts. *J. Mol. Catal. A: Chem.*, 115(3):473–493, 1997.
- [94] Y. Nitta. Effect of preparation variables on enantioselectivity of supported nickel catalysts modified with tartaric acid. *J. Catal.*, 74(2):382–392, 1982.
- [95] Y. Nitta. Effect of supports on enantioselectivity of modified Ni catalyst. *J. Catal.*, 79(2):475–480, 1983.
- [96] A. Wolfson, S. Geresh, M.V. Landau, M. Herskowitz. Enantioselective hydrogenation of methyl acetoacetate catalyzed by nickel supported on activated carbon or graphite. *Appl. Catal., A*, 208(1-2):91–98, 2001.
- [97] D. Jo, J. S. Lee, K. H. Lee. Enantio-differentiating hydrogenation of methyl acetoacetate over tartaric acid-modified nickel catalysts: effects of preparation method of supported nickel on activity and selectivity of catalysts. *J. Mol. Catal. A: Chem.*, 222(1-2):199–205, 2004.
- [98] M. Keane. The enantioselective hydrogenation of methyl acetoacetate over supported nickel catalysts: I. The modification procedure. *J. Catal.*, 136(1):1–15, 1992.
- [99] D. Wang, H.-J. Yan, Q.-M. Xu, M.-J. Han, L.-J. Wan. Surface structure of heterogeneous catalysts: Cinchona and tartaric acid on solid surface. *Top. Catal.*, 35(1-2):131–139, 2005.
- [100] M.-A. López-Martínez, I. J. Shannon. Tartaric acid-Ni supported catalysts obtained from hydrotalcite-like compounds: Effects of catalyst preparation variables on enantioselectivity. *Appl. Catal., A*, 435-436:123–130, 2012.

- [101] A. A. Choliq, J. Watanabe, T. Misaki, Y. Okamoto, T. Sugimura. Enantioselective hydrogenation of  $\beta$ -aryl- $\beta$ -ketoester over  $\alpha$ -hydroxy acid-modified Raney nickel catalysts: competitive hydrogenation with methyl acetoacetate. *Tetrahedron: Asymmetry*, 27(14-15):657–662, 2016.
- [102] H.-U. Blaser, H.-P. Jalett, M. Müller, M. Studer. Enantioselective hydrogenation of  $\alpha$ -ketoesters using cinchona modified platinum catalysts and related systems: A review. *Catal. Today*, 37(4):441–463, 1997.
- [103] E. Toukoniitty, P. Mäki-Arvela, N. Kumar, T. Salmi, D. Yu. Murzin. Continuous enantioselective hydrogenation of ethylbenzoylformate over Pt/Al<sub>2</sub>O<sub>3</sub> catalyst: Bed dilution effects and cinchonidine adsorption study. *Catal. Lett.*, 95(3/4):179–183, 2004.
- [104] C. F. McFadden, P. S. Cremer, A. J. Gellman. Adsorption of chiral alcohols on “chiral” metal surfaces. *Langmuir*, 12(10):2483–2487, 1996.
- [105] A. Ahmadi, G. Attard, J. Feliu, A. Rodes. Surface reactivity at “chiral” platinum surfaces. *Langmuir*, 15(7):2420–2424, 1999.
- [106] G. A. Attard. Electrochemical studies of enantioselectivity at chiral metal surfaces. *J. Phys. Chem. B*, 105(16):3158–3167, 2001.
- [107] J. Cronin, J. Reisse. Chirality and the origin of homochirality. In *Lectures in Astrobiology*, pages 473–515. Springer Berlin Heidelberg, 2005.
- [108] D. A. Duncan, W. Unterberger, D. C. Jackson, M. K. Knight, E. A. Kröger, K. A. Hogan, C. L. A. Lamont, T. J. Lertholi, D. P. Woodruff. Quantitative local structure determination of R,R-tartaric acid on Cu(110): Monotartrate and bitartrate phases. *Surf. Sci.*, 606(17-18):1435–1442, 2012.
- [109] M. Schaechter. *Encyclopedia of Microbiology*. Elsevier Science, 2009.
- [110] M. Ortega Lorenzo, S. Haq, T. Bertrams, P. Murray, R. Raval, C. J. Baddeley. Creating chiral surfaces for enantioselective heterogeneous catalysis: R,R-tartaric acid on Cu(110). *J. Phys. Chem. B*, 103(48):10661–10669, 1999.
- [111] M. Ortega Lorenzo, C. J. Baddeley, C. Muryn, R. Raval. Extended surface chirality from supramolecular assemblies of adsorbed chiral molecules. *Nature*, 404(6776):376–379, 2000.
- [112] M. Ortega Lorenzo, V. Humblot, P. Murray, C. J. Baddeley, S. Haq, R. Raval. Chemical transformations, molecular transport, and kinetic barriers in creating the chiral phase of (R,R)-Tartaric Acid on Cu(110). *J. Catal.*, 205(1):123–134, 2002.
- [113] R. Raval. Creating chiral architectures at metal surfaces. *J. Phys. Condens. Matter*, 14(16):4119–4132, 2002.
- [114] T. E. Jones, C. J. Baddeley. A RAIRS, STM and TPD study of the Ni/R,R-tartaric acid system: Modelling the chiral modification of Ni nanoparticles. *Surf. Sci.*, 513(3):453–467, 2002.
- [115] H.-J. Yan, D. Wang, M.-J. Han, L.-J. Wan, C.-L. Bai. Adsorption and coordination of tartaric acid enantiomers on Cu(111) in aqueous solution. *Langmuir*, 20(18):7360–7364, 2004.

- [116] U. Diebold. The surface science of titanium dioxide. *Surf. Sci. Rep.*, 48(5-8):53–229, 2003.
- [117] J. H. Braun, A. Baidins, R. E. Marganski. TiO<sub>2</sub> pigment technology: a review. *Prog. Org. Coat*, 20(2):105–138, 1992.
- [118] N. K. Awad, S. L. Edwards, Y. S. Morsi. A review of TiO<sub>2</sub> NTs on Ti metal: Electrochemical synthesis, functionalization and potential use as bone implants. *Mater. Sci. Eng. C*, 76:1401–1412, 2017.
- [119] M. A. Henderson. A surface science perspective on TiO<sub>2</sub> photocatalysis. *Surf. Sci. Rep.*, 66(6-7):185–297, 2011.
- [120] S. Bagheri, N. Muhd Julkapli, S. B. Abd Hamid. Titanium dioxide as a catalyst support in heterogeneous catalysis. *Sci. World J.*, 2014:1–21, 2014.
- [121] C. L. Pang, R. Lindsay, G. Thornton. Structure of clean and adsorbate-covered single-crystal rutile TiO<sub>2</sub> surfaces. *Chem. Rev.*, 113(6):3887–3948, 2013.
- [122] J. Jupille, G. Thornton, editor. *Defects at Oxide Surfaces*. Springer International Publishing, 2015.
- [123] O. Kubaschewski. The oxide handbook. *Berichte der Bunsengesellschaft für physikalische Chemie*, 86(8):761–762, 1982.
- [124] J. Ziólkowski. New method of calculation of the surface enthalpy of solids. *Surf. Sci.*, 209(3):536–561, 1989.
- [125] M. A. Henderson. A surface perspective on self-diffusion in rutile TiO<sub>2</sub>. *Surf. Sci.*, 419(2-3):174–187, 1999.
- [126] U. Diebold, J. Lehman, T. Mahmoud, M. Kuhn, G. Leonardelli, W. Hebenstreit, M. Schmid, P. Varga. Intrinsic defects on a TiO<sub>2</sub>(110)(1 × 1) surface and their reaction with oxygen: a scanning tunneling microscopy study. *Surf. Sci.*, 411(1-2):137–153, 1998.
- [127] S. Wendt, R. Schaub, J. Matthiesen, E. K. Vestergaard, E. Wahlström, M.D. Rasmussen, P. Thostrup, L. M. Molina, E. Lægsgaard, I. Stensgaard, B. Hammer, F. Besenbacher. Oxygen vacancies on TiO<sub>2</sub>(110) and their interaction with H<sub>2</sub>O and O<sub>2</sub>: A combined high-resolution STM and DFT study. *Surf. Sci.*, 598(1-3):226–245, 2005.
- [128] O. Bikondoa, C. L. Pang, R. Ithnin, C. A. Muryn, H. Onishi, G. Thornton. Direct visualization of defect-mediated dissociation of water on TiO<sub>2</sub>(110). *Nat. Mater.*, 5(3):189–192, 2006.
- [129] M. A. Henderson. Formic acid decomposition on the {110}-microfaceted surface of TiO<sub>2</sub>(100): Insights derived from <sup>18</sup>O-labeling studies. *J. Phys. Chem.*, 99(41):15253–15261, 1995.
- [130] H. Idriss, V.S. Lusvardi, M.A. Barteau. Two routes to formaldehyde from formic acid on TiO<sub>2</sub>(001) surfaces. *Surf. Sci.*, 348(1-2):39–48, 1996.
- [131] S. Chambers, M. A. Henderson, Y. B. Kim, S. Thevuthasan. Chemisorption geometry, vibrational spectra, and thermal desorption of formic acid on TiO<sub>2</sub>(110). *Surf. Rev. Lett.*, 5:381–385, 1998.

- [132] B. E. Hayden, A. King, M. A. Newton. Fourier transform reflection-absorption IR spectroscopy study of formate adsorption on  $\text{TiO}_2(110)$ . *J. Phys. Chem. B*, 103(1):203–208, 1999.
- [133] A. Mattsson, S. Hu, K. Hermansson, L. Österlund. Adsorption of formic acid on rutile  $\text{TiO}_2(110)$  revisited: An infrared reflection-absorption spectroscopy and density functional theory study. *J. Phys. Chem.*, 140(3):034705, 2014.
- [134] H. Onishi, Y. Iwasawa. STM-imaging of formate intermediates adsorbed on a  $\text{TiO}_2(110)$  surface. *Chem. Phys. Lett.*, 226(1-2):111–114, 1994.
- [135] H. Onishi, Y. Iwasawa. Removal of adsorbed organic molecules with scanning tunneling microscope: Formate anions on  $\text{TiO}_2(110)$  surface. *Jpn. J. Appl. Phys.*, 33(Part 2, No. 9B):L1338–L1341, 1994.
- [136] H. Onishi, T. Aruga, Y. Iwasawa. Switchover of reaction paths in the catalytic decomposition of formic acid on  $\text{TiO}_2(110)$  surface. *J. Catal.*, 146(2):557–567, 1994.
- [137] L.-Q. Wang, K. F. Ferris, A. N. Shultz, D. R. Baer, M. H. Engelhard. Interactions of  $\text{HCOOH}$  with stoichiometric and defective  $\text{TiO}_2(110)$  surfaces. *Surf. Sci.*, 380(2-3):352–364, 1997.
- [138] M. A. Henderson. Complexity in the decomposition of formic acid on the  $\text{TiO}_2(110)$  surface. *J. Phys. Chem. B*, 101(2):221–229, 1997.
- [139] D. I. Sayago, M. Polcik, R. Lindsay, R. L. Toomes, J. T. Hoefft, M. Kittel, D. P. Woodruff. Structure determination of formic acid reaction products on  $\text{TiO}_2(110)$ . *J. Phys. Chem. B*, 108(38):14316–14323, 2004.
- [140] A. Gutiérrez-Sosa, P. Martínez-Escolano, H. Raza, R. Lindsay, P.L. Wincott, G. Thornton. Orientation of carboxylates on  $\text{TiO}_2(110)$ . *Surf. Sci.*, 471(1-3):163–169, 2001.
- [141] Z. Chang, G. Thornton. Reactivity of thin-film  $\text{TiO}_2(110)$ . *Surf. Sci.*, 462(1-3):68–76, 2000.
- [142] R. Lindsay, S. Tomić, A. Wander, M. García-Méndez, G. Thornton. Low energy electron diffraction study of  $\text{TiO}_2(110)(2\times 1)\text{-[HCOO]}^-$ . *J. Phys. Chem. C*, 112(36):14154–14157, 2008.
- [143] M. Bowker, P. Stone, R. Bennett, N. Perkins. Formic acid adsorption and decomposition on  $\text{TiO}_2(110)$  and on  $\text{Pd/TiO}_2(110)$  model catalysts. *Surf. Sci.*, 511(1-3):435–448, 2002.
- [144] D. I. Sayago, M. Polcik, R. Lindsay, R. L. Toomes, J. T. Hoefft, M. Kittel, D. P. Woodruff. Structure determination of formic acid reaction products on  $\text{TiO}_2(110)$ . *J. Phys. Chem. B*, 108(38):14316–14323, 2004.
- [145] T. Qiu, M. A. Barteau. STM study of glycine on  $\text{TiO}_2(110)$  single crystal surfaces. *J. Colloid Interface Sci.*, 303(1):229–235, 2006.
- [146] I. Lyubinetsky, Z. Q. Yu, M. A. Henderson. Direct observation of adsorption evolution and bonding configuration of TMAA on  $\text{TiO}_2(110)$ . *J. Phys. Chem. C*, 111(11):4342–4346, 2007.

- [147] T. J. Lerotholi, E. A. Kröger, M. J. Knight, W. Unterberger, K. Hogan, D. C. Jackson, C. L. A. Lamont, D. P. Woodruff. Adsorption structure of glycine on  $\text{TiO}_2(110)$ : A photoelectron diffraction determination. *Surf. Sci.*, 603(15):2305–2311, 2009.
- [148] R. Tonner. Adsorption of proline and glycine on the  $\text{TiO}_2(110)$  surface: A density functional theory study. *ChemPhysChem*, 11(5):1053–1061, 2010.
- [149] Q. Guo, E.M. Williams. The effect of adsorbate–adsorbate interaction on the structure of chemisorbed overlayers on  $\text{TiO}_2(110)$ . *Surf. Sci.*, 433-435:322–326, 1999.
- [150] M. Buchholz, M. Xu, H. Noei, P. Weidler, A. Nefedov, K. Fink, Y. Wang, C. Wöll. Interaction of carboxylic acids with rutile  $\text{TiO}_2(110)$ : IR-investigations of terephthalic and benzoic acid adsorbed on a single crystal substrate. *Surf. Sci.*, 643:117–123, 2016.
- [151] J. Schnadt, J. N. O’Shea, L. Patthey, J. Schiessling, J. Krempaský, M. Shi, N. Mårtensson, P. A. Brühwiler. Structural study of adsorption of isonicotinic acid and related molecules on rutile  $\text{TiO}_2(110)$  II: XPS. *Surf. Sci.*, 544(1):74–86, 2003.
- [152] J. Schnadt, J. Schiessling, J. N. O’Shea, S. M. Gray, L. Patthey, M. K.-J. Johansson, M. Shi, J. Krempaský, J. Åhlund, P. G. Karlsson, P. Persson, N. Mårtensson, P. A. Brühwiler. Structural study of adsorption of isonicotinic acid and related molecules on rutile  $\text{TiO}_2(110)$  I: XAS and STM. *Surf. Sci.*, 540(1):39–54, 2003.
- [153] L. Patthey, H. Rensmo, P. Persson, K. Westermark, L. Vayssieres, A. Stashans, Å. Petersson, P. A. Brühwiler, H. Siegbahn, S. Lunell, N. Mårtensson. Adsorption of bi-isonicotinic acid on rutile  $\text{TiO}_2(110)$ . *J. Chem. Phys.*, 110(12):5913–5918, 1999.
- [154] P. Persson, S. Lunell, P. A. Brühwiler, J. Schnadt, S. Södergren, J. N. O’Shea, O. Karis, H. Siegbahn, N. Mårtensson, M. Bässler, L. Patthey. N 1s X-ray absorption study of the bonding interaction of bi-isonicotinic acid adsorbed on rutile  $\text{TiO}_2(110)$ . *J. Chem. Phys.*, 112(9):3945–3948, 2000.
- [155] M. Odelius, P. Persson, S. Lunell. Bi-isonicotinic acid on rutile (110): calculated molecular and electronic structure. *Surf. Sci.*, 529(1-2):47–58, 2003.
- [156] A. Tekiel, J. S. Prauzner-Bechcicki, S. Godlewski, J. Budzioch, M. Szymonski. Self-assembly of terephthalic acid on rutile  $\text{TiO}_2(110)$ : Toward chemically functionalized metal oxide surfaces. *J. Phys. Chem. C*, 112(33):12606–12609, 2008.
- [157] P. Rahe, M. Nimmrich, A. Nefedov, M. Naboka, Ch. Wöll, A. Kühnle. Transition of molecule orientation during adsorption of terephthalic acid on rutile  $\text{TiO}_2(110)$ . *J. Phys. Chem. C*, 113(40):17471–17478, 2009.
- [158] F. Zasada, W. Piskorz, S. Godlewski, J. S. Prauzner-Bechcicki, A. Tekiel, J. Budzioch, P. Cyganik, M. Szymonski, Z. Sojka. Chemical functionalization of the  $\text{TiO}_2(110)$ -(1 × 1) surface by deposition of terephthalic acid molecules. A density functional theory and scanning tunneling microscopy study. *J. Phys. Chem. C*, 115(10):4134–4144, 2011.
- [159] D. Costa, C.-M. Pradier, F. Tielens, L. Savio. Adsorption and self-assembly of bio-organic molecules at model surfaces: A route towards increased complexity. *Surf. Sci. Rep.*, 70(4):449–553, 2015.

- [160] E. Ataman, C. Isvoranu, J. Knudsen, K. Schulte, J.N. Andersen, J. Schnadt. Adsorption of L-cysteine on rutile TiO<sub>2</sub>(110). *Surf. Sci.*, 605(1-2):179–186, 2011.
- [161] C. T. Campbell. Ultrathin metal films and particles on oxide surfaces: structural, electronic and chemisorptive properties. *Surf. Sci. Rep.*, 27(1-3):1–111, 1997.
- [162] R. Persaud, T. E. Madey. Growth, structure and reactivity of ultrathin metal films on TiO<sub>2</sub> surfaces. In D.A. King, D.P. Woodruff, editor, *The chemical physics of solid surfaces*, volume 8. Elsevier, Amsterdam, 1997.
- [163] J. E. Bailie, G. J. Hutchings, S. O’Leary. Supported catalysts. In *Encyclopedia of Materials: Science and Technology*, pages 8986–8990. Elsevier, 2001.
- [164] M. Bäumer, H.-J. Freund. Metal deposits on well-ordered oxide films. *Prog. Surf. Sci.*, 61(7-8):127–198, 1999.
- [165] R. P. Gallenage, H. Yan, S. A. Tenney, N. Park, G. Henkelman, P. Albrecht, D. R. Mullins, D. A. Chen. Understanding the nucleation and growth of metals on TiO<sub>2</sub>: Co compared to Au, Ni, and Pt. *J. Phys. Chem. C*, 117(14):7191–7201, 2013.
- [166] D. W. Goodman. Model studies in catalysis using surface science probes. *Chem. Rev.*, 95(3):523–536, 1995.
- [167] P. L. J. Gunter, J. W. H. Niemantsverdriet, F. H. Ribeiro, G. A. Somorjai. Surface science approach to modeling supported catalysts. *Catal. Rev.*, 39(1-2):77–168, 1997.
- [168] S. P. Bates, G. Kresse, M. J. Gillan. A systematic study of the surface energetics and structure of TiO<sub>2</sub>(110) by first-principles calculations. *Surf. Sci.*, 385(2-3):386–394, 1997.
- [169] J. Zhou, Y.C. Kang, D.A. Chen. Controlling island size distributions: a comparison of nickel and copper growth on TiO<sub>2</sub>. *Surf. Sci.*, 537(1-3):L429–L434, 2003.
- [170] P. Li, J. Liu, N. Nag, P. A. Crozier. Dynamic nucleation and growth of Ni nanoparticles on high-surface area titania. *Surf. Sci.*, 600(3):693–702, 2006.
- [171] U. Diebold, J.-M. Pan, T. E. Madey. Ultrathin metal film growth on TiO<sub>2</sub>(110): an overview. *Surf. Sci.*, 331-333:845–854, 1995.
- [172] H. Onishi, T. Aruga, C. Egawa, Y. Iwasawa. Photoelectron spectroscopic study of clean and CO adsorbed Ni/TiO<sub>2</sub>(110) interfaces. *Surf. Sci.*, 233(3):261–268, 1990.
- [173] M.-C. Wu P. J. Møller. Epitaxial growth of ultrathin Ni films on NiO(100) and TiO<sub>2</sub>(110). *Surf. Sci.*, 279(1-2):23–32, 1992.
- [174] S. Bourgeois, P. Le Seigneur, M. Perdereau, D. Chandesris, P. Le Fèvre, H. Magnan. A surface EXAFS study of thin nickel deposits on (110) TiO<sub>2</sub> surfaces. *Thin Solid Films*, 304(1-2):267–272, 1997.
- [175] K. Fujikawa, S. Suzuki, Y. Koike, W.-J. Chun, K. Asakura. Self-regulated Ni cluster formation on the TiO<sub>2</sub>(110) terrace studied using scanning tunneling microscopy. *Surf. Sci.*, 600(10):117–121, 2006.
- [176] A. Sasahara, K. Hiehata, H. Onishi. Metal-to-oxide charge transfer observed by a kelvin probe force microscope. *Catal. Surv. Asia*, 13(1):9–15, 2009.



- [177] R. E. Tanner, I. Goldfarb, M. R. Castell, G. A. D. Briggs. The evolution of Ni nanoislands on the rutile  $\text{TiO}_2(110)$  surface with coverage, heating and oxygen treatment. *Surf. Sci.*, 486(3):167–184, 2001.
- [178] C. C. Kao, S. C. Tsai, M. K. Bahl, Y. W. Chung, W. J. Lo. Electronic properties, structure and temperature-dependent composition of nickel deposited on rutile titanium dioxide (110) surfaces. *Surf. Sci.*, 95(1):1–14, 1980.
- [179] S. A. Tenney, W. He, J. S. Ratliff, D. R. Mullins, D. A. Chen. Characterization of Pt-Au and Ni-Au clusters on  $\text{TiO}_2(110)$ . *Top. Catal.*, 54(1-4):42–55, 2011.
- [180] S. A. Tenney, W. He, C. C. Roberts, J. S. Ratliff, S. I. Shah, G. S. Shafai, V. Turkowski, T. S. Rahman, D. A. Chen. CO-induced diffusion of Ni atoms to the surface of Ni-Au clusters on  $\text{TiO}_2(110)$ . *J. Phys. Chem. C*, 115(22):11112–11123, 2011.
- [181] J. Zhou, S. Ma, Y. C. Kang, D. A. Chen. Dimethyl methylphosphonate decomposition on titania-supported Ni clusters and films: A comparison of chemical activity on different Ni surfaces. *J. Phys. Chem. B*, 108(31):11633–11644, 2004.
- [182] O. Ozturk, J. B. Park, T. J. Black, J. A. Rodriguez, J. Hrbek, D. A. Chen. Methanethiol chemistry on  $\text{TiO}_2$ -supported Ni clusters. *Surf. Sci.*, 602(19):3077–3088, 2008.
- [183] J. Dumesic. Migration of nickel and titanium oxide species as studied by in situ scanning transmission electron microscopy. *J. Catal.*, 99(1):79–87, 1986.
- [184] M. C. J. Bradford, M. A. Vannice. Catalytic reforming of methane with carbon dioxide over nickel catalysts I. Catalyst characterization and activity. *Appl. Catal. A*, 142(1):73–96, 1996.
- [185] C. Yang, C. Wöll. IR spectroscopy applied to metal oxide surfaces: adsorbate vibrations and beyond. *Adv. Phys.: X*, 2(2):373–408, 2017.
- [186] M. Xu, Y. Gao, Y. Wang, C. Wöll. Monitoring electronic structure changes of  $\text{TiO}_2(110)$  via sign reversal of adsorbate vibrational bands. *Phys. Chem. Chem. Phys.*, 12(15):3649, 2010.
- [187] W. N. Hansen. Electric fields produced by the propagation of plane coherent electromagnetic radiation in a stratified medium. *J. Opt. Soc. Am.*, 58(3):380, 1968.
- [188] W. N. Hansen. Reflection spectroscopy of adsorbed layers. *Symp. Faraday Soc.*, 4:27, 1970.
- [189] C. Yang, C. Wöll. IR spectroscopy applied to metal oxide surfaces: adsorbate vibrations and beyond. *Adv. Phys.*, 2(2):373–408, 2017.
- [190] J. A. Mielczarski R. H. Yoon. Fourier transform infrared external reflection study of molecular orientation in spontaneously adsorbed layers on low-absorption substrates. *J. Phys. Chem.*, 93(5):2034–2038, 1989.
- [191] A. Rieger, C. Sax, T. Bauert, C. Wäckerlin, K.-H. Ernst. Chiral molecules adsorbed on a solid surface: Tartaric acid diastereomers and their surface explosion on  $\text{Cu}(111)$ . *Chirality*, 30(4):369–377, 2018.

- [192] S. Baldanza, J. Ardini, A. Giglia, G. Held. Stereochemistry and thermal stability of tartaric acid on the intrinsically chiral Cu{531} surface. *Surf. Sci.*, 643:108–116, 2016.
- [193] K. L. Syres, A. G. Thomas, D. M. Graham, B. F. Spencer, W. R. Flavell, M. J. Jackman, V. R. Dhanak. Adsorption and stability of malonic acid on rutile TiO<sub>2</sub>(110), studied by near edge X-ray absorption fine structure and photoelectron spectroscopy. *Surf. Sci.*, 626:14–20, 2014.
- [194] W. Zhang, L. Cao, L. Wan, L. Liu, F. Xu. A photoelectron spectroscopy study on the interfacial chemistry and electronic structure of terephthalic acid adsorption on TiO<sub>2</sub>(110)-(1×1) surface. *J. Phys. Chem. C*, 117(41):21351–21358, 2013.
- [195] E. L. Bullock, L. Patthey, S. G. Steinemann. Clean and hydroxylated rutile TiO<sub>2</sub>(110) surfaces studied by X-ray photoelectron spectroscopy. *Surf. Sci.*, 352-354:504–510, 1996.
- [196] S. Yu, S. Ahmadi, M. Zuleta, H. Tian, K. Schulte, A. Pietzsch, F. Hennies, J. Weissenrieder, X. Yang, M. Göthelid. Adsorption geometry, molecular interaction, and charge transfer of triphenylamine-based dye on rutile TiO<sub>2</sub>(110). *J. Chem. Phys.*, 133(22):224704, 2010.
- [197] W. T. Petrie, J. M. Vohs. An HREELS investigation of the adsorption and reaction of formic acid on the (0001)-Zn surface of ZnO. *Surf. Sci.*, 245(3):315–323, 1991.
- [198] M. A. Henderson. An HREELS and TPD study of water on TiO<sub>2</sub>(110): the extent of molecular versus dissociative adsorption. *Surf. Sci.*, 355(1-3):151–166, 1996.
- [199] R. Lazzari, J. Li, J. Jupille. Spectral restoration in high resolution electron energy loss spectroscopy based on iterative semi-blind Lucy-Richardson algorithm applied to rutile surfaces. *Rev. Sci. Instrum.*, 86(1):013906, 2015.
- [200] H. Ashima, W. J. Chun, K. Asakura. Room-temperature-adsorption behavior of acetic anhydride on a TiO<sub>2</sub>(110) surface. *Surf. Sci.*, 601(8):1822–1830, 2007.
- [201] V. Humblot, S. Haq, C. Muryn, W. A. Hofer, R. Raval. From local adsorption stresses to chiral surfaces: (R,R)-tartaric acid on Ni(110). *J. Am. Chem. Soc.*, 124(3):503–510, 2002.
- [202] E. Chernysheva, W. Srour, B. Philippe, B. Baris, S. Chenot, R. F. Duarte, M. Gorgoi, H. Cruguel, H. Rensmo, H. Montigaud, J. Jupille, G. Cabailh, S. Grachev, R. Lazzari. Band alignment at Ag/ZnO(0001) interfaces: A combined soft and hard X-ray photoemission study. *Phys. Rev. B*, 97(23), 2018.
- [203] J. H. Moore, N. Spencer, W. Klemperer. Encyclopedia of chemical physics and physical chemistry. *Phys. Today*, 56:66–67, 2003.
- [204] A. G. Thomas, W. R. Flavell, A. K. Mallick, A. R. Kumarasinghe, D. Tsoutsou, N. Khan, C. Chatwin, S. Rayner, G. C. Smith, R. L. Stockbauer, S. Warren, T. K. Johal, S. Patel, D. Holland, A. Taleb, F. Wiame. Comparison of the electronic structure of anatase and rutile TiO<sub>2</sub> single-crystal surfaces using resonant photoemission and X-ray absorption spectroscopy. *Phys. Rev. B*, 75(3), 2007.

- [205] P. Borghetti, E. Meriggio, G. Rousse, G. Cabailh, R. Lazzari, J. Jupille. Photoemission fingerprints for structural identification of titanium dioxide surfaces. *J. Phys. Chem. Lett.*, 7(16):3223–3228, 2016.
- [206] C. M. Yim, C. L. Pang, G. Thornton. Oxygen vacancy origin of the surface band-gap state of TiO<sub>2</sub>(110). *Phys. Rev. Lett.*, 104(3), 2010.
- [207] T. Minato, T. Susaki, S. Shiraki, H. S. Kato, M. Kawai, K. Aika. Investigation of the electronic interaction between TiO<sub>2</sub>(110) surfaces and Au clusters by PES and STM. *Surf. Sci.*, 566-568:1012–1017, 2004.
- [208] V. E. Henrich, G. Dresselhaus, H. J. Zeiger. Observation of two-dimensional phases associated with defect states on the surface of TiO<sub>2</sub>. *Phys. Rev. Lett.*, 36(22):1335–1339, 1976.
- [209] Z. Zhang, S.-P. Jeng, V. E. Henrich. Cation-ligand hybridization for stoichiometric and reduced TiO<sub>2</sub>(110) surfaces determined by resonant photoemission. *Phys. Rev. B*, 43(14):12004–12011, 1991.
- [210] I. D. Cocks, Q. Guo, R. Patel, E. M. Williams, E. Roman, J. L. de Segovia. The structure of TiO<sub>2</sub>(110) (1 × 1) and (1 × 2) surfaces with acetic acid adsorption — a PES study. *Surf. Sci.*, 377-379:135–139, 1997.
- [211] W. R. Duncan, O. V. Prezhdo. Theoretical studies of photoinduced electron transfer in dye-sensitized TiO<sub>2</sub>. *Annu. Rev. Phys. Chem.*, 58(1):143–184, 2007.
- [212] C. Méthivier, V. Humblot, C.-M. Pradier. UHV deposition of the Gly-Pro dipeptide on Cu(110) by sublimation or electrospray ionization. *J. Phys. Chem. C*, 120(48):27364–27368, 2016.
- [213] J. N. O’Shea, J. B. Taylor, L. C. Mayor, J. C. Swarbrick, J. Schnadt. Molecular damage in bi-isonicotinic acid adsorbed on rutile TiO<sub>2</sub>(110). *Surf. Sci.*, 602(9):1693–1698, 2008.
- [214] E. Soria, E. Román, E.M. Williams, J.L. de Segovia. Observations with synchrotron radiation (20-120 eV) of the TiO<sub>2</sub>(110)-glycine interface. *Surf. Sci.*, 433-435:543–548, 1999.
- [215] J. Ben Taylor, Louise C. Mayor, Janine C. Swarbrick, James N. O’Shea, Joachim Schnadt. Charge-transfer dynamics at model metal-organic solar cell surfaces. *J. Phys. Chem. C*, 111(44):16646–16655, 2007.
- [216] A. J. Gellman, Y. Huang, X. Feng, V. V. Pushkarev, B. Holsclaw, B. S. Mhatre. Superenantioselective chiral surface explosions. *J. Am. Chem. Soc.*, 135(51):19208–19214, 2013.
- [217] T. E. Jones, C. J. Baddeley. An investigation of the adsorption of (R,R)-tartaric acid on oxidised Ni{111} surfaces. *J. Mol. Catal. A: Chem.*, 216(2):223–231, 2004.
- [218] W. A. Hofer, V. Humblot, R. Raval. Conveying chirality onto the electronic structure of achiral metals: (R,R)-tartaric acid on nickel. *Surf. Sci.*, 554(2-3):141–149, 2004.
- [219] V. Humblot, S. Haq, C. Muryn, R. Raval. (R,R)-tartaric acid on Ni(110): the dynamic nature of chiral adsorption motifs. *J. Catal.*, 228(1):130–140, 2004.

- [220] M. Mahapatra W. T. Tysoe. Structure and decomposition pathways of D-(-)-tartaric acid on Pd(111). *Surf. Sci.*, 629:132–138, 2014.
- [221] V. Humblot, M. Ortega Lorenzo, C. J. Baddeley, S. Haq, R. Raval. Local and global chirality at surfaces: Succinic acid versus tartaric acid on Cu(110). *J. Am. Chem. Soc.*, 126(20):6460–6469, 2004.
- [222] B. S. Mhatre, V. Pushkarev, B. Holsclaw, T. J. Lawton, E. C. H. Sykes, A. J. Gellman. A window on surface explosions: Tartaric acid on Cu(110). *J. Phys. Chem. C*, 117(15):7577–7588, 2013.
- [223] B. Behzadi, S. Romer, R. Fasel, K.-H. Ernst. Chiral recognition in surface explosion. *J. Am. Chem. Soc.*, 126(30):9176–9177, 2004.
- [224] C. Roth, K.-H. Ernst. Surface explosion chemistry of malic acid on Cu(110). *Top. Catal.*, 54(19-20):1378–1383, 2011.
- [225] NIST Mass Spectrometry Data Center. (R,R)-Tartaric acid, <https://webbook.nist.gov/cgi/cbook.cgi?id=c87694&mask=200#mass-spec>.
- [226] P. A. Redhead. Thermal desorption of gases. *Vacuum*, 12(4):203–211, 1962.
- [227] H. T. Le, R. Lazzari, J. Goniakowski, R. Cavallotti, S. Chenot, C. Noguera, J. Jupille, A. Koltsov, J.-M. Mataigne. Tuning adhesion at metal/oxide interfaces by surface hydroxylation. *J. Phys. Chem. C*, 121(21):11464–11471, 2017.
- [228] S. Scheiner. *Hydrogen bonding; a theoretical perspective*. Oxford University Press, New York, 1997.
- [229] M. Wühn, J. Weckesser, C. Wöll. Bonding and orientational ordering of long-chain carboxylic acids on Cu(111): Investigations using X-ray absorption spectroscopy. *Langmuir*, 17(24):7605–7612, 2001.
- [230] W. Zhang, A. Nefedov, M. Naboka, L. Cao, C. Wöll. Molecular orientation of terephthalic acid assembly on epitaxial graphene: NEXAFS and XPS study. *Phys. Chem. Chem. Phys.*, 14(29):10125, 2012.
- [231] Gwyddion, <http://gwyddion.net/>.
- [232] D. A. Chen, M. C. Bartelt, R. Q. Hwang, K. F. McCarty. Self-limiting growth of copper islands on TiO<sub>2</sub>(110)-(1 × 1). *Surf. Sci.*, 450(1-2):78–97, 2000.
- [233] H. C. Lee, B. M. Kim, C. K. Jeong, R. Toyoshima, H. Kondoh, T. Shimada, K. Mase, B. Mao, Z. Liu, H. Lee, C.-Q. Huang, W. X. Li, P. N. Ross, B. S. Mun. Surface segregation and oxidation of Pt<sub>3</sub>Ni(111) alloys under oxygen environment. *Catal. Today*, 260:3–7, 2016.
- [234] A. P. Grosvenor, M. C. Biesinger, R. St. C. Smart, N. S. McIntyre. New interpretations of XPS spectra of nickel metal and oxides. *Surf. Sci.*, 600(9):1771–1779, 2006.
- [235] M. C. Biesinger, B. P. Payne, L. W. M. Lau, A. Gerson, R. St. C. Smart. X-ray photoelectron spectroscopic chemical state quantification of mixed nickel metal, oxide and hydroxide systems. *Surf. Interface Anal.*, 41(4):324–332, 2009.

- [236] S. Halpegamage, Z.-H. Wen, X.-Q. Gong, M. Batzill. Monolayer intermixed oxide surfaces: Fe, Ni, Cr, and V oxides on rutile  $\text{TiO}_2(011)$ . *J. Phys. Chem. C*, 120(27):14782–14794, 2016.
- [237] J. G. Tao, J. S. Pan, C. H. A. Huan, Z. Zhang, J. W. Chai, S. J. Wang. Origin of XPS binding energy shifts in Ni clusters and atoms on rutile  $\text{TiO}_2$  surfaces. *Surf. Sci.*, 602(16):2769–2773, 2008.
- [238] M. Wagstaffe, H. Hussain, M. J. Acres, R. Jones, K. L. Syres, A. G. Thomas. Structure and reactivity of a model oxide supported silver nanocluster catalyst studied by near ambient pressure X-ray photoelectron spectroscopy. *J. Phys. Chem. C*, 121(39):21383–21389, 2017.
- [239] D. Bedeaux, J. Vlieger. A phenomenological theory of the dielectric properties of thin films. *Physica*, 67(1):55–73, 1973.
- [240] D. Bedeaux, J. Vlieger. A statistical theory of the dielectric properties of thin island films. *Physica*, 73(2):287–311, 1974.
- [241] J. Vlieger, D. Bedeaux. A statistical theory for the dielectric properties of thin island films. *Thin Solid Films*, 69(1):107–130, 1980.
- [242] D. Bedeaux, J. Vlieger. A statistical theory for the dielectric properties of thin island films: application and comparison with experimental results. *Thin Solid Films*, 103(3):265–281, 1983.
- [243] I. Simonsen, R. Lazzari, J. Jupille, S. Roux. Numerical modeling of the optical response of supported metallic particles. *Phys. Rev. B*, 61(11):7722–7733, 2000.
- [244] D. Bedeaux, J. Vlieger. *Optical Properties of Surfaces*. Imperial College Press, London, 2001.
- [245] R. Lazzari, I. Simonsen. GranFilm: a software for calculating thin-layer dielectric properties and Fresnel coefficients. *Thin Solid Films*, 419(1-2):124–136, 2002.
- [246] R. Lazzari. *Vers la maitrise de la croissance de couches minces: une étude par spectroscopie optique et d'électrons*. Ph.D. thesis, Université Paris XI, Orsay, 2000.
- [247] J. D. Jackson. *Classical Electrodynamics*, volume 67. Wiley & Sons, New York, 1975.
- [248] M. M. Wind, P. A. Bobbert, J. Vlieger, D. Bedeaux. The polarizability of a truncated sphere on a substrate II. *Physica A: Stat. Mech. Appl.*, 143(1-2):164–182, 1987.
- [249] M. M. Wind, J. Vlieger, D. Bedeaux. The polarizability of a truncated sphere on a substrate I. *Physica A: Stat. Mech. Appl.*, 141(1):33–57, 1987.
- [250] R. Lazzari, I. Simonsen, D. Bedeaux, J. Vlieger, J. Jupille. Polarizability of truncated spheroidal particles supported by a substrate: model and applications. *Eur. Phys. J. B*, 24(2):267–284, 2001.
- [251] R. Lazzari, S. Roux, I. Simonsen, J. Jupille, D. Bedeaux, J. Vlieger. Multipolar plasmon resonances in supported silver particles: The case of  $\text{Ag}/\alpha\text{-Al}_2\text{O}_3(0001)$ . *Phys. Rev. B*, 65(23), 2002.
- [252] Granfilm, <http://lnwww.insp.upmc.fr/axe4/oxydes/granfilm/granularfilm.html>.

## BIBLIOGRAPHY

---

- [253] M. Messaykeh. *A fundamental approach of the wetting at Zn/Al<sub>2</sub>O<sub>3</sub> interface: the effect of a Cr buffer*. Ph.D. thesis, Sorbonne Université, 2018.
- [254] E. Chernysheva. *Zinc oxide growth and its interfaces with metals observed by photoemission*. Ph.D. thesis, Université Pierre et Marie Curie, 2017.
- [255] E. D. Palik, editor. *Handbook of Optical Constants of Solids*. Elsevier, 1985.
- [256] Z. Pirzadeh. *On the coupling of the localized plasmon and interband transitions in nickel nanoantennas*. Thesis for the degree of licentiate of engineering, Chalmers University of Technology, Gothenburg, 2013.